Ferroelectric domains in barium titanate by Bragg coherent X-ray diffraction imaging

Jiecheng Diao

Thesis submitted for the requirements for the degree of Doctor of Philosophy

Supervised by Ian K. Robinson

Department of Physics and Astronomy

University College London

September 2022

Declaration

I, Jiecheng Diao, confirm that the work presented in this thesis is my own. Where information has been derived from other sources, I confirm that this has been indicated in the thesis.

Jiecheng Diao

September 2022

Abstract

My PhD work focused on studying the domain structures and the strain fields inside barium titanate (BaTiO$_3$) nanocrystals. The results on the domain structure study have already been published. The results on the stripe-like strain fields inside nanocrystals are finalized and there is a plan for publication.

The first question my PhD work wants to address is what the domain structures inside BTO nanoparticles exist and how they evolve with temperature and when crossing the phase transition. Bragg coherent X-ray diffraction imaging (BCDI) experiments on nominal 200 nm size BTO nanoparticles were carried out at the Diamond I13-1 beamline and the Advanced Photon Source 34-ID-C beamline. The 90° domain walls were tracked in detail when crossing the tetragonal-cubic phase transition. This is presented in Chapter 3.

Upon studying the domain structure inside BTO nanocrystals, some unexpected stripe-like strain fields were found. Crystals with clear facets were chosen to restore resolve the crystallographic direction, after which the strain field direction and periodicity were studied in detail. This is shown in Chapter 4.

To understand the temperature dependence of the strain stripes, in-situ BCDI experiments were done at ESRF ID-01 beamline. Faceted BTO nanocrystals were chosen for temperature study. The strain stripes were found to be stable and preserved at both tetragonal and cubic phase with at elevated temperatures. This is illustrated in Chapter 5.

The Finite element analysis (FEA) approach was utilized to understand the origins of the strain stripes. Different piezoelectric blocks were defined to simulate the domain structures inside a BTO crystal. 180° domain walls were found to give more strain stripes features than 90° domain walls in the simulation. This is covered in Chapter 6.

The same patch of BTO nanocrystals were also studied using an X-ray Free-electron Laser as a function of time delay after laser excitation. Rather than seeing any significant thermal expansion effects, the diffraction peaks were found to move perpendicular to the momentum transfer direction. This suggests a laser driven rotation of the crystal lattice, which is delayed by the aggregated

state of the crystals. Internal deformations associated with crystal contacts were also observed. These are shown in Chapter 7.

Acknowledgement

I would like to thank Prof. Ian Robinson for his kind supervision of my master and PhD study. Without his endless passions for science, I would never think a PhD could be this creative and interesting. His kind personality and strong knowledge in science is always an encouragement to me. I will always remember the many days and nights we spent around different beamlines. That is the highlight of my life.

I want to thank Ian's group members for all the time we worked together among different beamlines: Longlong, Ana and Tadesse. I want to thank Pavlo, Yaqi, Chunhai and Evgenios for their time and patience when teaching me how to grow epitaxial thin films. I want to thank the beamline staff at Diamond I13-1, I16, Advanced Photon Source 34-ID-C and European Synchrotron Radiation Facility ID-01 for all their help: Ross, Wonsuk, Steven, Edoardo, Xiaowen, Darren, Peng, Christoph and Gareth. I want to thank my collaborators for all the good time we spent together: Xiaowen, Luxi, Ana, Alice and Kieran.

I want to thank my wife Fangfang Zhu for her understanding and support when we are six thousand miles away during this four-year study. While I appreciate our relationship is not bothered by the long distance, I would like to stay together for the next period of my life.

Impact statement

The structure of the domains in barium titanate (BTO) nanocrystals are addressed in this thesis. Bragg coherent X-ray diffraction imaging (BCDI) was used to probe the displacement and strain distribution inside BTO crystals. Finite element analysis has been used to simulate the strain patterns from different domain configurations. Large 90° domains with size of 100nm were located in one BTO nanocrystal. New understanding of the classical phase reconstruction of the diffraction patterns was discovered: patterns with more than one centre usually failed. A useful trick was found to cut and split apart the two diffraction patterns on the detector images, and then reconstruct the two parts separately before combining the real space images together. The crystal was then heated up and cooled down across its tetragonal-cubic phase transition temperature of 120°C. The large 90° domains were found to come back at the same place after returning to the tetragonal phase from the cubic phase. During the BCDI experiments, some well-faceted crystals were observed by their strongly modulated diffraction fringes. This allowed the crystallographic orientations to be determined, fully in some cases, to establish a coordinate system to interpret the strains. When their strain components were calculated, some unexpected strain stripes were found. The directions of the strain stripes are mostly along {100} or {110} with a period of 30nm to 50nm. These strain components were found to exist in both tetragonal phase at room temperature and cubic phase at elevated temperature. These stripes and the conclusion that there is spontaneous domain formation in these 200nm crystals of BTO has never been seen before and may have significant impact on technology. It is worth noting that commercial multilayer ceramic capacitors, the preferred choice of today's electronics industry with production exceeding 1012 pieces per year, use nanosized BTO as their dielectric. Why the properties are enhanced by the nanomaterial are not fully understood at present, so the current thesis work is an important step towards that understanding.

Publications

(2020)

J. Diao, X. Shi, T. A. Assefa, L. Wu, A. F. Suzana, D. S. Nunes, D. Batey, S. Cipiccia, C. Rau, R. J. Harder, W. Cha and I. K. Robinson, Evolution of ferroelastic domain walls during phase transitions in barium titanate nanoparticles. *Physical Review Materials*, 2020. https://doi.org/10.1103/PhysRevMaterials.4.106001

J. Diao, M. Cherukara, R. Harder, X. Huang, F. Zhang, B. Chen, A. Ulvestad, S. Song, D. Zhu, D. Keen and Ian Robinson, Unusual breathing behavior of optically excited barium titanate nanocrystals. *Crystals*, 2020. https://doi.org/10.3390/cryst10050365

B. Chen, **J. Diao**, Q. Luo, J. Rawle, X. Liu, C. Nicklin, J. Shen, I. Robinson, In-situ investigation of crystallization and structural evolution of a metallic glass in three dimensions at nano-scale. *Materials & Design*, 2020. https://doi.org/10.1016/j.matdes.2020.108551

T. A. Assefa, Y. Cao, **J. Diao**, R. J. Harder, W. Cha, K. Kisslinger, G. D. Gu, J. M. Tranquada, M. P. M. Dean, and I. K. Robinson, Scaling behavior of low-temperature orthorhombic domains in the prototypical high-temperature superconductor La1.875Ba0.125CuO4. *Physical Review B*, 2020. https://doi.org/10.1103/PhysRevB.101.054104

(2021)

A. C. Estandarte, **J. Diao**, A. V. Llewellyn, A. Jnawali, T. M. M. Heenan, S. R. Daemi, J. J. Bailey, S. Cipiccia, D. Batey, X. Shi, C. Rau, D. J. L. Brett, R. Jervis, I. K. Robinson, and P. R. Shearing, Operando Bragg coherent diffraction imaging of LiNi0.8Mn0.1Co0.1O2 primary particles within commercially printed NMC811 electrode sheets. *ACS Nano*, 2021. https://doi.org/10.1021/acsnano.0c08575

L. Wu, S. Yoo, A. Suzana, T. Assefa, **J. Diao**, R. Harder, W. Cha, I. Robinson, Three-dimensional coherent X-ray diffraction imaging via deep convolutional neural networks. *NPJ Computational Materials*, 2021. https://doi.org/10.1038/s41524-021-00644-z

(2022)

X. Liu, X. Zhou, Q. Liu, **J. Diao**, C. Zhao, L. Li, Y. Liu, W. Xu, A. Daali, R. Harder, I. Robinson, M. Dahbi, J. Alami, G. Chen, G. Xu, K. Amine, Multiscale understanding of surface structural effects on high-temperature operational resiliency of layered oxide cathodes. *Advanced Materials*, 2022. https://doi.org/10.1002/adma.202107326

T. Liu, J. Liu, L. Liu, L. Yu, **J. Diao**, T. Zhou, S. Li, A. Dai, W. Zhao, Y. Ren, L. Wang, T. Wu, R. Qi, Y. Xiao, J. Zheng, W. Cha, R. Harder, I. Robinson, J. Wen, J. Lu, F. Pan, K. Amine, Origin of structural degradation in Li-rich layered oxide cathode. *Nature*, 2022. https://doi.org/10.1038/s41586-022-04689-y

(Other submitted works)

A. F. Suzana, S. Liu, **J. Diao**, L. Wu, T. A. Assefa, R. Harder, W. Cha, and I. K. Robinson, Structural explanation of the dielectric enhancement of barium titanate nanoparticles grown under hydrothermal conditions. (Submitted to Advanced Functional Materials)

L. Wu, W. Wang, T. A. Assefa, A. F. Suzana, **J. Diao**, R. J. Harder, W. Cha, M. P. M. Dean and I. K. Robinson, Anisotropy of Antiferromagnetic Domains in a Spin-orbit Mott Insulator. (Submitted to Physical Review Letter)

Contents

List of Tables

List of Figures

xvii

Chapter 1. Principles of X-ray

X-rays conform with wave-particle duality in quantum physics, where both wave and particle (photon) properties can be quantified. Considering the wave properties, X-rays are a form of electromagnetic radiation and its frequency spans from 30 PHz (10^{12} Hz) to 30EHz (10^{18} Hz) in the spectrum. They obey the general optical laws including reflection, refraction and diffraction. When considering the photon properties, X-rays can interact with matter by scattering (either elastic or inelastic) and absorption (fluorescence, photo-electron emission, Auger electrons). Important for experiments, X-rays can be counted.

Rontgen discovered the X-ray in 1895, which earned him the first Nobel prize in physics in 1901. Later, Rontgen found the X-ray is produced by using high energy electrons to hit a material target. This is still the efficient way to produce X-ray, as the typical lab-based X-ray tube using electrons to hit copper anode for this purpose. There are two types of X-rays generated through hitting the atom: characteristic X-rays and bremsstrahlung. When an electron hit on an atom, it could knock out the electron at the inner shell. The outer shell electron would then fill the inner vacancy and emit X-ray radiation that is characteristic according to the element. This is the so-called characteristic X-ray, which was discovered by Barkla in 1909 and won the Nobel prize in 1917. An empirical law was put forward by Moseley in 1913, which describes the frequency of characteristic X-ray been proportional to the square of atomic number ($f \propto Z^2$). Different to characteristic X-ray, Bremsstrahlung radiation doesn't have a typical frequency, but rather a broad distribution. This is produced when the incoming electron is slowed down when hitting the atom rather than knocking out electron on shell. According to the energy conservation, the energy of emitted X-ray would be the same with the energy loss due to the slowing down of electron.

The high penetration property of X-ray was immediately exploited to take transmission photo for medical application after the discovery. Hongzhang Li is the first Chinese to take the X-ray photo, who was a Chinese diplomat visiting Germany at that time. He took the X-ray photo seven month after the discovery of X-ray, in which he saw a bullet directly in his left face. He wrote the first

description of X-ray in Chinese: Clothes, flesh, blood, wood and stone are all gone away. The only thing left in photo are hardware and bones (凡衣服、血肉、木石诸质，尽化烟云；所留存镜中者，惟五金类及骨殖全副而已). He called this X-ray method "bone photography" in Chinese (照骨术). We now know that the photoelectric absorption of the X-ray beam is roughly proportional to the cube of atomic number and inverse cube of energy ($\tau \propto \left(\frac{Z}{E}\right)^3$). The harmful effect of X-ray to human tissues was gradually found, after cases of burns, hair loss and even death been reported due to continuous exposure to X-ray. Therefore, the static X-ray photo is usually performed instead of a dynamic one in modern medical radiography to reduce the exposure dose.

In this chapter, the scattering process is emphasized, which is directly linked to our present works.

1.1 X-ray Scattering

1.1.1 Classical scattering theory

Classical scattering is also termed as coherent scattering or Thomson scattering. As a transverse electromagnetic wave, X-ray can be diffracted to form constructive or destructive interferences. The only essential particle that interacts with the X-ray is the electron (as discussed below). Diffractions from other sources, such as atom, molecule, crystal or glass, can be viewed as the geometric and mathematical combination of the electron scattering. Different form factors are also developed to mathematically deduce the relations, as shown in below.

(a) An electron

The classical way to evaluate the scattering from a free electron is to put it in the X-ray beam and treat it as radiation source by vibration. Then the amplitude and intensity at a given point is formed. The intensity per unit area per unit time is an observable quantity and given by the Thomson scattering equation:

$$I_e = I_0 r_0^2 P \tag{1.1}$$

I_0 is the intensity at electron source. P is the polarization factor. For unpolarized X-ray beam, this factor is $\frac{(1+cos^2\psi)}{2}$. r_0 is the classical radius, or Thomson scattering length, given by:

$$r_0 = \frac{e^2}{4\pi\varepsilon_0 mc^2} = 2.82 \times 10^{-5}\text{Å} \ (SI) \tag{1.2}$$

e is the elementary charge (1.602×10^{-19} C). m is the electron mass (9.109×10^{-31} kg). ε_0 is the permittivity of free space (8.854×10^{-12} F/m). c is speed of light (2.998×10^8 m/s).

The first interesting fact is that the above equations prove the electron to be the only essential particle for diffracting X-rays, because the scattered intensity is direct proportional to charge and inverse proportional to the density mass. The neutron has no charge, so it will not scatter the incident X-ray. The proton has the same charge as electron, but the density mass is 1836 times bigger, making its scattering intensity 1836^2 times smaller.

The second interesting fact is that the Thomson scattering equation describes the total scattering from free electron. When consider the bounded electron in atom, the Thomson scattering equation still works. However, it split into coherent scattering part (Thomson scattering) and incoherent scattering part (Compton scattering).

$$I_e = I_{coh} + I_{Incoh} = I_e f^2 + I_e(1 - f^2) \tag{1.3}$$

f is the **scattering factor of an electron** and can be expressed as a function of scattering vector Q at point r:

$$f = \int \rho(r)e^{iQr}dv \tag{1.4}$$

Scattering vector is defined as:

$$Q = k_i - k_f \tag{1.5}$$

Here the $\rho(r)$ means the electron density inside the electron cloud, which can be thought of as a probability distribution. k_i and k_f are the incident and scattered wave vectors.

(b) An atom

The scattering from an atom with Z electrons can be viewed as a superposition of scattering from each electron. Therefore, the total coherent scattering can be expressed as:

$$I_{coh} = \sum_{j=1}^{Z} f_j^2 I_e = \left(\int \rho_j(r) e^{iQr} dv \right)^2 I_e \qquad (1.6)$$

The sum of these scattering factor from different electrons is usually defined as the **atomic form factor**, given by

$$f^0(Q) = \sum_{j=1}^{Z} f_j = \int \rho_a(r) e^{iQr} dr \qquad (1.7)$$

Here the $\rho_a(r)$ means the electron density in the atom.

(c) A unit cell

Similarly, the scattering from a unit cell with Z atoms can be viewed as the sum of each atom. This will form a new factor called **unit cell structure factor**, given by:

$$F_u(Q) = \sum_{j=1}^{Z} f_j^0 = \int \rho_u(r) e^{iQr} dr \qquad (1.8)$$

Here the $\rho_u(r)$ means the electron density in unit cell.

(d) A crystal

The interesting story happens in the scattering of a crystal, where it has periodic structure. A single electron has no periodicity, so is the atomic orbitals in one atom. The primitive unit cell will not have periodicity according to its definition. The lattice vector can be defined as:

$$R_n = n_1 a_1 + n_2 a_2 + n_3 a_3 \qquad (1.9)$$

Due to the periodicity of the lattice, the **scattering factor of a crystal** can be factorized as the product of unit cell form factor and lattice sum:

$$F_c(Q) = \sum F_u(Q) e^{iQr} \sum e^{iQR_n} \qquad (1.10)$$

The lattice sum is described by Bragg's law or Laue equation next, after which the unit cell form factor is discussed.

Bragg's law is first proposed by W.H. Bragg (the father) and W.L. Bragg (the son) in 1913, who won the Nobel prize in 1915 for determining crystal structure using X-ray. Figure 1.1 shows a typical diagram for illustrating Bragg's law. The incident X-ray beam is scattered by the plane of atoms. The optical path length difference (OPLD) for the scattering from two adjacent crystal planes is the function of d-spacing and incident angle. If the scattering from two adjacent crystal plane is in phase, or equivalently the OPLD equals to integer multiple of X-ray wavelength, then the constructive interference occurs and yields the strongest intensity. This relation is described by Bragg's equation:

$$L_{OPLD} = 2dsin\theta = n\lambda \qquad (1.11)$$

For fulfil this equation, there is clearly an upper limit for the X-ray wavelength:

$$\lambda < 2d \qquad (1.12)$$
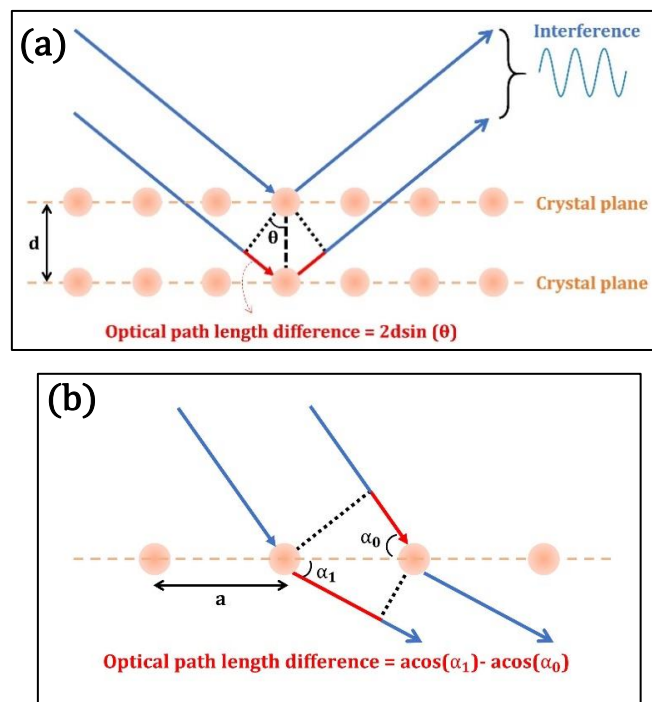
Figure 1. 1The schematic diagram to illustrate constructive diffraction condition. (a) Bragg geometry. (b) Laue geometry.

Bragg's law only involves the lattice point in real space and the diffraction condition can be simply deduced from geometry. Therefore, it gives a clean image of how diffraction happens in the viewpoint of crystal plane.

Laue deduced a similar relation between incident and diffracted X-ray beam, which is now termed as Laue equations. Laue also received Nobel prize in 1914 for the discovery of X-ray diffraction by crystals, one year ahead of Bragg. (This Nobel prize medal was dissolved by aqua regia in World War II and recast in 1952 using the same gold.)

A complete derivation of Laue's equations is shown in reference [1]. Here only a simple view of Laue's equation is given. From equation in X, the scattered intensity from a crystal is given by the multiplication of lattice sum and unit cell form factor. If only the lattice sum is considered, which is given by:

$$F_{l.s.} = \sum e^{iQR_n} \tag{1.13}$$

This equation would reach the maximum if

$$Q \cdot R_n = 2\pi x \ (x \ is \ integer) \tag{1.14}$$

Mathematically, a reciprocal space lattice can be generated similar to real space equation in:

$$G_m = mb_1 + m_2 b_2 + m_3 b_3 \tag{1.15}$$

The new lattice constants are defined as:

$$b_1 = 2\pi \frac{a_2 \times a_3}{a_1 \cdot (a_2 \times a_3)}; \ b_2 = 2\pi \frac{a_3 \times a_1}{a_2 \cdot (a_3 \times a_1)}; \ b_3 = 2\pi \frac{a_1 \times a_2}{a_3 \cdot (a_1 \times a_2)} \tag{1.16}$$

According to this definition, the real space and reciprocal space constant satisfy:

$$a_i \cdot b_i = 2\pi \ (i = 1,2,3) \tag{1.17}$$

This gives:

$$G_m \cdot R_n = 2\pi y \ (y \ is \ integer) \tag{1.18}$$

Combing the equation and gives the famous Laue condition:

$$Q = G \tag{1.19}$$

Figure 1.b is a schematic diagram for deriving Laue equation in one dimension. When the optical path length difference for the two adjacent atoms are the integer times of X-ray wavelength, then the diffracted X-rays are in phase and give constructive interference:

$$L_{OPLD} = a \cdot \cos \alpha_1 - a \cdot cos\alpha_0 = n\lambda \tag{1.20}$$

This equation can be expressed in vector view, which gives:

$$a \cdot (k_i - k_f) = a \cdot Q = h\lambda \tag{1.21}$$

This is the Laue equation in one dimension. The Bragg condition is a special case of Laue condition, where the Bragg's law can be deduced from Laue equation. Combining equations and proper multiplying the two sides gives

$$G^2 = 2k_i \cdot G = -2k_f G \tag{1.22}$$

Substituting G with Laue equation gives the Bragg's laws.

1.1.2 Other scattering effects

(a) Compton scattering

Compton scattering is one example of incoherent scattering or inelastic scattering. In such case, the scattered photon has lower energy or longer wavelength than the incident photon. This relationship is deduced by Compton in 1923:

$$\lambda_{in} - \lambda_{out} = \frac{h}{m_e c}(1 - cos\theta) \tag{1.23}$$

The Compton scattering length is defined from this equation as:

$$r_c = \frac{h}{m_e c} = 2.42 \times 10^{-2}\text{Å} \tag{1.24}$$

Sometimes the reduced the Compton scattering length is used, which involved replacing the Planck constant h in equation with reduced Planck constant $\hbar$. This gives a value of 3.86×10^{-3} Å.

Cross-section is a term to quantitatively describe the probability of a process happens during the collision of two particles. For example, the scattering cross-section can be defined as the possibility of an incoming photon been scattered by

an atom. The scattering cross-section of barium element is given in Figure 1.2. At 9 KeV, the Thomson scattering is still the major part that contribute to the total scattering. However, the Compton scattering cross-section exceeds Thomson scattering at about 100 KeV.
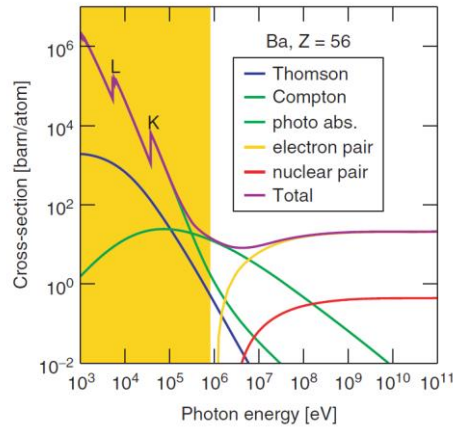
Figure 1. 2 Cross-section of X-ray interaction with barium element. Image from [2].

(b) Debye-Waller factor

From a lattice dynamic point of view, the actual atoms in crystal have thermal vibrations instead of being static at lattice node. This fluctuation can be added into consideration by modifying the atomic form factor. The so-called Debye-Waller factor is usually added for compensating the thermal vibration, which takes the form of $e^{-\frac{Q^2\langle u^2\rangle}{3}}$. Q is the scattering vector and $\langle u^2\rangle$ is the mean square displacement from the scattering center. The value of Debye-Waller factor varies on temperature and atomic species.

1.2 X-ray sources and instrumentations

1.2.1 Lab X-ray source

Figure 1.3 shows a Rigaku Smartlab X-ray diffractometer at the UCL physics department. In X-ray tube, the tungsten filament first generates electrons upon heating. These electrons are then accelerated by electrical field towards the rotating copper anode. With a proper electron energy, X-ray comprising of a white radiation and characteristic radiations would be generated. Different monochromators can be applied to select the radiation needed. For example, Ge monochromator can be used on the incident beam side to select only Cu $K_{\alpha 1}$

radiation, which has an energy of 8.04 KeV and a wavelength of 1.54056 Å. Graphite single crystal monochromator can be applied on the receiving side to select both Cu $K_{\alpha1}$ and $K_{\alpha2}$ (λ=1.54439 Å), but eliminating K_β (λ=1.39222 Å) and most of Bremsstrahlung radiation. The vertical divergence of 0.01° is reached by a combination of a parabolically bent multi-layer mirror (Gobel mirror) and double crystal Ge monochromator. The horizontal divergence of 0.5° is achieved, which is determined by Soller slits. The length limiting slits are used to reduce the X-ray footprint.
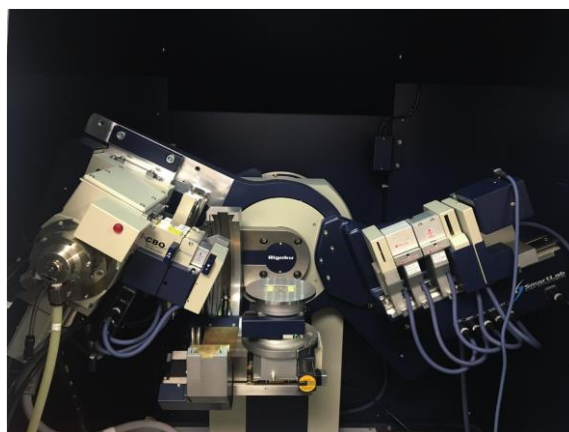
Figure 1. 3 A photo of Rigaku X-ray diffractometer at UCL physics department.

1.2.2 Synchrotron radiation source

Synchrotron radiation has many unique properties comparing with lab X-ray, the most prominent ones being the tunability (freedom to choose the X-ray wavelength) and brilliance. Unlike the lab X-ray, synchrotron X-ray radiation is generated through the radically acceleration of relativistic electrons. There are approximately 70 synchrotrons in construction or in use worldwide.

The synchrotron radiation source has several key components: electron gun; linear accelerator (LINAC); booster ring; storage ring and beamline hutches. Same as lab X-ray, the electron gun uses heated filaments to generate electrons. The generated electrons are injected into linear accelerator, where the electrons are packed in bunches and accelerated to an order of hundred million electron volts. For example, the LINAC in the Advanced Photon Source (APS) is designed to accelerate electrons to 200 MeV at 48 pulses per second. Then these electrons are put into the booster ring and further accelerated to the final designed energy. For example, Diamond Light Source (DLS) is a medium energy synchrotron

working at 3 GeV. European Synchrotron Radiation Facility (ESRF) and APS works at 6 GeV and 7 GeV, respectively. Booster ring originally works a few times per day to refill the storage ring, where the electrons are kept in a closed path and in operation to generate X-ray. For now, most synchrotrons use top-up mode, in which the booster ring works more frequently or continuously to provide constant beam current. The closed path can be usually divided into tens of segments, each contacting an arc path by bending magnets and a straight path used for insertion devices.

(a) Bending magnet

A bending magnet is used to create a homogeneous magnetic field over a distance, which mainly used to bend the trajectory of electrons to form a closed loop. It can also create a pencil beam in flattened cone shape.

First to be noted, the relativistic electrons move at a speed close to the light. The Lorenz factor can be expressed as

$$\gamma = \frac{E}{mc^2} = 1957E \qquad (1.25)$$

, where E is the storage ring energy. Therefore, for diamond light source, the Lorenz factor is about 5871.

Secondly, the relativistic Doppler effect changes the wavelength. The Doppler effect causes the sound wave more compact or an increase in frequency towards approaching the observer (red shift), comparing with a decrease in frequency when moving away from observer (blue shift). For the synchrotron electrons moving at a speed close to the speed of light, the doppler shift would modify the wavelength with an order of $(2\gamma)^{-1}$.

Thirdly, the Doppler effect also changes the radiation angle or the beam divergence. For relativistic electrons, the large Lorenz factor gives a small beam divergence in the order of γ^{-1}. This beam divergence defines the beam shape in the vertical direction. In the horizontal direction, there are electron angular changes which make the beam elongated horizontally.
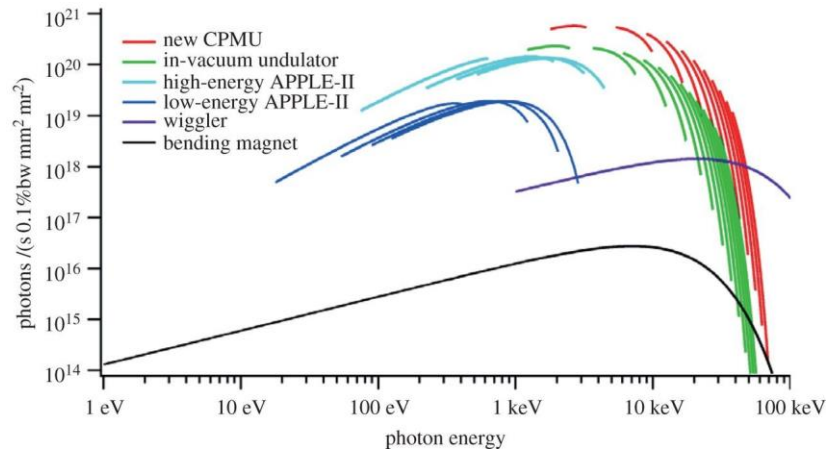
Figure 1. 4 Bending magnets and insertion devices spectral. Image from [3].

The bending magnet offers radiation with a broad frequency but a lower brightness, as shown in Figure 1.4. Therefore, the bending magnets beamline is helpful when large energy range is favoured, or the brightness is not the priority. For example, the APS 11-BM, which we use to do X-ray scattering and PDF study of BTO nanocrystal, is a bending magnet beamline.

(b) Insertion devices

Insertion devices are put in the straight path of the segment in a storage ring, which are the characteristics of third generation synchrotrons. The X-ray generated by the insertion devices are several orders of magnitude brighter than by the bending magnets, as can be seen in Figure 1.4. The two typical insertion devices are wiggler and undulator, both of which are made of a stack of magnets arrays. In both cases, the electrons are forced to vibrate horizontally through the insertion devices. The X-ray generated from each pair of magnets would add up in the forward direction, thus enhance the flux. The difference of a wiggler and an undulator is the degree of electron moved from their straight path.

For a wiggler, the electron is moved at an angle larger than the natural opening angle. Assuming the wiggler has N pair of magnets with same length and field, the generated radiations would be increased by a factor of 2N. Because such electron vibration happens in horizontal direction, the angular distribution is also increased by a factor of 2N horizontally.

For an undulator, the electron is moved with a degree smaller than the natural opening angle. In this case, the generated X-ray from each pair of magnets is in

phase with each other. Therefore, the brightness is no longer the adding of intensity, but the square, due to adding amplitude.

(c) Extremely brilliant source (EBS)

ESRF has gone through the upgrade for the so-called EBS. It consists of four components and the key part is a new storage ring that increase the intensity by a factor of 100. Figure 1.5 shows diffraction counting rate using the same BTO nanocrystals. The diffraction counts go to nearly 200 thousand counts per second at the brightest pixel at ESRF ID01, while at APS 34-ID-C the value is about 5 thousand. The enhanced intensity would make our measurement faster and increased signal-to-noise ratio.

Diffracted Intensity

Sept. 2019 @ DLS I13-1 [D=2.9m, px=55um]				
Crystal No.	SingleMax (cts/s)	TotalMax (cts/s)	Size-X (nm)	Size-Y (nm)
C3-650	19	64457	274	-
C6-867	43	418170	127	113

Mar. 2021 @ APS 34-ID-C [D=0.5m, px=55um]				
Crystal No.	SingleMax (cts/s)	TotalMax (cts/s)	Size-X (nm)	Size-Y (nm)
#180	1049	3958939	67	55
#662	1020	2653312	115	112
#705	5190	4153483	179	150
#725	1050	1070779	138	196
#746	1295	912788	129	199
#910	5608	1833387	202	281
#954	1543	1688621	152	143
#965	3985	3805087	197	168

Apr. 2021 @ ESRF ID01 [D=0.546m, px=55um]				
Crystal No.	SingleMax (cts/s)	TotalMax (cts/s)	Size-X (nm)	Size-Y (nm)
C1-#2330	5213	7051289	177	142
C2-#230605	196118	132951408	169	139
C3-#82516	133103	19292316	322	221
C4-#31538	51753	68599995	550	720
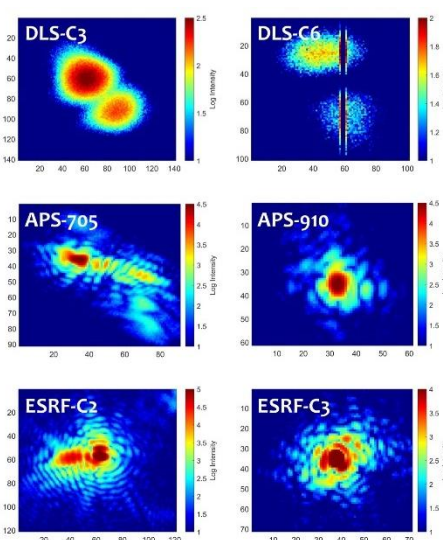
Figure 1. 5 The diffracted intensity at three different beamlines (DLS-I13, APS 34-ID-C, ESRF ID01) using the same BTO nanocrystals.

1.2.3 Beamline optics

For different scientific purposes, various beamline optics could be applied.

Monochromator can be termed as an energy filter. The coherence application of X-ray requires all the beam to have the same wavelength or photon energy. The X-ray generated from an undulator is the pink beam and need to be filtered by a monochromator. Both APS 34-ID-C and DLS I13-1 use the Si (111) double crystal monochromator (DCM). It consists of two silicon crystals setting parallel to each other. The incident X-ray beam is diffracted by 111 Bragg reflection of silicon, where the X-ray with exact wavelength will be collected at Bragg condition. A

second monochromator is used to both further filtering the energy and keep the X-ray beam to be straight. In the real case, the collimation of incident X-ray beam and crystal imperfection such as mosaicity would introduce the spread of X-ray beam, but silicon is close to perfect. The energy resolution for a typical Si (111) DCM is 2×10^{-4}.

As for focusing optics, because the real part of X-ray refractive index is small but very close to unity, it's hard to effectively bend the X-ray beam. The focal length for a conventional lens would be too large to be practical. To achieve the bending of X-ray so as to focus the beam, various methods have been developed by either refraction, total external reflection or diffraction.

(a) Compound refractive lens (CRL)

Because one conventional lens cannot substantially bend X-ray due to refractive index, one way to get around is to use many lenses. The European X-ray Free electron Laser (XFEL) Materials Imaging and Dynamic (MID) beamline uses two CRLs (primary lens stack CRL-1 and secondary lens stack CRL-2) to focus the X-ray beam. These CRLs are fabricated by drilling holes onto the beryllium block. The axes of these holes are coplanar, and the beryllium are used for low X-ray absorption. The advantage of CRL is easy alignment because it doesn't divert the X-ray beam. The disadvantage is that the absorption and intensity loss. CRLs are used widely in XFEL, where the brilliance is strong enough to compensate the loss. It's also used in synchrotrons like Diamond light source beamline I13-1.

(b) Kirkpatrick-Baez (K-B) mirrors

APS beamline 34-ID-C uses a pair of K-B mirrors to focus the pencil beam to around 600 nm in both horizontal and vertical direction [4-5]. Figure 1.6 shows a diagram of K-B mirror pairs with two cylindrical mirrors [6]. The X-ray beam comes at grazing angle and is reflected by the two mirrors placing horizontally and vertically, respectively. The advantage of such design including decoupling of vertical and horizontal focusing, small intensity loss and easily manufactured.

(c) Parabolic/toroidal mirrors

Such two mirrors system can be reduced to one to minimize the length of mirror system. ESRF ID-09 use both parabolic and toroidal mirrors to focus the incident beam. Figure 1.6 shows a figure of the toroidal mirror used in ID-09, which has a light bending along the beam path and strong bending perpendicular to the beam path. However, such bending surface is hard to manufacture and often induce aberrations.

(d) Fresnel zone plate (FZP)

FZP uses diffraction instead of reflection or refraction to focus the beam and is widely used in photography. FZP consists of numerous circular gratings which works like the famous Young's double slits experiment. The size of gratings can be controlled to be close to X-ray wavelength, so that the constructive interference can be achieved at a focal point downstream. The FZP has a good focal length which could go down to tens of nanometres. An order sorting aperture (OSA) is usually needed to define the beam after the FZP and before the sample. Diamond beamline I13-1 uses a 400 μm diameter FZP with 150 nm outer zone width and 20 μm OSA downstream [8].
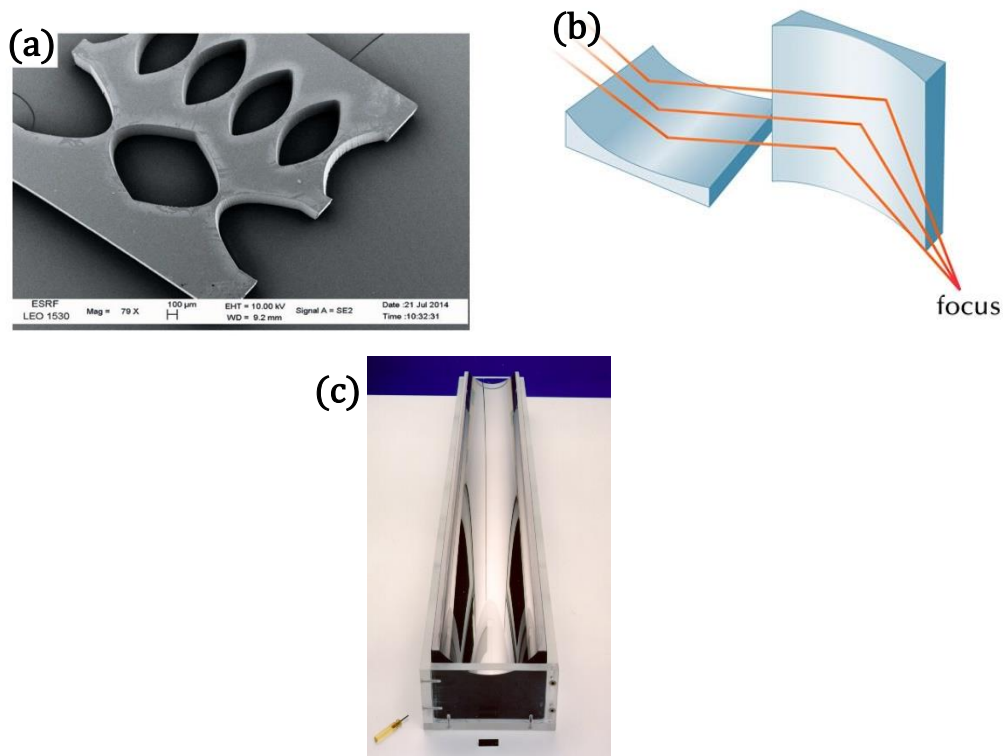
Figure 1. 6 (a) CRL made on diamond plate at ESRF. Image from [7] (b) KB mirror pairs. (c) Toroidal mirror.

1.3 X-ray scattering at Rigaku Smartlab

With the development of X-ray sources, so is the X-ray based methods and techniques. We are interested in using Lab-based X-ray diffractometer to determine the structure and quality of $BaTiO_3$(BTO) thin film samples. Therefore, this section is focused on the thin film related scattering techniques: θ-2θ scans, rocking curve scan, small angle x-ray reflectivity scan and reciprocal space map. A manual for operating these scans is shown in appendix A and B.

(a) θ-2θ Scan

In this case, θ means the incident beam angle and 2θ means the diffracted beam angle. For a Rigaku Smartlab, the incident angle is ω instead. The 2θ and ω are moving in a symmetry manner relative to the sample stage. The offset ω angle is set beforehand and kept compensating the sample surface plane angle. The standard epitaxial BTO thin films have tetragonal structure at room temperature with c axis pointing out-of-plane and a axis in-plane. Therefore, the θ-2θ scan is along 00L direction in reciprocal space. The two important pieces of information from a θ-2θ scan are the peak position and full width half maximum (FWHM), which correspond to the out-of-plane lattice constant and sample thickness, respectively. The peak position is related to the out-of-plane lattice constant via Bragg's law, as shown in equation 1.11. The relation between FWHM of diffraction peak and sample thickness is derived in detail and shown below.

Taking BTO thin film as an example and assuming there are N layers of d_{001}, which form a certain thickness. The signal measured from the detector are the amplitude of X-ray, which can be derived as:

$$|A(Q)| = \left| \sum_j e^{iQ \cdot r_j} \right| = \left| \sum_{j=0}^{N-1} e^{iQjd} \right| = \left| \frac{1 - e^{iQNd}}{1 - e^{iQd}} \right| = \frac{sin \frac{QNd}{2}}{sin \frac{Qd}{2}} \qquad (1.26)$$

The amplitude will reach the maximum if the denominator of equation X equals to 0. This gives the condition for the peak centre position:

$$Q_1 = \frac{2\pi}{d} n \; (n \; is \; integer) \qquad (1.27)$$

The amplitude will decrease to zero if the numerator equals to 0. This gives the condition for the end of the peak:

$$Q_2 = \frac{2\pi}{Nd} n \ (n \ is \ integer) \qquad (1.28)$$

Therefore, the full width half maximum of the centre peak (named ΔQ), or the full width of the fringes gives the sample thickness Nd by

$$Nd = \frac{2\pi}{\Delta Q} \qquad (1.29)$$

Next inverse this equation to real space. Assuming the two angles at full width half maximum are 1 and 2, then

$$\Delta Q = \frac{4\pi}{\lambda}(sin\theta_1 - sin\theta_2) = \frac{8\pi}{\lambda}\cos\theta \ sin\frac{\theta_{FWHM}}{2} \qquad (1.30)$$

Therefore, the sample thickness is given by:

$$Nd = \frac{\lambda}{4\cos\theta \ sin\dfrac{\theta_{FWHM}}{2}} \qquad (1.31)$$

This is the general equation for the sample thickness in thin film sample. In the limit of approaching 0, the thickness is expressed as

$$Nd = \lim_{\theta \to 0}\frac{\lambda}{2\theta_{FWHM}\cos\theta} \qquad (1.32)$$

This is similar to the Scherrer equation, which stated as:

$$\tau = \frac{K\lambda}{\theta_{FWHM}\cos\theta} \qquad (1.33)$$

The Scherrer equation works for polycrystalline materials, where τ stands for the average grain size. K is a dimensionless shape factor to account for integration over a given crystal shape. It can be used to minimize the difference between experiment and prediction.

(b) Rocking curve scan

Rocking curve scan is a scan over ω with fixed 2θ. Therefore, the rocking curve scan can follow H00 or 0K0 direction according to the sample stage rotation angle ɸ. A simple rocking curve scan perpendicular to 00L direction contains the

information of domain size. The domain size is the same discussed in θ-2θ scan above. The only difference is the direction has changed from 00L to either H00, 0K0, or something in between. If the domain sizes are close enough and regularly distributed, this periodicity will also show up in a rocking curve scan as the fringes.

(c) Reciprocal space map

Reciprocal space map (RSM) is two-dimensional (2D) map instead of one-dimensional (1D) scanning in the above two scans. Because the Rigaku Smartlab is equipped with 1D detector, this 2D mapping is acquired by a combination of θ-2θ scan and rocking curve scan, either H step with L scans or L step with H scans. L direction contains the out-of-plane information while H scan contains the in-plane information. Therefore, the RSM contains a combined information including out-of-plane lattice constant, in-plane lattice constant, in-plane domain periodicity, in-plane strain state.

(d) X-ray reflectivity

Small angle X-ray scattering is usually performed to measure the reflectivity of thin film sample. Due to the finite size effect, the resulting oscillations are related to the film thickness by:

$$\theta^2 - \theta_c^2 = N^2 \left(\frac{\lambda}{2d}\right)^2 \qquad (1.34)$$

1.4 Bragg coherent X-ray diffraction imaging

The Coherent Diffraction Imaging (CDI) was first proposed by Sayre dating back to 1952 and Ian Robinson performed the first Bragg Coherent Diffraction Imaging (BCDI) experiment on Au nanoparticles in 1991 [9-10]. Through 20 years development, BCDI is now a powerful X-ray technique for investigating the structures of nanocrystals in three dimensions on the 30 nm resolution scale using third generation synchrotrons. The advantage of BCDI is its high sensitivity to the distribution of nanoscale strains inside the nanocrystal under investigation [11]. BCDI is a 3-D imaging method that is particularly valuable for probing the responses of individual nanosized crystal grains embedded in an in-

situ environment, such as a polycrystalline material, a battery electrode, or a working catalyst particle [12-15].

1.4.1 Prerequisites

A BCDI experiment requires a coherent or partially coherent beam. The coherence of X-ray beam can be quantitatively determined by two coherence lengths: the longitudinal coherence length (temporal coherence length) and transverse coherence length (spatial coherence length) [16]. The longitudinal coherence length arises from the fact that the X-ray beam from the monochromator does not have a single wavelength, but rather a distribution over a range. The typical Si DCM working at (111) reflection, the wavelength distribution $\Delta\lambda/\lambda$ is about 1.3×10^{-4}. This results in a 500nm longitudinal coherence length. The transverse coherence length is due to the X-ray source not being point-like, so that the incoming X-ray is not purely plane wave. For a coherence beamline like DLS I13, this length is larger than 30 μm. In order to secure the coherence of incoming X-ray beam, the sample size should be smaller than the coherence length.

The other relevant length is the beam size, which can be adjusted by beam-defining slits and focusing optics. The slits are set to equal the transverse coherence length, and the beam can be focussed smaller afterwards. The sample size should be also smaller than the beam size in a BCDI experiment. For coherent optics, the focal size scales inversely with the entrance beam size, which can be adjusted for larger samples. Typical JJ slits sizes and beam sizes at sample stage at APS 34-ID-C are given in Table 1.1.

Table 1. 1 Horizontal and vertical slit sizes and their corresponding focus size at sample stage. Value measured by Wonsuk Cha.

Horizontal slits (μm)	Horizontal focus (nm)	Vertical slit (μm)	Vertical focus (nm)
30	690	70	450
25	810	60	550
20	970	50	670
15	1270	40	840

10	2500	30	960
		20	1510
		15	1960
		10	3580

1.4.2 Measurements and corrections

After illumination by the coherent beam, the diffraction pattern is collected by an area detector at the far-field position around a Bragg peak. Generally, this is done by rotating the sample stage in small steps and collecting 2D diffraction patterns, which are then stacked into a 3D diffraction pattern. The fringes surrounding a Bragg diffraction peak, due to the external shape of the crystals, can be oversampled with respect to their spatial Shannon-Nyquist frequency [17].

Several treatments are usually performed to raw diffraction patterns before feeding into the reconstruction scripts. Firstly, the white field corrections are needed to cancel out the variation due to the detector pixel sensitivity to the X-ray radiation. For example, APS 34-ID-C uses ASI Quad (512x512) Timepix chips with GaAs absorber, which needs to be corrected using a white field. Secondly, a dark field correction is done to remove the bad pixels on the detector. Thirdly, unwanted noise or diffractions from other crystals are cropped out. Then the binning of raw data is sometimes needed to lower down the data size, so as to decrease the working load of phase retrieval. Finally, zero padding can be used to adjust the pattern array size, which is also the size of reconstructed object array.

1.4.3 Iterative phasing

Because the detector in use only records the intensity of diffracted X-ray, which is the square of the amplitude, the phase information is lost in the measurement. To retrieve the missing phase, Sayre proposed to oversample the diffraction pattern at a frequency finer than $1/2a$, where a is the sample size [13]. As long as the question is overdetermined, there are two effective ways to get the phase back: One is through iterative phasing algorithms, which involve Fourier transforms between real space and reciprocal space back and forth. Figure 1.7

shows a typical phase retrieval loop. In this work, all the reconstructions are done through iterative phasing method. The other method is through machine learning, which does not involve Fourier transform [18].
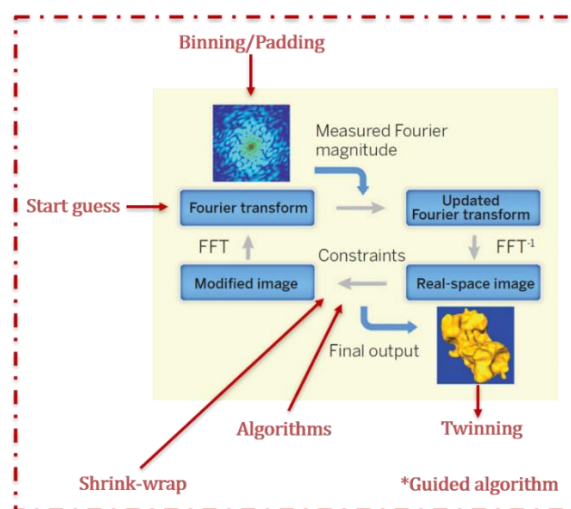
Figure 1. 7 A schematic showing of iterative phasing loop. Image remade from [17].

The iterative phasing starts with a guess support, which is an initial guess of the crystal shape. A prior knowledge of the sample shape could aid the convergence of the solution. Without prior knowledge, it is normally set to be a box with half the array size as a flat start. The starting support can also be a random object with any phase. This can be used to test the reproducibility of reconstructed results by vary the starting support. The phase retrieval can also start from previous reconstructions or self-built support, which are used to deal with in-situ battery data and LBCO single crystal in our previous works.

After feeding into the loop, the initial support is transformed back and forth between two spaces while the constraints are applied. The reciprocal space constraint is the measured diffraction pattern amplitude, while keeping its phase. The real space constraint is where the different algorithms are applied. Table 1.2 listed some algorithms used in this work. Some algorithms have been published already [19-23]. The others were written and added into the reconstruction package by Jesse N. Clark.

Table 1. 2 The descriptions of different algorithms.

Algorithms	Descriptions

ER [19]	$\rho_{i+1}=\rho_i' \cdot S$
ERs	$\rho_{i+1} = \|\rho_i' \cdot S\|^{1/2} \cdot \arg(\rho_i' \cdot S)$
ER-AMP	$\rho_{i+1} = \|\rho_i\| \cdot \arg(\rho_i')$
SF [20]	$\rho_{i+1} = (2 \cdot S - 1) \cdot \rho_i'$
SF-h-ER	Making shift of SF/ER based on iteration number.
ER-h-SF	
ER-SF-ER	
ERSF	
GHIO	$\rho_{i+1} = \rho_i' \cdot S + (1 - S) \cdot (\rho_i - \beta \cdot \rho_i') + 0.3 \cdot S \cdot (\rho_i' - \rho_i)$
HIO [19]	$\rho_{i+1} = \rho_i' \cdot S + (1 - S) \cdot (\rho_i - \beta \cdot \rho_i')$
HIO-OR	$\rho_{i+1} = \big(1 + \beta \cdot (\lambda - 1)\big) \cdot \rho_i' + (\beta - \lambda - \beta \cdot \lambda) \cdot S \cdot \rho_i - \beta \cdot \lambda \cdot \rho_i'$ $+ (1 + \beta) \cdot \lambda \cdot \rho_i' \cdot S$
pcj-HIO	$\rho_{i+1} = (1 + \beta) \cdot J(\rho_i', phmin, phmax) \cdot S + \rho_i - \beta \cdot \rho_i'$ $- J(\rho_i, phmin, phmax) \cdot S$ $J(\rho, phmin, phmax)$ is an operation for amplitude and phase. If the phase ph is smaller than $phmin$, then the amplitude amp is written by $amp \cdot cos(ph - phmin)$ while the ph would be written as $phmin$. If the phase ph is larger than $phmax$, then the amplitude amp is written by $amp \cdot cos(ph - phmax)$ and ph would be wrriten as $phmax$. Or else, the ph and amp would keep unchanged.
HIO-AMP	$\rho_{i+1} = (1 + \beta) \cdot \|\rho_i\| \cdot \arg(\rho_i') + \rho_i - \beta \cdot \rho_i' - \|\rho_i\| \cdot \arg(\rho_i)$
HIOb	$\rho_{i+1} = (1 + \beta) \cdot B(\rho_i' \cdot S, l, u) + \rho_i - \beta \cdot \rho_i' - B(\rho_i \cdot S, l, u)$ $B(\rho, l, u)$ is an operation for amplitude boost. If the amplitude of ρ is between dot product of maximum amplitude with u and l, it will be increased to the dot product of maximum amplitude with u.
HIOs	$\rho_{i+1} = (1 + \beta) \cdot \|\rho_i' \cdot S\|^{1/2} \cdot \arg(\rho_i' \cdot S) + \rho_i - \beta \cdot \rho_i' - \|\rho_i \cdot S\|^{1/2}$ $\cdot \arg(\rho_i \cdot S)$
HIOsr	$\rho_{i+1} = (1 + \beta) \cdot \|\rho_i' \cdot S\|^{3/4} \cdot \arg(\rho_i' \cdot S) + \rho_i - \beta \cdot \rho_i' - \|\rho_i \cdot S\|^{3/4}$ $\cdot \arg(\rho_i \cdot S)$

HIOso	Switch between HIO and HIOs. The default setting is to run one HIOs followed by four HIO.
HIOd	$$\rho_{i+1} = (1 + \beta) \cdot D(\rho_i' \cdot S, pow, th) + \rho_i - \beta \cdot \rho_i' - D(\rho_i \cdot S, pow, th)$$ $D(\rho, pow, th)$ is an operation for amplitude. If the amplitude of ρ is larger than dot product of maximum amplitude with th, then the amplitude would be $|\rho \cdot S|^{pow} \cdot \arg(\rho \cdot S)$. If smaller, then the amplitude would be $|\rho \cdot S|$.
HIOp	$$\rho_{i+1} = (1 + \beta) \cdot P(\rho_i' \cdot S, pow, perc) + \rho_i - \beta \cdot \rho_i' - P(\rho_i \cdot S, pow, perc)$$ $P(\rho, pow, perc)$ is an operation for amplitude. It considers the size of the data array Sz. It takes the value of $perc \cdot Sz$ as the threshold. If the amplitude is larger than threshold, then the amplitude would be $|\rho \cdot S|^{pow} \cdot \arg(\rho \cdot S)$. If smaller, then the amplitude would be $|\rho \cdot S|$.
HIOv	$$\rho_{i+1} = (1 + \beta) \cdot V(\rho_i' \cdot S, val) + \rho_i - \beta \cdot \rho_i' - V(\rho_i \cdot S, val)$$ $V(\rho, val)$ is an operation for amplitude. If the amplitude is larger than the dot product of maximum amplitude with val, then the amplitude would be set to average amplitude. Or else, the amplitude would be $|\rho \cdot S|$.
RAAR [21]	$$\rho_{i+1} = 0.5 \cdot \beta \cdot ((2 \cdot S - 1) \cdot (2 \cdot \rho_i' - \rho_i) + \rho_i) + (1 - \beta) \cdot \rho_i'$$
RAARv	$$\rho_{i+1} = 0.5 \cdot \beta \cdot (4 \cdot L(\rho_i' \cdot S, l) - 2 \cdot L(\rho_i \cdot S, l) - 2 \cdot \rho_i' + 2 \cdot \rho_i) + (1 - \beta) \cdot \rho_i')$$ $L(\rho, l)$ is an operation for amplitude. It first normalizes ρ and then multiple by l. Then it is rounded and normalized again.
GRAAR	$$\rho_{i+1} = 0.5 \cdot \beta \cdot ((2 \cdot S - 1) \cdot (2 \cdot \rho_i' - \rho_i + (\rho_i - \rho_i')) + \rho_i) + (1 - \beta) \cdot \rho_i')$$
ASR [22]	$$\rho_{i+1} = 0.5 \cdot ((2 \cdot S - 1) \cdot (2 \cdot \rho_i' - \rho_i) + \rho_i)$$
HPR [23]	$$\rho_{i+1} = 0.5 \cdot ((2 \cdot S - 1) \cdot (2 \cdot \rho_i' - \rho_i + (\beta - 1) \cdot \rho_i') + \rho_i + (1 - \beta) \cdot \rho_i')$$
MEM	If it is the first iteration, then $$\rho_{i+1} = \rho_i' \cdot S$$

	If it is not the first iteration, then
	$$\rho_{i+1} = \rho_i' \cdot e^{-\frac{|\rho_i' - \rho_i| \cdot S}{\langle |\rho_i' - \rho_i| \cdot S \rangle_{max}}} \cdot S$$

For illustration purpose, two ball shape crystals with radius of 16 pixels were built in 256×256×256 arrays. The first crystal (named Ball A) was assigned with zero phase inside. The second crystal (named Ball B), for comparison, assigned with $+ {}^{\pi}/_2$ on one hemisphere and $- {}^{\pi}/_2$ phase on the other hemisphere. The crystals were then fast Fourier transformed (FFT) back to the reciprocal space, where the phases were removed, and the amplitudes were squared to get the intensity. Figure 1.8 shows two crystals built and their corresponding diffracted intensity.
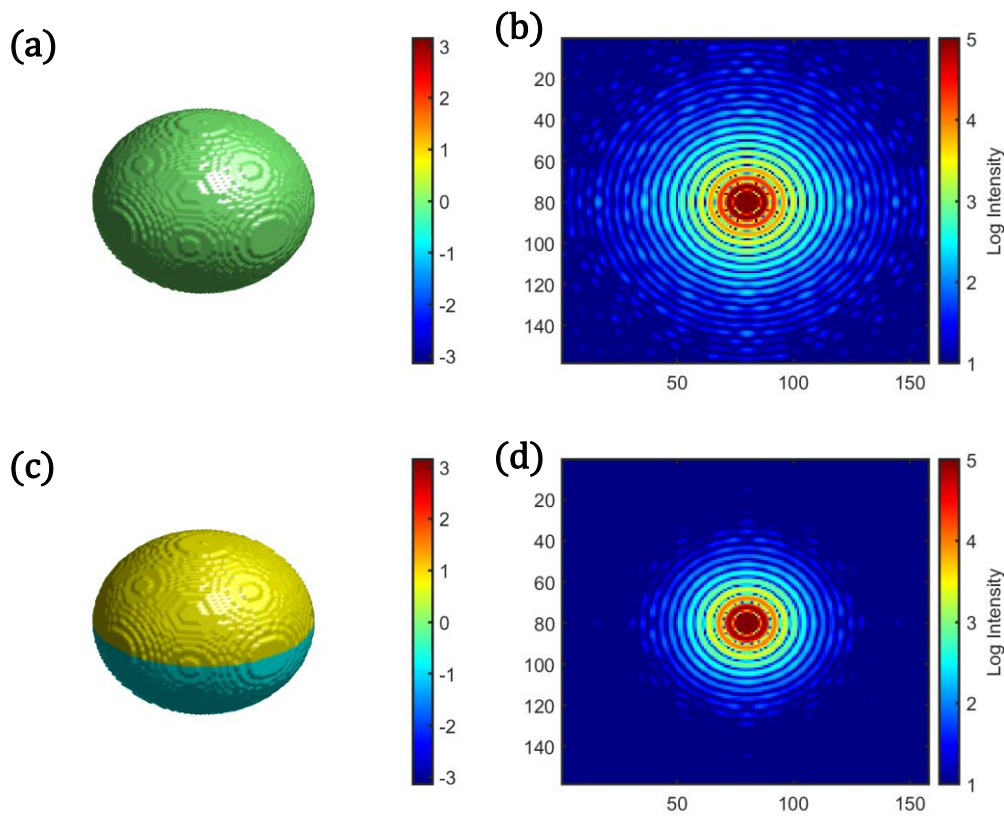
Figure 1. 8 Two simulated ball-shape crystal are listed. (a) Ball A with no strain. (b) The central slice of the diffraction is shown. The diffraction pattern was got from FFT of crystal in (a). (c) Ball B with different strain on hemisphere is shown. (d) The central slice of pattern got from Crystal in (c). The colour bars in (a) and (c) shows the phase.

The two typical ones in use are Error Reduction (ER) algorithm and Hybrid Input-Output (HIO) algorithm. In the ER algorithm, the amplitude of

reconstructed object is kept. The phase inside the object is also kept, but the amplitude and phase outside the support are set to 0. It has the advantage of fast convergence, but sometimes stagnates at local minima. While in the HIO algorithm, such amplitude and phase are decreased by a factor rather than going to 0. Practically, different algorithms are combined together to help avoid stagnation at local minima. Figure 1.9 shows one example of the error metrics changes through the reconstruction of the crystals in Figure 1.8. It has used a combination of ER and HIO algorithms for phase retrieval. Here the error metrics χ^2 are defined in the reciprocal space, by comparing the measured diffraction pattern and the Fourier transform of the reconstructed objects:

$$\chi^2 = \frac{\sum_i ||A_{calc}(i)|^2 - |A_{meas}(i)|^2|}{\sum_i |A_{meas}(i)|^2} \tag{1.35}$$

A similar definition can be drawn to depict the difference metrics D between different reconstructions:
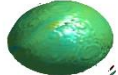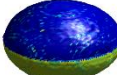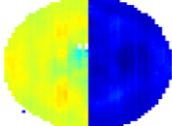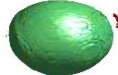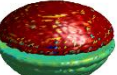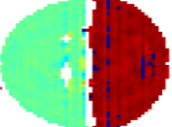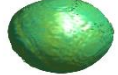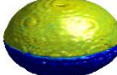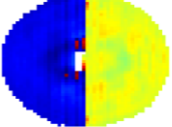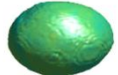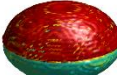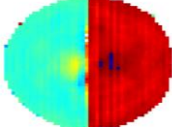
$$D = \frac{\sum_i ||A_{calc1}(i)|^2 - |A_{calc2}(i)|^2|}{\sum_i |A_{calc1}(i)|^2} \tag{1.36}$$
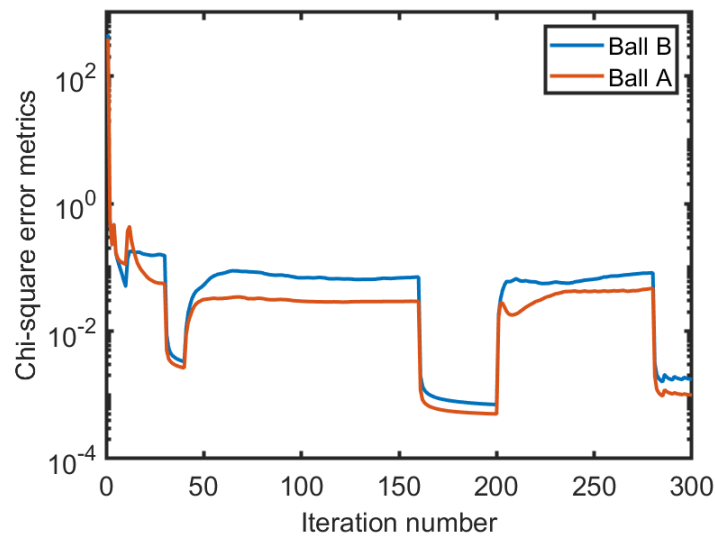
Figure 1. 9 The error metrics of each iteration in a reconstruction using a combination of ER and HIO algorithms. The phasing starts with ER algorithm and triggers at iteration 10, 30, 40, 160, 201, 280.

The reconstruction results from other combinations of algorithms are shown in Table 1.3. All the reconstructions are valid solutions with a confidence related to the chi-square error metrics.

Table 1. 3 The reconstructions of the crystals in Figure 1.8 using different combination of algorithms. The typical 300 iterations were run with a default trigger [10, 30, 40, 160, 201, 280].

Algorithm	Ball A		Ball B	
	Contour view	Slice view	Contour view	Slice view
ER+HIO	Script $\chi^2 = 0.086\%$		Script $\chi^2 = 0.175\%$	
ER+RAAR	Script $\chi^2 = 0.075\%$		Script $\chi^2 = 0.39\%$	
ER+HPR	Script $\chi^2 = 0.087\%$		Script $\chi^2 = 0.29\%$	
ER+ASR	Script $\chi^2 = 0.084\%$		Script $\chi^2 = 0.15\%$	

Phase
$-\pi$ ▬▬▬ π

Shrink-wrap (SW) can also be applied to help cropping out the low-density regions or noises in the reconstructed results [24]. It is a way to periodically update the support. One way to achieve this is transforming the support into reciprocal space, doing convolution with a shape function (usually gaussian kernel) and then transforming back to real space.

Figure 1.10(a) shows the SW thresholds and their corresponding reconstruction error metrics of Ball A. The turning point at 0.39 is believed to be where the SW

starts to cut the crystal. Figure 1.10(b) presents the reconstruction result using a threshold of 0.25. Figure 1.10(c) shows the SW variation of Ball B, where the turning point is around 0.36. Figure 1.10(d) shows the reconstruction result of 0.25 threshold.
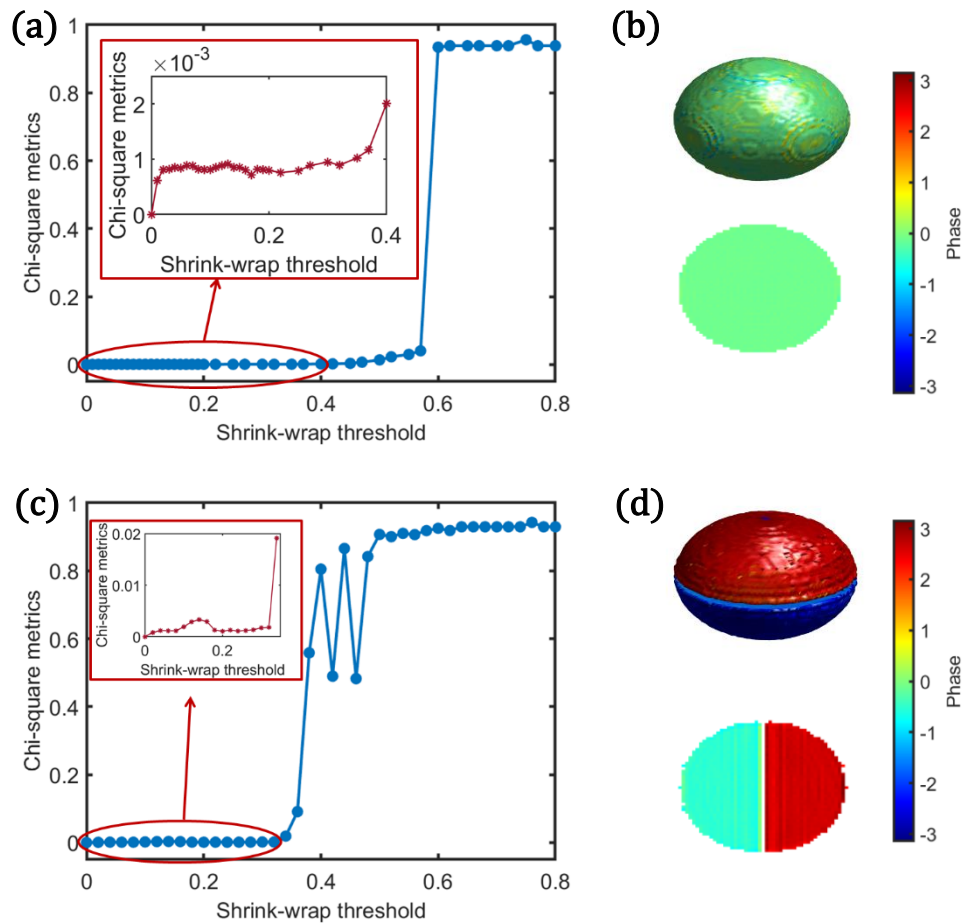
Figure 1. 10 (a) Error metrics variation when reconstructing Ball A using different SW threshold. (b) The reconstruction results of Ball A when using a shrink-wrap threshold of 0.25. (c) Error metrics variation when reconstructing Ball B using different SW threshold. (d) The reconstruction results of Ball B when using a shrink-wrap threshold of 0.25.

Guided algorithms (GA) are also used in this work [25]. Instead of having one initial support, GA starts with several starting guess, or so-called populations. After each reconstruction block (called generations), it stopped and determine which is the best reconstruction result. The normally used criterions are chi square error metrics or sharpness. When the best result is determined, several supports are generated based on this result to feed into another generation and

do reconstruction again. Low resolution method is usually used in first several generations to help reach the global minima faster.

The final reconstructed object is one set of the two conjugate results, as the two patterns with same amplitude and conjugate phase gives the same intensity. Therefore, the phase difference or derivative are more meaningful terms for discussion. In some cases when the phase range is over 2π, a script can be applied to unwrap the phase, based on its continuity in 2 or 3 dimensions.

To sum up, the phase retrieval is a case-to-case process. It works well for high-quality diffraction patterns, but for less good patterns some parameters may need to be optimized. Also, because the phase retrieval is prone to give multiple solutions, it's essential to always talk about the reconstructed results with their error metrics, usually the chi square defined above.

1.4.4 Applications

BCDI has the ability to probe the local displacement field and strain information inside the crystal with size up to 2 μm in typical beamline. It's already been applied to various materials systems and brough new insights into different fields.

(a) Amplitude and phase information

For every reconstructed image, there are both amplitude and phase information embedded. The amplitude, or so-called Bragg density, is a depiction of the distribution of electron density. Therefore, it defines the crystal shape and morphology. It is also sensitive to some defects. The additional phase information is directly related to the lattice distortion as illustrated by Ian Robinson et al in 2009 [11]. The linear relationship between the phase and the displacement field is exploited to explicitly map out the displacement inside nanocrystals since then.

Gold nanocrystals were widely studied partially because they have large atomic number and give strong diffraction single. Also, the crystal has only one element with a simple crystal structure. It's a good model system to explore the ability of BCDI. Still, many interesting physics have been observed in these systems. Xiong et al studied the copper evaporation onto the dewetted gold nanoparticles and

27

carried out both spatial and temporal measurement [231]. The copper diffusion into the gold nanocrystal upon time was determined by observing the amplitude and phase map as shown in Figure 1.11. The atomic diffusion channels could also be seen in the amplitude map.
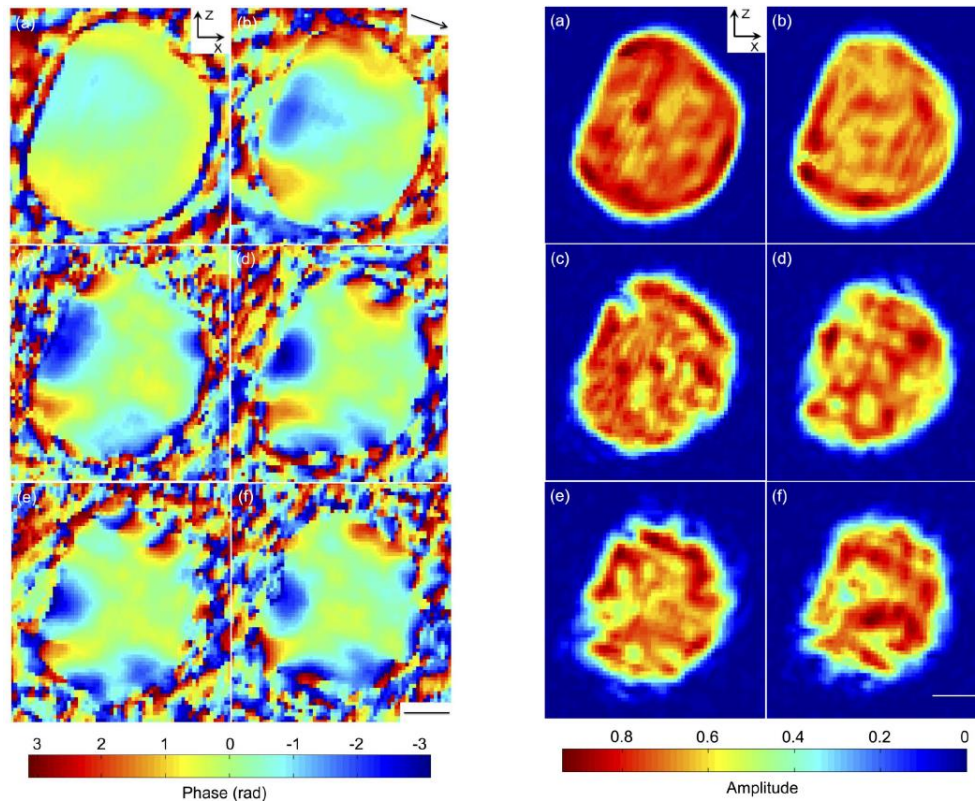
Figure 1. 11 The reconstructed phase (left) and amplitude (right) images of Au nanocrystal upon diffusion of Cu atoms. The diffusion times are 0 hrs (a), 2 hrs (b), 4 hrs (c), 6 hrs (d), 8 hrs (e) and 10 hrs (f). The scalebar is 100nm. [231]

(b) Probing dislocation

Because the displacement field can be carefully measured through BCDI, the dislocation could be determined by fitting the displacement around low-density core in BCDI images with linear elastic model. Figure 1.12 shows an example of mapping out the movement of dislocations inside $CaCO_3$ during growth and dissolution [14]. There are more dislocations forming during the growth of calcite crystal. However, during the dissolution, although the crystal volume shrinks a lot and back to the volume of initial stage, numerous dislocations still preserved inside.
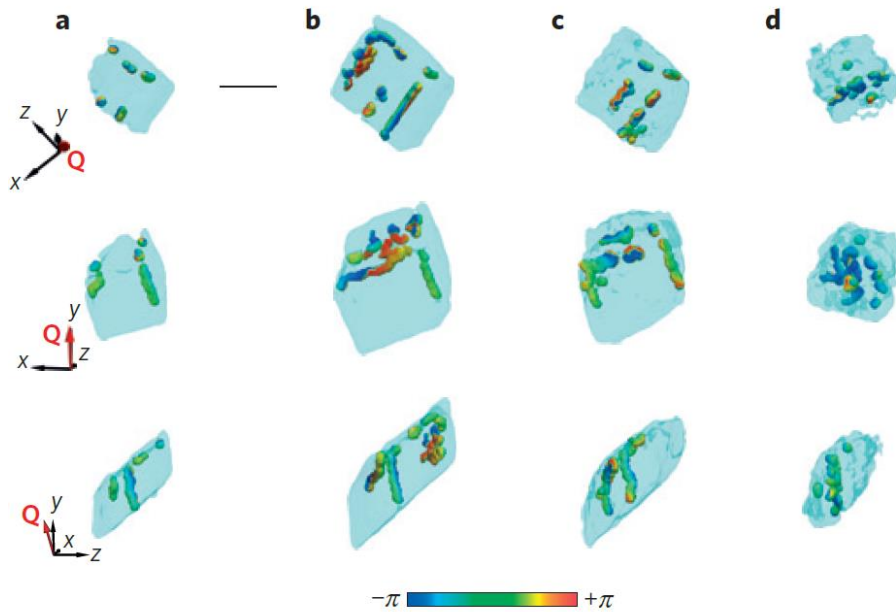
Figure 1. 12 Defects network within a calcite crystal at initial stage (a), after growth (b) and dissolution (c, d) [14].

The ability to probe the dislocation was widely used in battery study. Figure 1.13 shows an example of tracking the dislocation movement during charging of spinel $LiNi_{0.5}Mn_{1.5}O_4$ materials. The dislocation lines were found to move around during charging, indicating their instability. By examining the displacement field around dislocation lines, their types are determined to be edge dislocation.
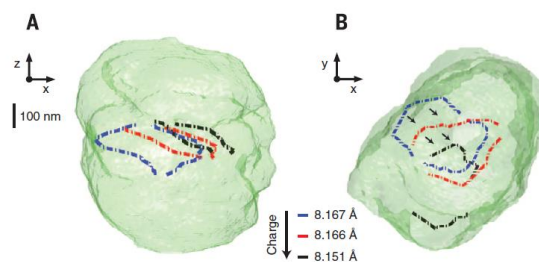
Figure 1. 13 Dislocation movements upon charging in lithium battery. [15]

(c) Strain mapping

Another important direction is to precisely measure the strain fields inside nanocrystals by more than three non-coplanar Bragg peaks. Figure 1.14 shows an example to use BCDI to study the effect of focused ion beam imaging on nanocrystal. The full strain tensors of Au nanocrystal were measured and calculated, which is shown in Figure 1.14 (c) and (d). Combined with finite

element analysis shown in (e) to (g), it indicates the strain is coming from Ga$^+$ implantation.
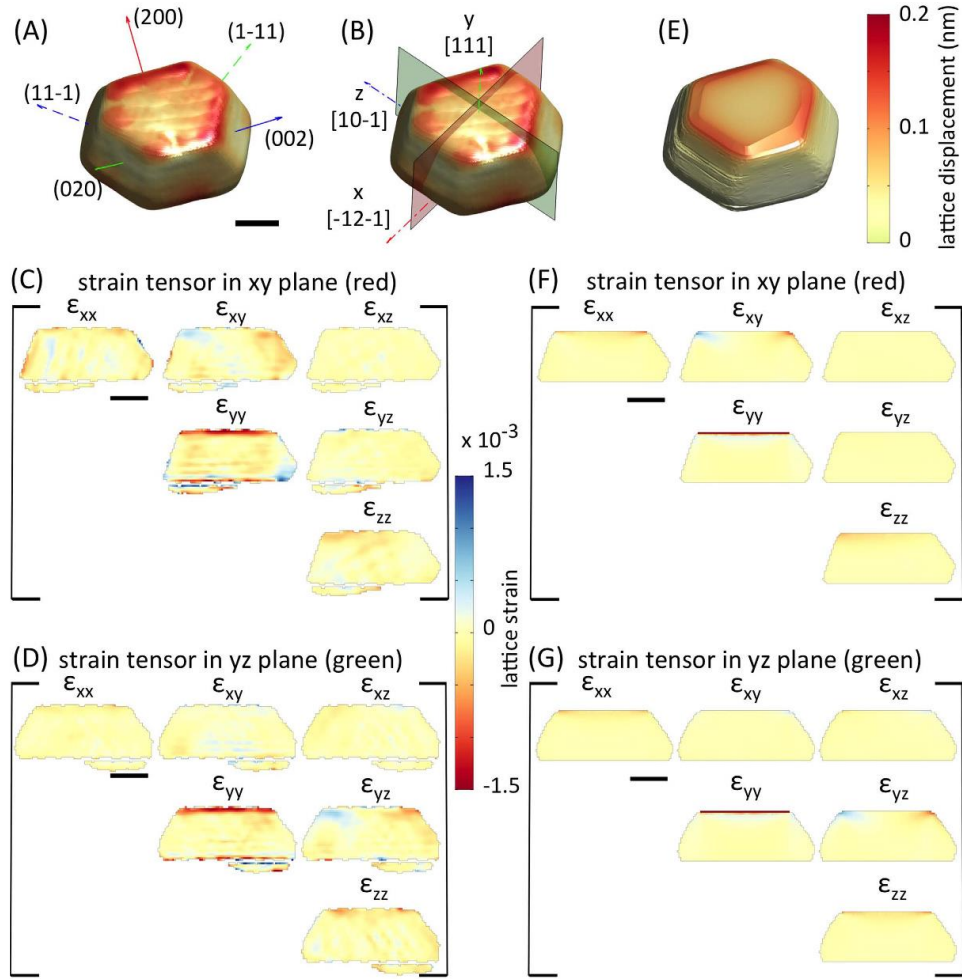
Figure 1. 14 Full 3D lattice strain tensor after focused ion beam imaging. [232]

1.5 Total scattering

The total scattering method is used in this thesis for determining the local structure of crystalline materials [26]. The basis of the method is to measure or calculate the total scattering structure function $S(Q)$, which is defined by:

$$S(Q) = \frac{I(Q)}{[b]^2} \qquad (1.37)$$

$[b]$ is the compositional averaged scattering amplitude of the atoms and $I(Q)$ is the total intensity containing Bragg peaks, elastic and inelastic diffuse scattering. The Bragg peaks are rising from periodic long-range structure. The elastic diffuse scattering contains the static local structure, ranging from short-range order to medium-range order. The inelastic scattering contains moving atoms dynamics.

Other structure functions could also be defined. For example, the reduced structure function, F(Q), could then be defined:

$$F(Q) = Q[S(Q) - 1] \qquad (1.38)$$

The atomic pair distribution $\rho(r)$ could be defined as:

$$\rho(r) = \rho_0 g(r) = \frac{1}{4\pi N r^2} \sum_u \sum_v \delta(r - r_{uv}) \qquad (1.39)$$

$g(r)$ is called the atomic pair distribution function and ρ_0 is the number density of atoms in the system of N atoms. δ is Dirac delta function.

The widely used reduced pair distribution function, $G(r)$, is defined as:

$$G(r) = 4\pi r \rho_0(g(r) - 1) \qquad (1.40)$$

Radial distribution function could be further defined:

$$R(r) = 4\pi r^2 \rho(r) = 4\pi r^2 \rho_0 g(r) \qquad (1.41)$$

From reduced structure function to reduced pair distribution function:

$$G(r) = \frac{2}{\pi} \int_{Q_{min}}^{Q_{max}} F(Q) \sin(Qr) \, dQ \qquad (1.42)$$

From reduced pair distribution function to structure function:

$$S(Q) = 1 + \frac{1}{Q} \int_0^\infty G(r) \sin(Qr) \, dr \qquad (1.43)$$

From reduced structure function to radial distribution function:

$$\frac{R(r)}{r} = \frac{2}{\pi} \int_0^\infty F(Q) \sin(Qr) \, dQ \qquad (1.44)$$

All of these distribution functions have their advantages and history. From the simulated structure, one can calculate the distribution function and compare them with the experimental scattering data.

The typical two sources to do these PDF experiments are X-ray and neutron sources. There are differences between neutron scattering and X-ray scattering, along with electron scattering. Firstly, X-ray is an electromagnetic wave that

interacts with the electrons, so the intensity is strongly dependent on the atomic factor. Light atoms make very few contributions to the diffracted intensity in the presence of some heavy atoms. Neutrons is however a particle wave that interacts with the nuclei. This makes neutrons scattering very sensitive to light atoms. In this PMN system, the O will give a very strong scattered intensity in neutrons scattering but not X-ray scattering. The second difference is that in X-ray we usually use the atomic form factor to describe the electron cloud shape, which is dependent on Q. Such a factor and scattering intensity will decrease sharply at high Q. Therefore, it's very hard for X-ray to get good quality data at high Q. However, the neutron doesn't have such a high-Q limitation, so it usually gives very good signal and works better at high Q. However, at low-Q range, the neutron scattering usually suffer from the Fourier ripples or termination errors and sometimes give meaningless information.

Chapter 2. Barium titanate oxide as a ferroelectric material

2.1 Polarization and ferroelectricity

2.1.1 A brief history

The understanding or even the discovery of the polarization related properties in materials takes a long time in history [27]. The pyroelectric phenomenon has been known for at least two thousand years, where it was first documented by the Greek philosopher Theophrastus [28-29]. The reason for this early discovery is that many natural materials show considerable pyroelectricity, such as tourmaline mineral [29]. The attempts to quantitatively study the pyroelectricity properties led to the discovery of piezoelectricity in 1880, when the Curie brothers realized the different pyroelectricity from uniform and non-uniform heating is caused by thermal stress [27,30]. The first ferroelectric material was reported in 1920, in which the polarization of Rochelle salt ($NaKC_4H_4O_6 \cdot 4H_2O$) was found to be reversible by external electric field [31]. But Rochelle salt has a complex structure containing four formula unit cells with 112 atoms, and it remained to be the only ferroelectric until the discovery of KH_2PO_4 (KDP) and its isomorphous crystals called KDP-ferroelectrics [32,33]. KDP series have a simpler crystal structure but involves hydrogen bond in the structure. Different possible arrangements of hydrogen lead to different orientation of (H_2PO_4) dipole units, so that the properties of KDP depends on the H-dynamic.

Theories were proposed to explain the origin of their ferroelectricity and many considered the hydrogen bond to be the essential condition for polar instability to give ferroelectricity [34-36]. However, this assumption was displaced with the discovery barium titanate ($BaTiO_3$, BTO) in the 1940s where no hydrogen bond exists in the crystal structure [37]. Due to the simplicity of its perovskite structure and its stability, BTO became one of the most studied ferroelectrics for decades. The big family of perovskite ferroelectrics also grew quickly, with $PbTiO_3$ (PTO) reported in 1950 and $Pb(Zr_xTi_{1-x})O_3$ (PZT) discovered in 1952 [38,39]. These materials remain to be the base materials for studying ferroelectricity until now. With the growth of the ferroelectric family, so followed the application of ferroelectric materials. BTO, for example, is widely used for its superior dielectric constant in the electronics industry. Recently, the

ferroelectric random-access memory (FeRAM) has been developed for the low power usage and fast write performance. BTO is a suitable material for such kinds of application because it is both cheap and lead-free [40,41].

2.1.2 Structure origin of ferroelectricity

Before entering a specific structure, it's interesting to revisit the definition of some crystallographic terms. These terms are well documented in textbooks of different fields, but sometimes used in a confused manner.

Table 2. 1 Crystallographic terms and their definitions.

Terms	Definitions [42-44]
Crystal structure	Often shorten to be "structure". It's the atomic distribution within a crystal. Only when neglecting all possible defects in the structure, should we consider the periodicity defines the lattice of the structure.
Lattices	An infinite set of geometric points (known as lattice nodes) that represent the translational symmetry of an ideal crystal. The number of possible lattices is infinite.
Bravais lattices	Description of geometric arrangement of lattice points, and therefore the translational symmetry of the crystal. There are 14 Bravais lattices in three dimensions: simple cubic, body-centred cubic, face-centred cubic, etc...
Lattice systems (Lattice types)	A grouping of lattices according to the axial system. There are 7 lattice systems in three dimensions: triclinic, monoclinic, orthorhombic, tetragonal, rhombohedral, hexagonal, cubic.
Crystal systems	A classification of lattice according to the point group. There are 230 unique 3-D space groups. These crystallographic space groups can be sorted into 7 crystal systems: triclinic, monoclinic, orthorhombic, tetragonal, trigonal, hexagonal, cubic.

Crystal families	A combination of crystal systems. There are 6 crystal families in three dimensions: triclinic, monoclinic, orthorhombic, tetragonal, hexagonal, cubic.
Geometric crystal class	A classification of the symmetry groups of the external shape of macroscopic crystals. There are 32 geometric crystal classes in three dimensions.
Arithmetic crystal class	A combination of geometric crystal classes (32) and corresponding Bravais lattice types (14). There are 73 arithmetic crystal classes in three dimensions. For example, the tetragonal structure has 7 geometric crystal classes: 4, $\bar{4}$, $4/m$, 422, $4mm$, $\bar{4}m2$, $4/mmm$; It has two Bravais lattice types: Primitive (P) and Body centred (I); This combines to 16 arithmetic crystal classes: 4P, 4I, $\bar{4}P$, $\bar{4}I$, $4/mP$, $4/mI$, 422P, 422I, 4mmP, 4mmI, $\bar{4}2mP$, $\bar{4}m2P$, $\bar{4}m2I$, $\bar{4}2mI$, $4/mmmP$, $4/mmmI$.

Ferroelectricity is a characteristic of the crystal with two or more identical and spontaneous orientation states in the absence of electrical field. These orientation states, namely the electric polarization, can be reversed or change from one to another by an external electrical field. This reversibility of polarization is a unique feature of ferroelectricity, as all substances have electrostriction and could react to the field in a non-reversible manner. Of the 32 geometric crystal classes, 11 classes are centrosymmetric with no polar properties, therefore appear neither ferroelectric nor piezoelectric. In the remaining 21 non-centrosymmetric geometric crystal classes, 20 of them exhibit the piezoelectric effect, that is the charge-stress coupling phenomenon. In these 20 piezoelectric crystal classes, 10 of them have a unique polar axis with spontaneous polarization. Because these spontaneous polarizations are temperature dependent, the 10 crystal classes are termed as pyroelectric crystal classes. Ferroelectric crystal classes can be considered as the subgroup of pyroelectric classes, as all ferroelectrics show pyroelectricity. However, it is suggested not to solely define ferroelectricity using a purely crystallographic

definition because of the experimental limitations in two ways: 1) Polarization reversibility may not be seen even when a material is ferroelectric. For example, the crystal imperfections, the electric conductivities, the temperature and pressure all affect the reversibility of polarization. 2) Polarization reversal does not necessarily mean a material is a ferroelectric. For example, the polarization can arise from a metastable phase due to the temporary application of a switching field [27].

Perovskite ferroelectrics have a chemical formula of ABO_3, where A and B are cations. In perovskite structure, there is a semi-empirical relationship known as Goldsmith factor or tolerance factor [45]. It calculates the geometry of atoms in cubic phase as:

$$t = \frac{R_A + R_O}{\sqrt{2}(R_B + R_O)} \tag{2.1}$$

R_A and R_B are the radius of A-site, B-site and oxygen ionic radii, respectively. If the tolerance factor is bigger than 1, it means the B-site cation is relatively smaller than A-site, so that it has more free space to move around in its oxygen octahedral cage. This smaller B-site is usually related to high dielectric or ferroelectric properties [46]. If tolerance factor is equal to 1, it means the A-site and B-site match in size perfectly. If tolerance factor is smaller than 1, it represents a smaller A-site relative to B-site and the A cation can move around its cage of oxygen neighbours.

2.1.3 Phase transitions

From low temperature to high temperature, most ferroelectrics would go from low symmetry to high symmetry lattices, although in some cases the highest symmetry phase is not achieved before the melting point. BTO has a perovskite structure, where the titanium cation sits at B site in the oxygen octahedral shell. The phase transition is presented in Figure 2.1(a), where it has a rhombohedral lattice (trigonal crystal system, R3m) at lower temperature, going into orthorhombic lattice (B2mm) at 203 K, and then to tetragonal lattice (P4mm) at 278 K, and finally goes into cubic lattice (Pm3m) at 393 K [47]. The lattice constant changes over temperature are shown in Figure 2.1(b) [48]. Interestingly, there is a gap in transition temperature between heating and

cooling down. Such a transition delay is usually seen in glasses, where the disorder system needs time and activation energy to cooperate with the transition. While in BTO, the disorder is believed to come from the different alignments of spontaneous polarization.
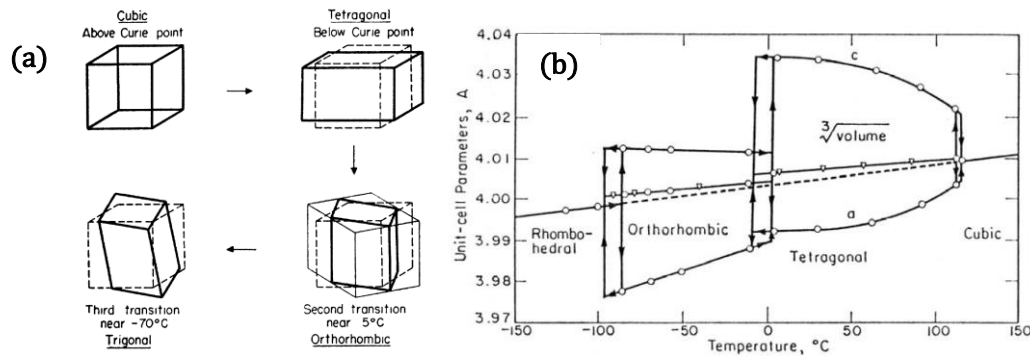
Figure 2. 1 (a) Phase transitions of BTO. Image from [47]. (b) The changes of lattice constant with temperature. Image from [48].

The ample phase transitions with different crystal systems lead to various properties. BTO shows ferroelectricity in rhombohedral, orthorhombic and tetragonal lattice systems, which are all termed as ferroelectric phases. The polar axes for the three ferroelectric phases are crystallographic 111, 110 and 100, respectively. BTO has no ferroelectricity in its cubic phase, at least globally, which is termed a paraelectric phase because its polarization responds linearly to the applied field.

Different phase diagrams could be generated when varying one factor and controlling the others. Two examples are given in Figure 2.2. The first graph shows the phase transition temperature is decreased with the increase of pressure [49]. The second graph shows the changes of Curie temperature with in-plane strain when the BTO thin film has the c-axis pointing out-of-plane [28]. The solid line is the result from thermodynamic calculations, while the points inside the graph are experimental result. This tetragonal-cubic phase transition could increase to more than 800 K with a -1.7% in-plane strain. This substantial strain is acquired by carefully choosing the substrate lattice constant supporting a thin film and is hard to acquire in single crystal, where numerous mechanisms would happen to relax the large strain. There are also phase diagrams for

domains, where different configurations of domain structures are of interest and mapped out [41].
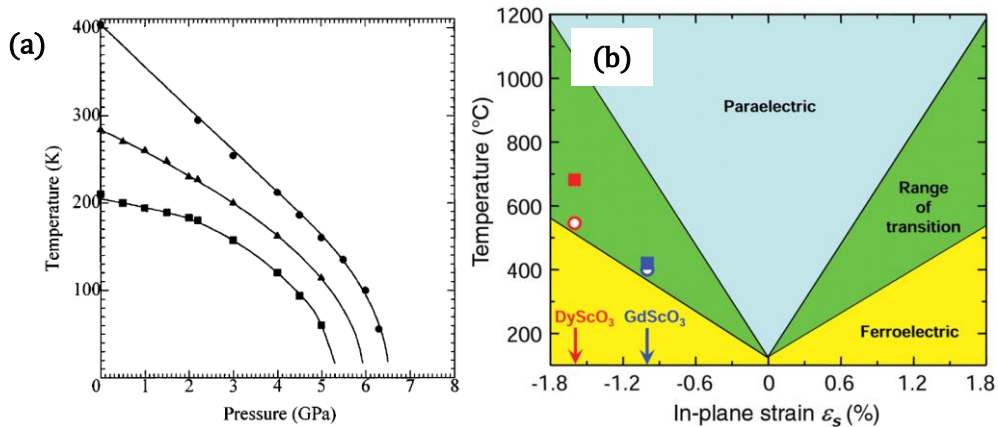
Figure 2. 2 General phase diagrams of BTO. (a) Experimental phase transition temperature as a function of pressure. The solid lines are guide for eyes. Image from [49] (b) Thermodynamic calculated and experimental cubic-tetragonal phase transition temperature (Tc) of (001) BTO thin film under biaxial in-plane strain. Image from [24]. The circles represent the results from reactive molecular beam epitaxy (MBE), while the cube represent the results from pulse-laser decomposition (PLD). The red colour denotes the BTO thin film grown on DyScO₃ substrate, while the blue colour denotes the GdScO₃ substrate. Images from [50].

2.1.4 Soft mode

Microscopic models and lattice dynamics have helped to understand the nature of ferroelectric phase transitions. The structural phase transition is usually defined as being either "displacive" type and "order-disorder" type. There is a longstanding discussion in the scientific literature about the relative merits of both models.

(a) Displacive model

The displacive model is straightforward, given the simplicity of perovskite ABO_3 structure. In the displacive model, the Ti^{4+} cation is displaced off-centre within the O^{2-} anion octahedron. The phase transition occurs when this average position changes its symmetry. Figure 2.3 shows a typical image of how the Ti^{4+} displacement happens in BTO unit cells.

The basis of displacive model could track back to 1950, when Slater proposed there is a long-range dipole force tending to destabilize the local high-symmetric configuration [51]. Now the model is built on the lattice dynamics, where one

lattice mode is considered to describe the displacive lattice instability [52].
Generally, there are three deformations to consider: long wavelength
homogeneous deformations (zone centre acoustic modes); long wavelength
inhomogeneous deformations (zone centre transverse optical modes); short
wavelength deformations (zone boundary optical modes). The long wavelength
inhomogeneous mode involves the ionic motions of all constituent atoms, which
is designated as the basic variable and is the so-called "soft mode" in a displacive
phase transition.

When getting close to the phase transition temperature T_c, the frequency of this
soft mode substantially decreases. This is why it is called soft mode or freezing
mode. Microscopically, the restoring force of vibrating positive and negative ions
are lost or weakened when approaching the T_c. Therefore, the ions are displaced
to new off-centre positions. The reducing soft mode frequency is described by
Cochran's law:

$$\omega_{TO}^2 = C(T - T_c) \tag{2.2}$$

C is a constant and is T_c is Curie temperature. In displacive model, the driving
force of phase transition is the softening of the zone centre transverse optical
mode.
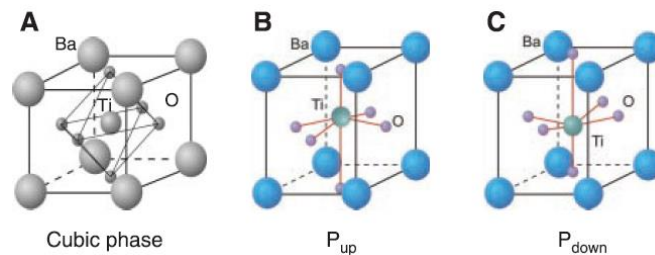
*Figure 2. 3 Typical crystal structure of BTO. (a) Cubic phase unit cell. (b)
Tetragonal phase unit cell with Ti⁴⁺ displaced upward. (c) Tetragonal phase unit
cell with Ti⁴⁺ displaced downward. Image from [53].*

(b) Order disorder model

The order disorder model involves partially occupied sites and the symmetry of
this occupancy. Figure 2.4 shows a typical eight-site order disorder model for
BTO, which is proposed in 1968 by Comes [54,55]. In this model, the Ba^{2+} (A-
site) and oxygen can be treated as static, while the Ti^{4+} (B-site) has eight

crystallographic 111 positions to occupy. The phase transition occurs when the breaking of occupational symmetry starts to happen. In an order-disorder phase transition, the soft mode as described in displacive model (zone centre transverse optical mode) does not change with temperature. However, another central mode describing the relaxation type excitation becomes strongly temperature dependent and showing damping, which can be used as a signature of order disorder type in spectroscopy [56]. This central mode frequency is linked with dielectric constant via the Debye relaxation relation.
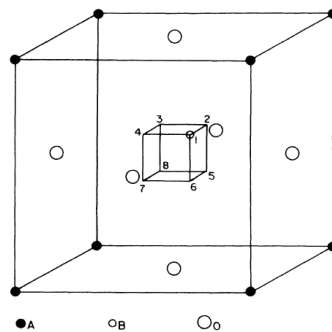
Figure 2. 4 Eight site model in a BTO unit cell. Image from [55]

The phase transition in a specific ferroelectric can be one or a mixture of both types. For example, the ferroelectric transition in PTO is reported to be the pure displacive type [57]. Historically, BTO was thought to be a textbook displacive type ferroelectric. Now it is well accepted as a combination of displacive and order-disorder type material [58-60]. This is quite relevant to the local structure, which is discussed in detail in Chapter 2.5.

2.1.5 Phenomenological theories

Phenomenological calculations based on Landau-Ginzburg-Devonshire has proven to be useful in studying ferroelectrics, such as predicting the phase transitions and describing temperature dependent properties. Most of the phase field simulations are also implicitly based on the continuum theory underlying the LGD theory. It is a purely macroscopic theory equivalent to mean field theory, where it averages out the long-range interactions and fluctuations to reduce a many-body problem to a one-body problem.

(a) Landau theory

Landau theory is a general theory for describing second-order phase transitions in 1937 but can also be extended to first-order phase transitions under external field as shown in later studies [61]. In Landau theory, the thermodynamic potential (or free energy, such as Gibbs free energy) of the system can be depicted as an analytic function of its order parameters, suitably defined. This function is then Taylor expanded in the form of different powers of order parameters near the phase transition temperature. This Taylor expansion only includes the even powers, as all the odd powers are omitted due to certain symmetries:

$$F(T, \eta) - F_0 = \frac{1}{2} a(T) \eta^2 + \frac{1}{4} b(T) \eta^4 + \frac{1}{6} c(T) \eta^6 + \cdots \qquad (2.3)$$

T is the temperature and η is the order parameter, which depicts the strength of perturbation linked to the structural change. This order parameter is constructed in such a way that it is non-zero in the low symmetry phase and zero in the high symmetry phase.

The physical reason for this expansion is related to the soft mode described above. Because restoring force of a certain lattice mode becomes frozen or soft when approaching the phase transition, the amplitude of this mode becomes large enough to supress all other modes. The total energy is the sum of all lattice modes, as in the Debye theory. This total energy can be approximated as the expansion of the amplitude of just this soft mode when it becomes dominant [62].

(b) Landau-Ginzburg-Devonshire theory

Many extensions and applications of Landau theory have been proposed with regard to different systems. One of the famous extensions is Landau-Ginzburg theory, which serves as a mathematical description of superconductivity. The Landau theory was applied to describe ferroelectricity by Ginzburg in 1945 and Devonshire in 1949 independently [63]. Therefore, the developed phenomenological theory for ferroelectricity is called Landau-Ginzburg-

Devonshire (LGD) theory. The crucial assumption for ferroelectrics, is to identify the order parameter as the polarization, thus the free energy can be written as:

$$F(T, P) - F_0(T) = \alpha_1 P^2(T) + \alpha_{11} P^4(T) + \alpha_{111} P^6(T) + \cdots - EP(T) \qquad (2.4)$$

α_1 is temperature dependent, crossing zero at the phase transition, and usually takes the form of:

$$\alpha_1 = \frac{T - T_c}{2\varepsilon_0 C_0} \qquad (2.5)$$

α_{11} and α_{111} are higher-order dielectric stiffness coefficients at constant stress.

When the electric field E=0, the polarization for the minimization of free energy can be calculated as

$$P^2(T) = \frac{-\alpha_{11} + \sqrt{\alpha_{11}^2 - 3\alpha_1 \alpha_{111}}}{3\alpha_{111}} \qquad (2.6)$$

Notably, this is a simple form in one dimension and considering only the polarization to be the order parameter. To depict a real ferroelectric system, more quantities need to be added [64-66]. For example, the elastic strain accounts for a zone-centre acoustic mode which causes the phase transition. However, it is not associated with the softening of polarization related zone centre optical mode. These factors can be added directly to the free energy expression and treated as secondary order parameters, because they are independent of the primary order parameter. If the polarization in three dimensions, the lattice systems with specific atoms and grain shape are treated in detail, then even more terms need to be considered [67,68]. In real case, certain modification of free energy expression is needed based on the question of interest.

2.1.6 Physical Properties

Both the soft mode theory and phenomenological LGD theory help to understand the properties of ferroelectric. Although the starting point is different, they do come to the same conclusion and show a inter connection.

(a) Dielectric property

The dielectric permittivity can be directly calculated from LGD theory. If only the second power of polarization is considered, then the expression for free energy can be written as:

$$F(T,P) - F_0(T) = \alpha_1 P^2(T) - EP(T) \tag{2.7}$$

The minimum free energy takes place at:

$$P(T) = \frac{1}{2\alpha_1} = \frac{\varepsilon_0 C_0}{T - T_c} E \tag{2.8}$$

The dielectric permittivity can be calculated as:

$$\varepsilon = \varepsilon_r \varepsilon_0 = (1 + \chi)\varepsilon_0 = \varepsilon_0 \left(1 + \frac{C_0}{T - T_c}\right) \tag{2.9}$$

The electric susceptibility in this equation is the famous Curie-Weiss law:

$$\chi = \frac{C_0}{T - T_c} \tag{2.10}$$

Figure 2.5a shows an example of the dielectric constant over temperature for BTO, where dielectric constant reaches 4500 at room temperature and reaches the maximum value at the Curie point [47]. However, this value is strongly dependent on the grain size and other factors, as illustrated later in this Chapter.

If the electric field is a harmonic alternating field, it can be expressed as:

$$E = E_0 e^{i\omega t} \tag{2.11}$$

Then the polarization is expressed as:

$$P = \varepsilon_0 \chi E_0 e^{i\omega t} = P_0 e^{i\omega t - \theta} \tag{2.12}$$

The ω means angular frequency and theta is the phase shift. The electric susceptibility in this case is also frequency dependent and complex. The real part and imaginary parts are called dielectric dispersion and dielectric loss, respectively.

The Curie-Weiss law can also be derived from the lattice dynamics point of view by either the displacive model or order-disorder model. Taking the displacive

model as an example, according to Lyddane-Sachs-Teller relation [69], the dielectric constants are connected to the optical phonon frequency:

$$\frac{\varepsilon_s(T)}{\varepsilon_\infty} = \frac{\omega_{LO}^2}{\omega_{TO}^2(T)}$$

(2.13)

The $\varepsilon_s(T)$ is static frequency of dielectric constant and ω_{TO} is transverse optical mode frequency, both of which will change with temperature. The ε_s is the high frequency dielectric constant and ω_{LO} is the longitudinal optical mode frequency, both of which can be viewed as constant over temperature. By substituting the equation 2.2, the Curie-Weiss law is obtained.

Ferroelectric materials behave similarly to ferromagnets in the sense of hysteretic behaviour. Figure 2.5b shows the hysteresis loop of BTO at room temperature [70,71]. When the external electrical field is applied to the sample, the inner spontaneous polarization will align accordingly and become parallel to the field when saturated. When this external field is removed, the polarization of a paraelectric material would decrease to zero. However, for ferroelectric material, the polarization would decrease to a nonzero value. Additional negative field is needed in order to switch the polarization direction. This hysteresis loop is also time dependent. Figure 2.5c presents the hysteresis loops at different temperatures [70,72].

(b) Piezoelectricity

Piezoelectricity quantifies the interaction between stress and electric field, measured as the derivative of polarization with respect to stress, of which the d_{33} component is the most important [53]. Some good piezoelectric performance materials are $Pb(Zr_xTi_{1-x})O_3$ (PZT, d_{33}=374 pC/N) and relaxor type single crystal such as $(PbMg_{1/3}Nb_{2/3})_{1-x}$-$(PbTiO_3)_x$ (PMN-PT, d_{33}=1500 pC/N) and $(PbZn_{1/3}Nb_{2/3})_{1-x}$-$(PbTiO_3)_x$ (PZN-PT, d_{33}=2200 pC/N) [73-76]. Single crystal BTO, however, has modest piezoelectricity at room temperature with d_{33}=90 pC/N along 001 crystal orientation, which is the polar axis in the tetragonal phase. A higher piezoelectricity with d_{33}=190 pC/N can be achieved by applying a sufficiently large electric field along the 111 crystal orientation [77-79]. By heating the BTO crystal from room temperature to the tetragonal-cubic phase

transition temperature, the d_{33} value rises from 90 pC/N to nearly 350 pC/N for 001 oriented BTO single crystals. While for 111 oriented BTO single crystals in the same temperature range, the d_{33} value decreases as temperature increases [78,80].
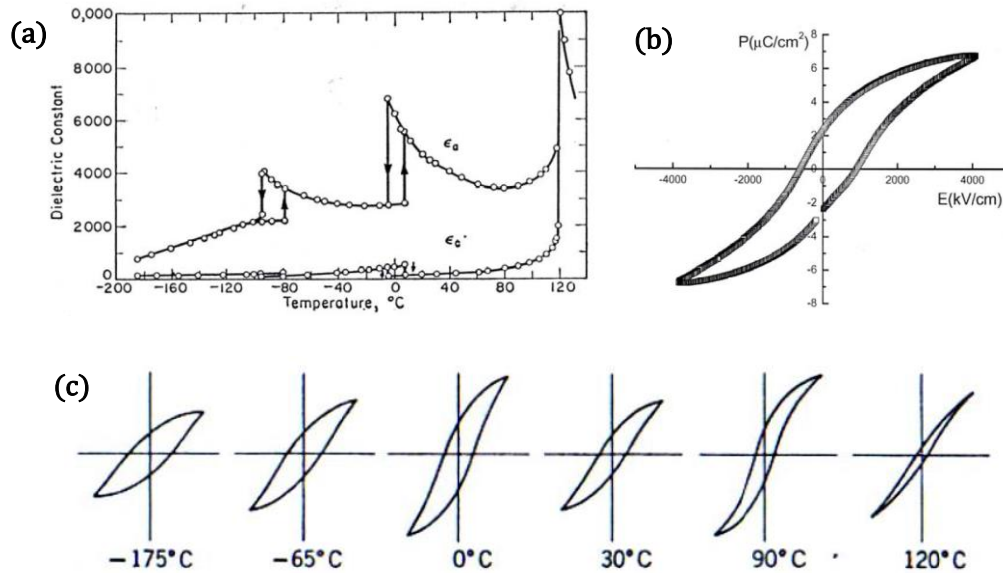
Figure 2. 5 (a) The dielectric constant of BTO along a and c axes. Image from [47]. (b) BTO hysteresis loops at room temperature with high resolution. Image from [71]. (c) The change in BTO hysteresis loops with temperature. Image from [72].

Recently, exceptional high piezoelectric BTO ceramics are prepared by different sintering techniques or hydrothermal synthesis. The d_{33} value can now reach 788 pC/N, making it a promising candidate for lead-free piezoelectric applications [81,82]. It's generally believed that the grain size and the domains are responsible for these high piezoelectric responses, though there are controversial views of whether it is the domain wall or domain width that matters [83-86].

Stress and strain are second rank tensors with 9 coefficients. Due to symmetry, only 6 of 9 coefficients are independent. The strain, for example, is expressed as below:

$$\varepsilon = \begin{bmatrix} \varepsilon_{xx} & \varepsilon_{xy} & \varepsilon_{xz} \\ \varepsilon_{yx} & \varepsilon_{yy} & \varepsilon_{yz} \\ \varepsilon_{zx} & \varepsilon_{zy} & \varepsilon_{zz} \end{bmatrix} = \begin{bmatrix} \varepsilon_{xx} & \varepsilon_{xy} & \varepsilon_{xz} \\ 0 & \varepsilon_{yy} & \varepsilon_{yz} \\ 0 & 0 & \varepsilon_{zz} \end{bmatrix} = \begin{bmatrix} \dfrac{\partial u_x}{\partial x} & \dfrac{1}{2}\left(\dfrac{\partial u_x}{\partial y} + \dfrac{\partial u_y}{\partial x}\right) & \dfrac{1}{2}\left(\dfrac{\partial u_x}{\partial z} + \dfrac{\partial u_z}{\partial x}\right) \\ 0 & \dfrac{\partial u_y}{\partial y} & \dfrac{1}{2}\left(\dfrac{\partial u_y}{\partial z} + \dfrac{\partial u_z}{\partial y}\right) \\ 0 & 0 & \dfrac{\partial u_z}{\partial z} \end{bmatrix} (2.14)$$

Such expression can also be written using number annotation:

$$\begin{bmatrix} \varepsilon_{xx} & \varepsilon_{xy} & \varepsilon_{xz} \\ 0 & \varepsilon_{yy} & \varepsilon_{yz} \\ 0 & 0 & \varepsilon_{zz} \end{bmatrix} \Rightarrow \begin{bmatrix} \varepsilon_1 \\ \varepsilon_2 \\ \varepsilon_3 \\ \varepsilon_4 \\ \varepsilon_5 \\ \varepsilon_6 \end{bmatrix} \qquad (2.15)$$

Stress and strain are quantitatively connected as:

$$\begin{bmatrix} \sigma_1 \\ \sigma_2 \\ \sigma_3 \\ \sigma_4 \\ \sigma_5 \\ \sigma_6 \end{bmatrix} = \begin{bmatrix} Q_{11} & Q_{12} & Q_{13} & Q_{14} & Q_{15} & Q_{16} \\ Q_{21} & Q_{22} & Q_{23} & Q_{24} & Q_{25} & Q_{26} \\ Q_{31} & Q_{31} & Q_{33} & Q_{34} & Q_{35} & Q_{36} \\ Q_{41} & Q_{42} & Q_{43} & Q_{44} & Q_{45} & Q_{46} \\ Q_{51} & Q_{52} & Q_{53} & Q_{54} & Q_{55} & Q_{56} \\ Q_{61} & Q_{62} & Q_{63} & Q_{64} & Q_{65} & Q_{66} \end{bmatrix} \begin{bmatrix} \varepsilon_1 \\ \varepsilon_2 \\ \varepsilon_3 \\ \varepsilon_4 \\ \varepsilon_5 \\ \varepsilon_6 \end{bmatrix} \qquad (2.16)$$

where the Q matrix is the stiffness matrix. A similar reversed expression would link the strain with stress by compliance matrix S. The relationship is $S = Q^{-1}$.

Piezoelectricity is a third rank tensor with 27 coefficients but could only have 18 distinct coefficients because of the symmetry of strain. Without electrical field, the polarization can be expressed as applied stress:

$$\begin{bmatrix} P_1 \\ P_2 \\ P_3 \end{bmatrix} = \begin{bmatrix} d_{11} & d_{12} & d_{13} & d_{14} & d_{15} & d_{16} \\ d_{21} & d_{22} & d_{23} & d_{24} & d_{25} & d_{26} \\ d_{31} & d_{32} & d_{33} & d_{34} & d_{35} & d_{36} \end{bmatrix} \begin{bmatrix} \sigma_1 \\ \sigma_2 \\ \sigma_3 \\ \sigma_4 \\ \sigma_5 \\ \sigma_6 \end{bmatrix} \qquad (2.17)$$

P_1, P_2 and P_3 are polarization along crystallographic x, y and z direction. Such abbreviation writing of stress tensor also simplified the piezoelectric coefficients, like d_{31} connects polarization P_3 with stress tensor σ_1. This is the case where force is along x direction and the polarization is along c axis.

Similarly, without stress, the spontaneous strain can be express as applied electric field:

$$\begin{bmatrix} \sigma_1 \\ \sigma_2 \\ \sigma_3 \\ \sigma_4 \\ \sigma_5 \\ \sigma_6 \end{bmatrix} = \begin{bmatrix} d_{11} & d_{21} & d_{31} \\ d_{12} & d_{22} & d_{32} \\ d_{13} & d_{23} & d_{33} \\ d_{14} & d_{24} & d_{34} \\ d_{15} & d_{25} & d_{35} \\ d_{16} & d_{26} & d_{36} \end{bmatrix} \begin{bmatrix} E_1 \\ E_2 \\ E_3 \end{bmatrix} \tag{2.18}$$

If further crystal symmetries are applied, then the independent piezoelectric coefficient would keep decreasing. For example, in cubic crystal lattice, all piezoelectric coefficients are zero. Considering the tetragonal BTO and picking up c-axis as the only polar axis, then the tensor matrix is simplified as:

$$\begin{bmatrix} P_1 \\ P_2 \\ P_3 \end{bmatrix} = \begin{bmatrix} 0 & 0 & 0 & 0 & d_{15} & 0 \\ 0 & 0 & 0 & d_{24} & 0 & 0 \\ d_{31} & d_{32} & d_{33} & 0 & 0 & 0 \end{bmatrix} \begin{bmatrix} \sigma_1 \\ \sigma_2 \\ \sigma_3 \\ \sigma_4 \\ \sigma_5 \\ \sigma_6 \end{bmatrix} \tag{2.19}$$

Where $d_{31}=d_{32}$ and $d_{15}=d_{24}$.

The physical meaning of these coefficients can be seen in Figure 2.6 [87].
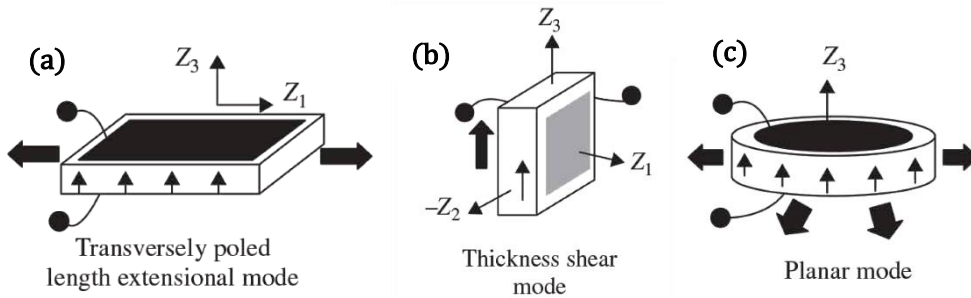
Figure 2. 6 Measurements of different piezoelectric coefficient of a ceramic. (a) A measurement of coefficient d_{33}. Both applied stress and polarization measurement are taking along Z_3 axis. (b) A measurement of coefficient d_{31}. Stress is applied along Z_1 axis and the polarization is measured along Z_3 axis. (c) A measurement of coefficient d_{15}. Force direction is along Z_3 axis but force normal is Z_1 axis. The polarization is measured along Z_1 axis. Image from [87].

2.1.7 Influencing factors

As discussed above, the phase transition temperatures of BTO could vary a lot in literature, where various factors are reported to be influential. For example, the strain, pressure, the crystal size, and/or the perfection of the crystal could

substantially change the transition temperature. This may take the form of different synthesis routes and processing techniques, which then involves defect chemistry, incorporation of foreign atoms, aggregation, porosity, residual stress and so on. It is possible that the influence is coming through the domain structure of the crystal, which is affected by all these factors, and so we are interested to discover the cause-effect relationships. Due to this complexity, it is not surprising that there are masses of scientific literature focused on this topic and sometimes it's hard to compare the exact value, given that different papers are using different samples. However, it's still useful to track the trend within each experiment, which would coincide with each other. Also, the dependent variables are intertwined themselves.

Taking the tetragonal-cubic phase transition as an example, the Gibbs energy of a ferroelectric system is written as a series power expansion of polarization, as stated in LGD theory:

$$G = G_0 + \frac{1}{2}\beta(T - \theta)P^2 + \frac{1}{4}\Upsilon P^4 + \frac{1}{6}\delta P^6 \qquad (2.20)$$

G is Gibbs energy; P is polarization; β, Υ and δ are phenomenological coefficients; θ is Curie-Weiss temperature. The tetragonal distortion can be quantified as tetragonality, which can be described as the square of polarization:

$$\eta = \frac{c}{a} - 1 = kP_s^2 \qquad (2.21)$$

$\frac{c}{a}$ is tetragonality, k is the difference of the electrostrictive coefficients $Q_{11} - Q_{12}$.

The Curie transition temperature is also related to polarization, therefore can be described by tetragonality:

$$\frac{Q}{T_c} = \frac{\beta}{2}P_s^2 + \frac{1}{4}\left(\frac{\partial \Upsilon}{\partial T}\right)P_s^4 = \frac{\beta}{2k}\eta + \frac{1}{4k^2}\left(\frac{\partial \Upsilon}{\partial T}\right)\eta^2 \qquad (2.22)$$

Q is the heat of transition and T_c is the Curie temperature.

Through these equations, it can be seen that the tetragonality (or tetragonal related strain), the spontaneous polarization and Curie temperature are directly connected for a given system.

The most studied factor in BTO is the size effect. The grain-size effect has been reported for more than 60 years, when Kniepkamp and Heywang talking about the dielectric properties of polycrystalline BTO [88]. This size effect has been under intensive studied especially after 1990, when both the preparation and characterization methods were well developed for studying miniaturization of BTO grains. From equations above, the tetragonality, the Curie temperature and spontaneous polarization are coupled together, therefore they will change in a similar manner as the size decreases.

Tetragonality tends to show little change when the grain size is in or above micrometer size. When the grain size goes down to hundreds or tens of nanometer, the tetragonality would show a decreasing trend. Again, this decreasing curves with grain size varies from one study to another. Figure 2.7 shows the tetragonality of different BTO samples. The first graph shows the tetragonality for BTO single crystal remains the same from 1 m down to 0.3 μm, when it starts to decrease [89]. The lattice system goes into cubic when the size is 0.12 μm. The second graph shows another study of BTO fine crystal [90]. This time the crystal still shows tetragonality over 1.004 when size is about 40 nm. The crystal goes into cubic phase suddenly when the size is 30 nm or less. What temperature?
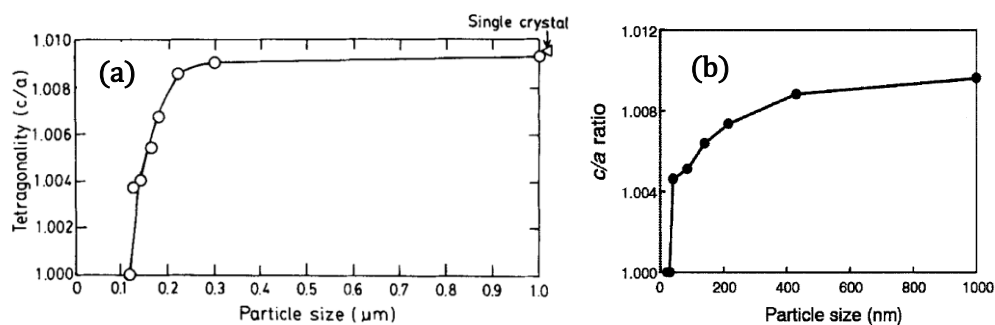
Figure 2. 7 The tetragonality changes with particle size. Image from [89,90].

Curie temperature is expected to be connected to tetragonality, as explained above. As the particle size decreases at a given temperature, the tetragonality is seen to decrease as well, so it is expected that the Curie temperature will be lower for smaller particles too. Figure 2.8a shows the Curie temperature changes

over tetragonality in BTO single crystal. When single crystal sizes go down to 0.12 μm, the Curie temperature decreases to about 70° [90].
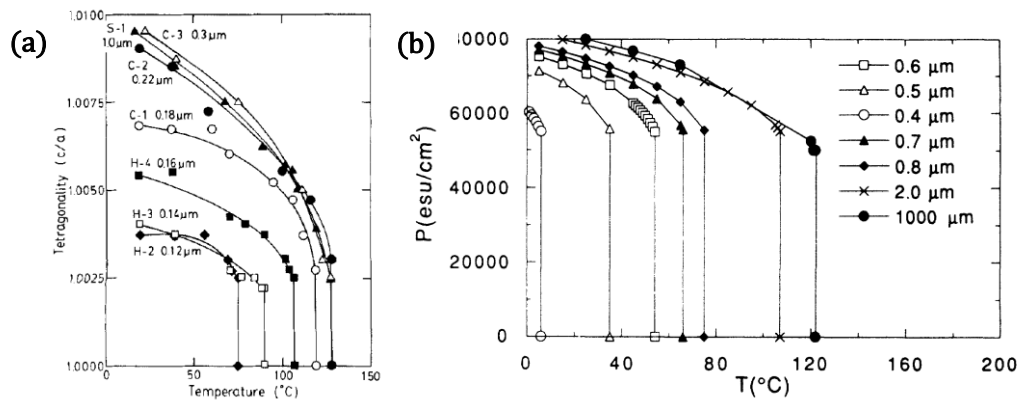
Figure 2. 8 (a) Curie temperature differences and tetragonality difference as a function of grain size. Image from [61] (b) Polarization differences and Curie temperature differences as a function of different grain size. Image from [90].

Polarization also shows a decreasing tendency when the size goes down to sub micrometre range. Figure 2.8b shows the polarization as a function of crystal size and temperature. For this specific series of samples, the crystal with size of 0.4 μm has no polarization at room temperature. When the size geos from 0.5 μm to 2.0 μm, the polarization increases from 66000 esu/cm^2 to more than 80000 esu/cm^2 [91].

The dielectric constant of BTO is found to increase when the size goes from bulk down to micrometres and reaches a maximum at about 1 μm [92,93]. Temperature data of dielectric constant are shown in Figure 2.9 for particles of different sizes, decreasing from 1200 nm to 50 nm. Smaller grain BTO particles have smaller dielectric constant. There are different reasons to explain the appearance of an optimum size, all related to the nanoscale structure. A first view is that there is a bigger mobility of domain walls at this particular size that leads to a maximum dielectric constant [93,94]. A second view is that it's the twinning behaviour that determine the favourable size. When the crystal size decreases to micrometre, the minimization of residual strain results in a twinning structure becoming favourable. However, for the finest BTO crystals, with sizes down to hundreds of nanometres, the formation of domain wall becomes too costly compared to the volume transformation changes for transformation [95-97].
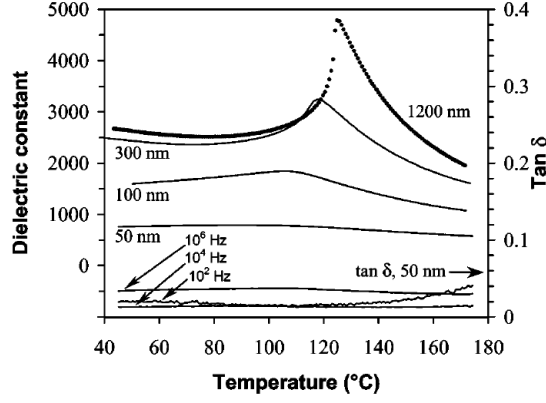
Figure 2. 9 The changes of dielectric constant of BTO crystals of different grain size with temperature. Image from [95].

The optimum "critical" size is thought to be the smallest size when the BTO particle could still preserve ferroelectricity [98]. Though the idea itself is controversial, there are supporting experimental results. As can be seen in the two examples in Figure 2.7, the critical sizes are 0.12 μm and 30 nm, respectively. The theoretical predicted critical length (thickness) for BTO thin film is 2.4 nm [99]. There are several phenomenological reasons to explain the appearance of critical size:

1) Depolarization field could play a key role in this size dependent behaviour [100,101], unlike in the bulk crystal material, where numerous mechanisms exist to compensate the charge generated by polarization. When the crystal size keeps decreasing, it reaches a point where there is no way to compensate this charge. Then the depolarization field could be sufficiently strong for the crystal phase to become unstable. The depolarization field can be described as:

$$E = -\frac{L}{\varepsilon_0}P \tag{2.23}$$

The energy of depolarization field can be denoted as:

$$W = \frac{1}{2}\int \frac{\varepsilon}{\varepsilon_0}L^2 P^2 dV \tag{2.24}$$

2) Charged defects are inevitable for chemically prepared BTO samples, where the hydroxyl ion could reside as defects on oxygen sites and result in cation vacancies for charge compensation [102,103]. This can be confirmed by spectroscopy, in which the narrowly spaced infrared

51

absorption bands are interpreted as the stretching mode for hydroxyl ions in the unit cell of tetragonal BTO [104,105]. Apparently, these charged defects could serve to stabilize the local polar ordering and might be expected to disturb the phase transition.

3) The effect of elastic constraint could also make a play in this critical size effect. As described above, when the grain size decreases to sub-micron size, the crystals are substantially untwined due to the increasing domain wall energy cost. From our BCDI experiments in Chapter 3 for the nominal 200nm BTO particles, the twin structure happens in less than one-seventh of the crystals. When the size goes to the limit, the transformation strain could be prevented even if there is a transformation driving force.

Anyway, the reasons behind the critical size haven't come to a consensus, which is one of our pursuits in the current and future studies.

2.2 Ferroelectric domain structure

"Domain" is a term to describe a region of crystal having the same order parameter. In ferroelectrics, this order parameter is spontaneous polarization. Before stepping into the specific domain structures, the techniques to visualize the domains are described first. The two most widely used techniques are scanning electron transmission microscopy (STEM) and piezo response force microscopy (PFM), both of which are good at dealing with thin film samples.

2.2.1 Characterization techniques

To map out the atomic polarization for thin film sample, high-angle annular dark-field (HAADF)-STEM is often performed, where an annular dark-field detector is put at high angle to measure the incoherently scattered electrons. Such intensity is proportional to the square of the atomic number (Z^2) with good accuracy [106], which is why HAADF is often called "Z-contrast" TEM. Two-dimensional (2D) gauss fitting is usually applied to determine the atom central position, by which the relative displacement between different types of atoms can be extracted.

HAADF-STEM images of typical perovskite $SrTiO_3$ (STO), $BaTiO_3$ (BTO) and $PbTiO_3$ (PTO) are shown in Figure 2.10. The atomic numbers for strontium,

barium, lead and titanium are 38, 56, 82, 22, respectively. The strontium and titanium atomic number are closer, so that the contrast is less obvious. Both atoms, as ions, show bright spots in the STEM image and the oxygen ions can also be visible as dark points in Figure 2.10a [107]. The polarization direction can be described as the titanium atom displacement relative to oxygen.

Figure 2.10b presents the STEM image of BTO. The barium atomic number is twice larger than the titanium, thus barium atom appears to be much brighter than titanium in STEM image [108]. Although in some cases, the Ti-O columns can be clearly seen, but for the other conditions only barium and titanium ions can be identified with confidence. Therefore, it's more natural to compare the displacement between barium and titanium ions. The polarization is interpreted as being along the direction where the titanium ion is displaced relative to barium ion.
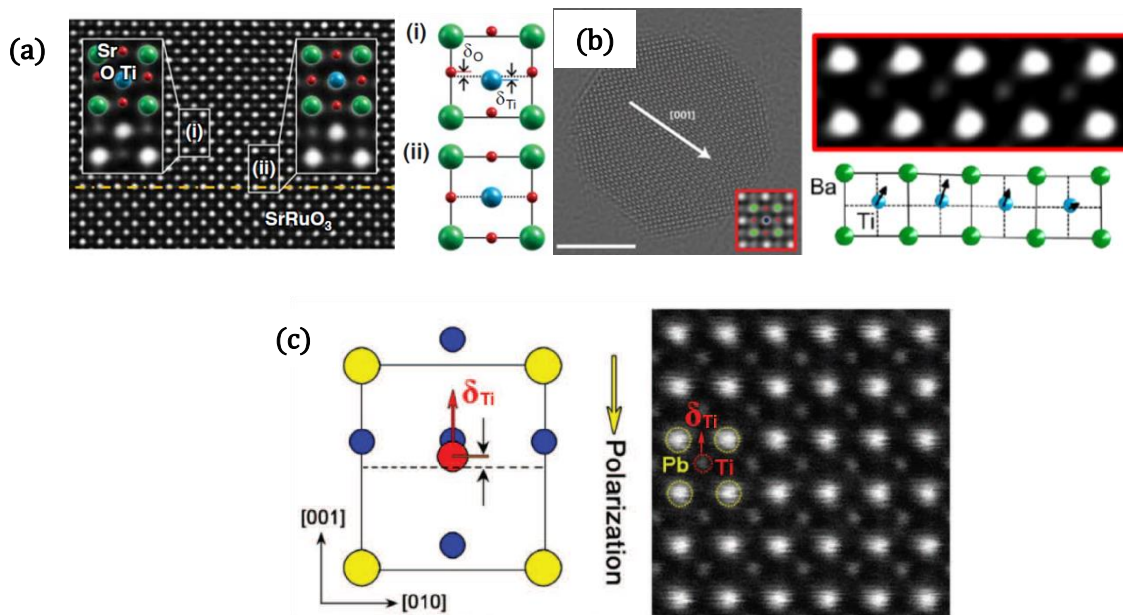
Figure 2. 10 HAADF-STEM images of classical ferroelectrics. (a) STEM image of STO where the polarization can be identified as parallel to titanium displacement to oxygen. Image from [107]. (b) STEM image of BTO, where the polarization can be seen as parallel to the titanium displacement with respect to barium. Image from [108]. (c) STEM image of PTO, where the polarization is viewed as anti-parallel to the titanium displacement with respect to lead. Image from [109].

As for PTO shown in Figure 2.10c, lead atom number is nearly four times bigger than titanium, which make the contrast even larger [109]. In PTO, the valence s electrons of lead tend to form some directional bonding with oxygen p-orbital. As

a result, the PbO$_{12}$ cage has Pb-O bonding distances of 2.54 Å, 2.80 Å and 3.2 Å. Titanium is also displaced within the TiO$_6$ octahedral cage with bonding distances of 1.78 Å, 1.97 Å, and 2.37 Å [110]. The polarization direction is the lead ion displacement direction relative to titanium.

Gradient phase analysis (GPA) is a quantitative method to map out the displacement and strain field of crystal lattice based on high resolution STEM image. As illustrated in [111-113], GPA takes the advantages of both real-space and reciprocal-space information. The intensity distribution in a STEM image can be described as a Fourier series:

$$I(r) = \sum_g \left| H_g(r) e^{2\pi i g * r} \right| \tag{2.25}$$

$I(r)$ is the intensity of the STEM image at position r. g is the undistorted lattice reciprocal lattice vector, or the periodicity corresponding to the Bragg reflection. Practically, the operation is Fourier transform the STEM intensity image back to reciprocal space to get diffraction pattern. The Fourier coefficient $H_g(r)$ is a complex value where the phase is preserved in GPA. It can be viewed as the local Fourier component, can be obtained by Fourier filtering by:

$$H_g(r) = A_g(r) e^{iP_g(r)} \tag{2.26}$$

Amplitude $A_g(r)$ is associated with the local contrast of lattice fringe; Phase $P_g(r)$ is the lateral position of the lattice fringes. The phase $P_g(r)$ can be further deduced to describe the displacement field $u(r)$ by:

$$P_g(r) = 2\pi g \cdot u(r) \tag{2.27}$$

By measuring two phase images $P_{g1}(r)$ and $P_{g2}(r)$ from two non-colinear reciprocal space vectors g_1 and g_2, the two-dimensional displacement field $u_{2D}(r)$ can be fully determined as:

$$\boldsymbol{u}_{2D}(\boldsymbol{r}) = -\frac{1}{2\pi}\left(P_{g1}(\boldsymbol{r})a_1 + P_{g2}(\boldsymbol{r})a_2\right) \tag{2.28}$$

a_1 and a_2 are the real space lattice vector, as corresponding to the reciprocal space vector g_1 and g_2. If we project displacement field onto x direction

$(\boldsymbol{u}_{2Dx}(\boldsymbol{r}))$ and y direction $(\boldsymbol{u}_{2Dy}(\boldsymbol{r}))$, then the 2D strain tensor can be further deduced as:

$$\varepsilon = \begin{bmatrix} \varepsilon_{xx} & \varepsilon_{xy} \\ \varepsilon_{yx} & \varepsilon_{yy} \end{bmatrix} = \begin{bmatrix} \dfrac{\partial \boldsymbol{u}_{2Dx}(\boldsymbol{r})}{\partial x} & \dfrac{\partial \boldsymbol{u}_{2Dx}(\boldsymbol{r})}{\partial y} \\ \dfrac{\partial \boldsymbol{u}_{2Dy}(\boldsymbol{r})}{\partial x} & \dfrac{\partial \boldsymbol{u}_{2Dy}(\boldsymbol{r})}{\partial y} \end{bmatrix} \tag{2.29}$$

Thus, the intensity distribution in a STEM image can be linked quantitatively to the displacement and strain field. Nowadays the GPA is a common plug-in in commercial TEM. Figure 2.11 shows the GPA study of an edge dislocation in silicon [112].
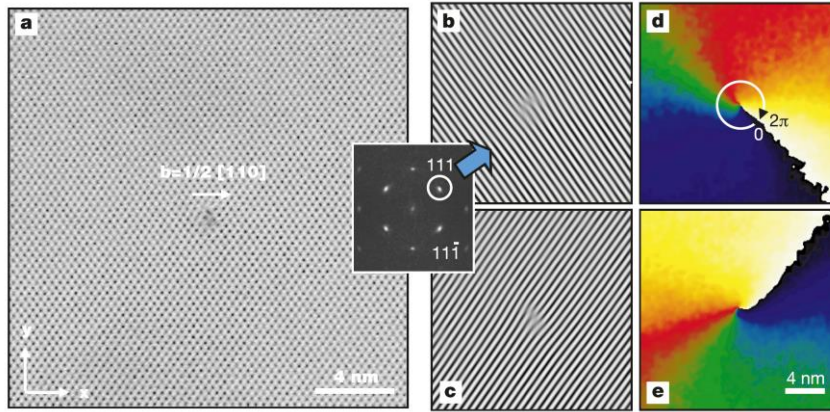
Figure 2. 11 Geometric phase analysis of an edge dislocation. (a) High resolution electron microscope image in $1\bar{1}0$ *orientation. (b)* 110 *lattice fringes by Fourier filtering. (c)* $11\bar{1}$ *lattice fringes by Fourier filtering. (d) Phase image of* 110 *lattice fringes. (e) Phase image of* $11\bar{1}$ *lattice fringes. Image from [112].*

Another widely used method for looking at perovskite thin films is the Piezo response Force Microscope (PFM). It is one of the variants of the big Scanning Probe Microscopy (SPM) family including Atomic Force Microscopy (AFM) and Scanning Tunnelling Microscopy (STM). There are clear differences among those techniques: AFM is a mechanical detection method, where the tip-surface force is measured through the mechanical motion of cantilever [114,115]. There are many works presenting nice surface roughness images mapped out by AFM; STM is a current detection method, which is sensitive to tip-bias voltage; PFM is an electromechanical detection method, where an electric bias is generated by applying a current to the tip, and surface deformation is then captured.

PFM is first proposed by Gruverman in 1996, before which there are already some works proposing the principle of PFM in AFM and STM systems [116]. The most basic mode of PFM is the static mode, where a direct current is applied to the sample surface. The field induced strain along the field direction can be expressed as:

$$Z = \pm d_{33}V \qquad\qquad (2.30)$$

where the domain will expand if the polar axis is along the field direction and contract if opposite.

Due to poor sensitivity to the static piezo response, the static mode has limited used in real cases. Instead, a dynamic mode is preferred, which uses an alternating current to increase the sensitivity by three orders of magnitude. This is now the 'basic' setup in commercial PFM. In such case, if the electric field is Vcos(t), then the first harmonic component of surface vibration (or surface piezo response) is measured in the form of amplitude Acos(t+). Figure 2.12 schematically shows the working modes of PFM including the vertical PFM (VPFM) and the lateral PFM (LPFM) [117].

For the VPFM, only the cantilever deflections are measured, which corresponds to the vertical (out-of-plane) force. Thus, the VPFM is sensitive to the polarization component that pointing out-of-plane. The amplitude of VPFM image can be expressed as $d_{33}V$, which is proportional to piezoelectric coefficient d_{33}. While the sign of phase in VPFM denotes the polarization direction of domains. The plus means the polarization is in the same direction with electric field, while the minus means opposite.

For the LPFM, only the torsion of the cantilever is measured, which relates to the in-plane polarization. The amplitude of VPFM image is linearly related to the shearing piezoelectric coefficient in the form of $d_{15}V$. The phase also means the direction. To map out the whole 3D polarization distribution, two perpendicular LPFM measurements are required, together with one VPFM measurement.
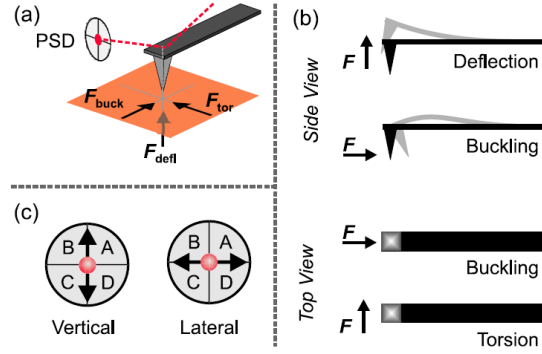
Figure 2. 12 Possible movements of the cantilever due to forces acting on the tip. Image from [117].

However, in most real cases, the ferroelectric thin films are polycrystalline, containing domains that have different orientations. Under such condition, the amplitude map is coupled to all the piezoelectric coefficients that are relevant. To solve for the polarization in such conditions, it's useful to set up two sets of coordinates: tensor in laboratory coordinates d_{ij} and crystallographic coordinates d'_{ij}. They are connected with a general Euler rotation matrix (θ, ϕ, φ). For example, in tetragonal structure where the piezoelectric tensor is simplified in equation X.X, the response coefficient can be expressed as follows:

$$d_{33} = [(d'_{31} + d'_{15})sin^2\theta cos\theta + d'_{33}cos^3\theta]V \qquad (2.31)$$

Again, PFM is only a qualitative method to image the domain configuration in thin film samples. Over decades, many advanced methods have been developed for better accuracy and signal-to-noise ratio (SNR). For example, in resonant mode, the cantilever working at a frequency close to its natural resonance can acquire a larger amplitude at a higher efficiency [118]. This resonance can be either predefined, or experimentally determined at every position before measurement using a feedback loop. This is the so-called Dual Amplitude Resonance Tracking method (DART) [117,119].

2.2.2 Classical domain structure in ferroelectric

The driving force of the domain formation is a pair of competing energies: the energy cost of the domain wall formation and the energy gain from domain formation [120]. The energy from domain formation E_1 can be expressed as:

$$E_1 = Uw \qquad (2.32)$$

U is energy volume density (constant); σ is the energy density of domain wall (constant). If thin film is considered, where there is a one-dimensional size limitation, the wall energy density of unit area E_2 can be expressed as:

$$E_2 = \frac{\sigma d}{w} \tag{2.33}$$

The total energy is the sum of two terms, which is given by:

$$E = E_1 + E_2 = Uw + \frac{\sigma d}{w} \tag{2.34}$$

This total energy reaches the equilibrium at

$$\frac{dE}{dw} = 0 \tag{2.35}$$

This gives the relation:

$$w^2 = \frac{\sigma d}{U} \tag{2.36}$$

Here, the w means the domain width or domain size; the d means the sample thickness in thin film sample. Kittel first proposed this square-root relation of domain size to thin film thickness in magnetic system, where the U stands for magnetostatic energy volume density [121,122]. Mitsui and Furuichi applied this equation in ferroelectrics, in which the U stands for electric energy density per unit volume [123]. Now this square-root relation is widely termed as Kittel's law. Notably, the above equation is a simplified version of the derivation of Kittel's law. If a specific system is treated, more accurate expression of U can be formed. For example, Kittel's law for 180° domain stripes can be expressed as [124]:

$$w^2 = \frac{\pi^3 \varepsilon_0 \left(1 + \sqrt{\varepsilon_x \varepsilon_z}\right)}{8.42 P^2} \sigma d \tag{2.37}$$

ε_0 is the dielectric constant of vacuum, ε_x and ε_z are the dielectric constants along a and c axes, respectively.

The Kittel's law is derived for thin films where two dimensions are infinite but found to be universal in other geometries. An extension of Kittel's law to single

crystal can be made with the assumption that the crystal is a cube with six parallel facets. This is shown as follow:

$$w^2 = \frac{\sqrt{2}\sigma}{2\left(\frac{U_x}{d_x} + \frac{U_y}{d_y} + \frac{U_z}{d_z}\right)} \qquad (2.38)$$

Here, the $U_i(i = x, y, z)$ means the contributions of volume energy density from the domain facets along i direction. The size of a domain along the i'th direction is denoted as $d_i(i = x, y, z)$. This square-root relation could work as a guideline for the domain size but does not mean to be quantitative or accurate. In a real sample, a deviation from this square-root relation is commonly seen, where the sample size and shape are reported to make a big difference [125,126].

Generally, the domain walls that are formed in ferroelectrics can be divided into two types: pure ferroelectric domain walls and ferroelastic domain walls. The pure ferroelectric domain walls separate 180° domains, where the polarizations between adjacent domains are anti-parallel to each other, as shown in Figure 2.13a. The ferroleastic domain walls are also ferroelectric but involve changes of elastic strain upon formation. The ferroelastic domain walls are structurally the same as twin boundaries, where the two adjacent domains have mirror symmetry near the domain wall. The types of ferroelastic domain walls are determined by lattice system, not the specific atoms. For the Perovskite tetragonal phase, only 90° ferroelastic domain is allowed; for the orthorhombic phase, 60°, 90° and 120° ferroelastic domains are allowed. As for rhombohedral phase, 71° and 109° domains can be formed. These angles are commonly used for naming the ferroelastic domain walls, however, the angle is approximate with an accuracy of ~1° because it is based on the exact lattice parameters of the material. In BTO for example, if the lattice constants are set to be a=3.99Å and c=4.03Å, then the exact ferroelastic angles are [127]

$$\alpha = arctran\left(\frac{c}{a}\right) = 90.57° \text{ or } \beta = 180° - \alpha = 89.43° \qquad (2.39)$$

Figure 2.13b shows a sketch of 90° ferroelastic domains in tetragonal lattice.
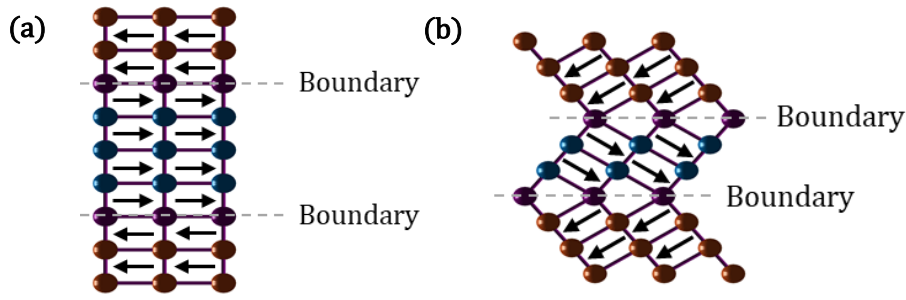
Figure 2. 13 Sketches of domain wall. (a) 180° domain walls (b) 90° domain walls.

In thin film samples, where the boundary conditions can be carefully tuned, the domain configuration in-plane and out-of-plane is of great interest and leads to the so-called domain engineering. This interesting topic will be discussed further below in our future plans section.

2.2.3 Flux-closure domains and vortices

Recently, there has been a trend to locate and quantify new topological structures in ferroelectrics, which are the equivalent of important magnetic analogue configurations, because these may have great potential for functional electronic devices [101]. Topological structures are caused by manipulation of local degrees of freedom (DOFs) such as lattice, charge, spin and orbit. In ferroelectrics, however, the spin and orbit DOFs do not make any noticeable contributions, so the DOFs of these systems are dominated by lattice and charge DOFs. These freedoms are linked with energy, where the lattice DOF is the competition of elastic energy, while the charge DOF consists of electrostatic energy and polarization gradient energy [128,129]. To form a flux-closure domain, theoretical works suggest the depolarization field plays a key role. Under large residual depolarization fields, which is equivalent to poorly screened charge conditions, classical polydomain are favoured, such as 90° and 180° domains in tetragonal BTO. If the depolarization field is too small, the material is effectively screened and the monodomain is favoured. Therefore, to form a rotational polarization domain, a proper depolarization field is required [130,131].

Although vortices have been well studied in magnetic materials, their equivalent polar vortices in ferroelectrics are poorly understood. Even the existence of

polar vortices or it's prerequisite flux-closure domain were debatable and used to be a big unknown question. The initial theoretical study that supported the existence of flux-closure domains was published only in 2004 [130]. This used first-principles Monte Carlo simulation to study the polarization field in PZT films under a residual depolarization field and a pretty large compressive strain (-2.65%), as shown in Figure 2.14. Under such strict conditions, the authors managed to see polar vortices in the side view. In 3D, these vortices build up uniform lateral vortex tubes. Ivan et al. also uses *ab initio* simulations to study PZT nano disk and nanorod confined structures, in which they found vortices at 64K [132].
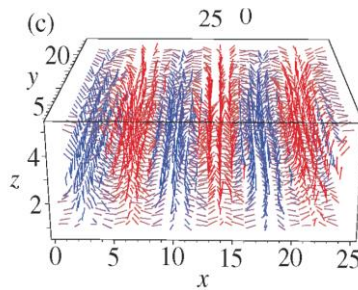
Figure 2. 14 Simulated polarization in PZT thin film under -2.65% compressive strain. Image from [130].

After these theoretical predictions, some indirect experimental results followed. For example, in 2009, BTO nanodots with self-defined stripes were reported using TEM, as shown in Figure 2.15 [133]. These BTO nanodots are created by focused ion beam (FIB) milling of a bulk single BTO crystal. The author tried to explain these stripe features as some hierarchical twin boundaries that oriented in a self-confined way.
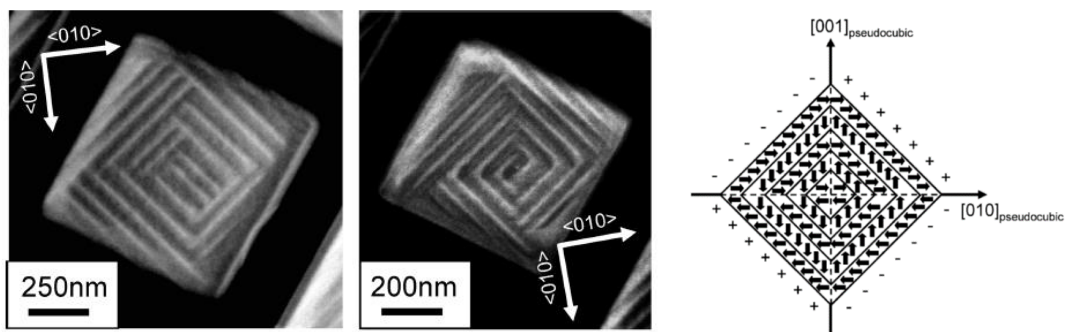
Figure 2. 15 HAADF-STEM image of BTO nanodots and a sketch for possible domain configuration. Image from [133]

Rodriguez *et al* reported characteristic features of PZT nanodots via PFM also in 2009, as shown in Figure 2.16 [134]. They also build a nanodot of 7.6 nm × 2.4 nm in size with -0.9% compressive strain and simulated their VPFM and LPFM image. Such resemblance between experimental results and simulation suggests a possibility of vortices.
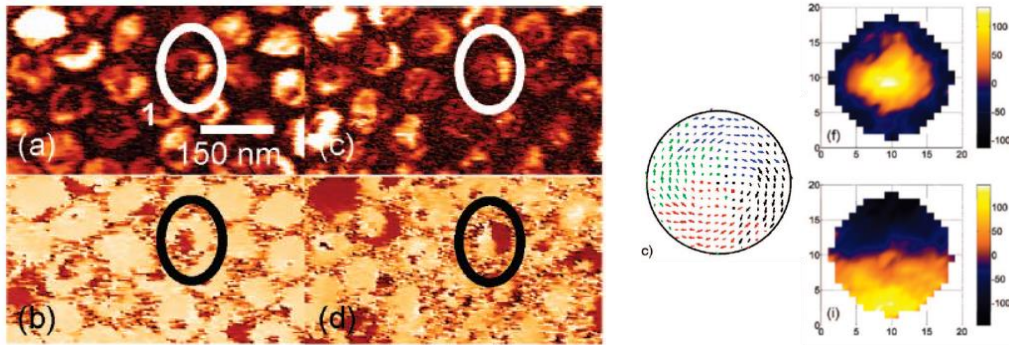
Figure 2. 16 The left graph is the PFM results of BTO nanodots. (a) VPFM amplitude image; (b) VPFM phase image; (c) LPFM amplitude image; (d) LPFM phase image. The right graph is the simulation results, including the polarization order, the VPFM amplitude and LPFM phase. Image from [134]

In 2010, McGilly *et al* reported possible vortices in BTO lamellae, where two arrays of twin domains form a zigzag structure at interface [135]. Such a zigzag structure is obvious in STEM image in Figure 2.17, but it failed to show up in the corresponding PFM image.
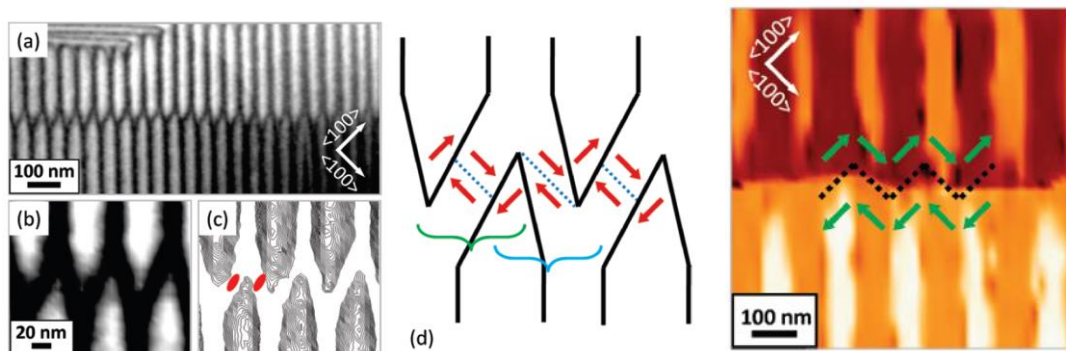
Figure 2. 17 The left graph shows the STEM image of the zigzag structure. The middle graph shows a sketch of the polarization order at interface. The right graph shows the PFM image. Image from [135]

Later in 2010, the same group reported seeing flux closure domain with sizes up to micrometres [136]. Figure 2.18a shows the LPFM result on BTO lamella. This single crystal had been fully switched to a-c domains by application of sufficient

electrical field. After the electric field was removed, they found the domain structures in BTO relaxed gradually. Figure 2.18b shows LPFM of a partially relaxed structure, where 180° in-plane domains are forming. After relaxing the sample for a few hours, the structure gradually evolved into that shown in Figure 2.18c. In two orthogonal LPFM images, four-fold flux closure domains can be seen.
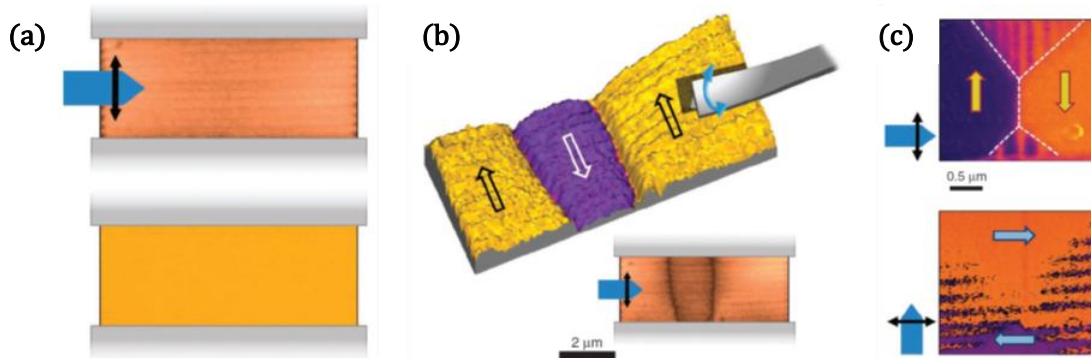
Figure 2. 18 (a) LPFM result of BTO lamella. (b) LPFM of a partially relaxed BTO lamella. (c) LPFM image of BTO lamella after several hours of relaxation. Image from [136]

A further breakthrough came in 2011. Taking advantage of HAADF-STEM, directional views of flux-closure domains were obtained with sub-angstrom resolution. Figure 2.19 shows the TEM image of a typical flux closure domain in a BiFeO$_3$ (BFO) thin film grown on TbSsO$_3$ (TSO) substrate. BFO has an orthorhombic structure at room temperature, so the elastic domains are 109° relative to each other. Figure 2.19a shows one 109° domain. Figure 2.19b show a complete flux-closure domain, consisting of two 109° elastic domain walls and two 180° electrical domain walls [137]. Although such structures show little curvature of polarization except at the boundary, which is still far different from vortices, it is still a breakthrough to see that a flux closure domain can be formed by carefully selecting the materials and construction them into complex multidomain arrangements. A similar work is also published that year, shown in Figure 2.19c [138], is a three-fold vortex measured in a PZT thin film. Although in the title the authors called it a continuous electric dipole rotation, actually the only place seen to be rotating is the small block on the bottom.
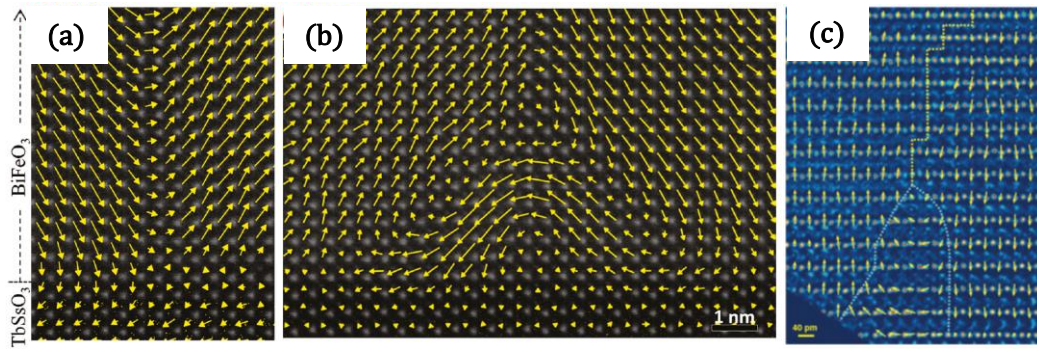
Figure 2. 19 HAADF-STEM image showing flux-closure domains. Images from [137,138]

In 2015, flux-closure domains in PTO were discovered in a complex STO(10 nm)/PTO(36 nm)/STO(3 nm)/PTO(28 nm)/GSO system [139]. The GPA of the thin film shows a regular distribution of out-of-plane strain tensor. Selected areas were chosen for mapping the atomic arrangements, shown in Figure 2.20. Although the authors call these "flux closure quadrants", the flux is not closed in the sense that they only rotate 270° in the images. But again, finding these rotational domains in the PTO/STO system is already a breakthrough, which serves like a platform or playground in ferroelectric study. By learning the possible local topological structures, it can be envisaged that general design rules could be elaborated to create larger configurations for specific purposes in the future.
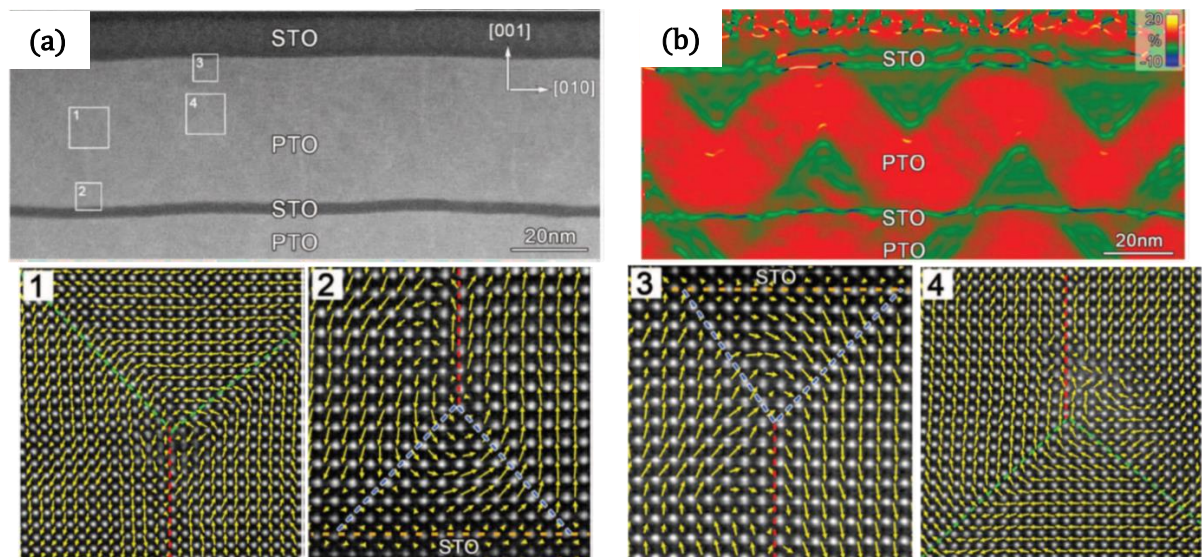
Figure 2. 20 Flux closure domains in PTO/STO thin film. (a) HAADF-STEM image. Zoom-in micrographs of box area with number 1-4 are showing at the bottom. (b) GPA analysis. Image from [139].

In 2016, a full vortex array was found in a PTO/STO superlattice, as shown in Figure 2.21 [140]. The two adjacent vortices are clockwise and anti-clockwise, so that they can share the boundary with each other. These vortex arrays appear to be elongated in the third dimension, suggesting the 3D structure to be vortex tubes. A Phase field simulation was also presented to support the experimental result.
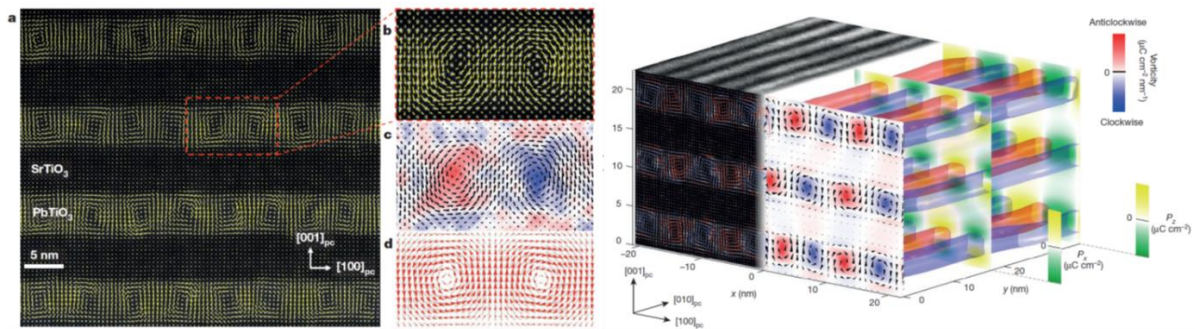
Figure 2. 21 HAADF-STEM image on the top and side of PTO/STO superlattice film. Phase field simulation is also presented. Image from [140].

2.2.4 Skyrmion and meron bubble

A magnetic skyrmion describes a magnetic configuration of a chiral-lattice magnet with its spin directions forming a vortex-like topology. This has drawn interest for potential applications such as racetrack memory. The corresponding structure in ferroelectrics is, however, less obvious and hard to characterize. Recently, polar skymion-like bubbles were experimentally confirmed in a PTO/STO thin film system, utilizing the lattice mismatch strain in the heterostructure [141-142]. Figure 2.22 shows the main result. By some pre-knowledges from dark-field TEM, the polar skyrmion bubbles were first simulated in a thin film in Figure 2.22a (black box). At the centre, the polar direction is upward. There are two clear boundaries on two sides, where the vortices are formed. The polar direction rotates a total circle of 360° when going through this skyrmion bubble. Such a structure agrees with the experimental observation shown in Figure 2.22c (blue box), which is the polar order derived from the atomic positions in HAADF-STEM image. The three section views of the simulated skymions show that at the top and bottom position of such skyrmion, the polarization is hedgehog-like with a Neel type domain wall. In the middle position, the polarization is vortex-like with a Bloch type domain wall. The

calculated ADF image and polar order match the TEM image as well. This class of topological structure is usually quantified by a "skyrmion number", N. Different definitions have been put forward based on situations, for example:

$$N = \frac{1}{4\pi} \iint u \cdot \left(\frac{\partial u}{\partial x} \times \frac{\partial u}{\partial y}\right) dx dy \qquad (2.40)$$

u is normalized local dipole moment. For the model building in this paper, the skymion number N is +1 for all slices.
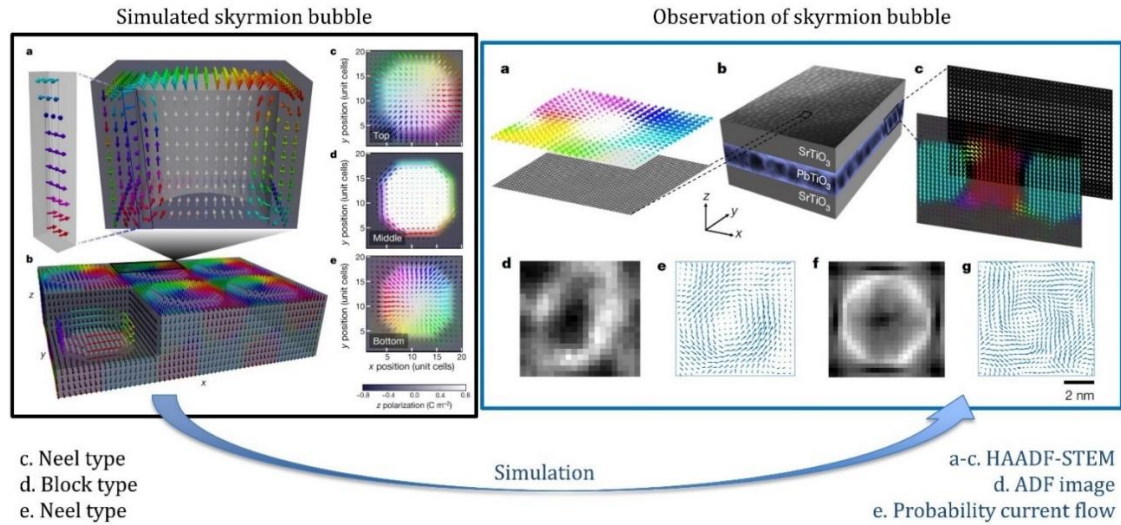
Figure 2. 22 Simulated skyrmion bubbles and the experimental proof of possible skyrmion bubbles in PTO/STO system. Image revised from [141].

Notably, because STEM only measures the projection of atomic position, it doesn't visualize the polar skyrmions directly. Instead, by combination of TEM image and simulation model, it infers a polar skyrmion bubble structure.

A "Meron" is considered to be half a skyrmion. The polar direction rotates 180° when crossing a meron bubble, which is half the magnitude of skyrmion. Wang et al reported the first observation of regularly distributed merons in 5nm thick PTO/STO thin film [143]. Figure 2.23 shows two meron bubbles with both phase field simulations and HAADF-STEM images. The sizes of merons are roughly 5nm, and they appear only at the stripe walls. These merons are regularly distributed and the spacing between two domains along a stripe line is 8nm on average. Such meron arrays have also been found in other system including PTO/GSO and PTO/SSO. The density of merons is dependent on in-plane strain:

the meron and anti-meron density first increases with strain and decreases after reaching the peak value at about 2.25%.
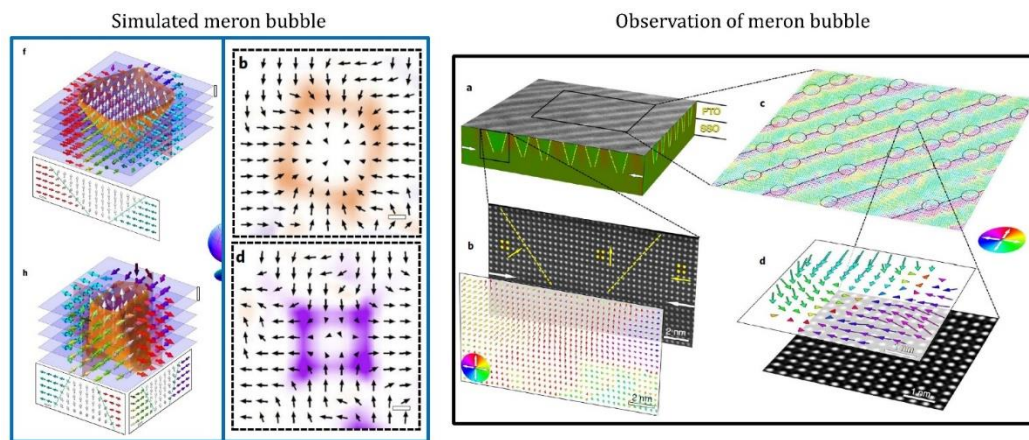
Figure 2. 23 Simulated meron structures and experimental observation by HAADF-STEM. Image from [143].

In this section, different works are listed to show the development and understanding of vortices step by step. Despite the observation of these hierarchical structures, the easily overlooking point is whether the structure inferred from the image is correct or not. Most of these results are based on HAADF-STEM, which only shows the projection views that is both 2D-projected and averaged out. All the usual caveats about TEM sample preparation and use of very thin specimens apply to the results. The PFM result has a significant resolution limit and is only a rather qualitative method. Therefore, it's better to view the above results as a taste of possibilities instead of the finished textbook.

2.3 Core-shell model

Core-shell models are widely used in nanoparticle research. Often composed of inner and outer shells of two different materials, the most general model is when the central core and outer shell differs in some order parameters. In BTO, there are at least two kinds of core-shell models that attract scientific interest. The first and the most studied core-shell includes a pure tetragonal BTO core and a chemically doped BTO shell. This is commonly used as a multilayer ceramic capacitor in industry [144,145]. The growing industrial interest for miniaturization of electronic devices has accelerated the study in this particular direction.

The second core-shell structure was proposed by Wada and Hoshino [146-148]. This core-shell model does not contain any dopant but pure BTO crystal. It consists of an inner tetragonal core, some band of transition material and an outer cubic shell, as shown in Figure 2.24a. For a typical 200nm diameter BTO crystal, the inner tetragonal core would span more than 50nm in radius and the outer cubic shell occupies the last 10nm in radius, according to the model. The experimental proof of this model comes from X-ray powder diffraction, shown in Figure 2.24b. For their fine crystal sample, specially synthesized, the adjacent 200 and 002 peaks are not sharp. There is a large amount of intensity between the two peaks that cannot be fitted by pure tetragonal structure using Rietveld refinement. These scattering data, however, agree well with the core-shell model proposed. We are particularly interested in this core-shell model and have performed a series of BCDI study on the commercial BTO nanocrystals. However, the XRD profile of our samples only shows two sharp peaks with a width corresponding to the particle size, which does not favour a core-shell model. We attribute this difference to the sample, where the samples from Wada's group are claimed to be fine crystal with almost no defect [148]. We are tackling this problem on two fronts: while we are making experimental advances by learning how to synthesize BTO nanoparticles, we did simulations to predict the characteristics of core-shell model in a BCDI experiment. Figure 2.24c shows the simulated BTO crystal and the corresponding Bragg diffraction pattern. The simulated crystal has displacement field accumulated on two sides, because the Q-vector is set to be 110. The coherent Bragg diffraction pattern shows three peaks in the vicinity of each other. These outer two peaks represent the inner core and the outer shell, while the middle peak comes from the assumed transition region.
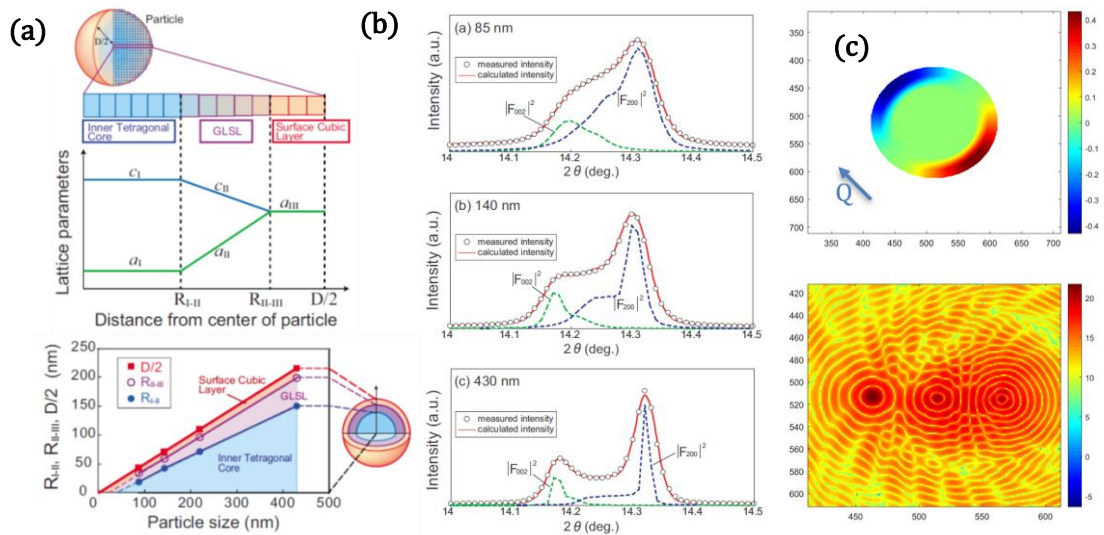
Figure 2. 24 (a) The sketches of core-shell model. Image from [147]. (b) XRD profile of BTO fine crystal from Wada's group. Image from [148]. (c) Simulated image from a core-shell model and its diffraction pattern.

2.4 Polar nanoregions

2.4.1 Relaxor ferroelectrics

The relaxor ferroelectrics, simply called relaxors, are ferroelectric materials that show dielectric relaxation in the time domain. They show several distinct differences from normal ferroelectrics [149]:

(a) No well-defined Curie temperature

(b) Strong frequency dispersion of dielectric permittivity

(c) Frequency dependent temperature of maximum dielectric loss and dielectric permittivity

For (a), the specific phase transition temperature is one of the defining characteristics in comparing crystals and glasses. In one interpretation for relaxors, the poorly defined Curie temperature means that different regions would transform from paraelectric phase to ferroelectric at different temperatures, rather than developing full long-range order. (b) and (c) describes the same frequency dependence, but from different points of view. Figure 2.25 shows a typical dielectric permittivity curve of ferroelectrics and relaxors [150]. Ferroelectrics show a distinct anomaly as shown in Figure 2.25a. The relaxors can be divided into two categories according to their response to temperature, as shown in Figure 2.25b and c. This will be discussed in the next section. In both

types, with the increasing frequency of applied field, the maximum dielectric permittivity decreases, while the temperature for the maximum dielectric permittivity increases.
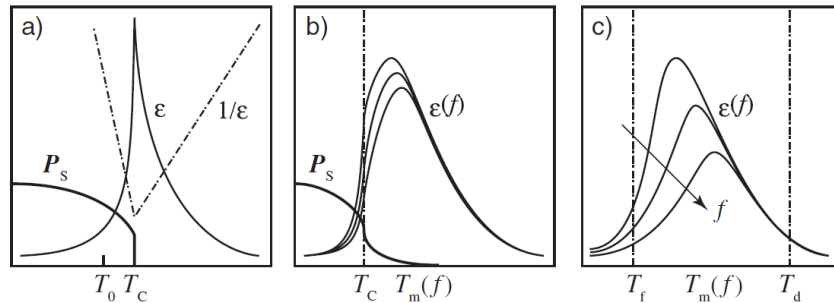
Figure 2. 25 Dielectric permittivity as a function of temperature. (a) First order ferroelectric (b) Ferroelectric with a diffuse transition. (c) Canonical relaxor. Image from [150].

All the known relaxor materials include some kinds of composition disorder. The most studied PMN and PMN-PT relaxors involve chemically disordered B-site cations [151,152]. The solid solution type BSTO, for example, has a ferroelectric BTO phase and paraelectric STO phase. The proper mixing of BTO and STO would lead to inhomogeneous ferroelectric regions embedded in paraelectric regions [153]. Aliovalent cation doping in both ferroelectrics and paraelectric could lead to relaxors, like the La-doped PTO and Bi-doped STO [154,155].

However, some disordered systems like PZT show no dielectric relaxation. BTO also shows disorder local structure and polar nanoregions or precursors in cubic phase, but it also has no dielectric relaxation. This is covered in Chapter 2.5.

2.4.2 Polar nanoregions in relaxors

Polar nanoregions (PNRs) are defined as finite-sized regions, either dynamic or static, with a nonzero spontaneous electrical polarization [156]. While the definition of PNRs is straightforward, the details depend on specific systems. It's better to understand the development of polar nanoregions through the transitions of relaxors. The relaxors experience a series of transformation upon cooling:

(a) Paraelectric state $(T > T_B)$

When above the Burns temperature, T_B, relaxor materials are paraelectric. There is no evidence of any noticable static polar nanoregions in this state.

(b) Type-I relaxor state ($T_B > T > T^*$)

Somewhere between the Burns temperature T_B and an intermediate temperature T^*, the polar nanoregions start to nucleate. These polar nanoregions are both dynamic and have random polarized direction. This dynamic means the polar nanoregions could flip their direction due to thermal excitation.

The Burns temperature is first seen as the deviation from a linear relation between optical refractive index and temperature and can be measured by Raman spectroscopy [157,158].

(c) Type-II relaxor state ($T^* > T > T_f$)

Between the intermediate temperature T^* and the freezing temperature T_f, the PNRs start to form larger clusters. The flipping dynamic of PNRs becomes slowed down, so that the static component of polarization starts to appear. The PNRs are considered both partially dynamic and static in this state.

The combination of Type-I and Type-II relaxor state is called ergodic state, because they share some similar characteristics. The most important feature is that the PNRs have random distributions of polarization direction, so there is no preferred polarization macroscopically.

(d) Type-III relaxor state ($T_f > T$)

When the temperature decreases below the freezing temperature T_f, the relaxor goes into non-ergodic state. In this state, the local polarization becomes frozen. The local symmetry deviates from high symmetry phase, while macroscopically the crystal still has high symmetry. PNRs are considered to be fully static in this state.

(e) Ferroelectric state ($T_c > T$)

It should be noted that not all relaxors have this ferroelectric phase transition, in which case there is no T_c at all. Canonical relaxors have this phase transition. One

important example is the well-studied PbMg$_{1/3}$Nb$_{2/3}$O$_3$ (PMN). But there do exist some relaxors which could transform to have long range ferroelectric ordering at the transition temperature T_c. For example, the PMN-xPT (0.05<x<0.35) would have such a ferroelectric phase transition [159]. However, the PNRs are still detectable in this ferroelectric state, therefore their coexistence with polar order is favoured. These two kinds of polar ordering, namely the PNRs and ferroelectric domains, exist at different length scale and contribute to the same long-range ferroelectric order [160].

The PNRs are probed and studied by a number of spectroscopic techniques such as diffuse X-ray and neutron scattering, EXAFS, acoustic emission and dielectric spectroscopy [161-165].

The direct observations are given by TEM and PFM. Figure 2.26a shows some dark field TEM results of PMN [166]. The image of PNRs and chemical ordering regions (CORs) are obtained by inverse Fourier transform of the TEM images. The size of PNRs is 15 nm~25 nm, and the size of CORs is 5 nm. Figure 2.26b shows another example of PMN seen by high resolution TEM at the top-left panel [167]. The top-right panel presents the FFT of the TEM image, and the bottom-left panel shows the schematically the distribution of PNRs.
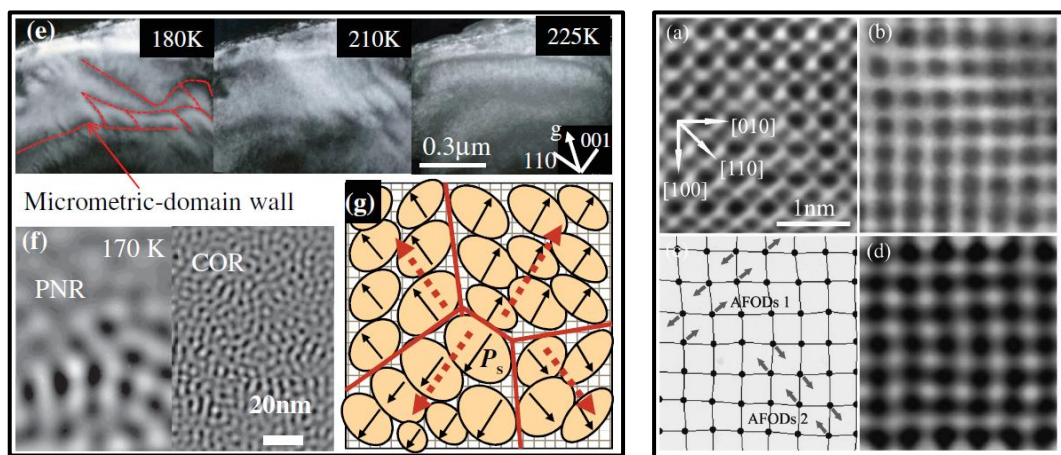
Figure 2. 26 Left panel are the 111 reflection dark field TEM image of PMN and related PNR image and COR image. A sketch of the PNRs is also plotted. Image from [138]. Right panel shows the 001 reflection TEM image of PMN, it's FFT image, a schematic diagram of Pb displacement and computer simulated image from FFT image. Image from [167].

PFM, as illustrated in Chapter 2.21, is effective in measuring the static or dynamic polarization via local piezo response. An autocorrelation image could be further generated from the autocorrelation of PFM image:

$$C(r_1, r_2) = \sum_{x,y} D(x,y)D(x + r_1, y + r_2) \qquad (2.41)$$

D(x,y) is the piezo response value at position (x,y). The shape of autocorrelation function provides the symmetry and regularity of the polarization [168].

To measure the short-range order, one way is to average over the autocorrelation functions in all in-plane directions should be taken and expressed as [169]:

$$\langle C(r) \rangle_{short} = \sigma^2 e^{-(\frac{r}{\langle \xi \rangle})^{2h}} \qquad (2.42)$$

r is the distance from central peak. $\langle \xi \rangle$ is the average correlation radius. The exponent h is a measure of the roughness of the polarization surface.

If the long-range order is considered, its contribution can be expressed as:

$$\langle C(r) \rangle_{long} = (1 - \sigma^2)e^{\left(-\frac{r}{r_c}\right)}\cos\left(\frac{\pi r}{a}\right) \qquad (2.43)$$

a is the period of structure and r_c is the long-range correlation length.

Then the full autocorrelation function considering both short-range and long-range order can be summed up:

$$\langle C(r) \rangle = \langle C(r) \rangle_{short} + \langle C(r) \rangle_{long} = \sigma^2 e^{-(\frac{r}{\langle \xi \rangle})^{2h}} + (1 - \sigma^2)e^{\left(-\frac{r}{r_c}\right)}\cos\left(\frac{\pi r}{a}\right) \qquad (2.44)$$

Figure 2.27 shows the PFM results and corresponding autocorrelation images of PMN, PMN-PT10 and PMN-PT20 [168,170]. PMN has small regions in the PFM image, and they are static for 5-20min. Using the short-range autocorrelation function $\langle C(r) \rangle_{short}$, the average correlation length is estimated to be around 46nm. PMN-PT10 shows nanoregions in size of tens of nanometers in PFM image, which is larger than pure PMN. The full autocorrelation function is mapped out in Figure 2.27d, which shows oscillation along crystallographic 110 direction. This indicates the short-range order is along the 110 direction. The short-range correlation length is fitted to be 70nm and the long-range

correlation length is 800nm in PMN-PT10. PMN-PT20 shows strong ferroelectric ordering in PFM image, while the long-range correlation length is about 2~2.5 μm.
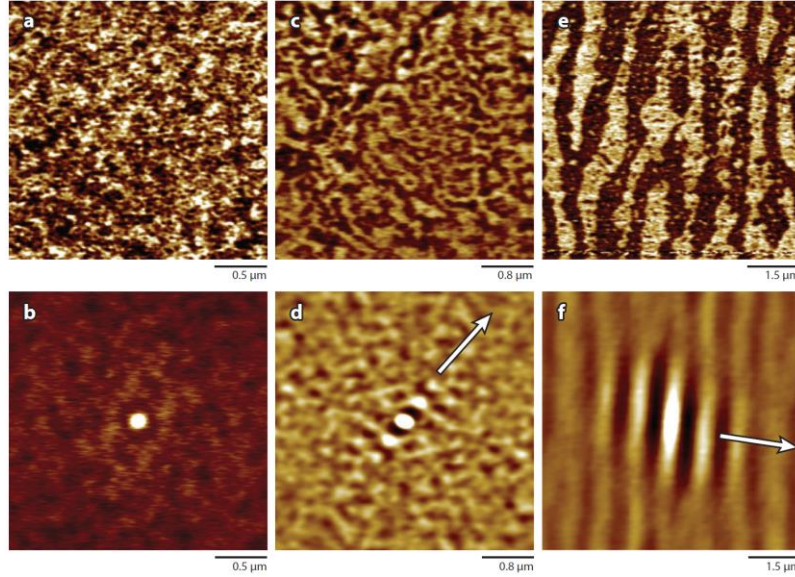
Figure 2. 27 (a), (c) and (e) are PFM images of PMN, PMN-PT10, PMN-PT20. (b), (d) and (f) are corresponding autocorrelation images. Image from [168].

However, it should be noted that even in the same system, the size of PNRs could be quite distinct from different measuring techniques. Even the validity of the methods is not solid and raises concerns in their own fields. For example, it's strange to get both PNRs and CORs from purely a dark field TEM image. As the TEM expert Yimei Zhu once put it, many TEM based works could published in good journals like Nature or Science, but they cannot publish in electron microscopic journals for technical reasons. Therefore, the over interpretation of data might also appear in this Chapter, and it is fully based on the readers to judge whether this is true or only a possibility.

PNRs work well in describing the relaxor properties. For example, the dielectric relaxation can be explained by PNRs via the Vogel-Fulcher law:

$$f = f_0 e^{\frac{E_a}{k(T_m - T_f)}} \tag{2.45}$$

T_m is maximum dielectric permittivity temperature. E_a is an activation energy. f_0 is saturation frequency.

To understand the formation and mechanism of PNRs in relaxors, different models have been proposed. Some widely used models include a compositional fluctuation model, a super paraelectric model and a dipole glass model.

The compositional fluctuation model proposes the disordered hetero-valent cation at equivalent crystallographic position to be the compositionally disordered. The local compositional disorder would lead to regions with distinct local Curie temperature and different transition temperature. Such regions are called the polar nanoregions in this model.

The super paraelectric model is an extension of the compositional model and resembles its magnetic counterpart super-paramagnetism. The polar regions are thought be embedded in a paraelectric matrix and not interacting with each other. These polar nanoregions are dynamic and can flip due to thermal excitation, which resembles a spin glass.

2.5 Local structure

From low temperature to high temperature, BTO goes from low symmetry to high symmetry, following rhombohedral, orthorhombic, tetragonal and cubic lattice structures, in sequence. As described in Chapter 2.4, the soft mode theory supports a displacive type model. However, various local structure studies have revealed the existence of rhombohedral local distortions in all crystal phases of BTO, which indicates the order-disorder component.

Figure 2.28 shows the Pair Distribution Function (PDF) results for BTO while crossing the rhombohedral to orthorhombic and orthorhombic to tetragonal phase transitions [171]. The atomic displacement shows no noticeable difference in all these crystal phases. Because the PDF is only sensitive to local structure, different global structures could be formed by selectively choosing some of the eight site rhombohedral distortion directions. For example, the tetragonal could be formed by choosing four of the eight site directions, and the cubic phase is averaged out by all eight site directions.

PDF based refinement using reverse Monte Carlo (RMC) also supports the Ti displacement to be zone-centred rhombohedral like. Figure 2.28c shows the atomic structure after refinement and their calculated diffuse scattering in the

planes [172]. The RMC calculation uses large supercells instead of the small boxes used in Rietveld refinement [173]. It refines the atomic displacement to fit both G(r) and S(r). However, the work has been criticised because too many degrees of freedoms exist in the RMC method, so it gives an impression of the structure, rather than a unique answer. Bias is often introduced in the selection of RMC model parameters, and this could lead to different detailed results from the random numbers used to perform RMC.
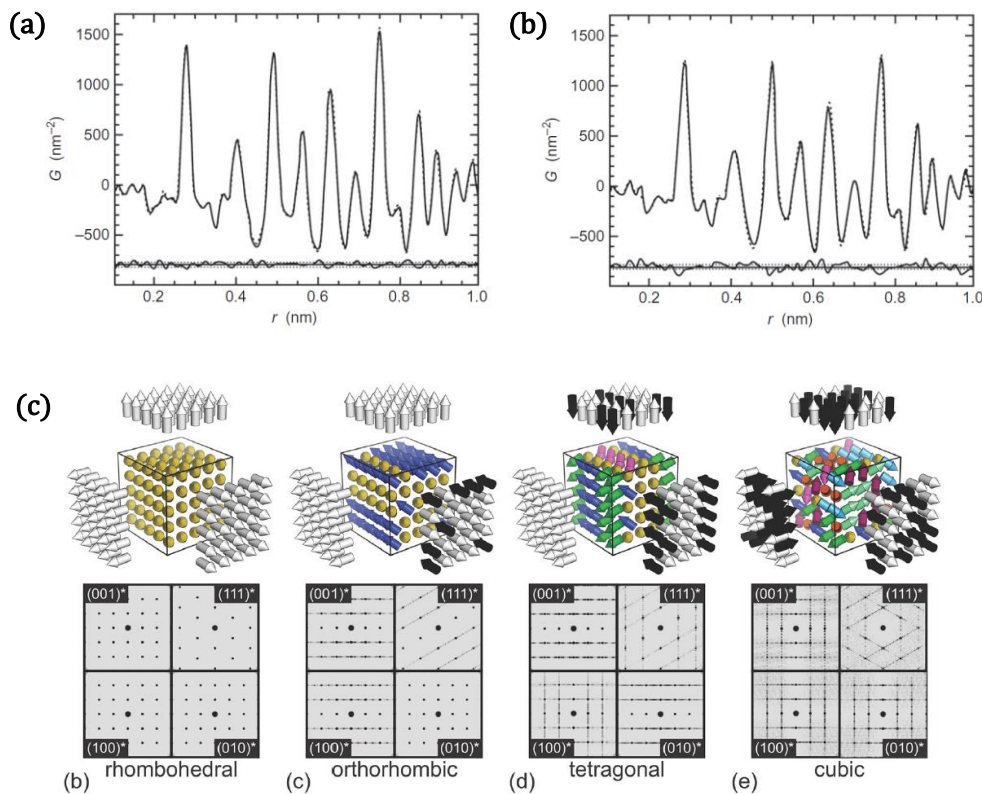
Figure 2.28 (a) PDF result of BTO passing through rhombohedral to orthorhombic phase transition. (b) PDF result of BTO going through orthorhombic to tetragonal phase transition. In both cases two PDF profiles are superimposed and their difference is shown below. The solid line is above phase transition, and the dash line is below. Image from [171]. (c) A portion of simulation results of each phase are shown, with corresponding calculated diffuse scattering in the planes indicated. Image from [172].

X-ray absorption fine structure (XAFS) also confirms a different local structure relative to the global structure. The combination the K-edge Extended XAFS (EXAFS) of Ba K-edge and X-ray absorption near edge structure (XANES) of Ti K-edge quantitatively support the eight-sight model. The local Ti displacement direction is calculated to be 11.7° away from the 111 directions towards the c

axis in tetragonal phase. Such displacement of Ti from oxygen octahedral centre is 0.19 Å at 35 K and 0.16 Å at 750 K [174].

Figure 2.29 shows first-principles calculated energy as a function of Ti distortion relative to Ba [175]. When the soft mode distortion is small (± 0.1 in image), the rhombohedral phase has the lowest energy of all phases, and the tetragonal phase is unstable.
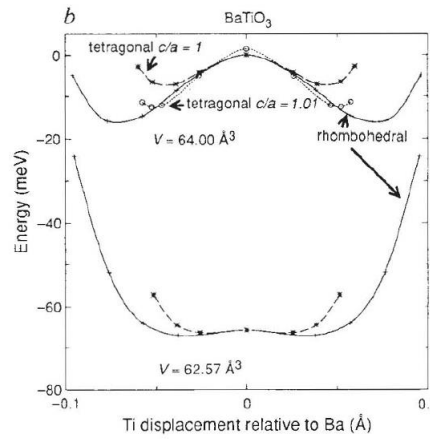
Figure 2. 29 Calculated energy as a function of soft-mode distortion in BTO. Image from [175].

Chapter 3. Evolution of Grain Boundaries during Phase Transitions in Barium Titanate Nanoparticles

Chapter published on Physical Review Materials, 4, 106001 (2020).

Jiecheng Diao[1,*], Xiaowen Shi[31], Tadesse A. Assefa[2], Longlong Wu[2], Ana F. Suzana[2], Daniel S. Nunes[1], Darren Batey[3], Silvia Cipiccia[3], Christoph Rau[3], Ross J. Harder[4], Wonsuk Cha[4] and Ian K. Robinson[1,2,*]

[1]*London Centre for Nanotechnology, University College London, London WC1E 6BT, UK*
[2]*Condensed Matter Physics and Materials Science Department, Brookhaven National Lab, Upton, NY 11793, USA*
[3]*Diamond Light Source, Oxfordshire, OX11 0QX, UK;*
[4]*Advanced Photon Source, Argonne National Lab, Lemont, IL 60439, USA*
Corresponding author: ucapiao@ucl.ac.uk; i.robinson@ucl.ac.uk

Contribution statement: Ian conceived the idea. Jiecheng and Ian designed the experiment. All authors contribute to the experiment. Jiecheng wrote the manuscript with the help of all authors.

3.1 Abstract

In this work, ferroelastic domain walls inside BaTiO$_3$ (BTO) tetragonal nanocrystals are distinguished by Bragg peak position and studied with Bragg coherent X-ray diffraction imaging (BCDI). Convergence-related features of the BCDI method for strongly phased objects are reported. A ferroelastic domain wall inside a BTO crystal has been tracked and imaged across the tetragonal-cubic phase transition and proves to be reversible. The linear relationship of relative displacement between two twin domains with temperature is measured and shows a different slope for heating and cooling, while the tetragonality reproduces well over temperature changes in both directions. An edge

---

- [1] Current affiliation: Department of Physics, New Mexico State University, Las Cruces, New Mexico 88003, USA
- & Department of Materials Science and Engineering, Rensselaer Polytechnic Institute, 110 8th Street, Troy, NY, 12180, USA

dislocation is also observed and found to annihilate when heating the crystal close to the phase transition temperature.

3.2 Introduction

Perovskite transition-metal oxides have been studied for decades because of both their broad applications and fundamental scientific questions. The displacement of Ti and Ba ions relative to the oxygen in unit cell leads to local polarization, which gives rise to exotic electrical properties such as elevated dielectric susceptibility, ferroelectricity and piezoelectricity [53, 128, 176, 177]. By analogy with well-studied magnetic systems, it is believed that it is not the local polarization in unit cell level that directly links with these macroscopic electrical properties, but rather via the formation and rearrangement of polarized nanodomains. Therefore, the study of domain structures, preferably in three dimensions (3D), is important for understanding and improving these properties. $BaTiO_3$ (BTO), for example, is frequently chosen as a lead-free functional material for both actuator and sensor applications [24, 178]. It goes through a series of crystal lattice systems: cubic, tetragonal, orthorhombic and rhombohedral upon cooling [47]. The corresponding transitions are first order with critical temperatures of 393 K, 278 K and 183 K, respectively, which can be adjusted by varying strain and sample size. The cubic-tetragonal phase transition temperature, for example, can be increased from 393 K to 813 K with 1.7% compressive strain [50] and can decrease to room temperature when the particle size is reduced to 3nm [179]. Recently, it was reported that the local structure remains locally rhombohedral throughout all phases [56, 60].

The phase transition is also complex, demonstrating both order-disorder and displacive character [59,180]. From the high symmetry cubic phase to the lower symmetry tetragonal phase, the paraelectric ensemble breaks into ferroelectric domains of uniform electric polarization, driven by the minimization of the sum of electrostatic and elastic energy [53, 128, 176, 177]. To accommodate local energy landscape and strain, different types of domains could be formed by rotation or translation of crystal regions or domains into different locations with well-defined domain-wall interfaces. For example, there are 71°, 109° and 180° domain walls in rhombohedral BTO [181]. In tetragonal BTO, the flipping of one

79

region of a crystal along a face-diagonal leads to a ferroelectric and ferroelastic 90° domain wall (twin boundary). While flipping along the long side of the tetragonal unit cell creates a ferroelectric-only 180° domain wall instead, in which the a-domain and c-domain are formed head-to-tail with each other [124, 135, 182]. The domain wall is said to be continuous which means it can only end in other domain walls or grain boundaries [183]. There are discontinuities of polarization in the perpendicular direction of domain walls, where the local displacements would be expected to accumulate. The formation of these domains depends strongly on boundary conditions, such as sample shape, while the size of domains in thin films has a square-root dependence on thickness, known as the Kittel scaling law [120].

Bragg coherent X-ray diffraction imaging (BCDI) is a synchrotron-based lens-less imaging method, which is well adapted to studying nanocrystals in three dimensions (3D). It is capable of imaging the shape and mapping out inner strain without damaging the nanocrystal [11, 184, 185]. In the BCDI experiment, the 3D diffraction pattern is collected in reciprocal space and inverted to real space with advanced phase retrieval algorithms [11]. Usually, a single hkl Bragg peak is selected in the reciprocal lattice with a total momentum transfer vector $\mathbf{Q}$ = h$\mathbf{a}$* + k$\mathbf{b}$* + l$\mathbf{c}$*. In a completely general way, this gives a 3D complex image of the crystal, capturing both its electron density function as the complex amplitude signal and a projection of the distortions as the corresponding phase signal. A simple linear relationship exists between the crystal displacement field $\mathbf{u}(\mathbf{r})$ and the observed image phase, $\phi(\mathbf{r}) = \mathbf{Q} \cdot \mathbf{u}(\mathbf{r})$ [11]. The amplitude, representing the average electron density, contains information about crystallinity and its isosurface can be used to visualize the shape of crystal. Any local displacement of the unit cells of the crystal parallel to $\mathbf{Q}$ will change the relative phase of the scattering from those unit cells relative to the rest of the crystal; when this occurs in regions large enough to be resolved the distortion can be visualized as a region or domain with a measurable phase appearing in the image. When the phase shift exceeds 2π, a proper phase unwrapping operation is needed to preserve the continuity of the displacement field.

The BCDI technique is sensitive to defects and has the unique ability to identify the dislocations and grain boundaries inside crystals by their characteristic strain (displacement) patterns [14, 15, 186, 187]. The interpretation of the phase as a projection of the displacement field is analogous to the Generalized Phase Approximation (GPA) used to interpret Transmission Electron Microscopy (TEM) images [188]. There have already been several studies of BTO by BCDI motivated by the ability to see its important domain structures. An important example is the discovery of an interesting electric-field driven vortex structure [189-191]. Here we take advantage of the unique properties of BCDI to investigate the domain structure and dislocations inside BTO nanocrystals upon crossing the cubic-tetragonal phase transition. In this work, we extend the BCDI method by considering the case of two nearby overlapping Bragg peaks, originating from different regions or domains of the same nanocrystal, to explore the structure and properties of the domain walls formed between them.

3.3 Experimental Methods

Commercial BTO powders with a nominal size of 200nm were diluted in a solution of Tetraethyl Orthosilicate (TEOS) and ethanol at a ratio of 1:75 in volume. This solution was then drop casted onto the silicon wafer and annealed in the furnace at around 973 K for 1h. This forms an amorphous SiO_2 bonding matrix, which is a common procedure for fixing nanoparticles on to a substrate in BCDI experiments, in order to avoid its movement due to beam pressure [192].

Ex-situ and In-situ experiments reported in this work were performed at two beamlines specialized in BCDI. At Advanced Photon Source (APS), beamline 34-ID-C uses a Kirkpatrick-Baez (KB) mirror focusing system to match a $70 \times 30 \ \mu m^2$ spatially coherent beam at 55 m from the source to the size of the sample. This gives a good signal level from 200 nm BTO nanocrystals. At Diamond Light Source (DLS) beamline I-13-1, we used a 400 μm aperture 220 m from the source to cut out a spatially coherent beam, which was focussed by a Fresnel Zone Plate (FZP) to the size of the sample. The signal level from this latter system was found to be at least ten times weaker. In both cases the sample was rotated in the coherent, monochromatic, focussed beam and the diffraction

pattern was collected on a Medipix-technology area detector. At APS, the detector distance was variable and for the measurement reported in this manuscript, we keep the detector at D=0.45 m. While at DLS, the detector was fixed at D=2.8 m.

When the beam is coherent over the dimensions of the sample, its diffraction pattern acquires interference fringes surrounding each Bragg peak. This diffraction pattern from the nanocrystal was measured in three dimensions at the 101 or 110 Bragg peaks by rotating the sample stage over a short range, typically $\pm 0.1°$ to $\pm 0.5°$. This rocking curve scan is equivalent to the 2D detector plane sweeping across the Ewald sphere and capturing the 3D volume of reciprocal space around the Bragg peak [11]. The amplitude of the diffracted X-ray is the square root of intensity, while the phase information is lost. This famous phase problem is solved by iterative algorithms, using the additional information obtained by oversampling the intensity distribution in the fringes of the coherent diffraction pattern surrounding the Bragg peak. In this work, a combination of Error-Reduction (ER) and Hybrid Input-output (HIO) algorithms are used to iteratively retrieve the phase until the error between the amplitude of the reconstruction and measured diffraction patterns decreased close to 0.1% [19].

3.4 Domain walls in tetragonal BTO nanocrystals

At room temperature, the 200 nm BTO nanocrystals have tetragonal structure, in which case the 90° and 180° type domain walls (DWs) are favourable because they are mechanically compatible with each other without crystal misfit and are electrically neutral. 90° type DWs separate ferroelastic and ferrolelectric domains, while 180° type DWs separate pure polarization domains. Figure 3.1 shows an example of a crystal twin structure captured inside a single tetragonal BTO nanocrystal. Figure 3.1a and 3.1c show the diffraction patterns of the 101 peak and the 110 peak from differently oriented tetragonal regions of the same crystal. The omega angle difference between the centres of mass (COM) of these two diffraction patterns is 0.6°. There are interference fringes crossing the entire reciprocal space region spanning between the two diffraction patterns centres seen on the area detector. Figure 3.1b shows the fringes on the detector frame at

the angle in the middle of the two COMs. The observation of continuous fringes is a clear indication that the 110 and the 101 peaks come from the same coherence volume in real space, so that their diffraction patterns can interfere coherently. This identifies them as coming from substructures of the same nanoparticle. This is confirmed by gradually moving the sample piezo stages transverse to the beam direction and seeing that the intensities of the two peaks increase and decrease simultaneously in a 600nm size X-ray beam. This confirms the Bragg intensities are coming from the same nanoparticle, for which the intensity variation is attributed to crystal moving in and out of the X-ray beam.

The diffraction patterns of the two peaks were reconstructed separately. Figure 3.1(d) is the reconstructed image from the 101 diffraction pattern in Figure 3.1(a), where the shape is plotted as an isosurface (single 3D contour level) of the amplitude and the surface is color-cued with the local value of the phase. There are two separate domains with a 50 nm wide gap in between. The two domains both have the same crystal orientation because they both contribute to the same 101 Bragg peak, but they have different phases (displacements, denoted by color in Figure 3.1(d)). This shows that the origins of their unit cells are shifted relative to each other. The average phases for the two 101 domains are -1.259$\pm$0.004 and 0.546$\pm$0.003 rad, respectively. Because the phase can only be determined modulo 2π, this phase difference corresponds to a displacement of 2.835*n+0.813Å between the two pieces along the Q-direction, where the n is an integer. 2.835 Å is the {101} d-spacing of BTO. The missing volume in between the two pieces implies there must be a third object, presumably an inserted piece of crystal with a different orientation, filling the gap. Figure 3.1(f), the reconstructed 3D image of the 110 pattern of figure 3.1(c), reveals a 50nm plate-shaped crystal, which is the missing part. The two reconstructed images in Figure 3.1(d) and 3.1(f) fit together well with each other, as shown in Figure 1e. We conclude that two 90° domain walls exist in the same nanoparticle, which are parallel in this case. The polarization direction would change across a ferroelastic domain wall, in the way that is illustrated in Figure 3.1(g).
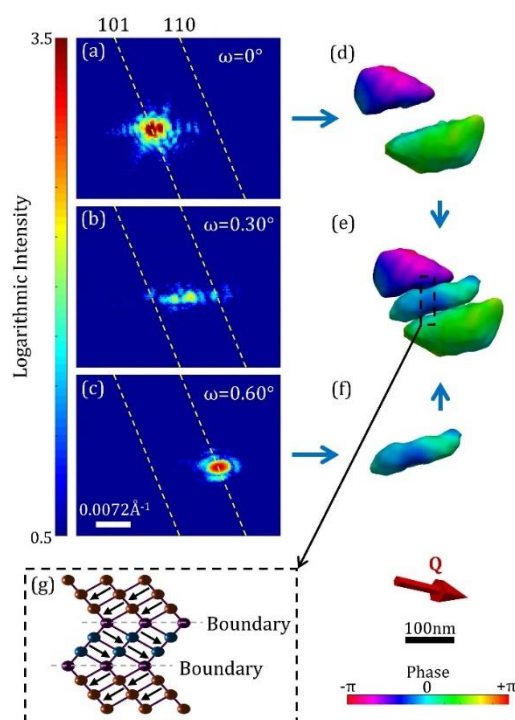
Figure 3. 1 Ferroelastic domain walls in BaTiO₃ nanocrystal at room temperature. (a)-(c) Diffraction patterns of a BaTiO₃ nanocrystal at the angles indicated. The location of the 101 and 110 powder rings on the area detector is plotted with yellow dash lines as guides to the eye. Omega is the self-rotation angle of the sample stage. (d) & (f) Reconstructed images of 101 and 110 diffraction patterns in (a) and (c), respectively, shown as isosurfaces of amplitude to give the shape of crystal. The colour on the shape of nanocrystal represents the complex phase, which can be reverted to displacement of crystal unit-cell origins. (e) A joint view of (d) and (f), which gives a good match in shape. (g) A sketch of the two parallel ferroelastic domain walls inferred from these data at the position indicated by a black box in (e), which shows changes in the polarization direction upon crossing domain wall. The Q direction is denoted, which is determined by the difference of the incident and diffracted X-ray beam wave-vectors. It denotes the Bragg reflection that was measured. The isosurface plots here and in the other figures were generated using the 3D visualization software Paraview [193].

In analyzing the 3D diffraction data to obtain these BCDI reconstructions, it was found to be effective to arbitrarily cut clearly split diffraction peaks into two halves and to reconstruct the two peaks separately before reassembling them. The cropping of intermediary fringes between the two peaks did not seriously distort the resulting images, perhaps because the contribution of the fringes was at a low level relative to the peak centres. Further details of the influence of the cropping are presented in Appendix. When the diffraction patterns of nanoparticle in Figures 3.1 was reconstructed without splitting, shown in Figure

E1, there was found to be seriously misaligned with missing volumes in both cases. The combined double diffraction patterns, complete with the intermediary fringes, should still be the Fourier transform of the complete, assembled particle, so we would like to understand the reasons for this reconstruction failure. Similar misbehaviour was reported for calculated diffraction patterns of a model nanocrystal containing an epitaxial interface between regions of different lattice constant [194]. We, therefore, undertook simulations of double diffraction patterns from known structures.

3.5 Simulated BTO bicrystal nanoparticles

Simulations were performed to test this behaviour of the reconstruction algorithms, which are shown in Figure 3.2. A model BTO nanoparticle, resembling that of Figure 3.1, with three domains was built in a $512\times512\times512$ array. The two domains on the top and bottom have a hemispherical shape with a 32 pixels radius, while the middle domain has a cylinder shape that matches the two hemispheres with a height of 16 pixels. The object was Fourier transformed to generate its diffraction pattern, whose amplitude was then reconstructed using the usual algorithms [11]. The diffraction pattern and reconstructed images are presented in Figure 3.2(a) and 3.2(e). Then the object was split into separate arrays for the hemispheres and the cylinder, separately Fourier transformed and then recombined as complex diffraction patterns to preserve the interference between the parts. When the two centres were the same, the result is shown in Figure 3.2(a), while the split peak behaviour was simulated offsetting the diffraction patterns before they were added together, using different gaps between the diffraction pattern from middle cylinder domain and the pattern from the two hemispheres, shown in Figure 3.2(b-d).

The 3D diffraction patterns in Figure 3.2(a-d) were recentred to their common centre of mass (COM) before phase retrieval using the standard methods to give the images in Figure 3.2(e-h) [11]. Moving the two patterns apart from each other, making them misaligned from the array centre, is equivalent to introducing phase ramps inside each of the particle segments in real space. From the definition of the discrete Fourier transform, it can be seen that each single pixel shift in reciprocal space corresponds to a 2π phase ramp across the

array in real space. When the gap between two patterns was 5 pixels in Figure 3.2(b) and 3.2(f), the reconstruction was successful: the crystal still has the full shape, but there is an opposite phase gradient generated introduced in the different domains, positive for the cylinder and negative for the hemispheres. When the gap was increased to 15 pixels, in Figure 3.2(c) and 3.2(g), the ramp becomes stronger, as expected, but the middle domain becomes misaligned and displaced into one side. There are missing crystal volumes inside the middle cylinder domain. Finally, when the gap reached 40 pixels, in Figure 3.2(d) and 3.2(h), the middle domain becomes completely misaligned. Strong phase ramps and distorted density showed up in the middle cylinder domain and there is a phase gradient in two hemisphere domains.

The two hemispheres are one object and give one diffraction pattern, while the central cylinder is the other object and gives the other diffraction pattern. The centres of each of these two diffraction patterns is not the centre of array. In our reconstruction script, the phase ramps are removed at the end of all iterations. If the array centre is not the centre of diffraction pattern, it would give the phase ramp artefact. As can be seen in Figure 3.2(h), the two hemisphere has a slow phase ramp, which means their diffraction pattern is close to the array centre. While the cylinder has a much sharper phase ramp, meaning that it's far away from the array centre.

This behaviour of the reconstruction algorithms is presently unexplained, but the simulation results do reproduce the experimental behaviour found in Figure E1. We have nevertheless confirmed that the peak splitting is the cause of the apparent misalignment of reconstructed domains. It also justifies our strategy of reconstructing the split peak diffraction patterns separately and manually overlaying the images, which also avoids removing the phase ramps, which would have appeared otherwise. For the nanoparticle in Figure 1, the splitting of two peaks, due to twin boundary, gave separate reflections at 101 and 110. The peak separation in reciprocal space is of order 0.02 $Å^{-1}$, which is considerably more than the 15 pixels needed to disrupt the correct reconstruction of the model ensemble nanoparticle in Figure 3.2(c). This double peak reconstruction

failure using standard method is also reported in simulation works, where different algorithms are proposed to solve this problem [194].
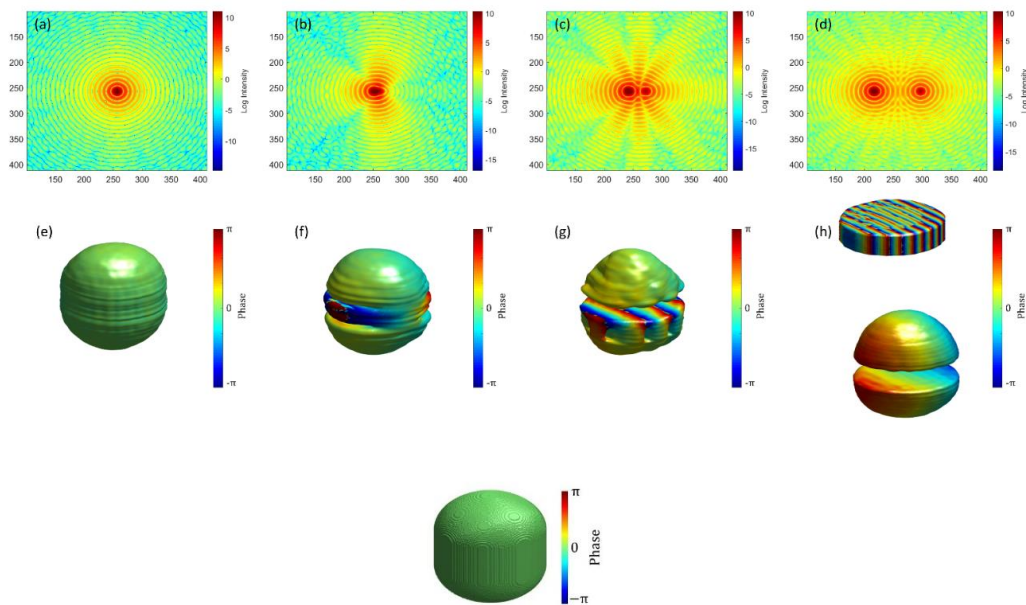
Figure 3. 2 Simulation of split peak diffraction pattern reconstructions. A nanoparticle with three domains was used to generate a 3D diffraction pattern of which the central slice is shown in a 512×512 pixel array. The two peaks corresponding to the hemispherical sides and cylindrical centre were given an extra gap offsetting the two diffraction patterns by 0, 5, 15, 40 pixels from (a) to (d). Their reconstructed images are shown as isosurfaces colored by the image phase in (e) to (h), respectively. The initial object is also shown at the bottom.

3.6 Evolution of ferroelastic domain walls under phase transition

A 200nm BTO nanoparticle showing the twin-peak diffraction pattern was selected at 387.2 K. Similar to the example in Figure 3.1, it had its two peaks sitting on the 101 and 110 powder rings indicating the presence of an internal ferroelastic domain wall. Figure 3.3 shows the BCDI reconstruction, obtained directly from the double peak diffraction pattern, which clearly shows a 90° domain wall inside. At this elevated temperature, the peaks were close enough to reconstruct together without requiring separating. The cross-section view in Figure 3.3 shows the domain wall and two separated domains. The crystal planes of the two domains can be said to be parallel since they both have constant phase inside and there is a sharp jump of the displacement field across the twin boundary. The phase ramps caused by splitting peak is negligible compared with the large phase difference caused by domain walls, as indicated by standard error of average displacement in appendix. This crystal also shows a small hole

and spiral-shaped displacement distribution around the hole, which is an indication of a dislocation, whose details are discussed below.
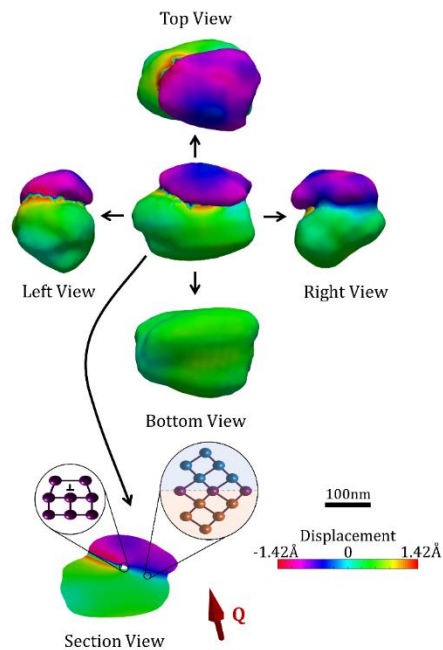
Figure 3. 3 BCDI isosurface image of a BaTiO₃ nanoparticle containing two domains separated by a ferroelastic domain wall at 387.2K. Five orthogonal views and a cross-section are shown, as labelled, along with the Q vector for the section view.

This nanoparticle was chosen to be tracked during heating across the tetragonal-to-cubic phase transition temperature, nominally at 393 K. The sample was heated with a Boralectric ceramic heater stage, directly under the wafer, for improved mechanical stability. This was driven by a voltage-controlled power supply interfaced to EPICS/GDA. The temperature was monitored with a thermocouple as shown in the figure below.
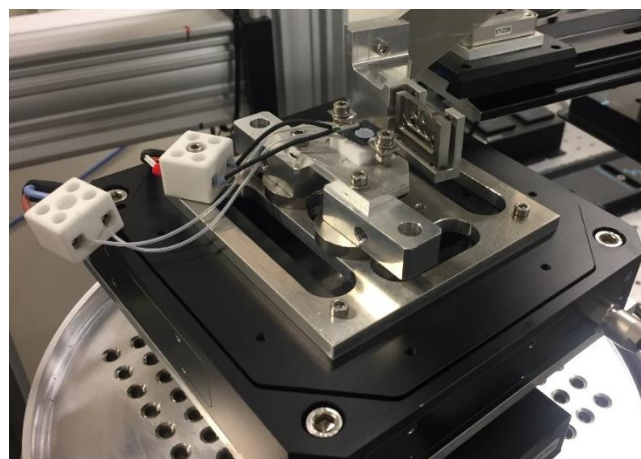
Figure 3.5 shows a series of reconstructed images and corresponding slice of this nanoparticle bi-crystal going from tetragonal structure to cubic structure and back to tetragonal structure again by changing the temperature. When heating up the crystal before the phase transition, the shape of the crystal remains unchanged, but the relative displacement of the two domains (colour) becomes small. After heating up to the cubic structure, the two domains are seen to merge into a single-color shape. Now in the cubic phase, the displacement differences have diminished, while new regions of both tensile and compressive strain have appeared on the surface of the image. When the crystal is cooled down back into the tetragonal phase, the twin boundary comes back at the same position, so this transformation appears to be reversible, showing that the domain wall location is remembered by the nanoparticle.
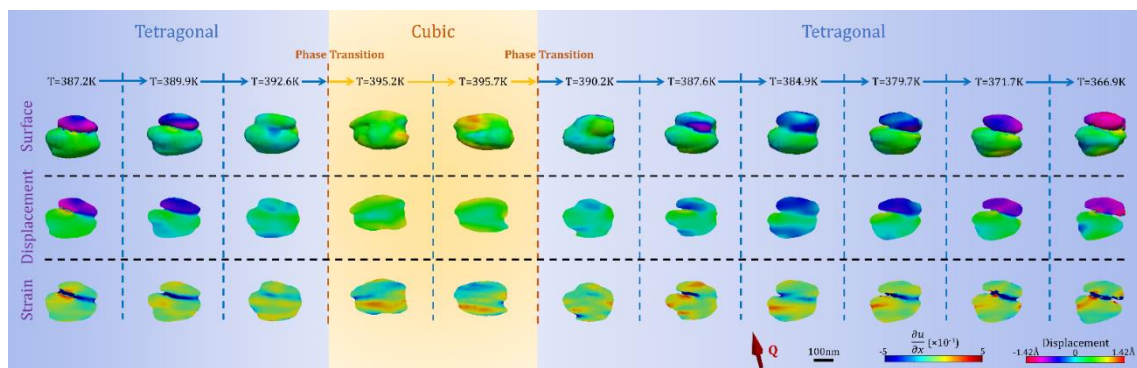
Figure 3. 5 Images of a BaTiO₃ nanoparticle upon crossing through its tetragonal-cubic phase transition. The top row is a series of contour views of the isosurface. The second row shows phase (displacement) cross-section maps taken in the middle of the nanocrystal, while the bottom row shows strain (a derivative of displacement) maps as a function of temperature.

The measured relative displacement of the two domains during heating up and cooling down are shown in Figure 3.6(a) in solid line. The displacement field decreases when increasing the temperature and *vice versa*. The standard error of each point is discussed in the appendix. Close to phase transition temperature, there appears to be a linear relationship of displacement difference with temperature on both heating and cooling. However, the slope during cooling is -0.21, which is steeper than -0.48 while heating up. The goodness of fit is discussed in the appendix. The tetragonality of this crystal during heating and

cooling, derived from the position of diffraction peak centre, are shown in Figure 3.6(a) in dash line. Comparing with both, the tetragonality reproduces well. However, there is a clear delay in the displacement field between cooling and heating. This difference in slope can be thought of as a form of hysteresis, commonly observed in phase transitions, coupled with the experimental limitation of waiting a sufficient time for the structure to equilibrate at each temperature. To estimate the width of the domain wall, the displacement is plotted along a line passing vertically in Figure 3 across the twin boundary in the region away from the dislocation, shown in Figure 3.6(b). The width of the domain wall, where the sharp displacement slope could be seen, is below 30nm, which is the estimated spatial resolution of the image. The change of the phase across the step between the two crystals has a clear temperature dependence as the phase transition at T=393 K is approached.

The displacement inside a domain is interpreted as the crystal distortion projected onto the Q vector, or crystal plane displacement determined by the Bragg reflection. The average displacement between the ferroelastic domains is not caused by the accumulation of crystal distortion, but the structure of the ferroelastic domain wall instead. Because our spatial resolution is the same as the observed width of domain wall, the structure of the domain wall cannot be resolved and the displacement is smeared out at the domain wall position, as seen in Figure 3.6(b). However, the relative displacement between the two domains is a good way to quantify the influence of a ferroelastic domain wall when the temperature changes. In this case, the relative displacement between the two domains is seen to increase linearly near the phase transition temperature. The reason for this change is not clear. There are possibilities that this change is coupled with the changing of domain wall width, or the local distortion at the domain wall becomes sharper due to the change of tetragonality.
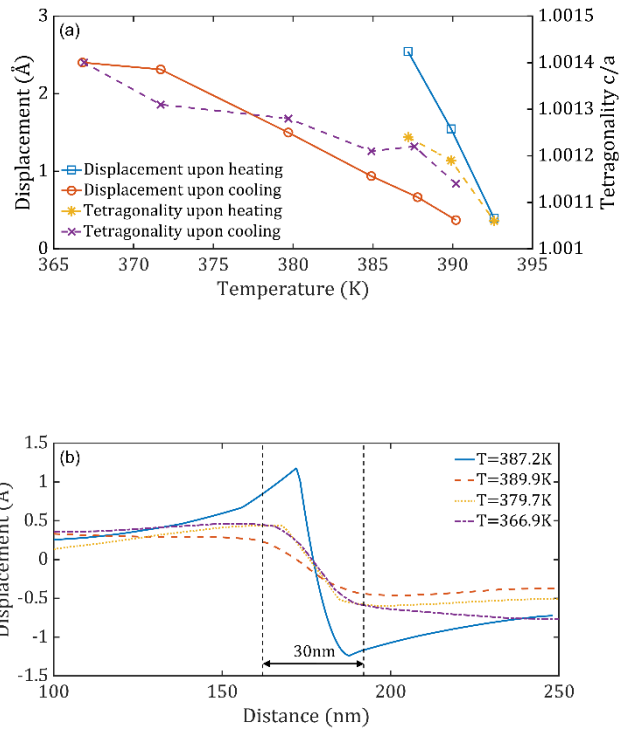
Figure 3. 6 (a) Average displacement difference between the two domains upon heating and cooling are shown in solid line. Tetragonality of this crystal over heating and cooling are shown in dash line. (b) Line plot of displacement over distance across the twin boundary.
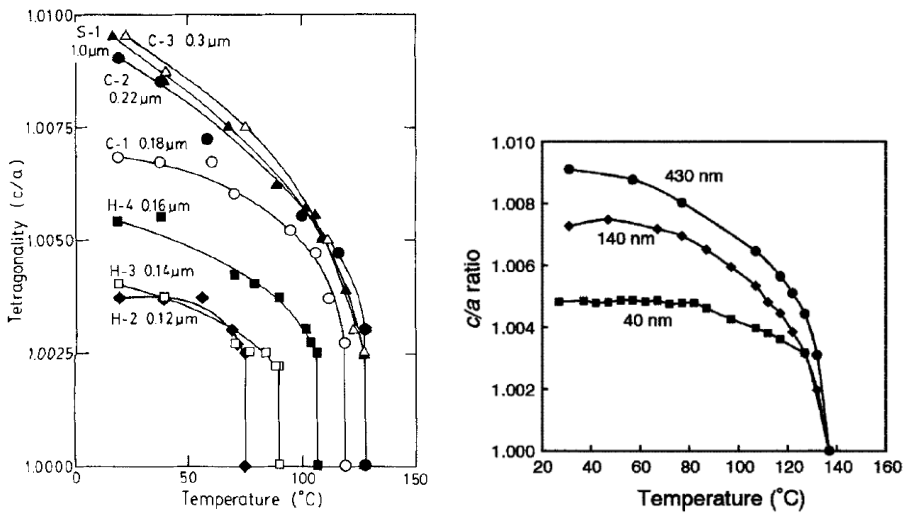
Figure 3. 7 Tetragonality variations with temperature in other's BTO samples. [89,90]

For a comparison reason, Figure 3.7 listed some tetragonality changes with temperature in other people's work. Their tetragonality is larger, typically more than 1.0024, while in our crystal the value is around 1.0012 around phase transition. But it should be noted that the BTO sample has very different

tetragonality for different samples. Also, our value is for selected single crystal, while the values from literatures are the average value of powders.

3.7 Dislocation annihilation upon heating

Figure 3.8(a) and 3.8(b) show further details of the dislocation at the centre of the ferroelastic domain wall inside the bi-crystal. When the temperature is 387.2 K, the dislocation is located at the centre of crystal. The length of this dislocation is 178 nm. Upon heating up to 389.9 K, this dislocation is found to move to the left side and the length decreases to 125 nm. Further heating up to 392.6 K, although the crystal is still in the tetragonal phase, causes the dislocation to diminish again and then disappear. This dislocation does not come back during the cooling stage of the experiment.
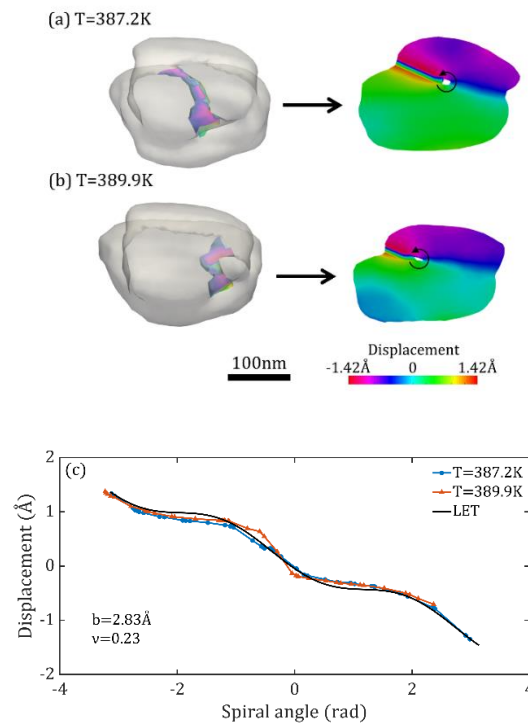
Figure 3. 8 Dislocation annihilation upon heating. (a) Reconstructed crystal image at 387.2 K. (left) A dislocation line through crystal is coloured. (right) A slice view across the dislocation line. (b) Same as (a), but temperature is 389.9 K. (c) displacement field plotted vs rotation angle around the low-density core. Both experimental results and simulated curve from linear elastic theory are presented.

To identify the type of dislocation, the displacement field surrounding the low electron density core is plotted as a function of rotation angle in Figure 3.8(c). The experimental data show a roughly linear trend of crystal displacement over

angle superimposed with two clear modulations. This is the characteristic of an edge dislocation, for which is superimposed the simulated displacement field according to linear elastic theory (LET), with details provided in the Appendix. The experimental data give a reasonable match with the simulated results.

3.8 Conclusion

We studied the structure and arrangement of domain walls in 200 nm BTO nanoparticles by BCDI both at ambient temperature and across the tetragonal-cubic phase transition temperature. Domains and domain walls are commonly found in these particles, giving rise to split coherent diffraction peaks. For successful BCDI reconstruction with large peak split, it was necessary to separate the peaks and manually reassemble the reconstructed 3D images afterwards. Ferroelastic domain walls were identified and characterized at room temperature. At temperatures close enough to the tetragonal-cubic phase transition, the split peaks of a particle containing a ferroelastic domain wall were successfully reconstructed using both peaks together. This allowed us to determine the sub-Ångstrom relative displacement between two domains, tracking its disappearance on approaching the phase transition to cubic phase and reappearance when cooling back to tetragonal phase. We found a linear relationship between the relative displacement of the two 90° domains over heating and cooling close to the tetragonal-cubic phase transition. The domain wall location was reproducible in this 200 nm BTO nanoparticle. An edge dislocation line was found at the centre of the twin boundary inside this crystal close to the transition temperature. This dislocation annihilated upon ramping up the temperature and did not return upon cooling.

Chapter 4. Polar domains in tetragonal barium titanate nanocrystals at room temperature

Ferroelectric domains of roughly 100nm in size were identified in Chapter 3. These large ferroelectric domains have characteristic Bragg peaks on the two adjacent (101) and (110) powder rings. When performing the Bragg coherent x-ray diffraction imaging (BCDI) experiment on a randomly oriented powder sample, a sub-micron focused beam was used. In such case, the co-existence of the two peaks on the two powder rings could be checked by moving the beam around the sample. If the two peaks were found to turn on and off simultaneously, then they were marked as coming from the same crystal. If the two peaks were behaving differently to the movement of the X-ray beam, then they were marked as coming from two separate crystals. After going through more than a hundred of crystal patterns during several consecutive beamtimes at Advanced Photon Source (APS), the chance of finding both Bragg peaks from same crystal in commercial barium titanate (BTO) samples was no more than 10%. The majority of the Bragg peaks were found to only have one peak with no surrounding satellites. It suggests that the ferroelectric domains of 100nm in size are peculiar in the commercial BTO samples. Regarding the actual status and the structure in those single Bragg peak crystals, we can make a few assumptions:

(a) The majority of the crystals preserve a single domain structure. The whole crystals have only one polarization direction, so that a large amount of surface charge would be generated.

(b) The crystals may have 180° domains, which don't cause the splitting of Bragg peak between the two powder rings, which would need 90° domains instead.

(c) Instead of having a rigorous single polarized domain or a number of 180° domains, the crystals could have small polar domains. If the domains are small enough or distortions of a different symmetry, it may result in the symmetric breaking of one crystal peak, but not necessarily breaking into two Bragg peaks on the two powder rings as illustrated in Chapter 3.

To further explore the BTO crystal structures and examine the existing assumptions, further detailed BCDI experiments on BTO nanocrystals were done at APS 34-ID-C. During the experiment, the crystals with clear facets were being targeted because these allow us to retrieve the full set crystallographic directions from the final reconstructed images. By mapping out the displacement field and the derived strains, some unexpected strain-stripes networks have been discovered. These stripes are understood as internal boundaries within the crystal. The distribution of the strain stripes and their behaviours with temperatures are illustrated in the rest of this Chapter and also in Chapter 5.

Contribution statement: Jiecheng and Ian designed the experiment. Jiecheng, Ian, Ross, Wonsuk, Ana, Longlong have helped with the BCDI experiment. Emil carried out the PDF fitting to the scattering data. Jiecheng wrote the manuscript with the help of Ian.

4.1 Ex-situ BCDI experiment and data processing

4.1.1 Experimental details

The commercial 200 nm BTO nanocrystals were suspended in ethanol solution with 1% Tetraethyl Orthosilicate (TEOS) before drop-casting onto silicon wafers and calcined at 973 K in air for 1h. Figure 4.1 shows a scanning electron microscopy (SEM) image of the BTO nanoparticles before and after the TEOS calcining. The crystals have sizes ranges from 100 nm to 1 μm. There is no noticeable change relative to the shape and size before and after the TEOS calcining. As shown in Figure 4.1(b), the crystals have big facets on the surface, but the shape is not perfect cubes. The TEOS is intended to create a thin SiO_2 coating to stabilize the crystals, but this is not detectable in the SEM images.

After calcining, the BTO samples were put onto the sample stage at APS 34-ID-C for an *ex-situ* BCDI experiment. The 600 nm X-ray beam, which is defined by the coherence-defining JJ slits and focused by the Kirkpatric-Baez (KB) mirrors, was selected to illuminate a small number of the crystals. The default 9 KeV energy was chosen for illuminating the sample. The Timepix detector was set to the {110} Bragg angle and placed 0.5 m away from the sample stage, not too close for satisfying the far-field imaging and oversampling ratio, and not too far for finding the diffraction of the crystals easily. The setup of the geometry is schematically

illustrated in Figure 4.2. The 11 crystals on the plate are the reconstructions of 11 different BTO crystals. These crystals were not physically sitting next to each other as in the schematic graph but laid out for illustration. Each of these crystals was selected because of big facets showing up on their surface, with their actual position unknown in the sample. The incident beam is also only an illustration. During the experiment, the incidence angle on the substrate was between 3° and 5° to have a proper X-ray footprint, not too large so that it's hard to find crystal peaks, and not too small so that the crystal peaks are relatively sparse and isolated.
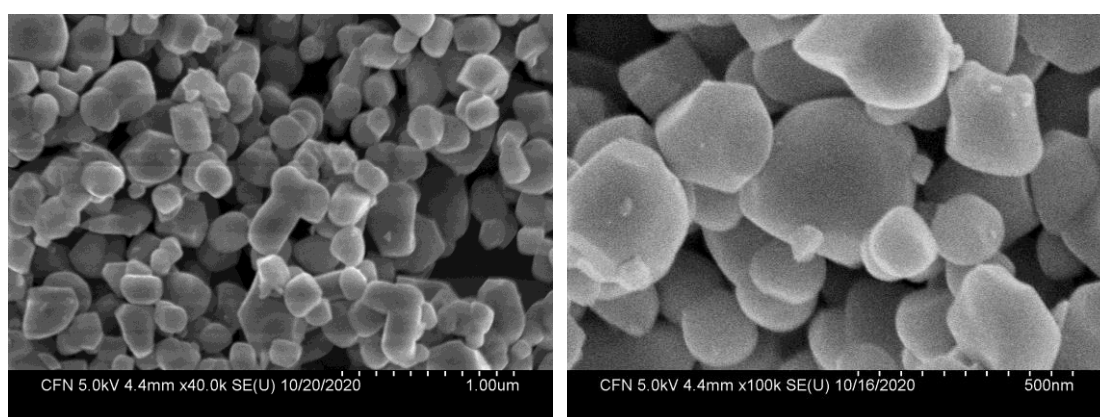
Figure 4. 1 SEM image of BTO nanoparticles with a nominal size of 200nm. (a) Commercial BTO powders with no TEOS calcining. (b) Commercial BTO powders with TEOS calcining at 973 K for 1h.

The crystal being illuminated by the X-ray beam in Figure 4.2 shows directional fringes. There are periodic fringes in all directions surrounding the diffraction centre, which contain the crystal size information in three dimensions. Several long tails of the fringes can also be observed, which indicates the existence of strong surfaces or interfaces. The reconstructed crystal shape has four big facets as marked by Facet A to D in the figure. The reconstruction details and the reorientation of this crystal, called BTO-32, are discussed in the next section.
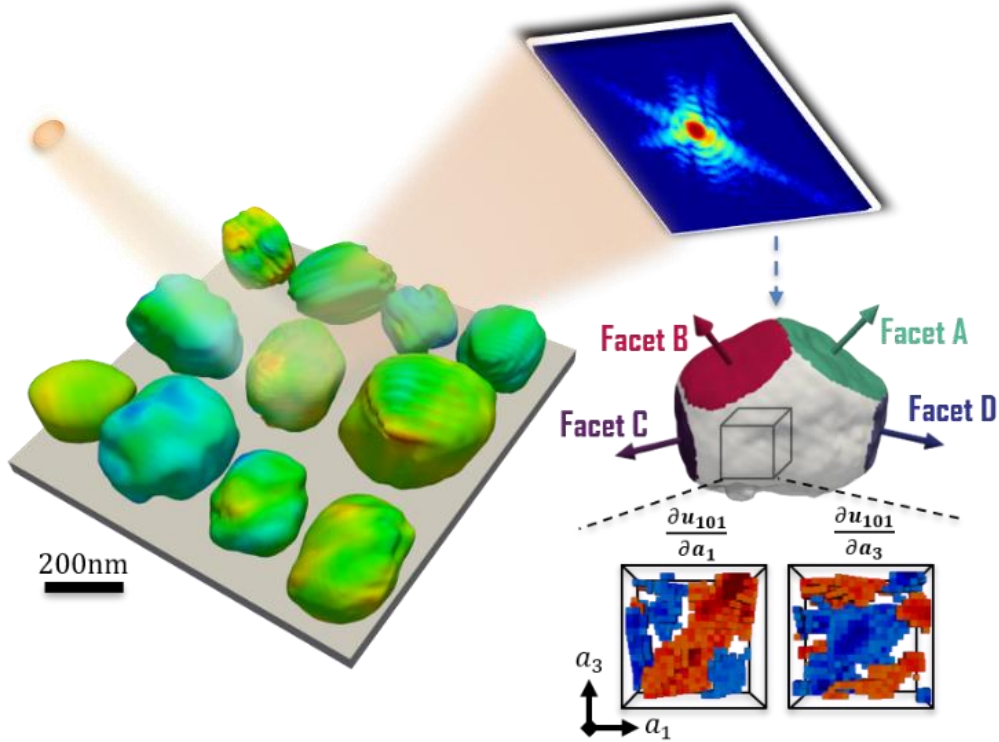
Figure 4. 2 Schematic showing of the geometry for BCDI experiment on the BTO nanoparticles. The three-dimensional (3D) coherent diffraction patterns of one isolated nanocrystal were measured at (101) reflections, which was then reversed to the real space image and showed four big facets on the surface.

4.1.2 Reconstruction parameters confirmations

The crystal with four well-defined facets in Figure 4.2 was chosen for detailed study of the convergence of the reconstruction. The chi-square error metrics χ^2 and difference metrics D are used for evaluating the goodness of the calculated diffraction of the reconstructions in agreeing with the measured intensity distributions. Their definitions are defined in Equation 1.35 and 1.36 in Chapter 1. The detailed descriptions of the parameters and the algorithms used in BCDI reconstruction are provided in detail in Chapter 1.

(a) Shrink-wrap evaluations

The shrink-wrap is the support updating method as illustrated in Chapter 1 [24]. For this crystal reconstruction, the Gaussian smoothing function was used to help cropping out the noise and the artefact. There are also other methods like box filtering or keeping the support as constant voxels.

Figure 4.3(a) shows how the chi-square error metrics vary with the shrink-wrap threshold. There is a change-of-slope turning point in this plot where the

threshold roughly equals to 0.23. Before the turning point, the slope is smaller, and it is considered that the shrink-wrap is still helping to crop out the artefact. After the turning point, the slope becomes larger and it is believed that the updated support is so strong and narrow, that it starts to cut out the volume of the real crystal image. The reconstructed images with contour views and slices views are shown in Figure 4.3(b). There are clear noises and artefacts in the images when threshold equals to 0.05 and 0.1. When the threshold goes beyond 0.25, the crystal shrinks in size and loses the real volume. Between 0.1 and 0.25 the images are very similar, so considered to be correct. Therefore, the shrink-wrap with a threshold of 0.20 is used for the reconstruction of this crystal.
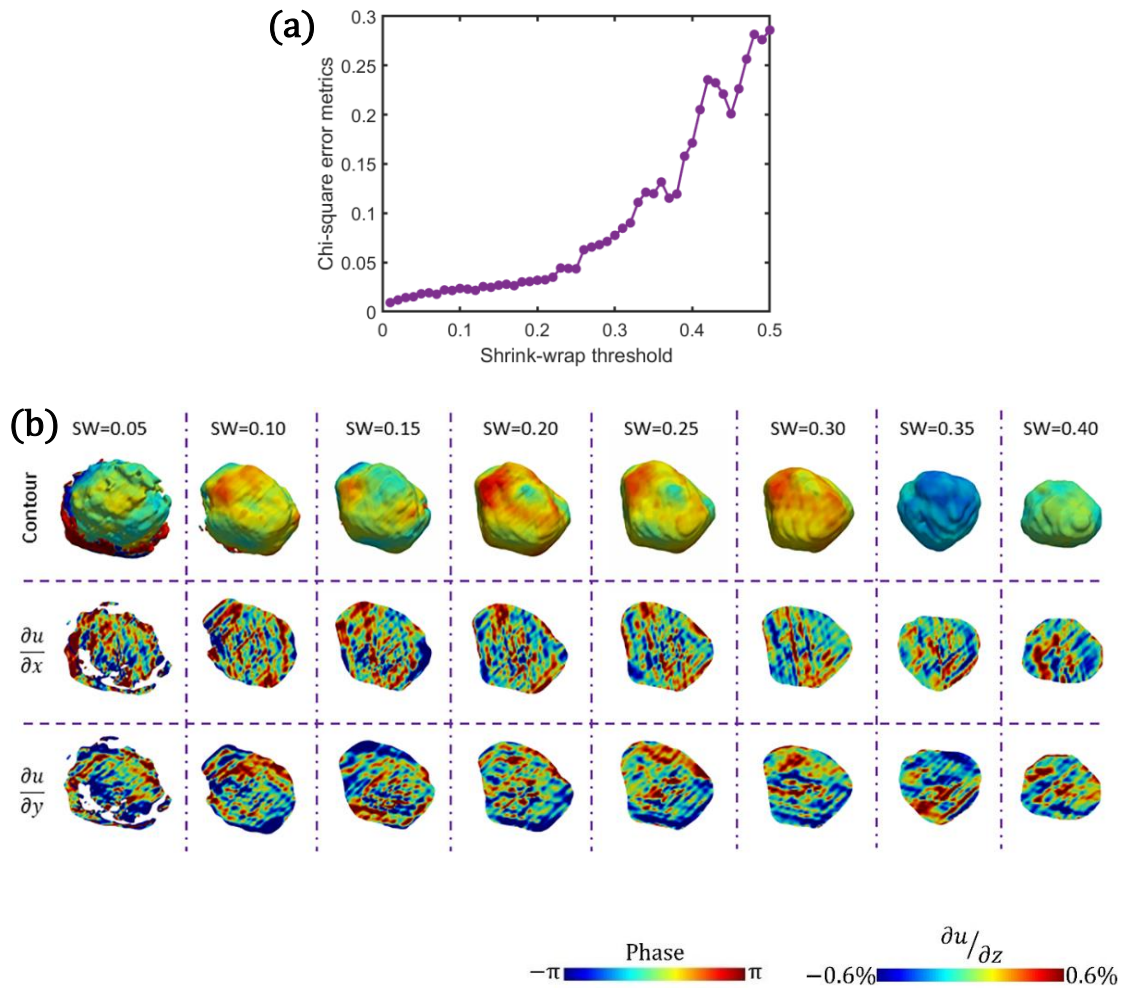
Figure 4. 3 The reconstructions vary with the shrink-wrap thresholds. (a) Plot of chi-square error metrics with respect to the shrink-wrap thresholds. (b) The final reconstructed images using the shrink-wrap threshold from 0.05 to 0.40 with a 0.05 step size. The first row is the iso-surface contour view coloured by displacement, while the second and the third rows are slices showing the two derivatives of displacement in lab coordinates.
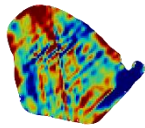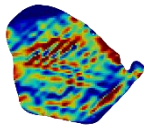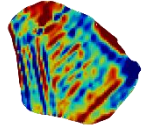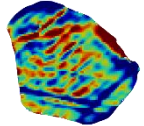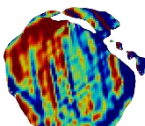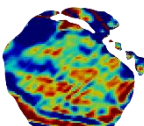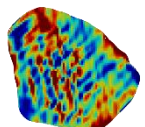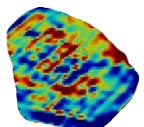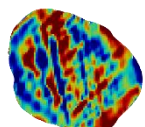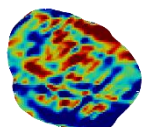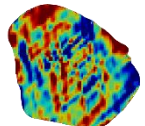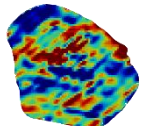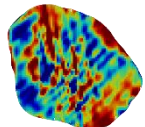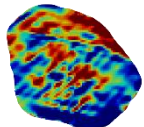
(b) Algorithms evaluations
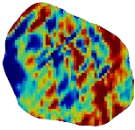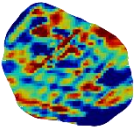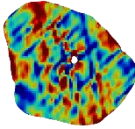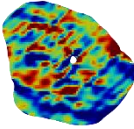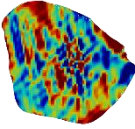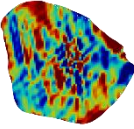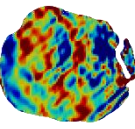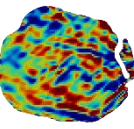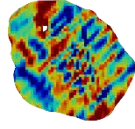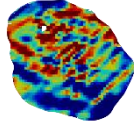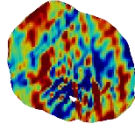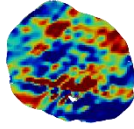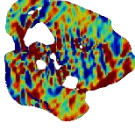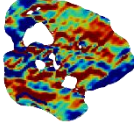
Some typical combinations of algorithms were tested and compared. The details of the algorithms are listed in Chapter 1. The guided algorithm (GA) was turned on with a trigger of [5,180], which means that the first algorithm would go through 1 to 5 iterations, while the second algorithm would turn on from 6 to 180 iterations, and then turning back to first iteration again.

The Error Reduction (ER) + Hidden Point Removal (HPR) combinations gives the lowest chi-square error metrics of 1.7%. Quite a few combinations also give reasonable chi-square matrices around 2.0%. For example, the typical ER + Hybrid Input Output (HIO) gives a chi-square of 2.1%. While some combinations are not working well in this case. For example, the ER+HIO-AMP gives a chi-square more than 10%. In this Chapter, the typical ER+HIO is used for reconstructing the crystal.

Table 4. 1 The chi-square error metrics of the reconstructions using different algorithm combinations.

Algorithm combinations	Crystal χ^2 metrics	Reconstructed images $\partial u/\partial y$ -0.6% ▬▬ 0.6%	Reconstructed images $\partial u/\partial z$ -0.6% ▬▬ 0.6%
ER + HPR	1.7%		
ER + DM	1.9%		

ER + HIOv	1.9%		
ER + HIOb	2.0%		
ER + HIOso	2.0%		
ER + DMr	2.0%		
ER + Guided HIO	2.1%		
ER + HIO	2.1%		
ER + HIOsi	2.3%		

ER + ASR	2.5%		
ER + RAAR	2.6%		
ER + RAARv	2.6%		
ER + HIOp	3.1%		
ER + GRAAR	3.6%		
ER + HIO-OR	3.7%		
ER + HIO-AMP	10%		

(c) GA parameters

The GA would run the reconstruction with defined population and generation. The population is the number of reconstructions run parallel to each other. The generation defines how many iteration blocks are run, each of which contains the typical 200 or 300 iteration loops. Figure 4.4 shows some GA parameters that are usually adjusted for optimizing the reconstruction, including population, generation, low resolution method, GA return matrices, breed mode. The start guess is also usually used for testing the reproducibility of the final reconstruction.
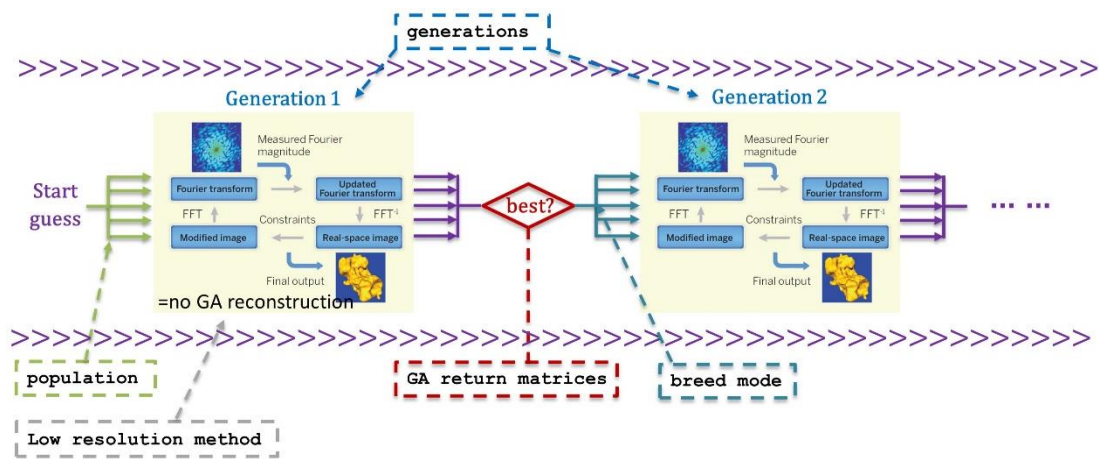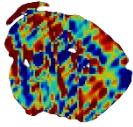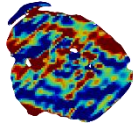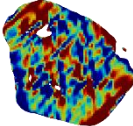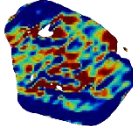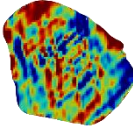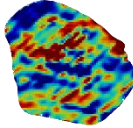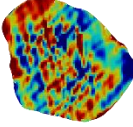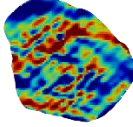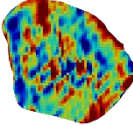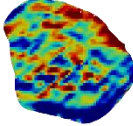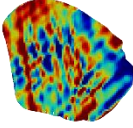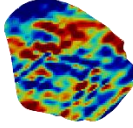
Figure 4. 4 A simplified GA flow chart is presented.

The selection of the result after each generation is determined by the GA return metrics. The GA metrics that are generally used were tested and shown in Table 4.2. The average of iterates gives the lowest chi-square error metrics. All the other methods been tested also give good and very similar chi-square. The sharpness metric is used for reconstructing the crystal.

Table 4. 2 Different GA return metrics and their chi-square error metrics when reconstructing the crystal.

GA return metrics	Crystal χ^2 error metrics	Reconstructed images	Reconstructed images
		$\partial u / \partial y$ -0.6% ▇▇▇ 0.6%	$\partial u / \partial z$ -0.6% ▇▇▇ 0.6%

Average of iterates	2.0%		
Average of half iterates	2.0%		
Sharpness $\sum\|\rho(r)\|^4$	2.1%		
Largest area of the support	2.2%		
Chi-square matrices χ^2	2.2%		
Total variation norm	2.2%		

The breeding of the new starting guess is determined by the breed mode. The general modes were tested and shown in the Table 4.3. In the table, "a" represent the best population iterate determine by the GA metrics, while "b" is the current population iterate. Of all the breeding mode been tested in this work, the "avg_ab" works the best.

Table 4. 3 Different breed modes and their chi-square error metrics when reconstructing crystals.

Breed mode	Crystal χ^2 error metrics	Reconstructed images $\partial u / \partial y$	Reconstructed images $\partial u / \partial z$
'avg_ab': $\dfrac{(A_a e^{\phi_a} + A_b e^{\phi_b})}{2}$	1.6%		
'max_ab': $\langle A_a, A_b \rangle_{max} \cdot e^{\frac{(\phi_a + \phi_b)}{2}}$	1.9%		
'sqrt_ab': $\sqrt{A_a e^{\phi_a} \cdot A_b e^{\phi_b}}$	2.0%		
'sqrt_ab_pa': $\sqrt{A_a \cdot A_b} \cdot e^{\phi_a}$	2.0%		
'max_ab_pa': $\langle A_a, A_b \rangle_{max} \cdot e^{\phi_a}$	2.0%		
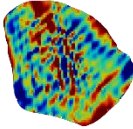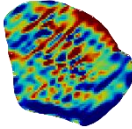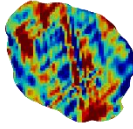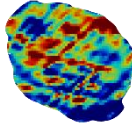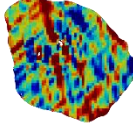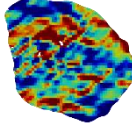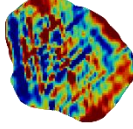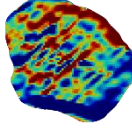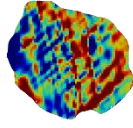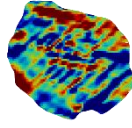
'pixel_switch': Random mixing	2.0%		
'avg_ab_pa': $\frac{(A_a + A_b)}{2} \cdot e^{\phi_a}$	2.3%		

The low-resolution method starts with a low-resolution (LR) diffraction pattern for the iterations for the first several generations. The LR data are obtained from the measured data by multiplication by a spherical function. To smooth the diffraction pattern, some smoothing functions could be used for constructing the low-resolution diffraction pattern. One big Gauss distribution is to use a single 3D Gauss function to multiple with the diffraction pattern. The default sigma value is 0.1 and can be adjusted according to the array size.   Many small gauss distributions, on the other hand, uses many small gauss functions all through the data array. The default number of Gauss functions used are 20 but can be adjusted. The Laplacian and sinc method are to use a Laplacian filter or a sinc function to smooth the image rather than Gauss filter.

In our script, these functions are built-in already and can be added through 'params.GA_lres_type='gauss'; % or 'gauss-many', 'laplacian', 'sinc'.

By default, it is used for the first 3 generations in the total 5 generations reconstructions. The last 2 generations use the original diffraction pattern for retrieving the details. The result from different low-resolution methods and without the low-resolution methods are shown in Table 4.4. For the reconstruction of this crystal, the low-resolution methods give much better chi-square error metrics than without low-resolution methods. Of all the methods been tested, the one big gauss distribution works the best.

Table 4. 4 Different low-resolution methods and their chi-square metrics when reconstructing the crystal.
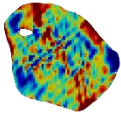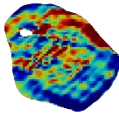
Low resolution method	Crystal χ^2 error metrics	Reconstructed images $\partial u / \partial y$ −0.6% ▬ 0.6%	Reconstructed images $\partial u / \partial z$ −0.6% ▬ 0.6%
One big gauss distribution	1.6%		
Laplacian distribution	1.8%		
Many small gauss distributions	2.1%		
Sinc distribution	2.2%		
No low resolution	5.9%		
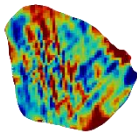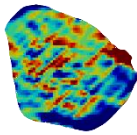
(d) Reproducibility evaluations

To test the reproducibility of the reconstruction, multiple reconstructions with different starting points were performed. Two general random supports were used for the start: The random object (RO) defines the starting image as a

random object with the size of the support with zero phase. The random phase (RP) defines the starting image as a box shape object with a size relative, normally 50%, to the data array. But the phase is randomly distributed from -π to π. The 10 RO reconstructions 10 RP reconstructions were performed for the crystal reconstruction. The results are shown in the Table 4.5. The relatively low chi-square metrics and difference metrics indicates the good reproducibility in the reconstruction of BTO-32.

Table 4. 5 The chi-square metrics and difference metrics of the base reconstruction and 20 repeated reconstructions. The base reconstruction has a flat start with box-shaped object and zero phase. 10 RO reconstructions start with random object and zero phase. 10 RP reconstructions start with box object and random phase.

Reconstruction Number	Crystal χ^2 error metrics χ^2	Difference metrics D
Base	1.6%	0%
RO 1	2.0%	2.1%
RO 2	2.0%	2.1%
RO 3	2.0%	2.1%
RO 4	2.0%	2.1%
RO 5	2.0%	2.1%
RO 6	2.0%	2.1%
RO 7	2.0%	2.1%
RO 8	2.0%	2.1%
RO 9	2.0%	2.1%
RO 10	2.0%	2.1%
Images of RO1	$\partial u / \partial y$ -0.6% ▬ 0.6%	$\partial u / \partial z$ -0.6% ▬ 0.6%
RP 1	1.7%	1.3%
RP 2	1.7%	1.3%

RP 3	1.7%	1.3%
RP 4	1.7%	1.3%
RP 5	1.7%	1.3%
RP 6	1.7%	1.3%
RP 7	1.7%	1.3%
RP 8	1.7%	1.3%
RP 9	1.7%	1.3%
RP 10	1.7%	1.3%
Images of RP1	$\partial u / \partial y$ -0.6% ▇▇ 0.6%	$\partial u / \partial z$ -0.6% ▇▇ 0.6%

4.1.3 Reorientation of reconstructed crystal

For a typical powder sample, all the nanocrystals are randomly distributed so that the X-ray beam could hit more than one crystal at a time. One might consider making the X-ray beam size close to the sample crystal size and carefully aligning a specific crystal grain into the centre position. By keeping this crystal at the beam centre and searching at reciprocal space, different Bragg reflections from a single crystal could be achieved [232, 233]. This has been achieved by others, but practically it was found to be necessary to isolate a crystal by manipulation or by clearing the surrounding area, because the "sphere of confusion" of the diffractometer is not good enough to remain exactly at a single location better than the focussed beam size.

Experimentally, however, it's more efficient to measure only one Bragg reflection of the ensemble of crystals naturally available in a powder sample. In such cases, without a secondary reference reflection, the crystallographic orientations are unknown. The only known direction is that of the Q-vector, which is determined by the X-ray incident and diffracted direction in experiment and denotes the corresponding crystallographic Bragg reflection.

After reconstructed the crystal with credibility, the Q direction is available in the final image in the lab coordinates, which is given by

$$Q = k_f - k_i \tag{4.1}$$

$$k_f = [\sin\delta\cos\gamma\,,\sin\gamma\,,\cos\delta\cos\gamma]; \; k_i = [0,0,1] \tag{4.2}$$

The k_i and k_f are the direction vector of the incident and the diffracted X-ray beam. The δ and γ are the detector horizontal and vertical angles.

To retrieve the correct crystallographic axes, at least two non-collinear crystal directions are needed. In this work, the additional information comes from identifying and calibrating the angles between the facets of the crystal morphology. Figure 4.5 (a) to (c) shows three orthogonal views of the BTO-32 crystal in laboratory coordinates. Several flat facets are observed and labelled A, B, C and D, as shown in Figure 4.5 (d) and (e). The Q vector is also plotted, which is the known crystallographic (101) or (011) direction. Since, for tetragonal structure, (101) is equivalent to the (011) direction, so for simplicity, the Q vector is denoted as (101) only.
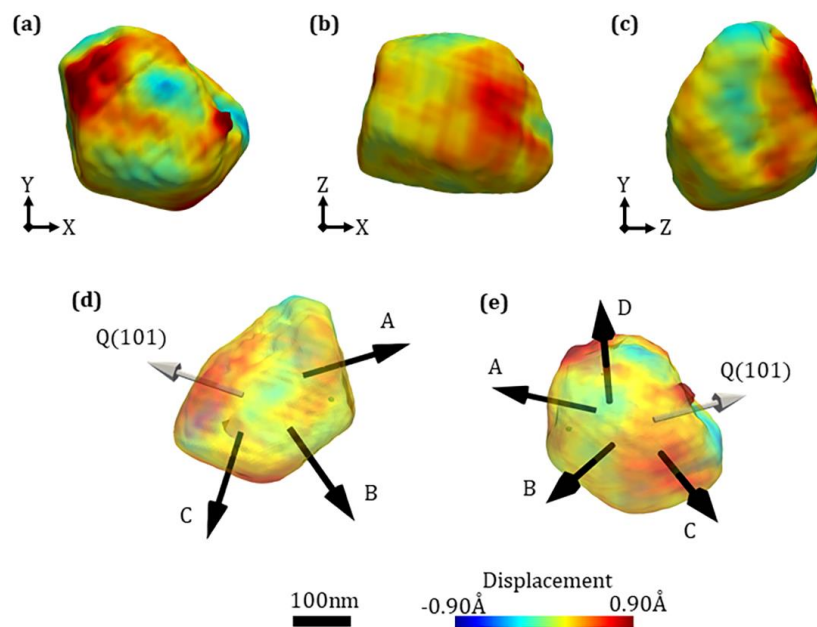
Figure 4. 5 Different views of the BTO-32 crystal showing clear facets. (a)-(c) Three orthogonal views of the crystal shape in laboratory coordinates of the experiment. (d)-(e) The facets are marked with black arrows, while the Q vector is denoted by grey arrow.

In any single crystal, because of the symmetry of its unit cells, there are fewest surface defects along "low-index" directions and these tend to show the largest facets in the crystal morphology. These facets tend to be "close-packed" with the least number of low-coordinated surface atoms/ions. From low temperature to high temperature, BTO has rhombohedral, orthorhombic, tetragonal and cubic structure, respectively. All these crystal structures tend to have pseudo cubic {100}, {110} and {111} facets. To determine the facet coordinates, the inclined angles between these facets are mapped out and shown in Table 4.6. The reference angles between pseudo cubic {100}, {110} and {111} are also presented.

Table 4. 6 Incline angles between different facets and the Q vector of the crystal.

	A	B	C	D	Q	{100}	{110}	{111}
A		109.0°	54.4°	90.6°	35.6°	-	-	-
B	-		54.7°	90.4°	144.6°	-	-	-
C	-	-		89.0°	90.0°	-	-	-
D	-	-	-		90.5°	-	-	-
Q	-	-	-	-		-	-	-
{100}	-	-	-	-	-	90.0°	45.0°/90.0°/135.0°	54.7°/125.3°
{110}	-	-	-	-	-	-	60.0°/90.0°/120.0°	35.3°/90.0°/144.7°
{111}	-	-	-	-	-	-	-	70.5°/109.5°

Because the Q direction is 101, Facet A and B have the reference angle with Q between {111} and {110}. Facet C has characteristic angle with A and B between {111} and {100}. If the Facet A is marked as 111, then Facet B, C, D can be identified as (-11-1), (010) and (10-1), respectively.

After identifying the crystallographic direction of each facet, the rotational relation between the laboratory coordinates and crystallographic coordinates can be determined. This rotation matrix was calculated through a Matlab script based on the Horn's quaternion-based method [195, 196], which is to find the minimum of a global factor S defined by:

$$\langle S \rangle_{min} = \langle \sum_{i=1}^{N} \left| R * A(x_i, y_i, z_i) + T - B(x_i', y_i', z_i') \right|^2 \rangle_{min} \qquad (4.3)$$

$A(x_i, y_i, z_i)$ is the vector in new coordinates while $B(x_i', y_i', z_i')$ is the corresponding vector in original coordinates. These two are the inputs given. For example, we have the coordinates of Q and four facets directions for BTO-32, which are the input $B(x_i', y_i', z_i')$. The new crystallographic directions we defined, like (101) for Q and (111) for Facet A, are the input $A(x_i, y_i, z_i)$. R is the possible rotation matrix, while T is the possible translation matrix. The global factor S is a sum of all the minus products from each vector. The problem is solved by finding the minimum S so as to get the best rotation matrix R. The crystal is then rotated according to the best rotation matrix R and saved to vtk file for visualization.

After reoriented the crystal to the new coordinates, the Cartesian X, Y and Z direction are assumed to be the crystallographic (100), (010) and (001) direction, respectively. Therefore, the three orthogonal directions are defined as a_1, a_2 and a_3.

4.2 Discovery of strain stripes networks

In this study, the structure of the interior of the crystal is of interest. To explore this inner information inside the crystal, different slices were taken. Figure 4.6 shows 15 slices across the crystal. Slice 1 to 5 are the slices perpendicular to the crystallographic a_1 direction (or called (100) direction). Slice 3 is the central slice across the crystal centre, while the other slices are 50nm apart from the adjacent slices. Similarly, slices 6 to 10 are perpendicular to a_2 direction (or called (010) direction), and slices 11 to 15 are perpendicular to a_3 direction (or called (001) direction).
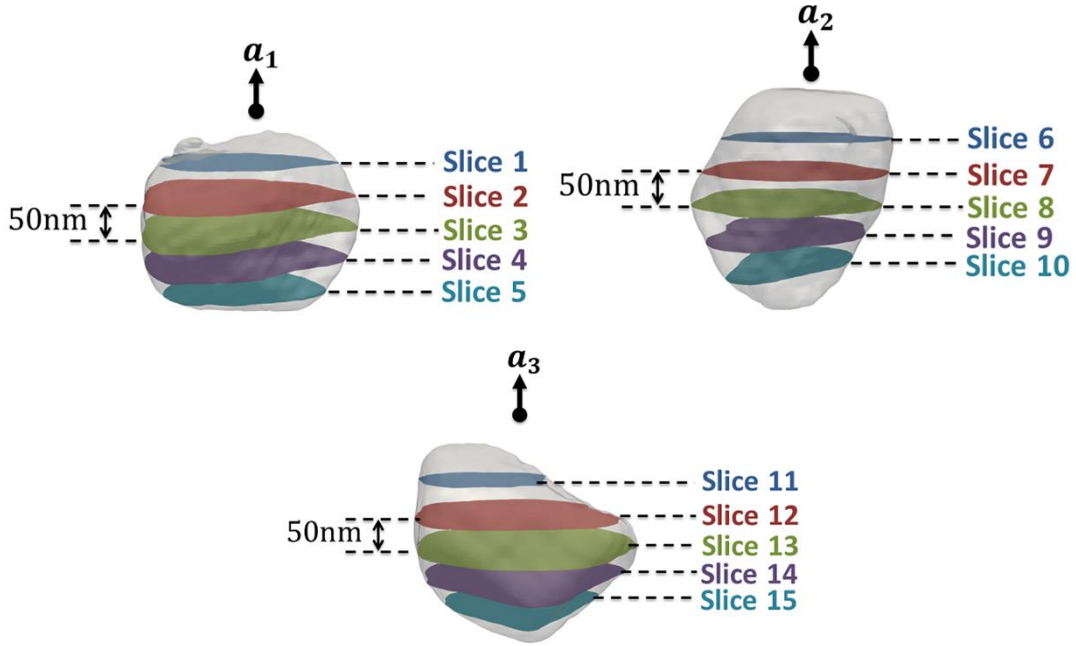
Figure 4. 6 Slices across the crystal to show the information inside. Slices 1 to 5 are perpendicular to the crystallographic a_1 direction, with a 50nm spacing. Slice 6 to 10 and 11 to 15 are perpendicular to a_2 and a_3 directions, respectively.

After selecting the proper slices, the phase images were taken and converted to the displacement field. The derivatives of the displacement field were taken along the three crystallographic axes (a_1, a_2, a_3). Because the displacement field derived from the phase image is a projected value onto the Q vector, the final results are linear combinations of strain components shown in equations below:

$$\frac{\partial u_{101}}{\partial a_1} = \frac{\partial(u_{100}\cos 45° + u_{001}\cos 45°)}{\partial a_1} = \frac{\sqrt{2}}{2}(\varepsilon_{11} + \varepsilon_{31}) \qquad (4.4)$$

$$\frac{\partial u_{101}}{\partial a_2} = \frac{\partial(u_{100}\cos 45° + u_{001}\cos 45°)}{\partial a_2} = \frac{\sqrt{2}}{2}(\varepsilon_{12} + \varepsilon_{32}) \qquad (4.5)$$

$$\frac{\partial u_{101}}{\partial a_3} = \frac{\partial(u_{100}\cos 45° + u_{001}\cos 45°)}{\partial a_3} = \frac{\sqrt{2}}{2}(\varepsilon_{13} + \varepsilon_{33}) \qquad (4.6)$$

The derivatives of displacement over the crystallographic a_1 and a_3 directions contain the sum of a normal strain component and a shear strain component, while the derivatives over the a_2 direction only contain the sum of two shear strain components.

Figure 4.7 shows the derivatives along all three directions in Slice 1 to 5. It could be seen that there are strain stripes roughly $45°$ in the derivatives along the a_1 and a_3 directions, but $90°$ in the derivatives along the a_2 direction. These strain stripes are distributed in all the Slices from 1 to 5, which indicates the presence of strain stripes all over most of the crystal volume.

To quantify the periodicity and direction of the strain stripes, the autocorrelation function is used. The correlation coefficients are the measurements of the dependence of the two variables. The widely used Pearson correlation coefficient r, if applying to the sample of n measurements, has the definition:

$$r = \frac{\sum_{i=1}^{n}(x_i - \bar{x})(y_i - \bar{y})}{\sqrt{\sum_{i=1}^{n}(x_i - \bar{x})^2 \sum_{i=1}^{n}(y_i - \bar{y})^2}} \tag{4.7}$$

The x_i and y_i are the ith measurement of the sample, while the $\bar{x}$ and $\bar{y}$ are the sample means. The Pearson correlation coefficient has a value range from -1 to 1. The value 1 means the two variables are perfect correlated positively, and the -1 means a perfect negative correlation. The value 0 means no correlation between the two.

Different correlations could be defined from the Pearson correlation. If the two input samples x and y are the same sample with different delay or shifting, then the autocorrelation function (ACF) could be defined [197, 198]. The normalized one-dimensional (1D) autocorrelation function r_{ACF} could be defined as the dependence of strain stripes to the distance as:

$$r_{ACF-1D}(d) = \frac{\sum_{i=1}^{D}(S_0 - \bar{S})(S_{i+d} - \overline{S_{i+d}})}{\sqrt{\sum_{i=1}^{D}(S_i - \bar{S})^2 \sum_{i=1}^{D}(S_{i+d} - \overline{S_{i+d}})^2}} \tag{4.8}$$

The S_0 and S_d are the strain gradient at zero position and the position with a shift distance of d. The $\bar{S}$ is the mean value of the strain gradient.

Similarly, the two-dimensional (2D) autocorrelation function could also be defined for an image or a 2D array. For the array size of $m \times n$, the 2D ACF could be defined as:

$$r_{ACF-2D}(d_x, d_y) = \frac{\sum_{i=1}^{m}\sum_{i=1}^{n}(S(i,j) - \bar{S})\big(S(i + d_x, j + d_y) - \bar{S}\big)}{\sqrt{\sum_{i=1}^{m}(S(i,j) - \bar{S})^2 \sum_{i=1}^{n}\big(S(i + d_x, j + d_y) - \bar{S}\big)^2}} \qquad (4.9)$$

d_x and d_y are the movement in x and y direction. $S(i,j)$ is the strain gradient at point (i,j) and $\bar{S}$ is the mean value.

Figure 4.8 shows the 2D ACF in 100 nm × 100 nm areas that cropped from the Slice 3. Figure 4.8(a) shows the position of the selected region in Slice 3. Figure 4.8(b) shows the enlarged view of strain gradient in the a_1 direction. Correspondingly, the Figure 4.8(c) shows the 2D ACF result of this strain gradient distribution along the a_1 direction, which is pointing out of the plane. There are also weak correlations along the (011) direction, which is obvious when observing the slice view in Figure 4.8(b). The strong correlation happens along the (010) and (001) directions, which is not so obvious in the slice view. The periods of the underlying correlations along (010) and (001) are about 50 nm. The period along the (011) direction is about 70 nm. It's possible the correlations along (010) and (001) are the origin, which results in the pattern seemingly along (011) direction.

The strain gradient along a_2 is shown in Figure 4.8(d) and along the a_3 direction is shown in Figure 4.8(f). The 2D ACF for these two gradients does not show dependence in all two directions, as shown in Figure 4.8(e) and 4.8(g). Rather the gradient over a_2 shows a 50 nm correlation along the (010) direction and the gradient along a_3 shows a 65 nm correlation along the (001) direction.
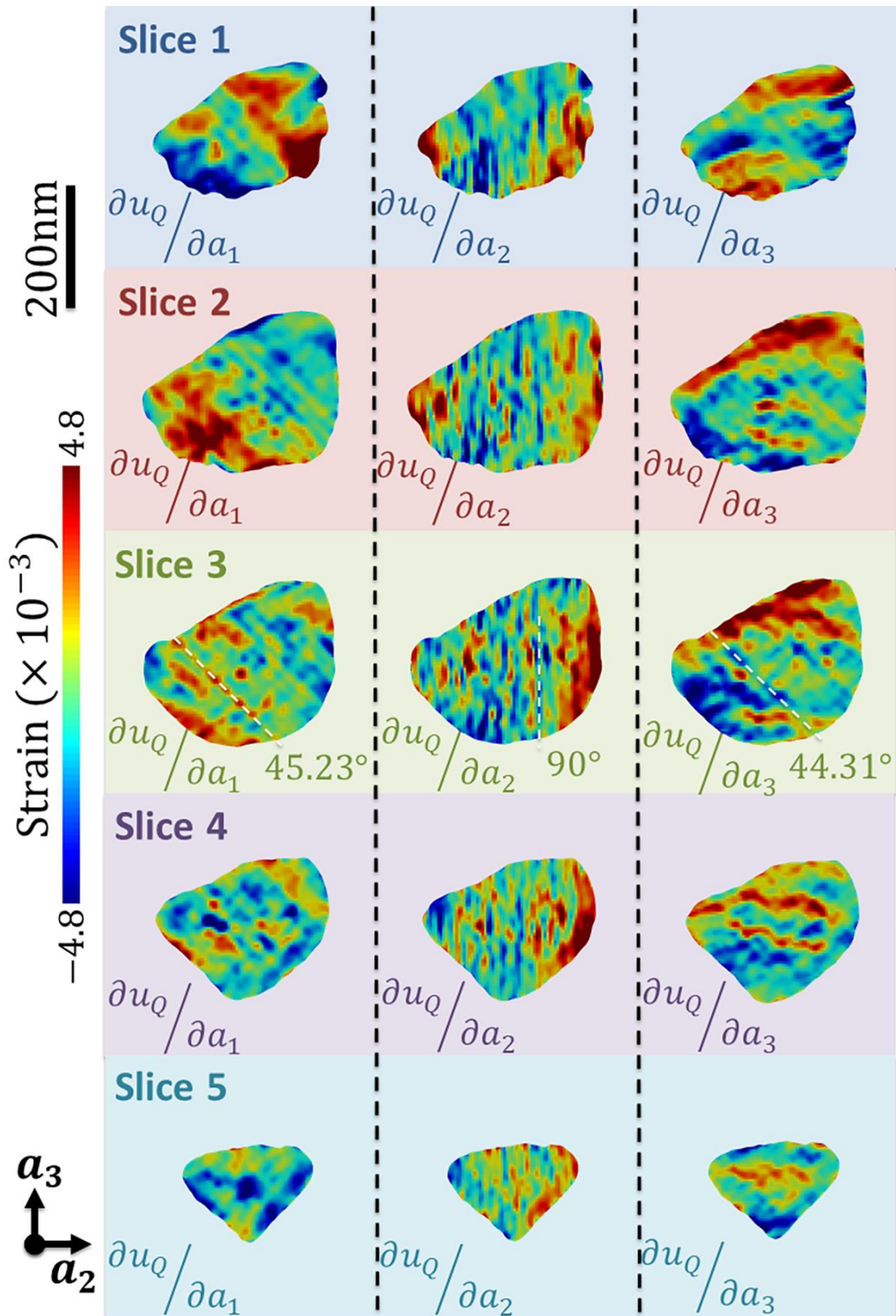
Figure 4. 7 The Slices 1-5 are presented to show the strain gradients. The images listed in the same row are from the same slice. The first column is the displacement derivatives along the a_1 direction. The second and third columns are the derivatives along the a_2 and a_3 directions, respectively.
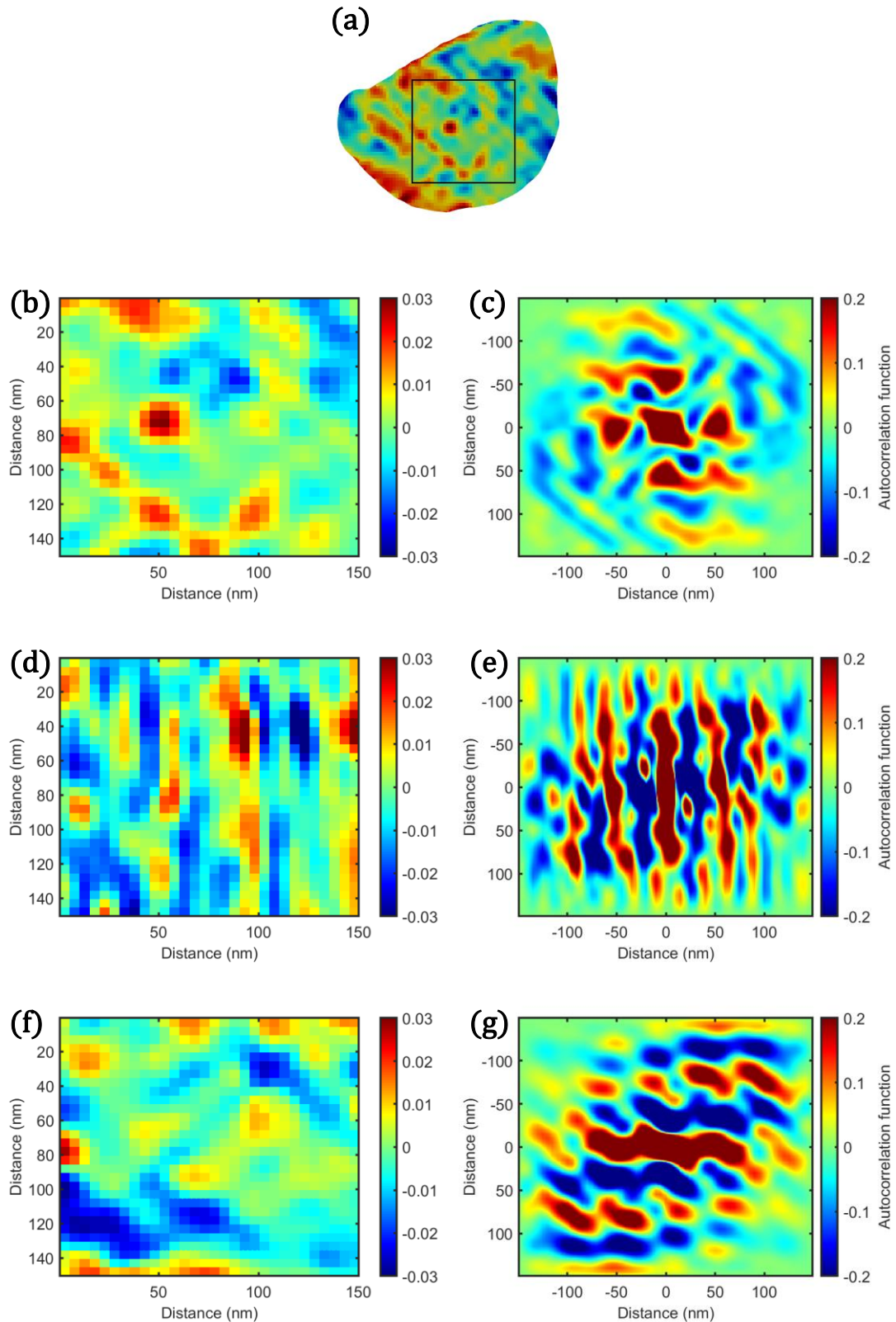
Figure 4. 8 The 2D ACF is applied to the selected region in Slice 3. (a) The $100\ nm \times 100\ nm$ region selected for the 2D ACF. (b), (d), (f) The strain gradients along the a_1, a_2 and a_3 directions. (c), (e), (g) The 2D ACF of the corresponding gradients.

Figure 4.9 shows the derivatives along three directions in Slice 6 to10. The strain stripes are roughly 48° relative to (100) direction, which is within error of 45°. Figure 4.10 shows the corresponding 2D ACF of 100 nm × 100 nm areas in Slice 8. The gradient over (100) direction has a dependence along (101) direction with a period of 30 nm. The gradient over (010) direction has correlation along (10-1) direction with a period of 90 nm. The gradient over (001) shows complex distribution in the ACF map. The strong dependence occurs at (001) and (100) directions with periods of 50 nm. There are also other correlations, but not as obvious.

Figure 4.11 shows the derivatives over three directions in Slice 11 to 15. The strain stripes are roughly 50° (also within error of 45°) relative to the (100) direction in the derivatives along the a_1 and a_3 directions, but 0° in the a_2 direction. Figure 12 presents the corresponding 2D ACF. The correlation of the gradient along a_1 is along the (100) direction and has a period of 110 nm. The correlation of the gradient along a_2 has smaller periods, which is about 50 nm along the (010) direction. The correlation for gradient over a_3 has a large period, roughly 120 nm along the (110) direction.
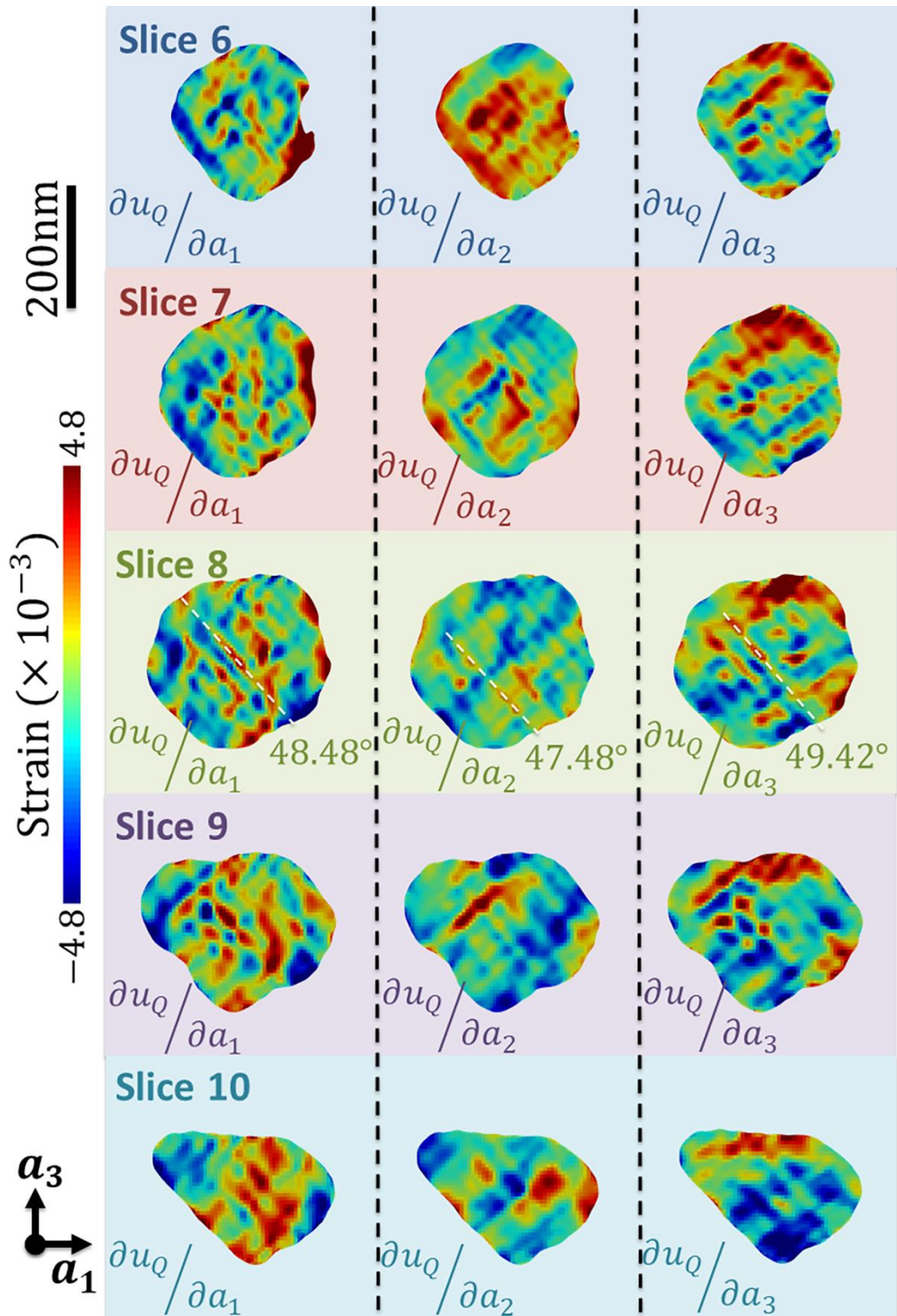
Figure 4. 9 Slices 6-10 are presented to show the strain gradients. The images listed in the same row are from the same slice. The first column are the displacement derivatives along the a_1 direction. The second and third columns are the derivatives along the a_2 and a_3 directions, respectively.

118
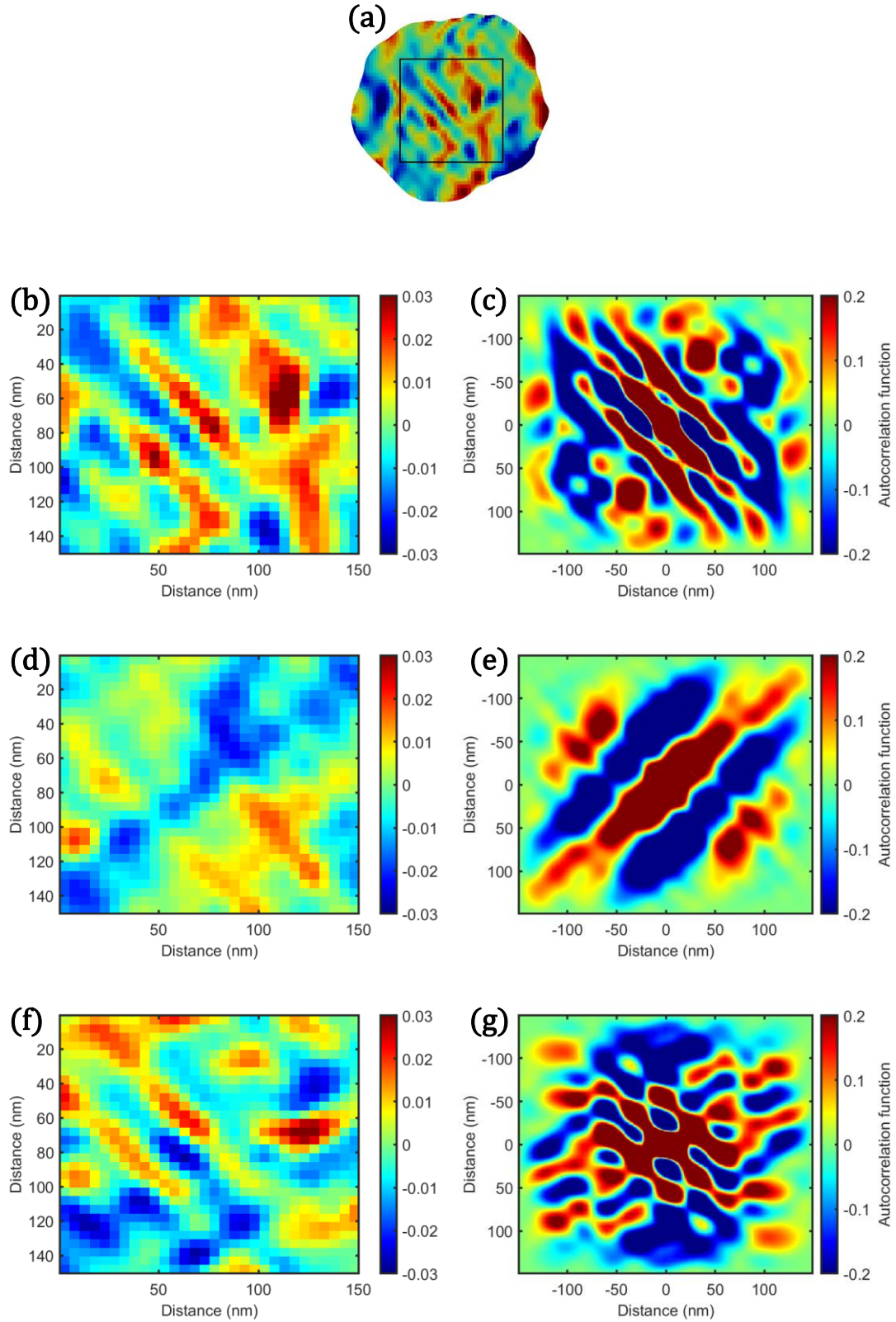
Figure 4. 10 The 2D ACF is applied to the selected region in Slice 8. (a) The $100\ nm \times 100\ nm$ region selected for the 2D ACF. (b), (d), (f) The strain gradients along a_1, a_2 and a_3 directions. (c), (e), (g) The 2D ACF of the corresponding gradients.
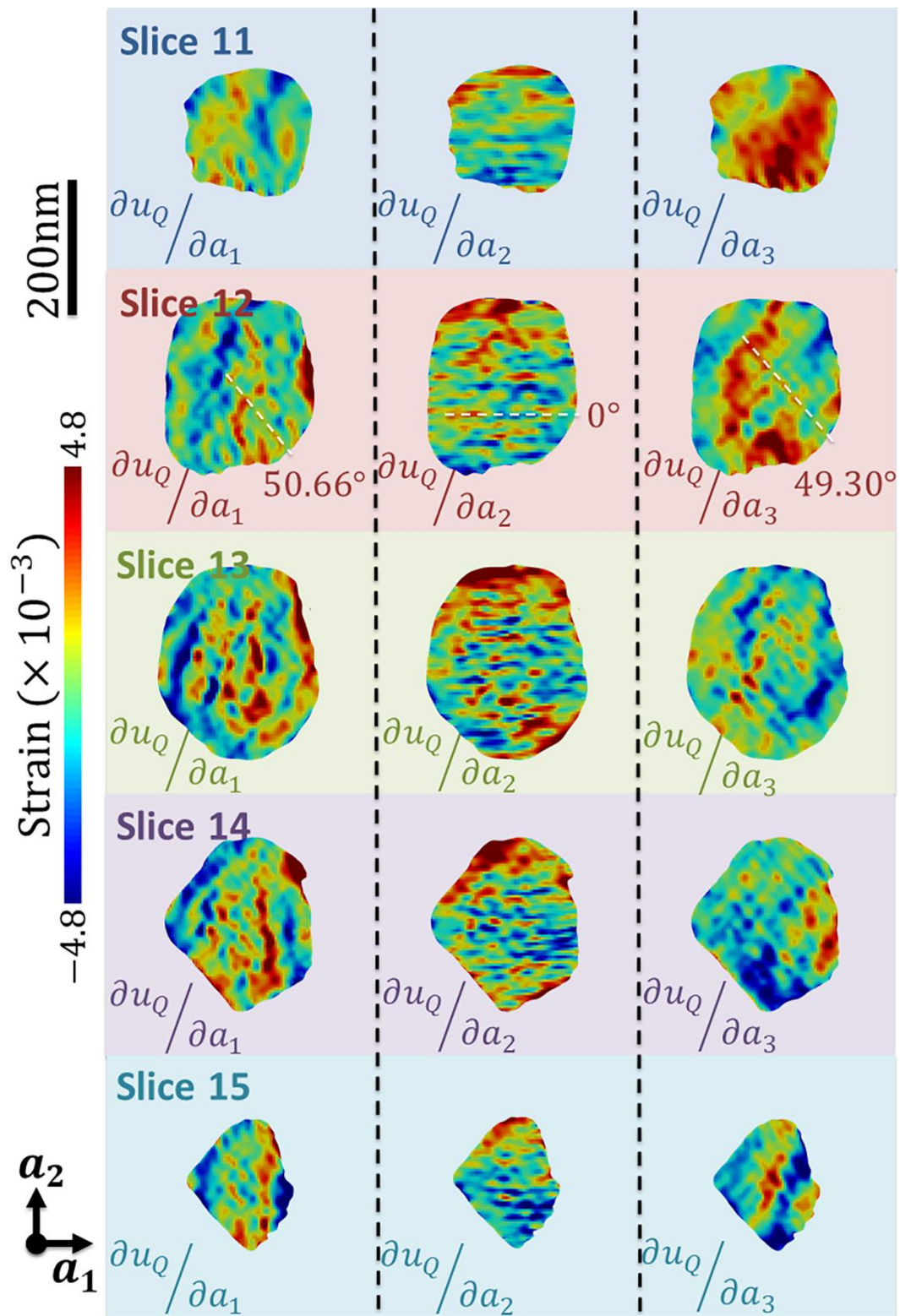
Figure 4. 11 Slices 11-15 are presented to show the strain gradients. Notations are the same as before.
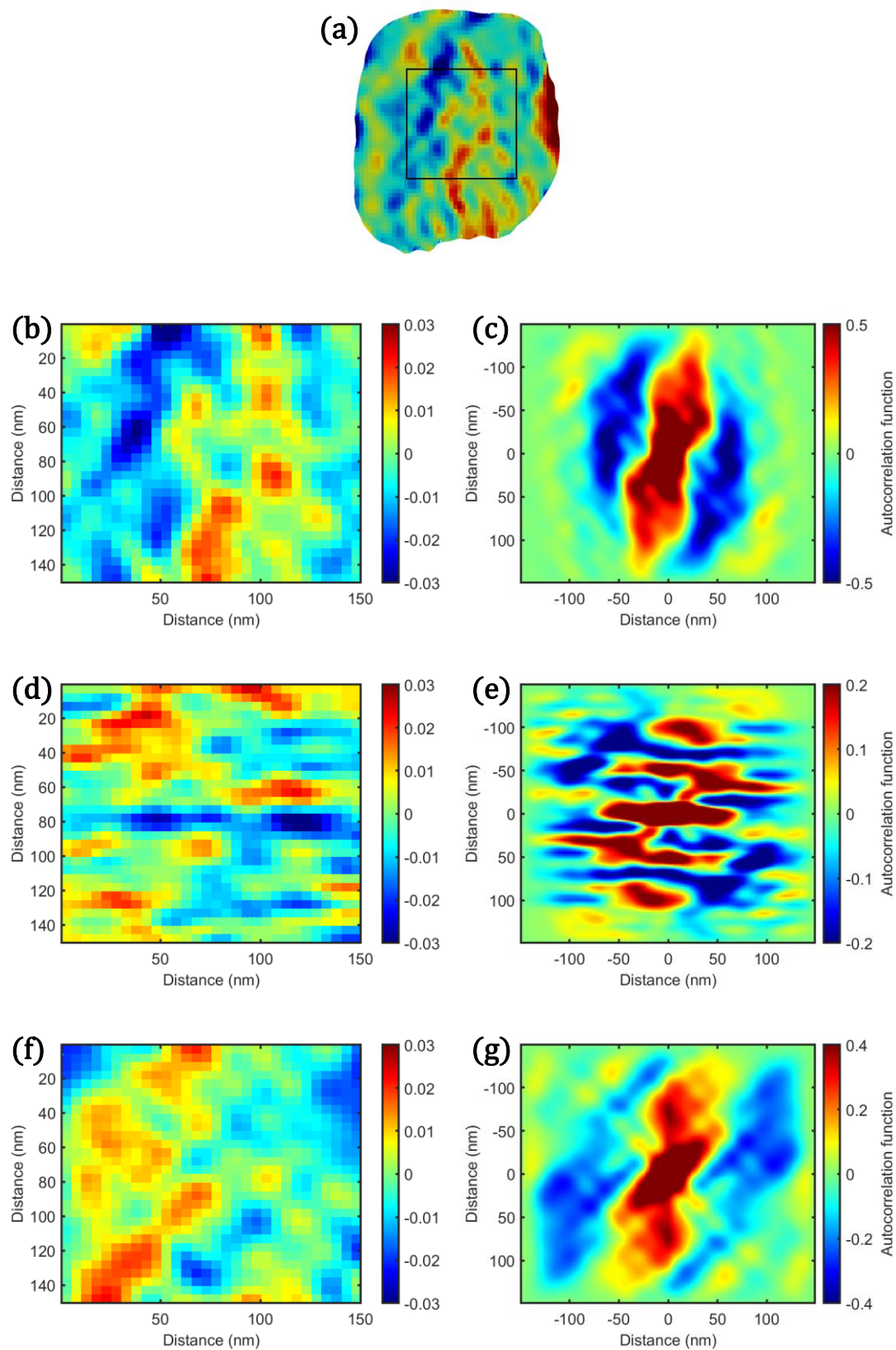
Figure 4. 12 The 2D ACF is applied to the selected region in Slice 12. Notations are as before.

The directions and periods of the strain gradients above are compiled together and shown in Table 4.7. The majority of the strain stripes are along three {100} directions and have periods of ~50 nm.

Table 4. 7 The directions and periods of strain stripes shown in Figure 8, 10 and 12. The Columns represent the periods of the strain stripes, while the rows represent their directions.

	~30 nm	~50 nm	65~70 nm	90~120 nm
(100)		$\left(\dfrac{\partial u_Q}{\partial a_3}\right)_{a_1 a_3}$		$\left(\dfrac{\partial u_Q}{\partial a_1}\right)_{a_1 a_2}$
(010)		$\left(\dfrac{\partial u_Q}{\partial a_1}\right)_{a_2 a_3}; \left(\dfrac{\partial u_Q}{\partial a_2}\right)_{a_2 a_3}; \left(\dfrac{\partial u_Q}{\partial a_2}\right)_{a_1 a_2}$		
(001)		$\left(\dfrac{\partial u_Q}{\partial a_1}\right)_{a_2 a_3}; \left(\dfrac{\partial u_Q}{\partial a_3}\right)_{a_1 a_3}$	$\left(\dfrac{\partial u_Q}{\partial a_3}\right)_{a_2 a_3}$	
(110)				$\left(\dfrac{\partial u_Q}{\partial a_3}\right)_{a_1 a_2}$
(101)	$\left(\dfrac{\partial u_Q}{\partial a_1}\right)_{a_1 a_3}$			
(10-1)				$\left(\dfrac{\partial u_Q}{\partial a_2}\right)_{a_1 a_3}$

We interpret the strain stripes in Figure 4.7 to Figure 4.12 as polar domains or polar nanoregions (PNR). The idea of PNRs is well-documented in relaxor ferroelectrics, where different models using PNRs have successfully explained the characteristic frequency-dependent properties of the relaxors [156, 166, 199]. The definitions of PNRs are diverse for different systems and treated on a case-to-case basis. For example, PNRs are defined in paraelectric $SrTiO_3$ (STO) thin films to be the small regions with local polarization which are observed by high angle annular dark field scanning transmission electron microscopy (HAADF-STEM) [107]. We propose the PNRs in this work are the small regions with tens of nanometers in size and have {100} local polarizations, which is the direction of inner boundaries we see most often in the experiment.

4.3 BTO local structure by total scattering

There are different scientific languages to explain the origin of the electric polarizations, such as the change of Wannier function of the occupied band in quantum mechanics [200]. In the viewpoint of crystallography, the polarization involves the displacement of barium and titanium cation relative to the oxygen. For barium titanate, with a tolerance factor is 1.06, the titanium cation is the "loose" ion which has more space to move around in its oxygen octahedron. Therefore, the movement of titanium can be used to characterize the polarization in the unit cell level. Although both displacive and order-disorder features are observed in BTO, in either case, the displacement direction of the titanium cation from the centre of a unit cell reflects the symmetry breaking from cubic structure. The tetragonal lattice supports 001 displacement of the titanium cation, while the orthorhombic and rhombohedral lattices have 110 and 111 additional displacements, respectively.

The preparation methods of BTO have great impact on the final properties. For example, BTO nanocrystals with global structures of pure cubic, pure tetragonal or a mixture of cubic and tetragonal structure at room temperature could be made by changing the synthesis temperatures and solutions in hydrothermal synthesis [201-204]. Another complexity is the global structure could be very different to the local structure. The BTO samples with tetragonal and cubic global structures were found to have rhombohedral local structures [172, 173, 205]. The BTO samples synthesized in our lab in Brookhaven National Lab have tetragonal local structures, though the global structure is cubic.

To identify the global and local structures of the commercial BTO samples used in this work, total scattering experiments were done at APS 11-BM. Figure 4.13a shows the scattering data of these BTO samples. The clear and sharp (101) and (110) peaks confirm the global structure to be tetragonal. The d-spacing of the two Bragg reflections could be derived from the data to be $d_{110} = 2.8244$ Å and $d_{101} = 2.8390$ Å. This corresponds to the lattice constant of $a = 3.9943$ Å and $c = 4.0354$ Å, which gives a tetragonality of 1.0103. Figure 4.13b shows the temperature dependence of the lattice parameters in BTO nanocrystals. When increasing the temperature, the lattice constant a and c becomes close. Also, the

transition temperature for our commercial sample is well above 400 K, while the transition of bulk BTO crystal happens around 393 K.
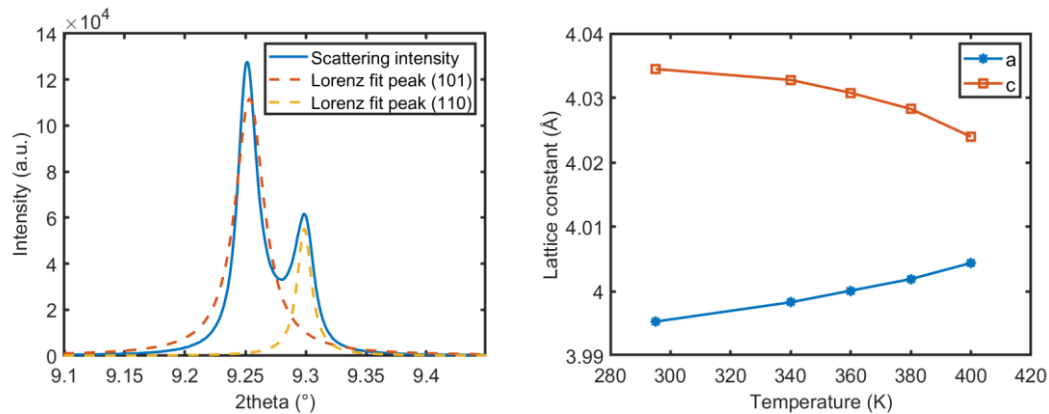
Figure 4. 13 X-ray diffraction data from BTO commercial samples measured at APS 11-BM. The X-ray wavelength is 0.4579Å.

As discussed in Chapter 1, from the total scattering structure function $S(Q)$, the reduced structure function $F(Q)$ can be derived. Then the reduced structure function can be transformed into real space to get the pair distribution function (PDF), G(r), which is similar to the radial distribution function, $R(r)$, in giving the average probabilities of finding atoms at certain radius from the atom central position. It has the ability to probe the averaged local structure by identifying the nearby atom neighbour distances.

The scattering data from the commercial BTO samples were fitted by four possible BTO crystal structures: cubic (Pm$\bar{3}$m), tetragonal (P4mm), orthorhombic (Amm2) and rhombohedral (R3m) in collaboration with Emil Bozin at Brookhaven National Lab. The fittings of the four models in short range, from 0Å to 11 Å, are given in Figure 4.14(a). The best fitting results are given by tetragonal P4mm model and orthorhombic Amm2 models, both gives an error of 9.7%. The P4mm model is more symmetric than Amm2 model, so the Amm2 model has more degrees of freedom (variables in the fit). The same error value indicates the extra variables of Amm2 model is actually not needed, so it degrades to the tetragonal model. The other two models give relatively large error. The cubic Pm$\bar{3}$m has an error of 14% and rhombohedral has an error of 16%.
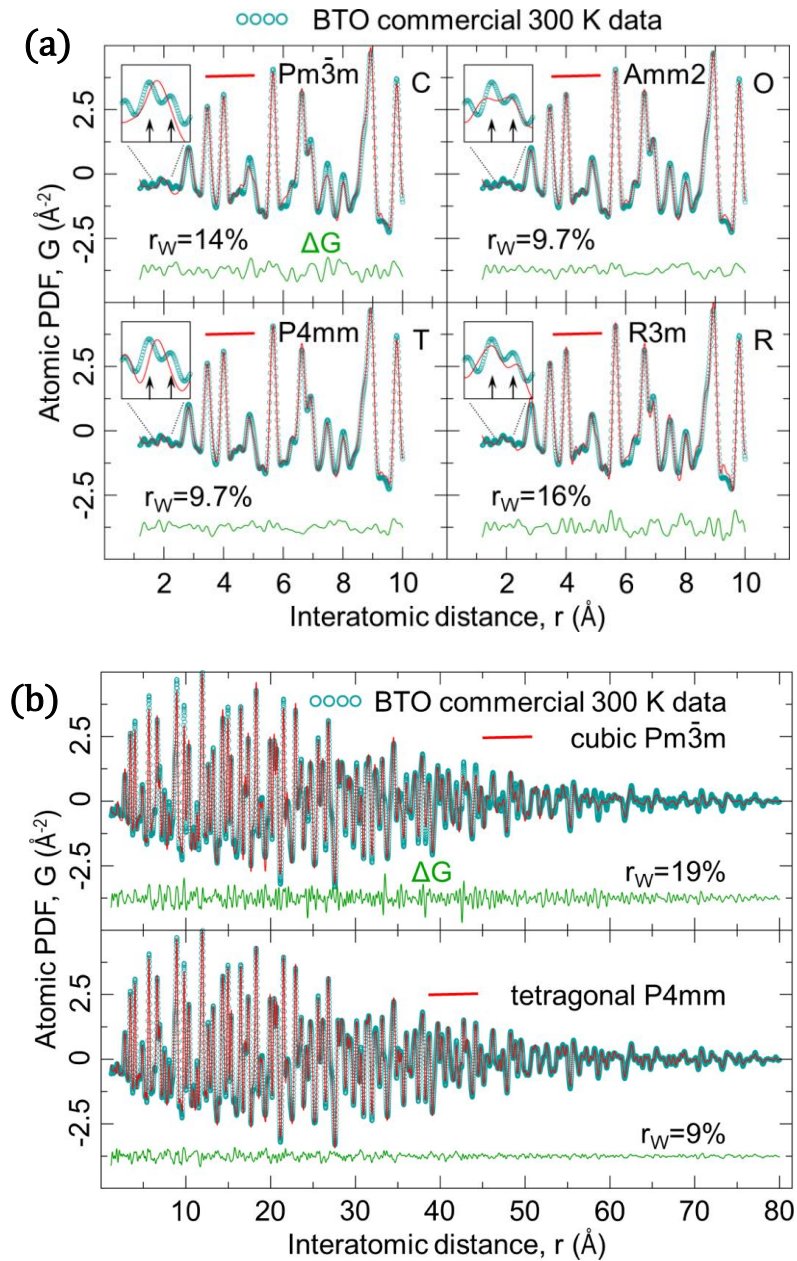
Figure 4. 14 The X-ray pair distribution function (PDF) of the same powder sample of BTO used throughout this work. The data were collected at the XPD beamline of NSLS-II. (a) The short-range fitting of the PDF using four crystal structures: cubic (Pm$\bar{3}$m), tetragonal (P4mm), orthorhombic (Amm2) and rhombohedral (R3m). (b) The long-range fitting of the scattering data using two crystal structures: cubic (Pm$\bar{3}$m), tetragonal (P4mm).

Figure 4.14(b) shows the fitting of the experimental scattering data to P4mm and Pm$\bar{3}$m model in the long range, from 0 Å to 80 Å. The tetragonal P4mm model gives an error of 9%, while the cubic Pm$\bar{3}$m gives an error of 19%. Both the short range and long-range fitting show that the local structure of commercial BTO samples is lower symmetry than cubic. The data are consistent

with the tetragonal structure identified by the (110)/(101) peak-splitting seen in Fig 4.13.

For the commercial samples in use for this study, both the global and local structures are confirmed to be tetragonal at room temperature. As discussed above, the BTO properties are sensitive to the preparation methods. In separate work, we have investigated other preparation methods and found cubic long-range structure, different from the commercial BTO nanocrystals studied here, while the local structure appears to be always low-symmetry, consistent with tetragonal [206].

In summary, ex-situ BCDI and X-ray pair distribution function experiments have been performed on BTO nanocrystals. Strain-stripe networks were found to distributed all over the crystal. The most common appearance of the strain stripes is along {100} directions with a period of 50 nm. Both the global and local structures of BTO samples were confirmed to be tetragonal.

Regarding the three hypotheses put forward in the beginning of this Chapter, the existence of BTO strain stripes overrules the idea of there being a single polarized domain all over the crystal. The idea of small, polarized domains is favoured by the results instead. The exact type and arrangement of domains causing the stripes, like whether they are 90° or 180° domains, cannot be exactly distinguished, but motivates the modelling study presented in chapter 6.

Chapter 5. Strain stripes network behaviour in barium titanate nanocrystals when crossing phase transition

To further explore the nature of the strain stripes reported in Chapter 4, *in-situ* Bragg coherent x-ray diffraction imaging (BCDI) experiments were performed on the selected barium titanate (BTO) crystals with ramping up temperatures at the European Synchrotron Radiation Facility (ESRF). Crystals were selected with facets and good fringes as good candidates and then heated up *in-situ* to cross the tetragonal-cubic phase transition.

There were two basic goals when designing the experiment. The first goal was to repeat the strain stripes results that was observed in the crystal studied in Chapter 4 to check its reproducibility. The second one was to track the behaviour of those strain stripes across the tetragonal-cubic phase transition. Prior to performing the experiments, several hypotheses were made:

(a) If the strain stripes exist at low temperature in the tetragonal phase but disappear after crossing the phase transition to cubic phase, it indicates the strain stripes are originated from the tetragonal lattice. Particularly, the strain stripes could be the domain walls in tetragonal phase, where the 90° and 180° domain walls are prevalent.

(b) If the strain stripes exist at low temperature and preserve after crossing the phase transition, then it indicates the origin of those strain stripes might not be directly linked to the global tetragonal phase. There could be some other local structure that forms the domain walls at high temperature even though the global structure is cubic.

(c) A third possibility would be that the strain stripes don't exist at low temperature initially, but only appear after heating across the phase transition and might be preserved when returning back to low temperature. Then it might indicate the annealing process play a big role in forming those strain stripes network.

With clear assumptions in mind, the *in-situ* BCDI experiments were performed at ESRF ID-01 beamline.

Contribution statement: Jiecheng and Ian designed the experiment. Jiecheng, Ian, Edoardo, Steven, Ana, Longlong have helped with the BCDI experiment. Jiecheng wrote the manuscript with the help of Ian.

5.1 Experimental details

The commercial samples were first suspended in a tetraethyl orthosilicate (TEOS) and ethanol solution with a volume ratio of 1:75. The mixed solution has then been dropped from a pipette onto a silicon wafer and heated up to 973 K for 2h in air. This drop-casting procedure followed by calcining proves to be useful for fixing nanocrystals, which were illuminated by the nano-focused X-ray beam [207]. The crystals of interest are the ones with nice crystalline facets. These would show up whenever the diffraction patterns show clear direction flares coming out of the central diffraction spots. To minimize the effort of tracking crystals upon subsequent heating, the samples were heated directly to 100℃ and kept at this temperature for searching for interesting crystals.

Instead of using video live views to search for crystals, which is the routine in beamlines APS 34-ID-C and DLS I13-1, we used the well-developed K-map tool available at ESRF ID-01. The users would define different ROIs on the detector, which are shown as the red boxes in Figure 5.1. Then a detailed spatial mapping of the sample could be carried out. For example, if the beam size is 2 μm × 2 μm, then a 2 μm step size could be used when scanning across the sample position. Whenever there is diffracted intensity coming into the ROI, the sum of the intensity was recorded and shown in the final K-map, schematically shown in Fig 5.1 as the red and yellow pixels in the four cubic mesh grids. If the incident angle is set to be low, the X-ray footprint would be large. Then the 200nm BTO crystals would not show up as just one pixel, but rather appearing in a few pixels of the K-map because of the elongated X-ray beam. After the sample mapping, the user would be able to revisit only the "hot pixels" for higher signal position, where mostly likely there are bright crystals or a strong powder ring.
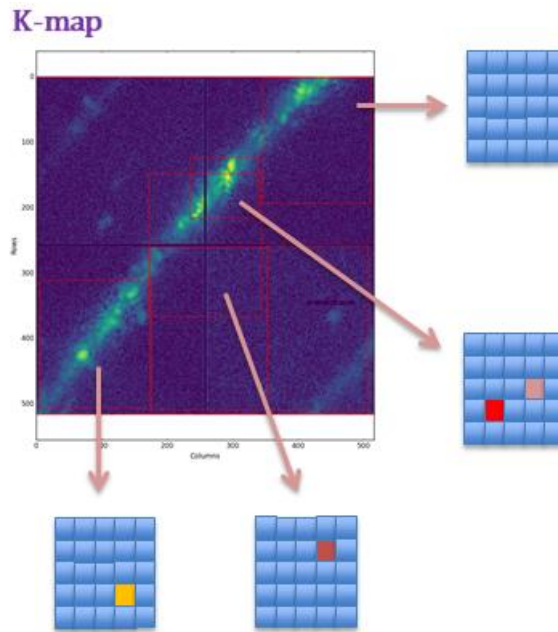
Figure 5. 1 The schematic drawing shows the K-map method, which is used at ESRF ID01 beamline. The red boxes are the ROIs chosen. After the sample mesh scan, each ROI would appear as an intensity in the pixel map as shown.

During the experiment, four crystals with facets were selected and tracked upon heating and cooling. Among the four crystals, two crystals (Crystal A and B) had good diffraction fringes and were studied in detail in this Chapter. The selected crystals have then been tracked while heating in 5 K steps to 433 K, which is well above the BTO tetragonal-cubic phase transition temperature. The crystals were then cooled down with the same 5 K steps. At each temperature step during heating and cooling, the BCDI measurements were carried out. To make sure the centre of the crystals is preserved, alignment scans were carried out before each BCDI measurement.

ID01 furnace is used for the heating. It is a resistive heater, with the heating element being in contact with an alumina crucible, on top of which the sample is pasted. It has two thermocouples, one inside the bulk of the crucible and an external one which is then attached as close as possible to the sample. The output of the first thermocouple is feeded into a PID controller (Eurotherm) that regulates the power applied to the heater. The output of the second thermocouple is instead what is read by the beamline computer and hence what you get in the data. The furnace's PID parameters are calibrated using this

second external thermocouple, based on the environment in which it is to be used (air, nitrogen, ...), prior to every experiment.

The X-ray energy was set to be 10.35 KeV, which corresponds to a wavelength of 1.1979 Å. For the BTO commercial samples at room temperature, the (110) powder ring sits at 24.51° and the (101) powder ring locates at 24.39°. When heated up, the a and c lattice constant of BTO would become closer, and so would the angles of the (110) and (101) powder rings. The two-dimensional (2D) Maxipix detector was placed 0.546 m away from the sample stage with a pixel size of 55 μm. The scanning step (dth) of the rocking curve scan was chosen to match the crystal size. For a typical 300 nm BTO crystal, a scanning step size of 0.02° was chosen. The determination of step size was adjusted by the sample size and the detector distance. To ensure a sufficient sampling, we make sure the fringes are more than 2 pixels in size. For X and Y direction, this can be directly seen on the detector. If the fringes are smaller than 2 detector pixels (55um×2), then we would increase the sample detector distance. This works the same for θ direction, but instead, we make sure the fringes are changing smoothly rather than appear and disappear in the next two frames.

Once the diffraction patterns were recorded, data processing steps were carried out to exploit the underlying information inside the two crystals (Crystal A and B). The diffractometer geometry at ESRF ID01 is the same as APS 34-ID-C, where the delta is the detector horizontal angle and gamma the vertical one.

5.2 Diffraction patterns behaviours as a function of temperature

The diffraction patterns from the two BTO crystals were first studied in reciprocal space directly before being inverted back to the real space images.

5.2.1 Intensity variations

The change of diffraction intensity is affected by many factors, which not only includes the crystal volumes and crystal phases, but also the alignments of the crystals and the flux variations of the incident beam. In this sense, the intensity is not a very quantitative value for the analysis. There were some degrees of controls in alignment, while the crystals were being measured, and, after the temperature became stabilised, multiple alignment scans were performed. Regarding the variation of incoming X-ray beam, because each BCDI

measurement took more than 10min, the flux was not found to change a lot in such a big time-window. The maximum intensity and the total intensity of the diffraction pattern of Crystal A and B were plotted as a function of temperature in Figure 5.2.

For the total intensity plot, there is a qualitative trend for Crystal A. The crystal A has an intensity between 2×10^8 and 2.5×10^8 counts/s when heated from 373 K to 418 K, and then dropped below 1.1×10^8 counts/s at 423 K. The intensity kept between 1.0×10^8 and 1.2×10^8 counts/s when further heated to 433 K and cooling back to 373 K. For Crystal B, the total intensity has a little vibration, but there is no clear variation trend. The intensity stays between 3.6×10^7 and 4.3×10^7 counts/s through all the heating and cooling process.
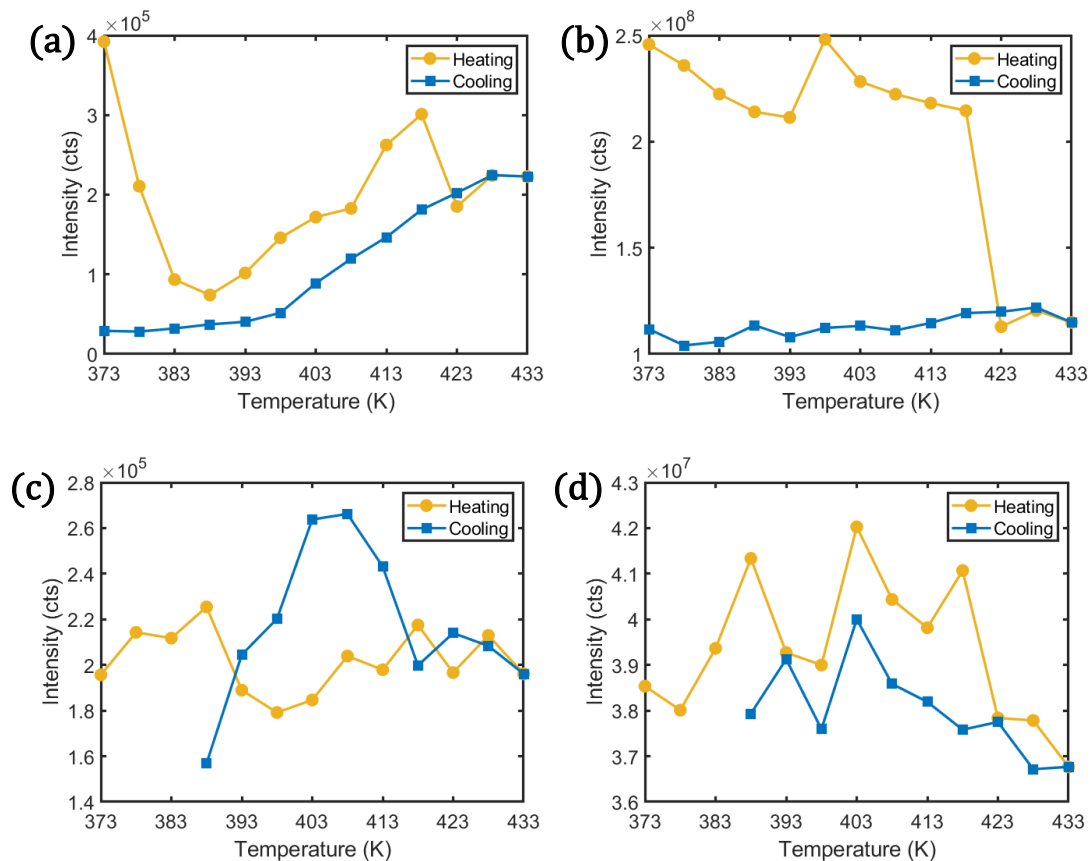
Figure 5. 2 The diffracted intensities of Crystal A and B are plotted as a function of temperature. The yellow lines with round dots show the heating period, while the blue lines with square dots present the cooling period. (a) The peak (maximum) pixel intensities from Crystal A are plotted. (b) The integrated (sum) intensities of all pixels from Crystal A are plotted. (c) The peak pixel intensities from Crystal B are plotted. (d) The integrated intensities of all pixels from Crystal B are plotted.

The sharp change of intensity in Crystal A but not crystal B could come from structural changes. One possibility would be that Crystal A goes through phase transition between 418 K and 423 K upon heating. The reason why the intensity doesn't come back when cooling down again suggesting that there may be a change of crystal structure or orientation, which is determined later in this section by the switching of crystal peak from the (101) powder ring to the (110) powder ring.

5.2.2 Rocking curve plots

Rocking curve plots, sometimes called the "mosaic spread", depict the intensity distribution, integrated across the Maxipix detector, when rotating the crystal across the Bragg condition. The full-width-half-maximum of crystal peaks in rocking curve plots could be used to determine the crystal size in one certain direction. This is, however, of less interest in this work as the crystal size does not appear to change significantly with temperature. The information of interest in this work is the shape of the rocking plots, which evaluates the uniformity of crystal structure and the degree to which it is broken into sub-domains.

The rocking curve plots of Crystal A at each temperature during the heating and cooling are shown in Figure 5.3. At some temperature points, the rocking curve scans have shapes with a single sharp peak, such as at 373 K before heating. At other temperature points, it has a jagged multiple-peak shape, as shown at 388 K upon heating. The scanning step size is 0.02° and the full-width-half-maximum of the peak is more than 0.1°, so the scanning is relative fine and has enough data points to cover the shape of the sharp peak. There is no clear explanation why at some temperatures, the peak is sharp, but at other temperatures it is not. But the possibilities could be the Crystal A is slightly unstable and rotates a bit during the theta scan. Or it could be there is structure changes happening of Crystal A during the heating.

Figure 5.4 shows the rocking curve plots of Crystal B during heating and cooling. In comparison to the variation in Crystal A, the Crystal B always keeps a sharp peak shape at all temperatures.
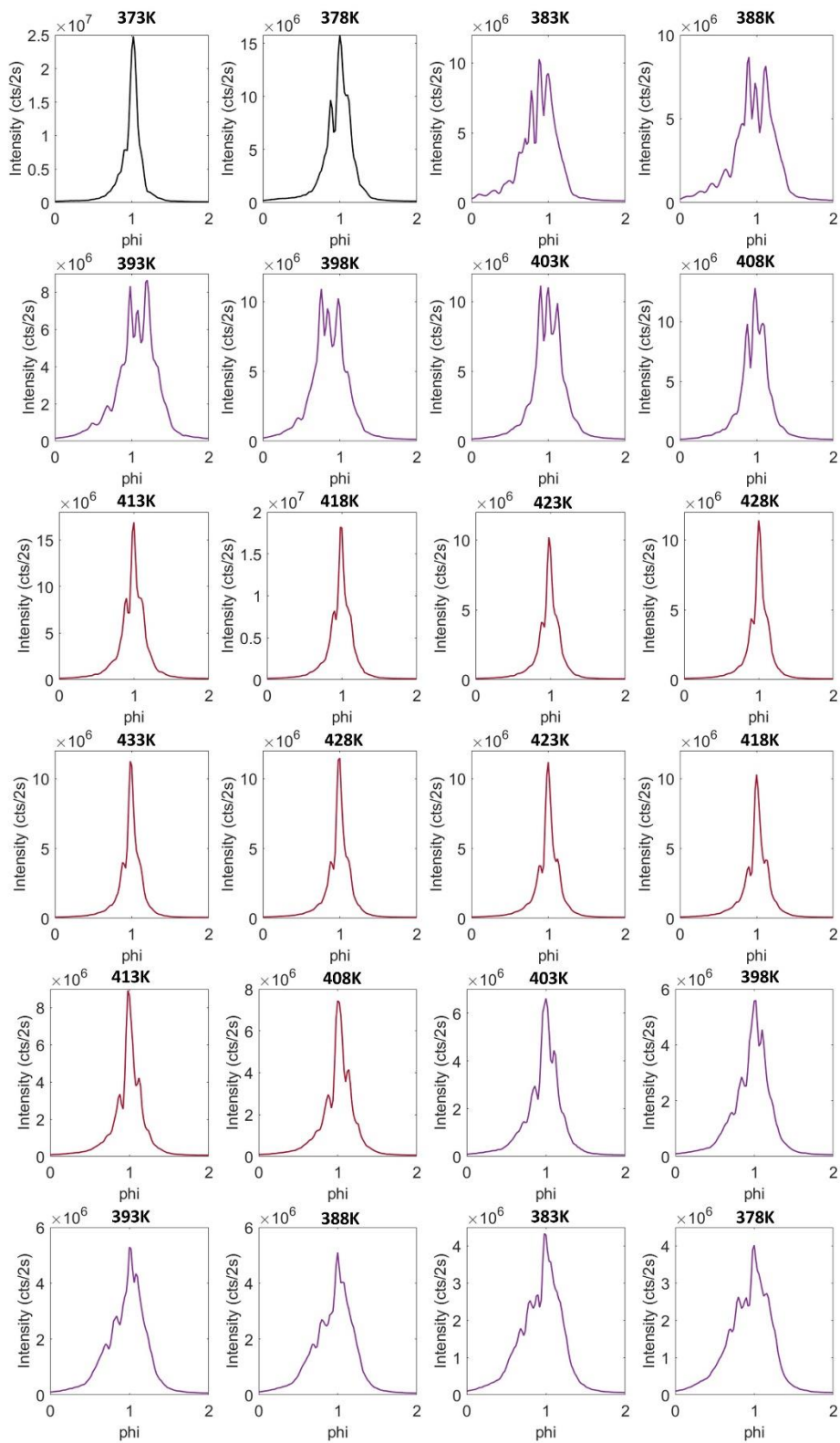
Figure 5. 3 The rocking curve plots of Crystal A are presented at different temperatures. The plots in yellow cover the heating range from 373 K to 428 K. The plot in red shows the highest temperature at 433 K. The plots in blue record the cooling range from 428 K to 378 K.
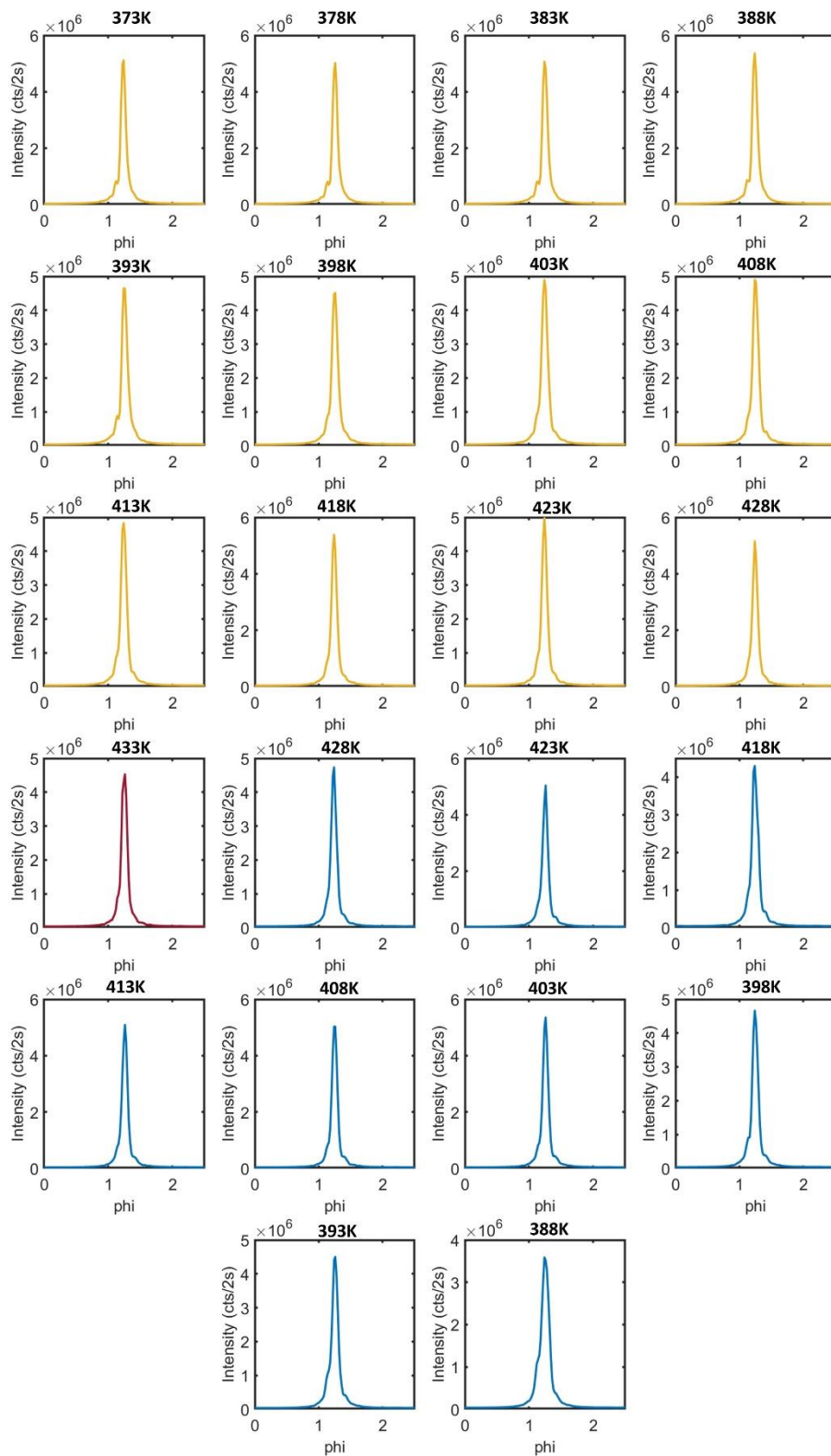
Figure 5. 4 The rocking curve plots of Crystal B are presented at different temperatures. The plots in yellow cover the heating range from 373 K to 428 K. The plot in red shows the highest temperature at 433 K. The plots in blue record the cooling range from 428 K to 388 K.

5.2.3 Central diffraction patterns

The two crystal diffraction patterns were being tracked all through the heating and cooling. The central slices of the diffraction patterns were plotted and shown in Figure 5.5 and Figure 5.6.

Figure 5.5 presents the central slices of Crystal A. The origin of reciprocal space (delta and gamma angles both zero) is at the bottom-right and increasing Bragg angle runs from the bottom-right corner of the detector to the top-left. The yellow and red dash lines are guides for the eyes, which are the powder ring directions of the (101) and (110) peaks of this crystal at 373 K. Multiple fringes with good visibility could be seen around the central spot, indicating the high quality of both datasets. One directional flare could be seen that coming from the left of the central spot, indicating the existence of one big facet. The flare extends from the (101) ring position all the way to the (110) ring, which suggests there may be a mixture of tetragonal domain orientations within the sample. Upon heating Crystal A from 373 K to 433 K, the diffraction patterns started from a base position and kept moving to the left of the detector when heating up. While cooling down, the diffraction pattern didn't move back. Instead, it kept moving to the left of the detector. The starting and the ending position of the central Bragg peak are indicated as the yellow and red dash lines in Figure 5.5.

This movement to the left could be understood as the Crystal A lattice satisfying the (101) diffraction initially. When it heated up, it goes through phase transition to cubic phase. When cooling back to tetragonal phase again, the c-axis doesn't appear in the previous crystallographic direction, rather becoming one of the previous a-axis directions. Therefore, under the Bragg diffraction geometry, the pattern is seen to migrate from the (101) powder ring to the (110) ring during the heating/cooling cycle.
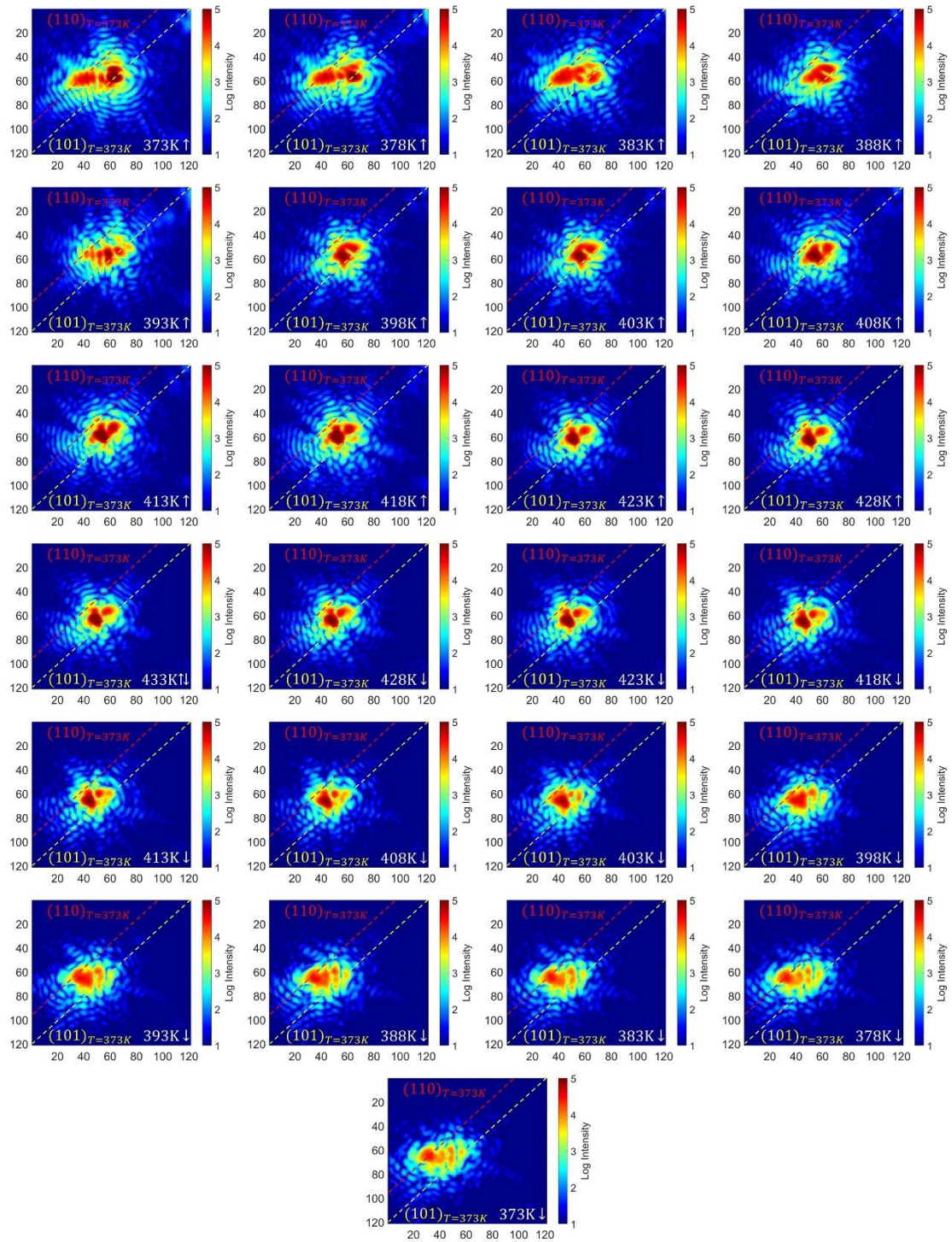
Figure 5. 5 The central diffraction patterns of crystal A are presented as a function of temperature. The yellow and red dash lines are the (101) and (110) powder ring directions given by the detector δ and γ angles. The central position of Crystal A's diffraction pattern at 373 K before heating up starts at the radius of the yellow dash line. But its central position moves over to the red dash line at 373 K after cooling down.
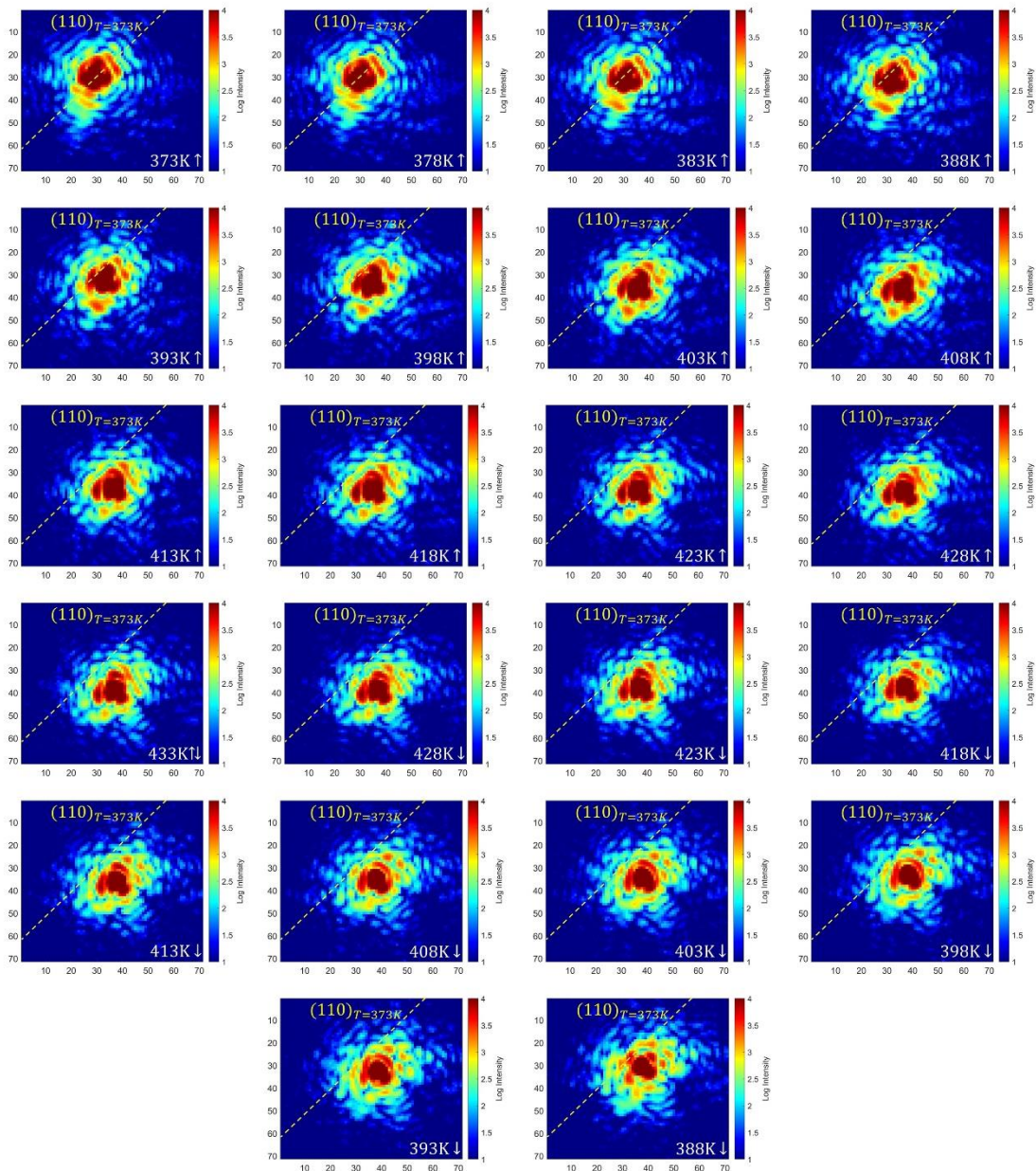
Figure 5. 6 The central diffraction patterns of the crystal B at different temperature are presented. The yellow dash line stays at the central position of Crystal B diffraction pattern at 373 K before heating up. The dash line is assigned to the (110) powder ring indices, based on the behaviour of the pattern through heating and cooling.

Figure 5.6 shows the central slices of Crystal B. The diffraction patterns are on the top-left panel of the detector. The powder ring passing through the central position is indicated by the yellow dash line. Upon heating up, the diffraction pattern is seen to move to the right on the detector and reached the farthest position at 433 K. During cooling down, the pattern continuously moves back to the original powder ring direction. Based on the fact that the tetragonal (110)

powder ring is outboard (larger Q) and (101) powder ring is inboard, the yellow dash line is considered to be the (110) powder ring of Crystal B at 373 K. Contrary to Crystal A, which switched the powder ring after crossing phase transition, the peak of Crystal B did move back towards the original powder ring position.

5.2.4 Lattice constant variations

In the powder X-ray diffraction experiment, the averaged lattice d-spacing could be calculated through the averaged peak position. The same information could be derived from the BCDI experiment as well. By calculating the angle of centre of mass (COM) of the single diffraction pattern, the d-spacing of the single crystal could be determined. The angle of the COM of the diffraction pattern contains two parts: one is the detector angle, the other one is the angle from Bragg peak to the calibrated Beam Zero position on the detector. One general procedure to calculate the d-spacing of single crystal is given below:

(a) Reading the detector δ and γ angle at each temperature step.

(b) Calculating the $\boldsymbol{Q_{xy}}$ vector on the detector plane by:

$$\boldsymbol{Q_{xy}} = (\sin \delta \cos \gamma , \sin \gamma) \tag{5.1}$$

(c) Calculating the distance of Bragg peak to the Beam Zero. Beam Zero is the point where the X-ray beam hits at when the detector is set to 0° angle. Then calculating the projection of this distance onto the $\boldsymbol{Q_{xy}}$ vector by:

$$d = \frac{\Delta \boldsymbol{p} \cdot \boldsymbol{Q_{xy}}}{|\boldsymbol{Q_{xy}}|} = \frac{(p_x - p_{x0}) \cdot \sin \delta \cos \gamma + (p_y - p_{y0}) \cdot \sin \gamma}{\sqrt{(\sin \delta \cos \gamma)^2 + (\sin \gamma)^2}} \tag{5.2}$$

This is schematically showing in Figure 5.7a.

(d) Calculating the extra horizontal and vertical angle caused by the Bragg peak position on the detector relative to the Beam Zero position:

$$\gamma_+ = \frac{d \cdot Q_y}{|\boldsymbol{Q_{xy}}|} = \frac{(p_x - p_{x0}) \cdot \sin \delta \cos \gamma + (p_y - p_{y0}) \cdot \sin \gamma}{(\sin \delta \cos \gamma)^2 + (\sin \gamma)^2} \sin \gamma \tag{5.3}$$

$$\delta_+ = \frac{d \cdot Q_x}{|\boldsymbol{Q_{xy}}|} = \frac{(p_x - p_{x0}) \cdot \sin \delta \cos \gamma + (p_y - p_{y0}) \cdot \sin \gamma}{(\sin \delta \cos \gamma)^2 + (\sin \gamma)^2} \sin \delta \cos \gamma \tag{5.4}$$

This is presented in Figure 5.7b.

(e) Calculating the 2θ angle and then the d-spacing of the diffracting crystal planes.

$$2\theta = \cos^{-1}(\cos(\delta + \delta_+) \cdot \cos(\gamma + \gamma_+)) \tag{5.5}$$

$$d_{hkl} = \frac{\lambda}{2\sin\theta} \tag{5.6}$$
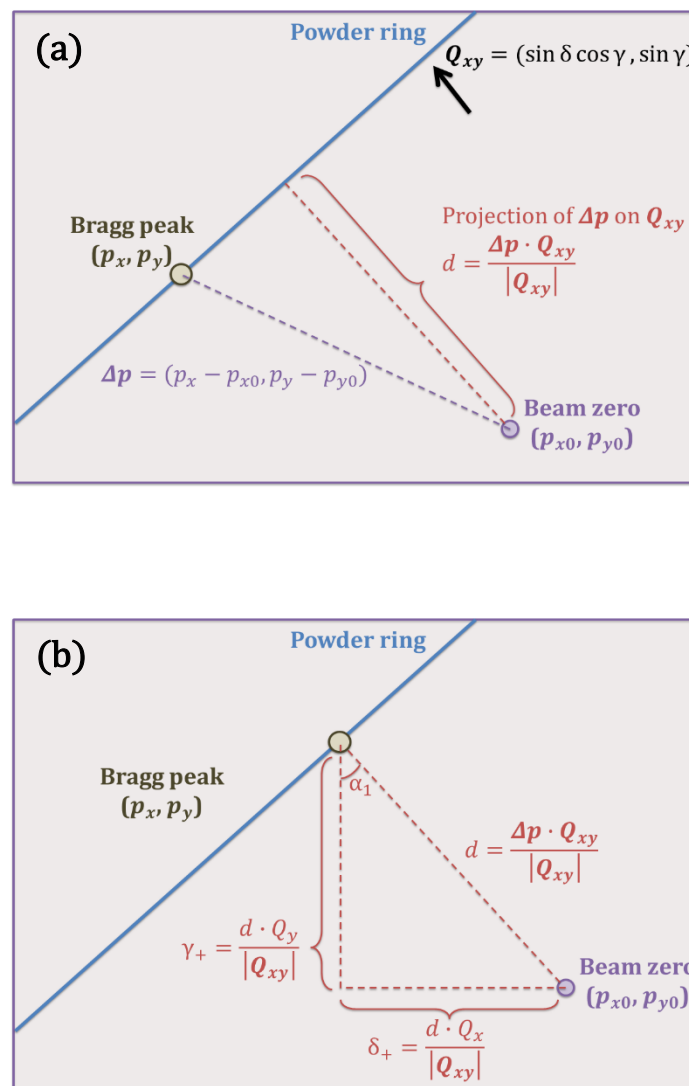
Figure 5. 7 The illustrations show the calculation of the d-spacing of the single crystal from the position of the peak on the detector.

Through the procedure above, the d-spacing of the diffracted plane in Crystal A and B were calculated for all temperatures, as shown in Figure 5.8.
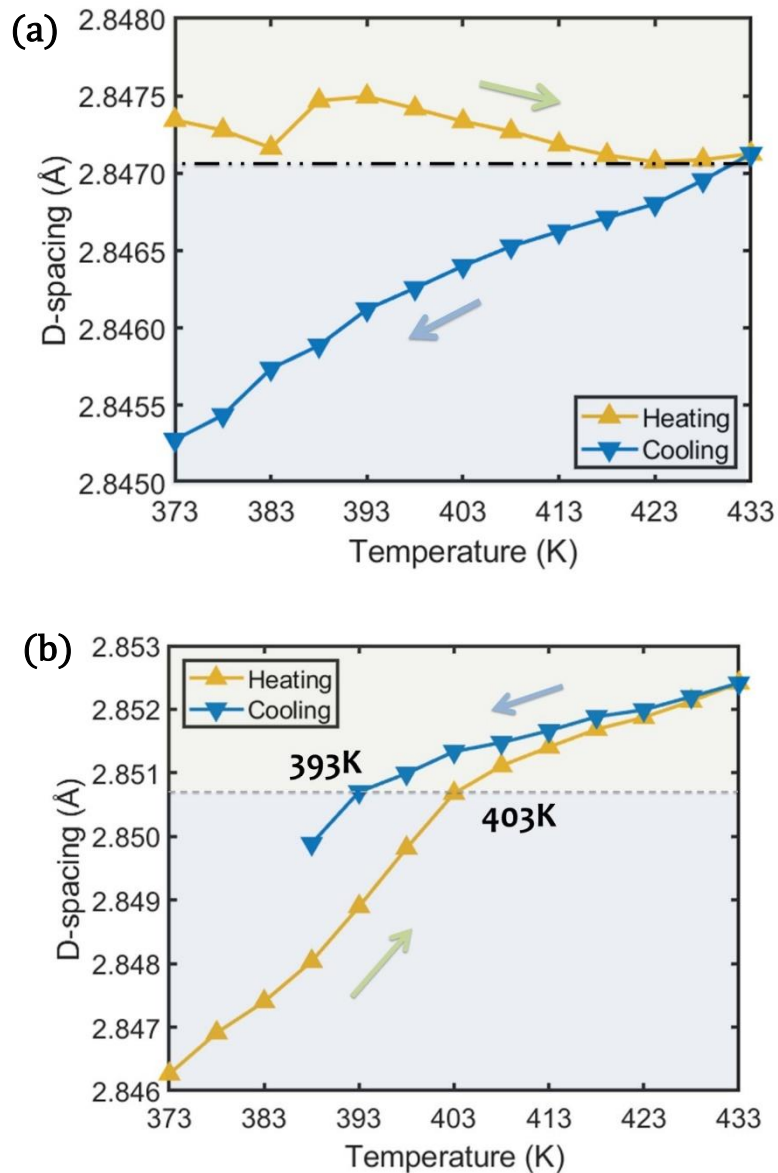
Figure 5. 8 The d-spacing variations of Crystal A and Crystal B during heating and cooling are presented in (a) and (b). It should be noted that the lattice constant change in Crystal A is smaller than Crystal B.

For Crystal A, the d-spacing of the diffracted crystal plane decreased a bit when heated from 373 K to 383 K. There was a jump in d-spacing from 383 K to 388 K, which is not well understood. After 393 K, the d-spacing was linearly decreased until 423 K, after which the d-spacing went up again at a much smaller slope. The turning point 423 K is considered to be near the phase transition temperature, so the negative slope before 423 K is caused by a decrease of tetragonality, while the positive slope after 423 K is the thermal expansion of the cubic lattice. When

cooling down from 433 K to 373 K°C, the d-spacing of Crystal A went down linearly.

For Crystal B, the d-spacing increased linearly at a sharp slope when heated from 373 K to 403 K. After 403 K, the d-spacing was still increasing, but at a much smaller slope. Therefore, the phase transition is considered to happen around the turning point 403 K. When cooling down from 433 K, the d-spacing decreased at a small slope. The turning point, indicating the phase transition, appears to be at 393 K. This transition temperature is about 10 K lower than the transition temperature during the heating, noting that the temperature resolution is about 5 K. Ferroelectric perovskites commonly have hysteresis [208]. The temperature delay of phase transition could be explained by a kinetic barrier, with extra energy needed for arranging the domain structure when going into tetragonal phase.

There may be a few factors that contributing to the error. From the Eq. (5.6) we can see the resolution of wavelength λ and angle θ would matter.

The energy resolution from the double silicon (111) crystal monochromator is 1.3×10^{-4}.

The angle is influenced by the detector pixel size. We are calculating the centre of mass (COM) of the diffraction pattern rather than finding the brightest pixel. Therefore, our resolution should be finer than the pixel size. If taking one pixel as the limiting resolution, the resolution is 0.0058 deg. When approaching to minimum, sinx is approaching to x, so we can take 0.0058 as the resolution.

Combining these two factors together, the propagated error is

$\sqrt{(1.3 \times 10^{-4})^2 + (\frac{0.0058}{\theta})^2}$. For a typical theta equals to 24.4°, the error is 0.0027.

5.3 Strain stripes behaviours over temperatures in reconstructed crystals images

After learning the behaviour of the diffraction pattern directly in the last section, the two crystals were then reconstructed to acquire the real space crystal images to further explore the strain stripes network behaviour as a function of temperature.

5.3.1 Reconstruction parameters confirmation

The reconstruction parameters were carefully checked and confirmed on selected diffraction patterns before applying to all the data. An example of detailed checking of the parameters in two simulated crystals can be seen in the Appendix. Similar parameter checking of crystal BTO-32 can be found in Chapter 4. In this section, several general reconstruction parameters were studied for confirming the convergence of the reconstruction.

5.3.1.1 Shrink-wrap evaluations

Three diffraction patterns at typical temperature points were chosen to find an appropriate shrink-wrap value for reconstructing all the other diffraction patterns. For Crystal A, the diffraction peak at 373 K upon heating, the diffraction peak at 433 K and the diffraction peak at 373 K during cooling were chosen. For these three diffraction patterns, the reconstructions were run with a shrink-wrap value from 0 to 0.5 at a step size of 0.01. The final chi square error metrics were plotted as a function of shrink-wrap values, which is shown in Figure 5.9 (a). The first thing to notice is that the chi-square values are highly reproducible for adjacent tests, leading to smooth curves; there is no apparent propagation of the random numbers used to start the reconstructions. There are two slopes showing in these lines. In the first slope, the chi-square error metrics stay at a relative low value, while in the second slope the chi-square increases sharply. The turning points for the three diffraction patterns are 0.16, 0.17 and 0.16, respectively. Therefore, a shrink-wrap value of 0.10 was chosen for reconstructing all diffraction patterns of Crystal A.

For Crystal B, the first slope for the diffractions patterns at three temperatures roughly end at around the threshold of 0.25. Therefore, the shrink-wrap value of 0.15 was chosen.
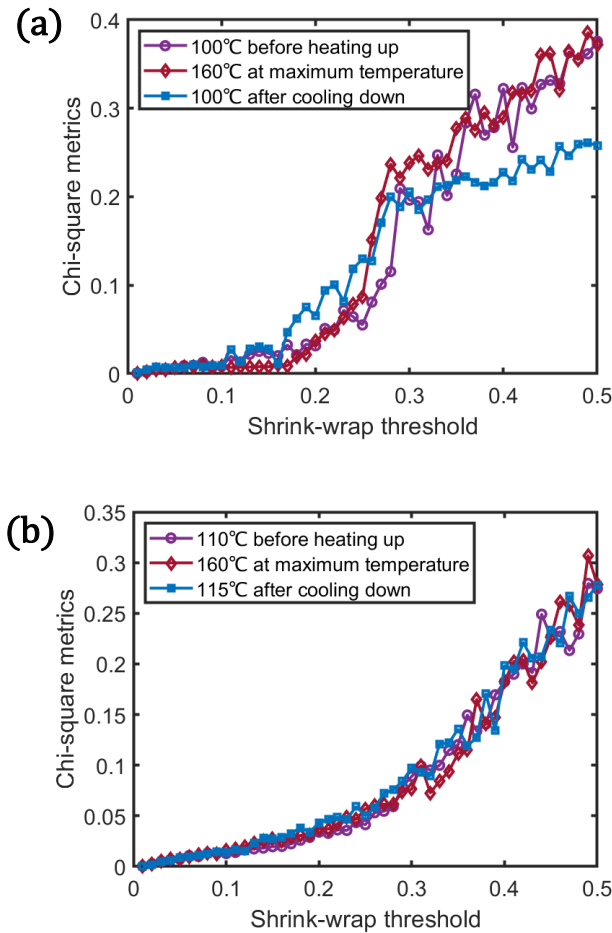
Figure 5. 9 The line plots show the chi-square metrics variations over the shrink-wrap values. Three typical diffraction patterns from both Crystal A and Crystal B were chosen for testing and plotted in this figure.
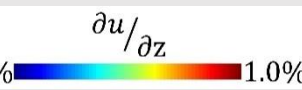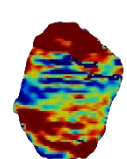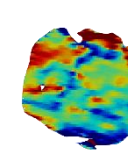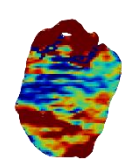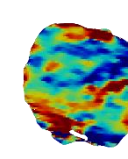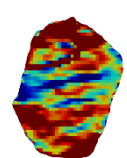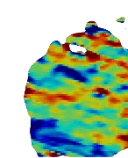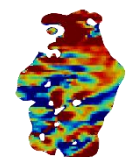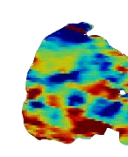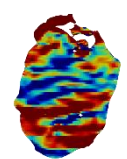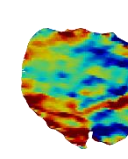
Another common way for reconstructing in-situ crystal data is to assume there is no big change in crystal shape. After optimising the support for the first measurement, it would then been fixed to reconstruct all the other measurements with the same support. In this way, all the differences between different measurements would goes into the reconstruction results. In this work, there is no knowledge if the shape would change or not. Therefore, all the crystals were reconstructed separately with random start and certain shrink-wrap value.
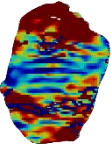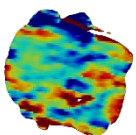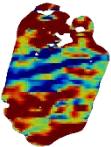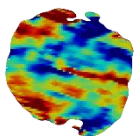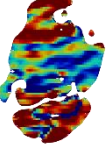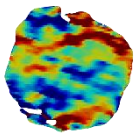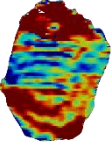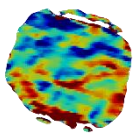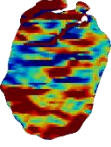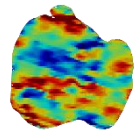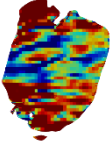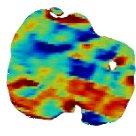
5.3.1.2 Algorithms evaluations

Different algorithm combinations were tested on the diffraction patterns from the two crystals. The chi-square error metrics are listed in Table 5.1. For Crystal A, the general combination ER plus HIO gives reasonable chi-square error metrics. This combination was then used for reconstructing all the

measurements of Crystal A. For Crystal B, the ER plus RAAR gives low chi-square error metrics and so this was used for the reconstruction.

Table 5. 1 The chi-square error metrics of the reconstructions using different algorithm combinations. The iteration-number triggers of the two algorithms were kept at [5,180] out of 300 iterations.

Algorithm combinations	Crystal A χ^2 error metrics	Reconstructed images $\partial u/\partial z$ -1.0% ▮▮ ▮▮1.0%	Crystal B χ^2 error metrics	Reconstructed images $\partial u/\partial z$ -1.0% ▮▮ ▮▮1.0%
ER+GHIO	1.6%		1.2%	
ER+HIO	0.84%		1.2%	
ER+HIO-AMP	1.0%		3.0%	
ER+HIO-OR	3.3%		1.4%	
ER+ASR	1.1%		1.2%	

ER+DM	0.79%		1.3%	
ER+DMr	1.3%		1.3%	
ER+GRAAR	3.6%		1.3%	
ER+HPR	0.89%		1.3%	
ER+RAAR	0.97%		1.1%	
ER+RAARv	1.3%		1.3%	

5.3.1.3 Guided-HIO (GA) parameters
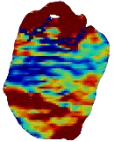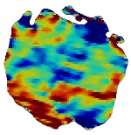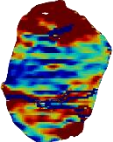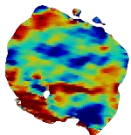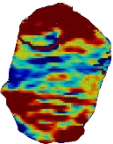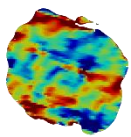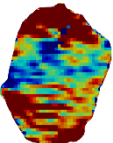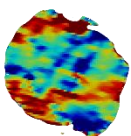
The guided-HIO method uses different decision methods for selecting the best result for the following iteration, as discussed in section 4.1.2.3. The final chi-square error metric is listed for the GA reconstruction of the two crystals in Table 5.2. In both Crystal A and B cases, the sharpness gives the lowest chi-square error metrics and so was chosen for reconstructing all the measurements.
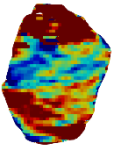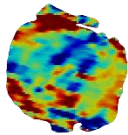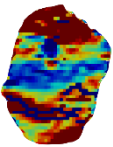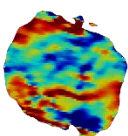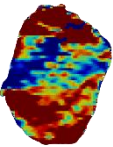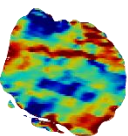
Table 5. 2 The chi-square error metrics using different returned metrics in GA reconstructions.

GA return metrics	Crystal A χ^2 error metrics	Reconstructed images $\partial u/\partial z$ -1.0% ■■■ 1.0%	Crystal B χ^2 error metrics	Reconstructed images $\partial u/\partial z$ -1.0% ■■■ 1.0%
Sharpness $\sum\|\rho(\mathbf{r})\|^4$	0.84%		1.1%	
Largest area of the support	0.84%		1.2%	
Chi-square matrices χ^2	1.0%		1.2%	
Total variation norm	0.95%		1.2%	
Average of iterates	0.84%		1.1%	
Average of half iterates	1.0%		1.1%	

Different breeding modes were also tested for the two crystals in Table 5.3. For Crystal A, the 'sqrt_ab_pa' gives the lowest chi-square. In the 'sqrt_ab_pa' mode, the amplitude of the new start is the geometric mean, the square-root of the product of the best iterate and current iterate, while the phase is kept as that of the current iterate. For Crystal B, the 'max_ab_pa' works the best. In this breed mode, the phase is again kept as the current iterate, but the amplitude is determined by the maximum amplitude between the best and current iterates.
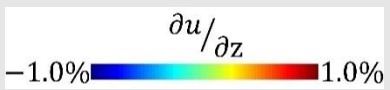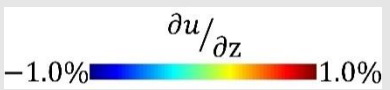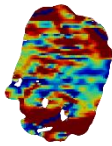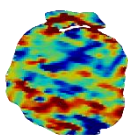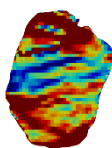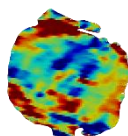
Table 5. 3 The chi-square error metrics using different breeding mode in GA reconstructions.
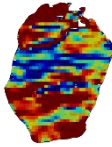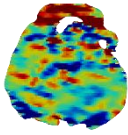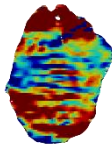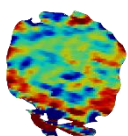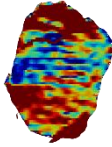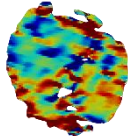
GA breeding mode	Crystal A χ^2 error metrics	Reconstructed images $\partial u / \partial z$ -1.0% ▬▬ 1.0%	Crystal B χ^2 error metrics	Reconstructed images $\partial u / \partial z$ -1.0% ▬▬ 1.0%
'sqrt_ab': $\sqrt{A_a e^{\phi_a} \cdot A_b e^{\phi_b}}$	0.84%		1.1%	
'max_ab': $\langle A_a, A_b \rangle_{max} \cdot e^{\frac{(\phi_a + \phi_b)}{2}}$	0.98%		0.97%	
'avg_ab': $\frac{(A_a e^{\phi_a} + A_b e^{\phi_b})}{2}$	0.81%		1.0%	
'sqrt_ab_pa': $\sqrt{A_a \cdot A_b} \cdot e^{\phi_a}$	0.58%		1.0%	

Method	Crystal A χ^2	Reconstructed image	Crystal B χ^2	Reconstructed image
'max_ab_pa': $\langle A_a, A_b \rangle_{max} \cdot e^{\phi_a}$	0.72%		0.96%	
'avg_ab_pa': $\frac{(A_a + A_b)}{2} \cdot e^{\phi_a}$	0.71%		0.97%	
'pixel_switch': Random mixing	0.61%		0.98%	

Different "low-resolution" methods, discussed in Section 4.1.2.3, have been tested for the reconstruction of the two crystals. For both crystals, the one big Gaussian-distributed low-resolution image appears to work the best.

Table 5. 4 The final chi-square error metrics after using different low-resolution methods in GA reconstructions of the two crystals.

Low-resolution method	Crystal A χ^2 error metrics	Reconstructed images $\partial u / \partial z$ -1.0% ▬ 1.0%	Crystal B χ^2 error metrics	Reconstructed images $\partial u / \partial z$ -1.0% ▬ 1.0%
No low resolution	1.6%		1.6%	
One big Gauss distribution	0.58%		0.96%	

Many small Gauss distributions	1.7%		1.7%	
Laplacian distribution	0.92%		0.97%	
Sinc distribution	0.76%		1.2%	

(d) Reproducibility evaluations

For testing the reproducibility of the reconstruction, every measurement is repeatedly reconstructed 20 times with different random phase or amplitude values within the wide starting supports (before shrink-wrap). The chi-square error metrics are checked and evaluated, so as to monitor potential differences among the reconstructions. Table 5.5 shows an example.

For Crystal A, the final reconstruction has a chi-square of 0.58%. The ten random object reconstructions, where the starting support has a random shape but zero phase, give the same error metrics of 0.91%. The ten random phase reconstructions, where the starting support has a box shape equals to 50% the size of array but with random phase, giving chi-square error metrics of 0.55%. The differences of these 20 reconstructions relative to the final reconstruction are also calculated, which gives a value smaller than 0.03%. This indicates the differences between the 20 random reconstructions and the base reconstruction are trivial.

For Crystal B, the error metrics are between 1.2% and 1.4%, which are a bit bigger than for Crystal A. The difference between the random reconstructions

and the base reconstruction ranges from 0.24% to 0.87%. These values are bigger than the difference in Crystal A. Given the complex nature of the diffraction pattern, these error and difference metrics are acceptable values. Although there is still some contribution from not reaching the global minimum best fit, we think that most of the remaining residual comes from noise in the data themselves. This was one of the motivations for this experiment to use the ESRF's upgraded "Extremely Brilliant Source" (EBS) facilities. Chi-square values below 1% have not yet been routinely achieved for data from APS, which are apparently still limited by counting statistics of diffraction patterns typically 10 times weaker than from ESRF.

Table 5. 5 The reproducibility test of the reconstructions.

Reconstruction Number	Crystal A		Crystal B	
	Error metrics χ^2	Difference metrics D	Error metrics χ^2	Difference metrics D
Base	0.58%	0	1.2%	0
RO 1	0.91%	0.0091%	1.3%	0.44%
RO 2	0.91%	0.0091%	1.3%	0.44%
RO 3	0.91%	0.0091%	1.3%	0.44%
RO 4	0.91%	0.0091%	1.3%	0.44%
RO 5	0.91%	0.0091%	1.3%	0.27%
RO 6	0.91%	0.0091%	1.3%	0.27%
RO 7	0.91%	0.0091%	1.3%	0.27%
RO 8	0.91%	0.0091%	1.3%	0.27%
RO 9	0.91%	0.0091%	1.3%	0.27%
RO 10	0.91%	0.0091%	1.3%	0.27%
RP 1	0.55%	0.023%	1.3%	0.41%
RP 2	0.55%	0.023%	1.3%	0.41%
RP 3	0.55%	0.023%	1.3%	0.24%
RP 4	0.55%	0.023%	1.4%	0.87%
RP 5	0.55%	0.023%	1.4%	0.87%
RP 6	0.55%	0.023%	1.4%	0.87%

RP 7	0.55%	0.023%	1.4%	0.87%
RP 8	0.55%	0.023%	1.4%	0.87%
RP 9	0.55%	0.023%	1.4%	0.87%
RP 10	0.55%	0.023%	1.4%	0.87%

* RO=random object reconstruction; RP=random phase reconstruction.

5.3.2 Reorientation of the reconstructed crystals

The method to resolve the crystallographic axis directions has been illustrated in Section 4.1.3 and was applied for the two crystals studied in this Chapter. Both the two crystals have facets, but the facets themselves were not as clear as BTO-32, sometimes having small hills and valleys on their surfaces. The facets were fitted manually to get their rough plane directions in lab coordinates using Paraview software. Table 5.6 shows the manually fitted directions of facets in Crystal A.

Table 5. 6 The fitted direction cosines of two facets of Crystal A in Lab coordinates. The Q direction is also listed.

Direction	Lab X component	Lab Y component	Lab Z component
Facet A	0.4260	-0.6128	-0.6656
Facet B	-0.2900	-0.9080	-0.2960
Q direction	0.7074	0.6760	-0.2064

The relative angles between these facets were calculated and listed in Table 5.7. Crystal A was seen to migrate from the (101) powder ring to the (110) powder ring upon heating and cooling, so its Q direction is (110) or (101) for both the tetragonal and cubic phases. Facet A is nearly 61° relative to the Q direction, which corresponds to a {110} facet. Facet C is nearly 118° relative to the Q direction, which corresponds to another {110} facet. If we label Q as (110) and A as (1-10), then B is (0-11) or (0-1-1). In this case, c-axis can be determined as the perpendicular to Q vector. If we label Q as (101) and A as (10-1), then B is (0-1-1) or (01-1). In this case, c-axis cannot be specifically identified.

Table 5. 7 The angle between the facets and Q vector of the crystal A. The standard angles between {100}, {110} and {111} are also listed for reference.

	A	B	Q	{100}	{110}	{111}
A		61.06°	88.60°			
B			118.08°			
Q						
{100}				90.00°	45.00°/90.00°/135.00°	54.74°/125.26°
{110}				-	60.00°/90.00°/120°	35.26°/90.00°/144.74°
{111}				-	-	70.53°/109.47°

The facets and Q direction of Crystal B in lab coordinates are listed in the Table 5.8, with their incline angles listed in Table 5.9. When taking the Q as (110), then facet B is (100) and A is (0-11).

Table 5. 8 The fitted direction cosines of two facets of Crystal A. Q direction is also listed.

Direction	Lab X component	Lab Y component	Lab Z component
Facet A	-0.2032	-0.5685	-0.7972
Facet B	-0.9300	-0.0633	-0.3622
Q direction	0.6929	0.6907	-0.2068

Table 5. 9 The angle between facets and Q vector of the crystal A. The standard angles between {100}, {110} and {111} are also listed for reference.

	A	B	Q	{100}	{110}	{111}
A		82.20°	111.63°			
B			47.50°			
Q						
{100}				90.00°	45.00°/90.00°/135.00°	54.74°/125.26°
{110}				-	60.00°/90.00°/120°	35.26°/90.00°/144.74°
{111}				-	-	70.53°/109.47°

5.3.3 Strain stripes behaviour of Crystal A

Of the two crystals that have been detailed reconstructed and studied, Crystal A is the one whose centre crossed between powder rings. During the heating and cooling that crossed the phase transition, the diffraction pattern moves from the (101) to the (110) powder ring. After reorienting Crystal A in the calculated crystallographic coordinates, the derivatives of the displacement over the crystallographic axis were taken to get the usual strain components. The three orthogonal crystallographic directions are defined as a_1, a_2 and a_3, being the principal (100), (010) and (001) axes, without knowing which is the c-axis. This procedure is illustrated in Chapter 4. Figure 5.10 shows the three strain combinations at three orthogonal slice views of the Crystal A at 100°C before heating. Strain stripes could be seen in these slices. Some stripe directions are marked by the white dash lines in the Figure 5.10. For the a_2-a_3 slices, all the three strain gradients show directional stripes, mostly distributed around 0° or 110° relative to the a_2 direction. For the a_1-a_3 slices, the strain gradients are clustered around 0° or 39°. For the a_1-a_2 slices, the strain gradients are either 0° or 90°. Of all the nine views in Figure 5.10, two views in a_2-a_3 slices, u_Q/a_2 and u_Q/a_3, show more distributions of strain stripes and were selected for the temperature study.

The strain images of crystal A were then examined during the heating and cooling experiment, for which the BCDI measurements were taken in 5 K steps. As described above, the crystal started at 373 K, was heated to 433 K, after which it was cooled down to 373 K again. The detailed reconstructions were carried out at each temperature. In order to locate the same slice position shown in Figure 5.10, the centre of mass (COM) of the reconstruction was selected as the geometric centre, and the slices were cut at the same distance relative to the COM. Figure 5.11 and Figure 5.12 present pairs of reconstructed slices (at the same position) showing two strain gradients through all the measured temperature points. As can be directly seen, the strain stripes were preserved even as the crystal temperature reached 433 K. From examining the d-spacing (Bragg peak position) of Crystal A in Section 5.2.4, the phase transition temperature had

been determined to be around 423 K during heating. Therefore, the local strain stripes are found to exist inside the crystal no matter whether the global phase is tetragonal or cubic. When the crystal cooled down to 373 K, the strain stripes were still preserved through the phase transition.
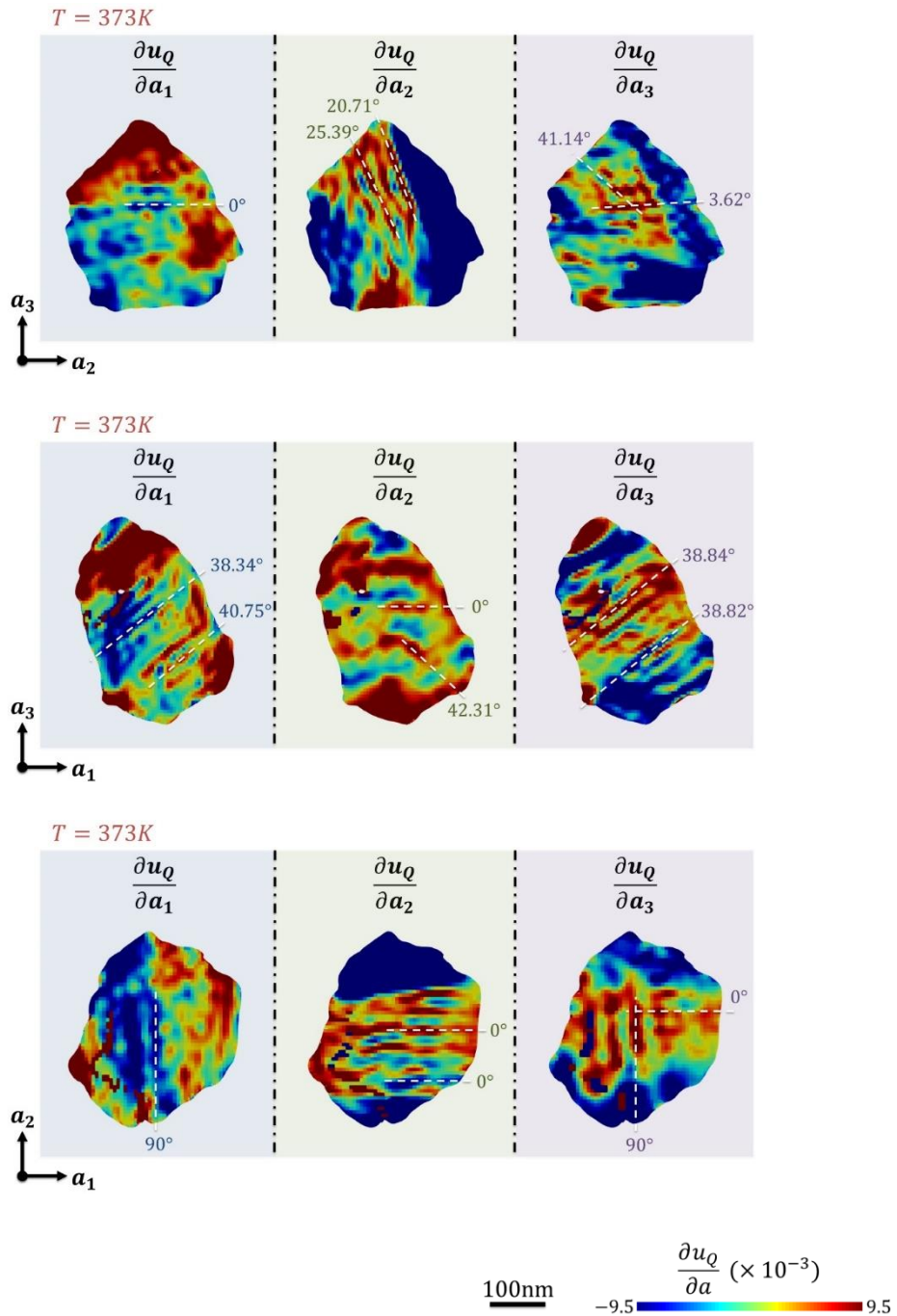
Figure 5. 10 The nine views of strain gradients are shown for Crystal A at 100°C before heating. The first row shows the a_2-a_3 slice, while the second and third rows show the a_1-a_3 and a_1-a_2 slices, respectively. In each row, the strain gradient along each a_1, a_2 and a_3 directions are listed. The white dash lines are guides for the eyes, discussed in the text.
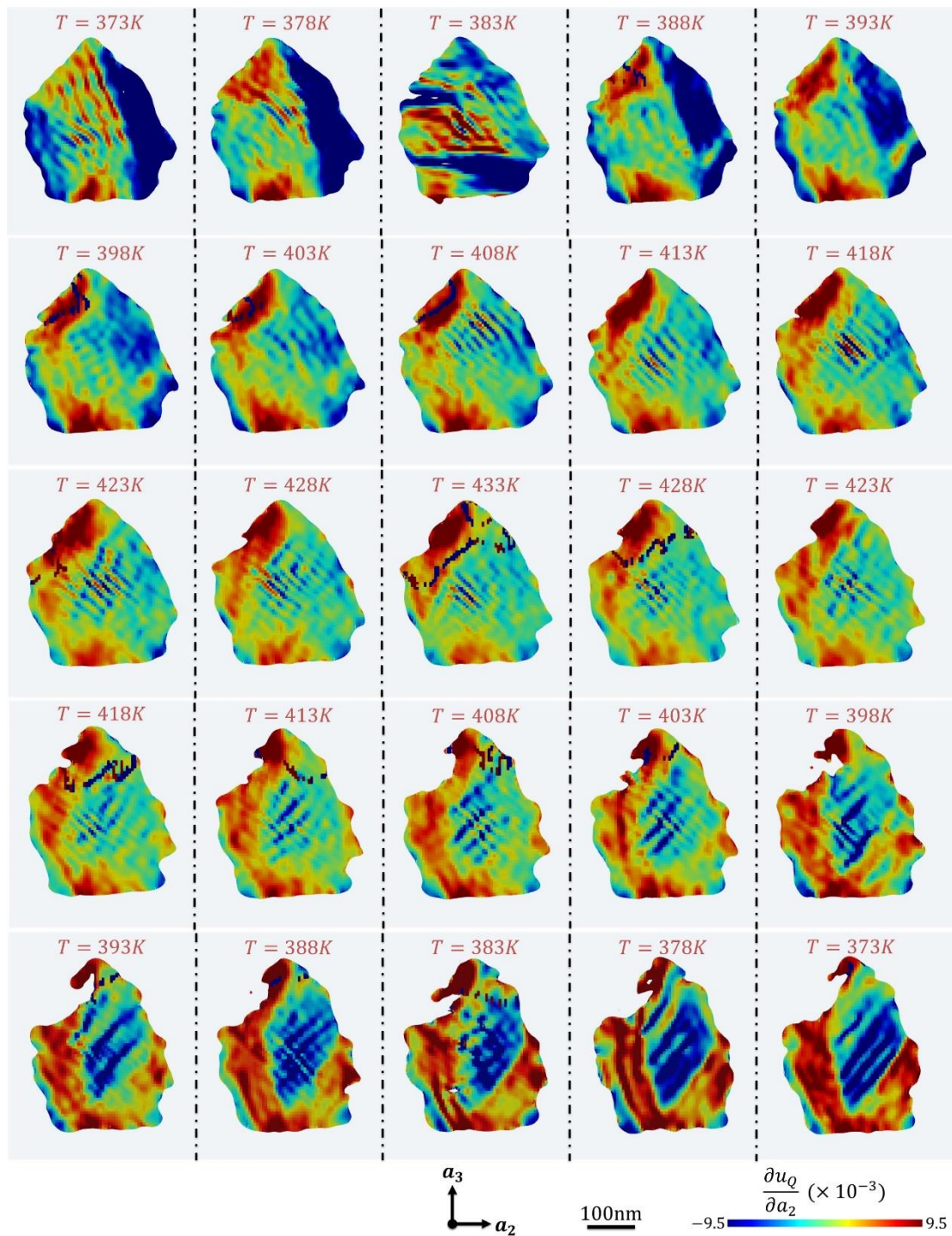
Figure 5. 11 Central section views of the a2-a3 slices of the strain combinations $\frac{\partial u_Q}{\partial a_2}$ at every temperature. The Crystal A went through heating from 373 K to 433 K in 5 K steps.
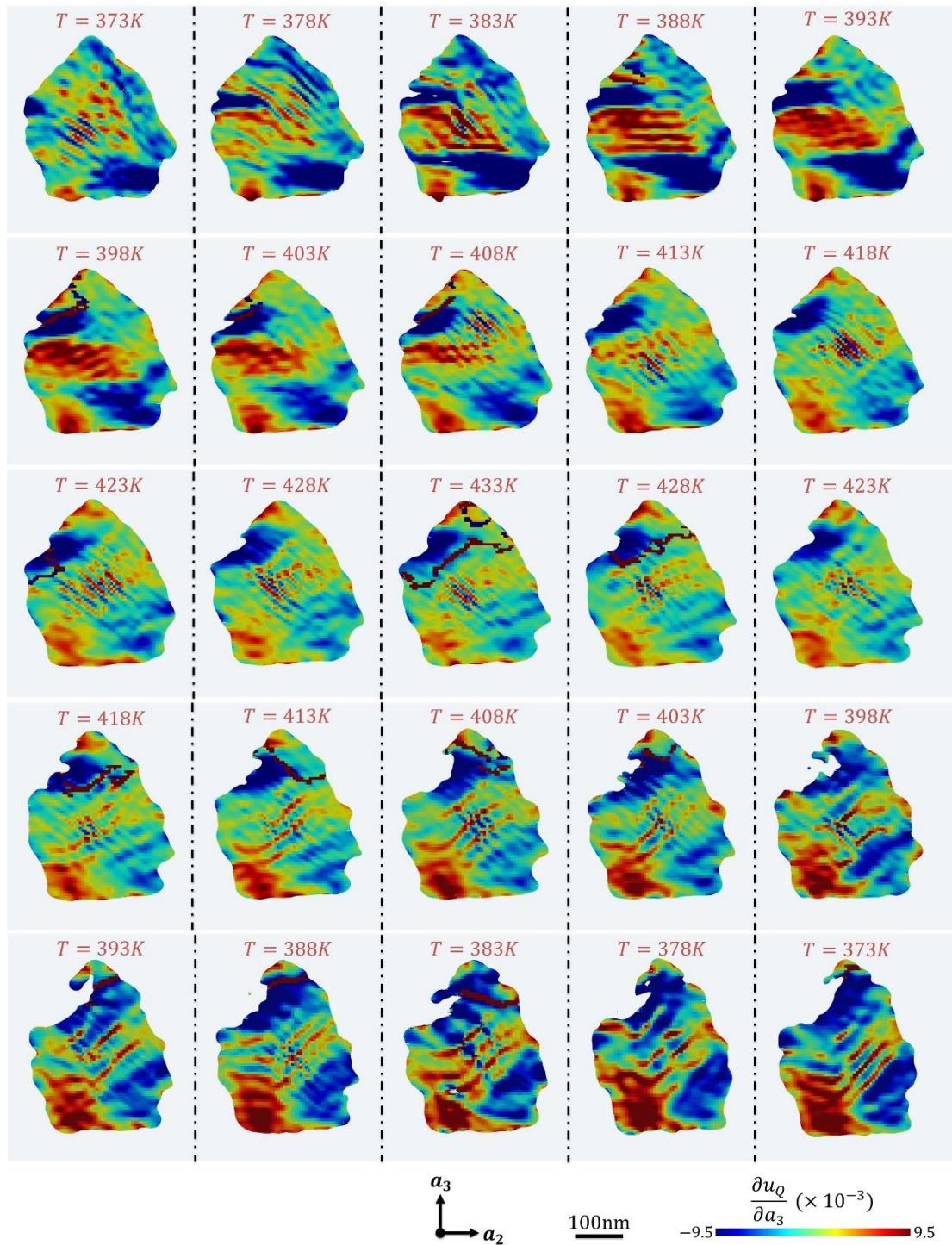
Figure 5. 12 Central section views of the a₂-a₃ slices of the strain combinations $\partial u_Q/\partial a_2$ at every temperature. The Crystal A went through cooling from 433K to 373 K in 5 K steps.

Even though the stripes are present at all temperatures their spacing and direction is seen to evolve. To qualitatively examine the periodicity of the strain stripes, the two-dimensional (2D) autocorrelation functions (ACFs) were carried

out, as shown in Figure 5.13 for the strain gradient over a_2 and in Figure 5.14 for the strain gradient over a_3.

In Figure 5.13, the period is big and not well defined initially at 373 K, but gradually becomes clearer upon heating. At 403 K, the period is well established, with a strong correlation along the diagonal direction, 45° with respect to the a_2 and a_3 axes. The period is roughly 25 nm. Upon further heating, the period keeps decreasing, coming to roughly 15 nm by 418 K. Upon further increase of the temperature, the period keeps the same size, but the strong directional correlation along 45° has faded. The crystal gradually forms correlations along both 45° and -45° relative to the a_2 axis. Upon cooling down, the correlation along 45° gradually is seen to fade away, while the correlation along -45° became clearer. After cooling to 413 K, the size of the period has increased to 25 nm and the correlation is strongly distributed along -45°. Further decreasing the temperature, the period increases again in size and becomes less well-defined.
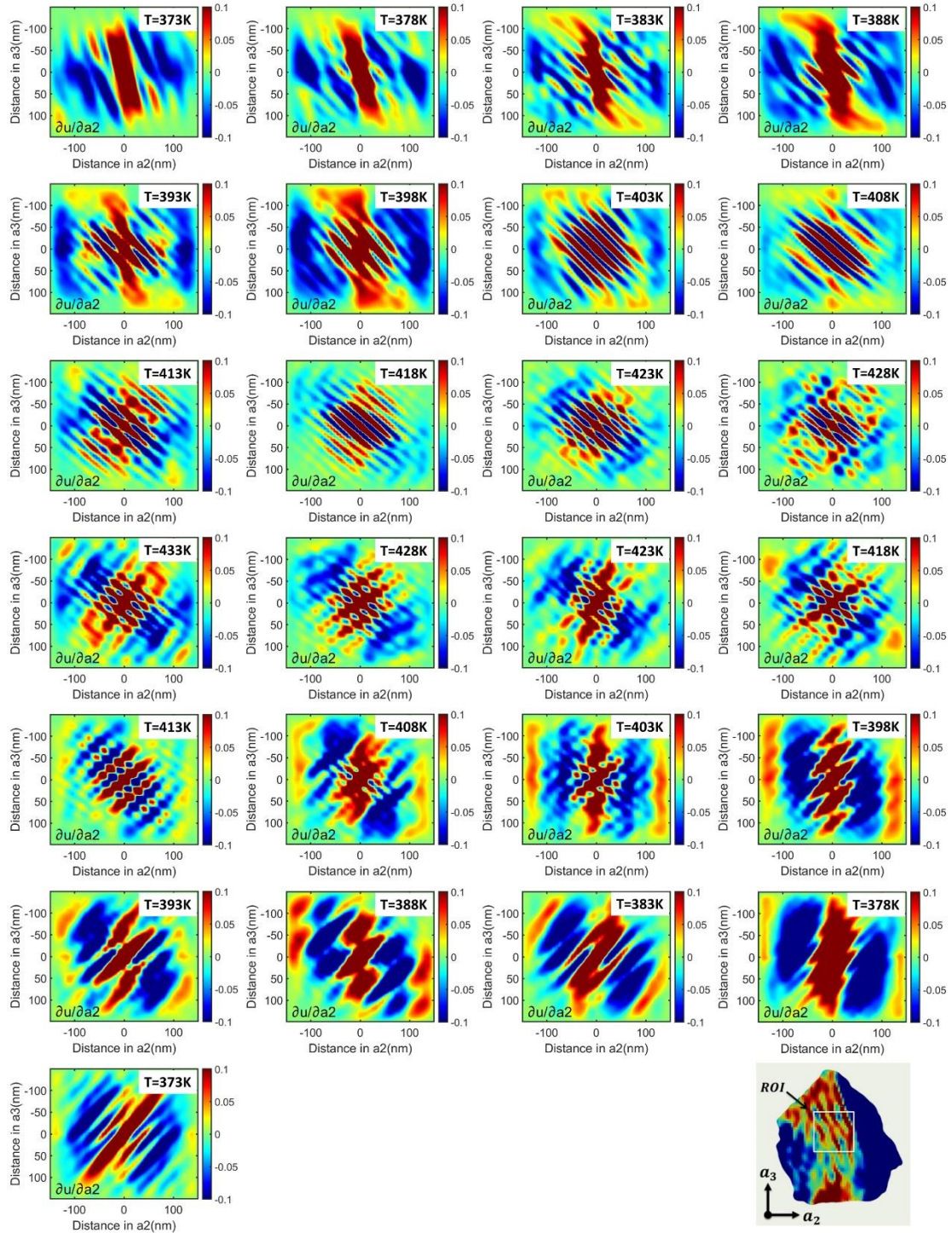
Figure 5. 13 The 2D Auto Correlation Function of the strain component $\left.\frac{\partial u_Q}{\partial a_2}\right.$
at every temperature in Figure 5.11.

The 2D ACF over a_3 direction in Figure 5.14 also shows a similar trend as seen in Figure 5.13. The period is poorly defined at low temperature initially but becomes clear when heated to 418 K, which is 10 K higher than in Figure 5.13. At 418 K, it has a period of 15 nm and strong correlation along the 45° direction

158

relative to a_2 axis, which is same as in Figure 5.13. Upon cooling, the correlation changes to the -45° direction as well.
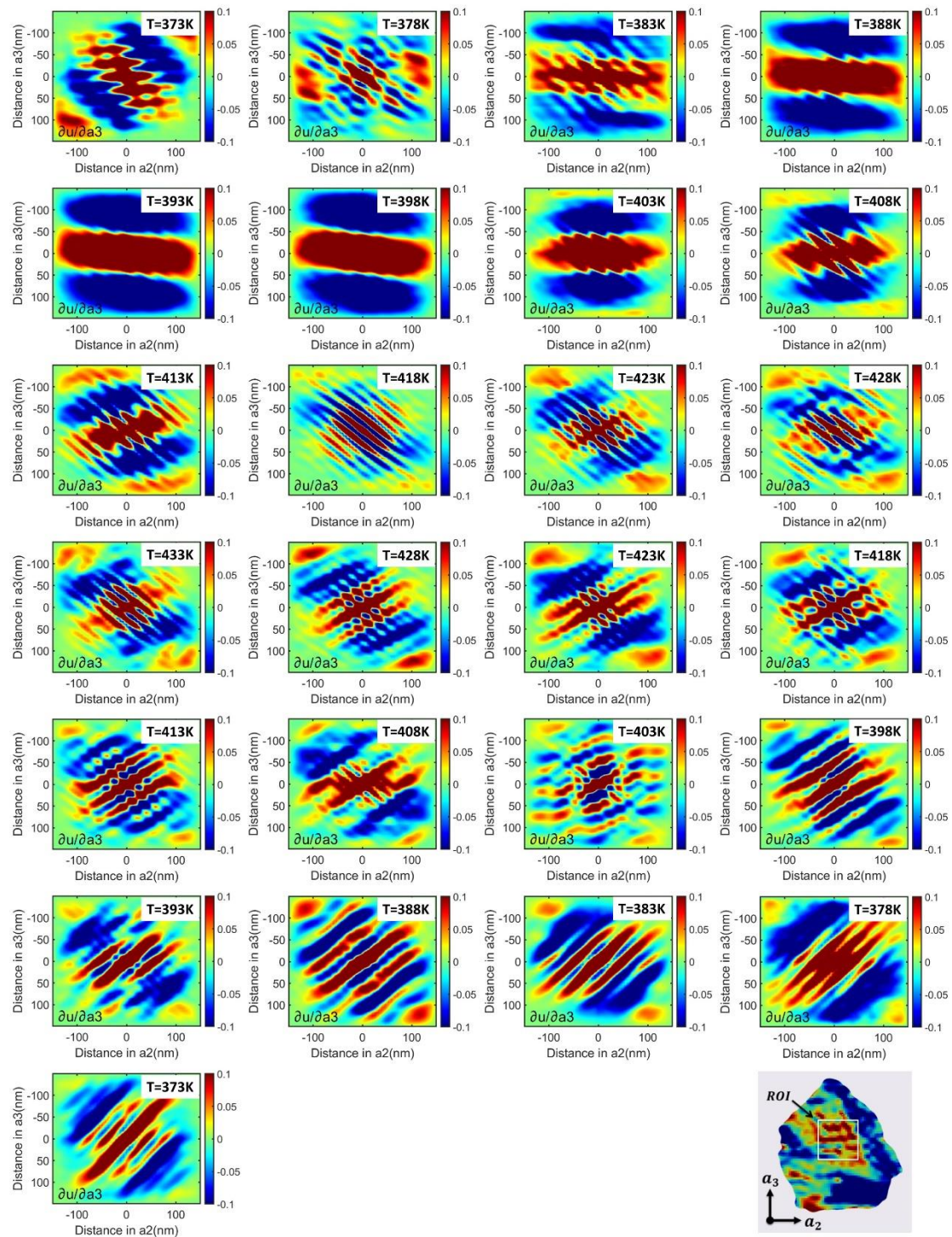
Figure 5. 14 The 2D Auto Correlation Function of the strain component $\frac{\partial u_Q}{\partial a_3}$ at every temperature in Figure 5.11.

159

The size of projection of stripes onto a_2 direction is generalized and plotted in Figure 5.15. The left panel shows the stripes of derivatives over a2 direction, which does not show much variation. The right panel shows the derivatives over a3 direction, which shows a decrease trend when heating up and an increase trend when cooling down.
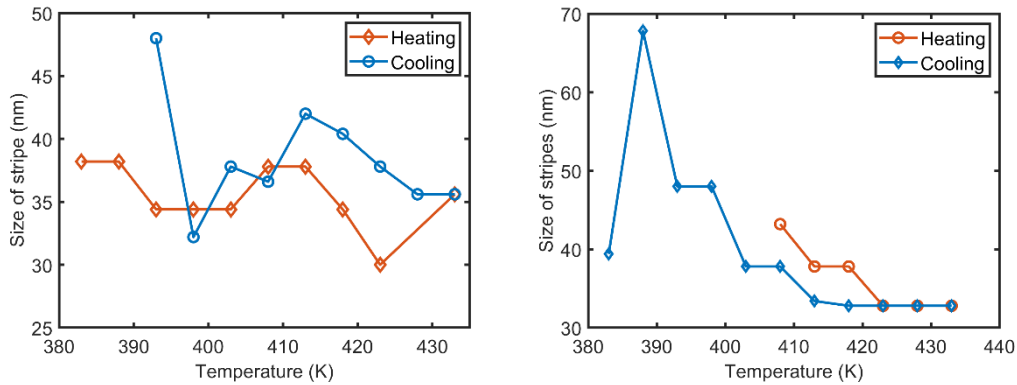
Figure 5. 15 The stripe size onto X direction over temperature.

The 90° switching of the period in both views occurs at roughly the same temperature as the crystal switching from (101) to (110) powder ring, which corresponds to a 90° switching of the predominant c-axis direction in the crystal lattice. The nice match of the two indicates that the strain stripes are connected to the tetragonal structure. This suggest the domain walls visualised by the strain stripe could be ferroelectric 90° domain walls.

5.3.4 Strain stripes behaviour of Crystal B

Crystal B initially had its diffraction peak on the tetragonal (110) powder ring but moved to the cubic (110) powder ring position upon heating and changed back to the previous powder ring upon cooling down. This indicates the crystal c-axis direction is the same before and after the phase transformation, unlike what was seen for Crystal A. Figure 5.16 shows the three slice-views of the Crystal B at 383 K upon heating. Each slice is presented with derivatives over three crystallographic directions, namely a_1 to a_3. The strain stripes distributions in Crystal B are less pronounced than in Crystal A. Of all the nine views in Figure 5.16, the strain component $\partial u_Q / \partial a_3$ in a_2-a_3 slice shows the best distribution of horizontal stripes and inclined stripes. This view is selected for the temperature study.
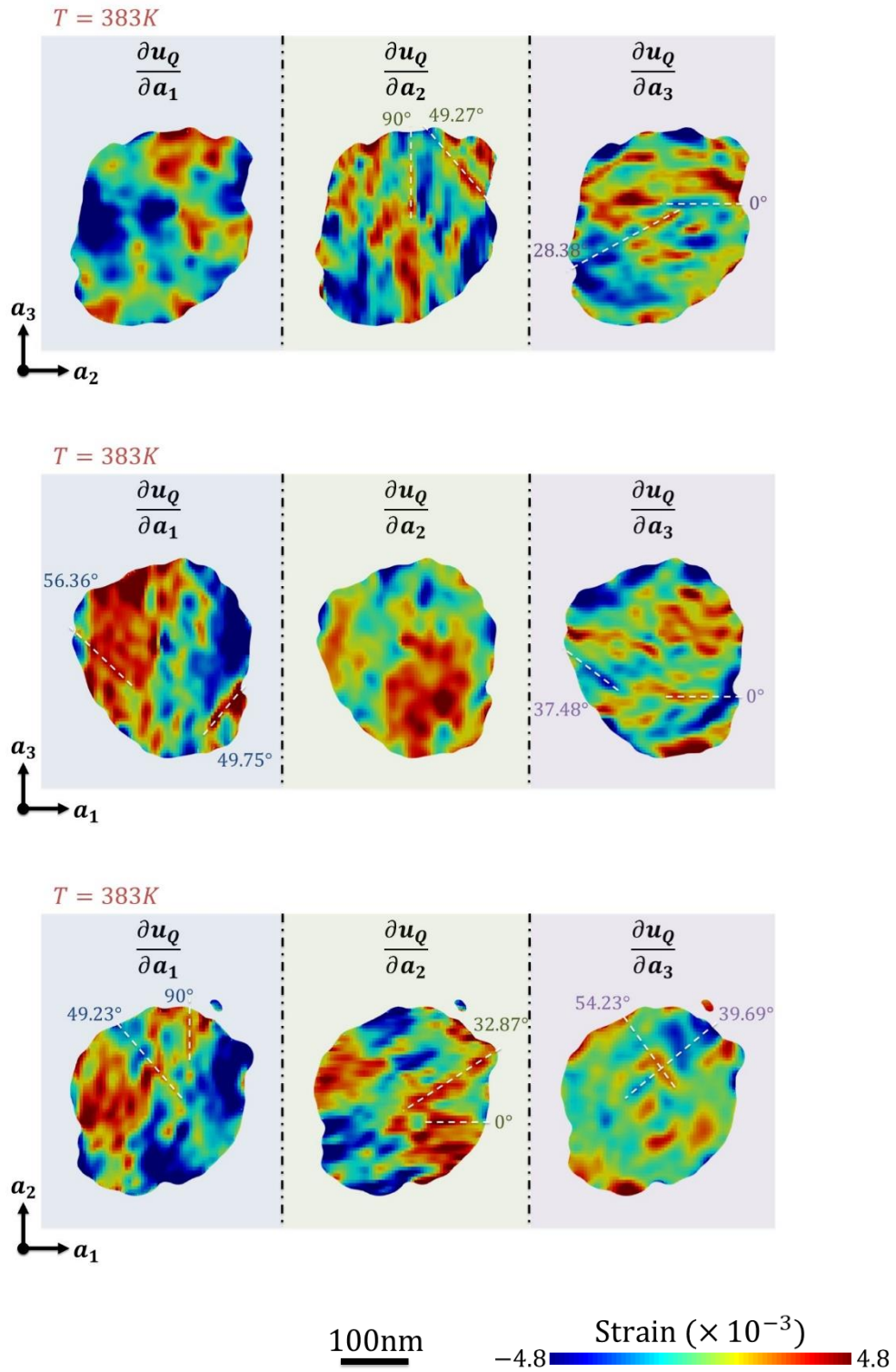
Figure 5. 16 The nine views of strain gradients are shown. The first row shows the a_2-a_3 slice, while the second and third rows show the a_1-a_3 and a_1-a_2 slices, respectively. In each row, the strain gradient along each a_1, a_2 and a_3 directions are listed. The white dash lines are guides for the eyes.
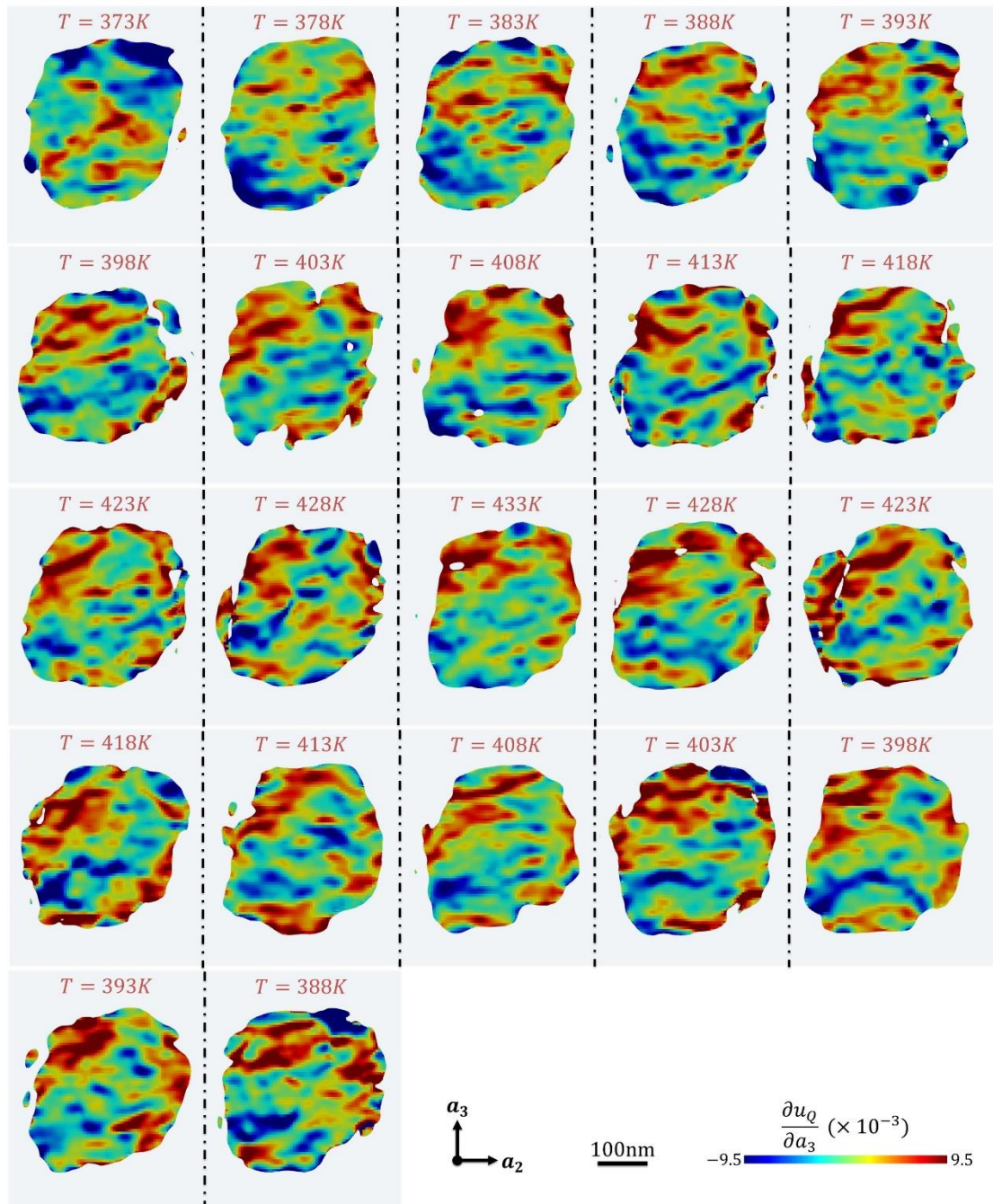
Figure 5. 17 The central section view shows the strain component $\partial u_Q / \partial a_3$ at every temperature. Crystal B went through heating from 100℃ to 160℃, and then cooled down to 115℃ in 5℃ steps.

The crystal B was heated to 433 K and then cooled down to 388 K. The strain gradient on the selected slice over temperatures are shown in Figure 5.17. Unfortunately, the strain stripes features are hardly observable in these slice views. But the strain is evolving during the heating and cooling. The magnitude of the strain remains around the same all through the phase transition. Because

the strain would accumulate on the domain wall boundaries, the strain of same order suggests that there may not be much nucleation and annihilation of domain walls upon heating and cooling across the phase transition.
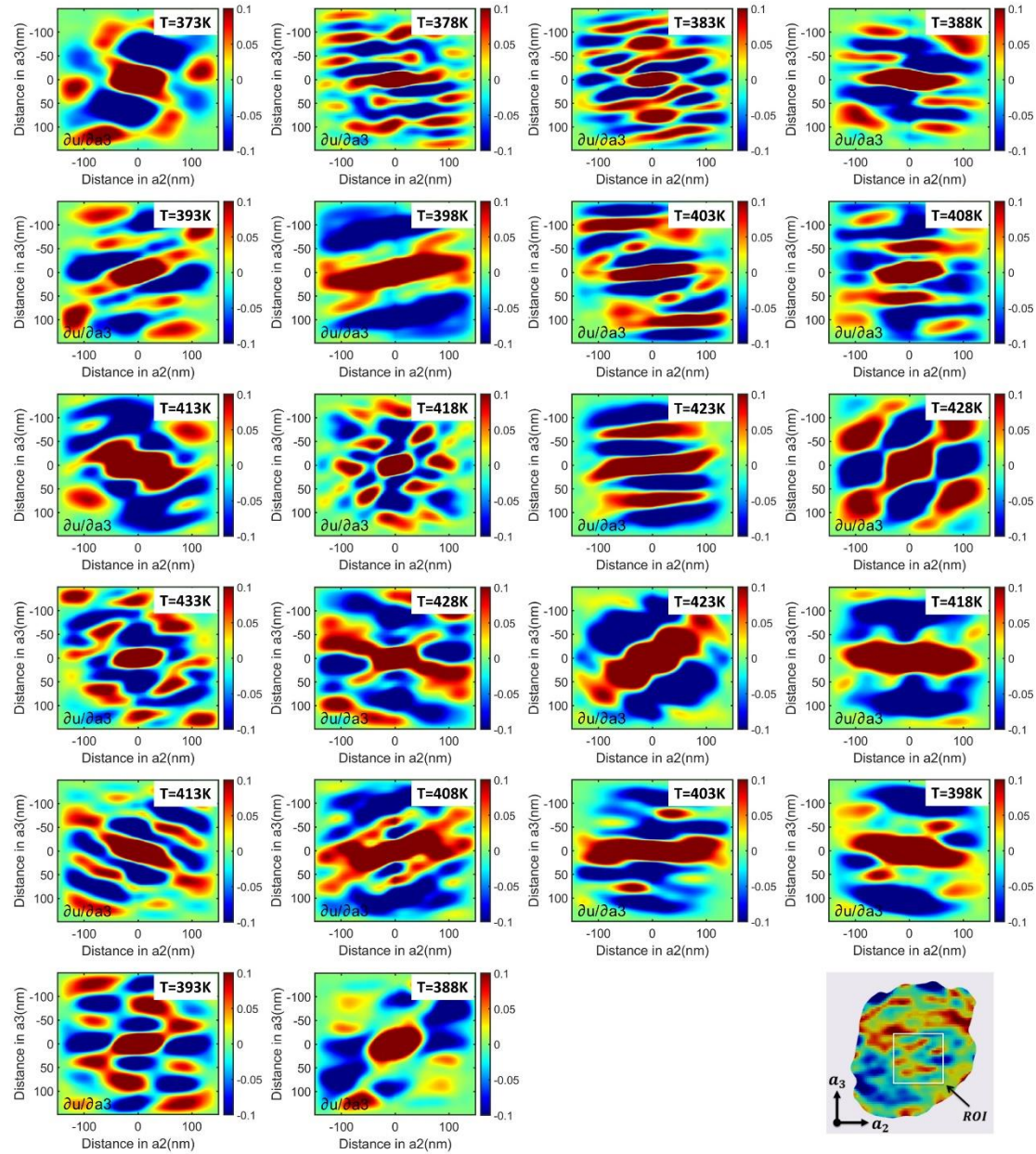
Figure 5. 18 The 2D Auto Correlation Function of the strain component $\partial u_Q / \partial a_3$ at every temperature in Figure 5.15.

The 2D ACF of the slices in Figure 5.17 were calculated and shown in Figure 5.18. The periodicity is not well defined at all but some temperatures. Upon heating, the Crystal B shows 50 nm periodicity along a_3 direction at temperatures from 378 K to 423 K with two peculiar points, 398 K and 413 K where the periodicity

was not well-defined. From 428 K onward and cooling down, the Crystal B either shows periodicity along diagonal direction between a_2-a_3 or not well-defined.

In summary, we have observed two crystals crossing their phase transitions from tetragonal to cubic via heating up, and from cubic to tetragonal via cooling down. In both crystals, the strain components are preserved at all temperatures. In Crystal A, the strain stripes switched direction after heating up and cooling down, which indicates the strain stripes could be the 90° ferroelectric domain walls.

We have measured an additional crystal through heating, but the crystal is smaller than Crystal A and B by a factor of 2. The reconstruction of the crystal turns out to be complex in shape and displacement. It also shows no obvious facet, which is necessary to restore the crystallographic direction.

This chapter has shown the details of a successful experiment at ESRF to understand the temperature dependence of the stripe structures discovered in BTO nanocrystals. In the best example, denoted Crystal A, the whole crystal is found to switch its c-axis direction after heating through the tetragonal-cubic phase transition and the stripes were seen to switch accordingly. This is an indication that the stripes could correspond to internal 90° ferroelectric domain walls. If so, based on the BCDI images, the domain structures are found to be still visible in the cubic high-temperature phase, suggesting the phase transition is not very distinct and that the nanocrystal retains some ferroelectric distortions even at the highest temperature explored.

However, the observation of strain stripe along cannot identify the nature for sure. There are still many uncertainties halted around and left for future study:

1) Statistics limitation. We only see some of the crystals having strain stripes. In this Chapter, for example, Crystal A has nice stripes while Crystal B does not. We attribute such behaviour to the complexity of the system. Even for the carefully grown strained thin films where the growth parameters are optimized, there are still regions where the domains are poorly defined. For our hydrothermal synthesized nanocrystals, there is hardly any control of the boundary conditions. The random distributed displacement field as seen in Crystal B should be no

surprise. For our best example, Crystal A, the strain stripes only appeared in some volume inside the crystal. But that could be the only region having orderly distributed ferroelectric domains, while in other areas the distributions are random. 2) The physics behind the strain stripes. We attribute the strain stripes to crystal structural reasons. We had thought about if any artefact coming into our calculation so as to give this stripe feature. One possibility would be Fourier termination ripples. Recently there are publications about the simulated stripes given by the ripples. We cut the data in size and did multiple reconstruction test. To our knowledge, there is no noticeable changes in stripes. In the future study, we are planning to dig into this question further.

Chapter 6. Finite Element Analysis Simulation

Phase-field modelling is widely used to predict the domain switching of ferroelectric (and other) materials and their evolution during phase transitions or under external stimuli [141, 209-211]. It normally involves calculating the free energy function as a function of one or more order parameters [212, 213]. For a ferroelectric system, the polarization is a typical choice for order parameter. Based on the problem, different polarizations could be chosen, like global polarization, spontaneous polarization, or induced polarization [214-216]. Different functional forms of theory could be explored and applied as well. In Section 2.1.5, the Landau-Devonshire theory is illustrated, in which the free energy is depicted as a function of polarization in equation 2.4. The equation could be further extended based on the problem. For example, strain or electric field could be included if that is the external stimuli and time could be added if time-dependence is needed. The functional form is always non-linear, which specifies a length scale to any instabilities which emerge in the polarization and consequential strain.

One feature of the results of phase-field modelling is that phase boundaries tend to be relatively diffuse and not sharp enough to represent sharp domain walls. Between two adjacent phases, where the order parameters are 0 and 1, the boundary region would have a gradient of the order parameters [217-219]. Phase-field modelling can focus on the evolution of microstructure without the need of tracking the boundary interfaces. But for our problem, the interfaces are believed to be the places where strain accumulated and of great interest. Therefore, we turned to use linear theory of piezoelectricity instead of the phase-field modelling.

The Finite element analysis (FEA) method was used to simulate and try to understand the strain stripes observed in the 200 nm BTO nanocrystals. FEA is a numerical method to solve general physical and engineering problems defined by coupled differential equations in 3D space. This involves subdividing the entity into small units and solving the partial differential equations of these smaller units under defined underlying principles and boundary conditions. In this Chapter, different geometries, domain combinations and configurations are

built and solved by FEA to generate strain pattern of certain boundary conditions. The goal is to compare the simulated strain patterns with the experimental results in Chapter 4&5, so as to verify which model works in an attempt to understand the origin of the observed strains. COMSOL Multiphysics is a commercial FEA software package which has the ability to solve the combined physics problems involving both mechanical and electrical properties, which are the two most interesting areas when solving ferroelectric materials. COMSOL provides powerful modelling editors and displays, a streamlined workflow and modifiable physical equations involved. All the simulations that have been done in this work are through COMSOL Multiphysics.

Contribution statement: Jiecheng conduct the simulation and wrote the manuscript with the guide of Ian.

6.1 Underlying principles in simulations
6.1.1 Elasticity
For an elastic material, the elastic modulus is defined as the coefficient of linear coupling of stress and strain by $\delta = {}^{\boldsymbol{T}}\!/\boldsymbol{u}$ ($\boldsymbol{T}$ is the stress, $\boldsymbol{u}$ is the strain). Depending on the ways of measuring strain and stress as well as their directions, different elastic moduli can be defined. The Young's modulus E describes the tensile elasticity where the stress and strain are in the same direction. Other moduli could also be defined, like bulk modulus for volume elasticity or shear modulus for elasticity caused by shearing stress, etc. The Poisson's ratio v is a constant that describes the deformation when the stress and strain are perpendicular.

When dealing with isotropic materials where the elasticity is the same in all directions, 2 elastic moduli or 1 elastic modulus plus one Poisson's ratio, are sufficient to determine all the other moduli. For orthotropic materials, in which the elasticity varies on the measured directions, there are 9 elastic moduli or constant which need to be defined. For example, one combination could be 3 Young's moduli (E_x, E_y, E_z), 3 Poisson's ratios (v_x, v_y, v_z) and 3 shear moduli (G_x, G_y, G_z). In this work, BTO ceramic properties at room temperature are considered, where it has a tetragonal structure globally. There is one c axis that differs from the other two equivalent a and b directions, so there are additional

symmetries relative to orthotropic materials. This results in 6 independent elastic moduli and constant, since $E_x = E_y$, $\nu_x = \nu_y$, $G_x = G_y$.

The elastic modulus is a scalar that relates the generated strain and the applied stress at certain direction. To relate the stress and strain tensor in vector space, elastic matrices are needed, strictly as a 4th-rank tensor. For orthotropic materials, according to the Hooke's law for elasticity, the stress and strain are linearly coupled by a compliance matrix C or equivalently by a stiffness matrix S. The compliance matrix of BTO that connects the stress to strain is defined as:

$$C = \frac{T}{u} = \begin{bmatrix} \dfrac{1}{E_x} & -\dfrac{\nu_{yx}}{E_y} & -\dfrac{\nu_{zx}}{E_z} & 0 & 0 & 0 \\[2mm] -\dfrac{\nu_{xy}}{E_x} & \dfrac{1}{E_y} & -\dfrac{\nu_{zy}}{E_z} & 0 & 0 & 0 \\[2mm] -\dfrac{\nu_{xz}}{E_x} & -\dfrac{\nu_{yz}}{E_y} & \dfrac{1}{E_z} & 0 & 0 & 0 \\[2mm] 0 & 0 & 0 & \dfrac{1}{2G_{yz}} & 0 & 0 \\[2mm] 0 & 0 & 0 & 0 & \dfrac{1}{2G_{zx}} & 0 \\[2mm] 0 & 0 & 0 & 0 & 0 & \dfrac{1}{2G_{xy}} \end{bmatrix} \tag{6.1}$$

In reverse, the stiffness matrix of BTO that connects the strain to stress, which is the inverse of the compliance matrix:

$$S = \frac{u}{T} = \begin{bmatrix} \dfrac{1-\nu_{yz}\nu_{zy}}{E_y E_z \Delta} & \dfrac{\nu_{yx}+\nu_{zx}\nu_{yz}}{E_y E_z \Delta} & \dfrac{\nu_{zx}+\nu_{yx}\nu_{zy}}{E_y E_z \Delta} & 0 & 0 & 0 \\[2mm] \dfrac{\nu_{xy}+\nu_{xz}\nu_{zy}}{E_z E_x \Delta} & \dfrac{1-\nu_{zx}\nu_{xz}}{E_z E_x \Delta} & \dfrac{\nu_{zy}+\nu_{zx}\nu_{xy}}{E_y E_z \Delta} & 0 & 0 & 0 \\[2mm] \dfrac{\nu_{xz}+\nu_{xy}\nu_{yz}}{E_x E_y \Delta} & \dfrac{\nu_{yz}+\nu_{xz}\nu_{yx}}{E_x E_y \Delta} & \dfrac{1-\nu_{xy}\nu_{yx}}{E_x E_y \Delta} & 0 & 0 & 0 \\[2mm] 0 & 0 & 0 & 2G_{yz} & 0 & 0 \\[2mm] 0 & 0 & 0 & 0 & 2G_{zx} & 0 \\[2mm] 0 & 0 & 0 & 0 & 0 & 2G_{xy} \end{bmatrix} \tag{6.2}$$

, where $\Delta = \dfrac{1-\nu_{xy}\nu_{yx}-\nu_{yz}\nu_{zy}-\nu_{zx}\nu_{xz}-\nu_{xy}\nu_{yz}\nu_{zx}}{E_x E_y E_z}$.

6.1.2 Electrical properties

BTO is a dielectric material with strong polarizations. The induced polarization density $\boldsymbol{P}$ induced by the applied electric field $\boldsymbol{E}$ is linearly related by

$$P = \varepsilon_0 \chi_e E = \varepsilon_0(\varepsilon_r - 1)E \tag{6.3}$$

, where ε_0 is the electric permittivity of free space and has a value of $8.854 \times 10^{-12} \, F \cdot m^{-1}$. ε_r is the relative permittivity of the material.

The electric displacement D is related to both polarization density P and electric field E by

$$D = \varepsilon_0 E + P = \varepsilon_0 \varepsilon_r E \tag{6.4}$$

For piezoelectric materials, however, the relative permittivity value also depends on the strain presented. The two permittivity values that generally used are at two extreme conditions: the free permittivity ε^T as the material is fully unconstrained, and the clamped permittivity ε^S, when the material is fully constrained. The two are linked by the piezoelectric coupling coefficient (as discussed next) by [220]

$$\varepsilon^S = \varepsilon^T(1 - \kappa^2) \tag{6.5}$$

Other conditions may also change the permittivity of a piezoelectric, like electric field and frequency.

6.1.3 Piezoelectricity
Piezoelectricity connects the electric quantities with mechanical quantities. The direct and converse piezoelectric effect have been described in Chapter 2. Piezoelectric coefficients (or constants) are defined to quantitatively describe the interaction of electric and mechanical quantities.

(a) Piezoelectric charge coefficient

As shown in Figure 5.1, the piezoelectric charge coefficient has two equivalent definitions. It can be described as the amount strain generated per unit of electric field applied. It can also be defined as the amount of polarization generated per unit of stress applied. This coefficient has a unit of $C \cdot N^{-1}$.

$$d = \frac{u}{E} = \frac{P}{T} = \begin{bmatrix} 0 & 0 & 0 & 0 & d_{15} & 0 \\ 0 & 0 & 0 & d_{24} & 0 & 0 \\ d_{31} & d_{32} & d_{33} & 0 & 0 & 0 \end{bmatrix} \tag{6.6}$$

(b) Piezoelectric voltage coefficient

Another constant that is also widely used is piezoelectric voltage coefficient. It describes the amount of strain experienced per unit of electrical displacement, or the amount of stress experienced per unit of electric field. It has a unit of $C \cdot m^{-2}$.

$$g = \frac{u}{D} = \frac{E}{T} \tag{6.7}$$

(c) Piezoelectric coupling coefficient

The electrical and mechanical energy, which are not shown in Figure 5.1, can be also coupled together by a piezoelectric coupling coefficient κ. This coefficient has the physical meaning of efficacy of energy transferred.

In summary, Figure 6.1 shows a map of mechanical and electrical properties and their connections in elastic and dielectric materials, which are the interest of this work.
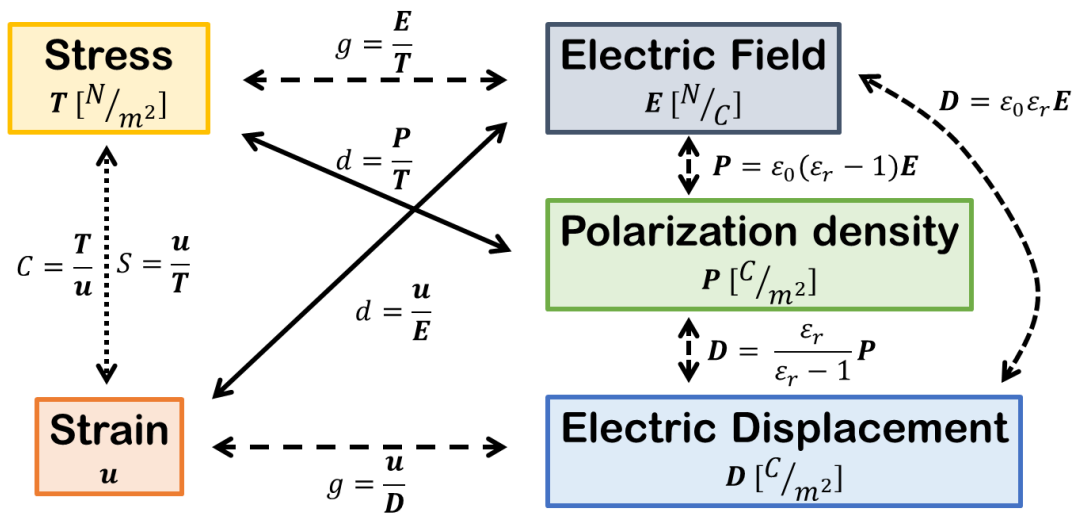
Figure 6. 1 The mechanical and electrical properties that are involved in this simulation. The relations between the properties are linked with equations.

6.1.4 Principal equations

In this work, electrostatic conditions are used, where only the electric fields from static charges are considered, while the moving charges are omitted. For a volume V in free space, the electric displacement field $\boldsymbol{D}$ can be derived by Gauss's Law:

$$\nabla \cdot \boldsymbol{D} = \rho_V \tag{6.8}$$

, where ρ_V is the electric charge density.

The electric potential, Φ, can be derived by Faraday's Law:

$$\Phi = -\int_r^\infty E dx \qquad (6.9)$$

, where E is the electric field.

For stress measures in stationary condition, 2nd Piola-Kirchhoff stress tensor S is used to relate the forces F_V and areas V in reference configuration by:

$$0 = \nabla \cdot S + F_V \qquad (6.10)$$

6.2 Procedures
6.2.1 Building object geometry

Object geometries were built to form a bulk model crystal using smaller pieces made of primary blocks. The bulk represents the nanocrystal, while the constituting primary blocks represent the domains inside the nanocrystal. The BTO crystals have rhombohedral, orthorhombic, tetragonal and cubic structures at different temperatures, all of which can be considered as pseudo cubic structure [70]. We are interested in modelling experimental strain patterns that form quadratic grids, so chose cubic shape geometries. This allows the shapes of domains to possibly preserve the facets of unit cells. The cubic shape geometries made up of 6×6×6 primary cubes were first built as a model for simulation, as shown in Figure 6.2a.

When it comes to the local structure, we note that BTO is reported to be locally rhombohedral in all crystal phases from both X-ray and neutron Pair Distribution Function (PDF) studies [172, 173, 205]. If considered as a pseudo cubic lattice, the rhombohedral unit cells have eight {111} directional polarizations. Eight {111} facets can be used to construct an octahedron in space, but such structures could not fill the space by themselves. Instead, {110} facets were used in this work to construct rhombic dodecahedron structures, as shown in Figure 6.2b. The structure was made up of five layers of rhombic dodecahedrons, which can fill the space alone and each has twelve {110} facets.
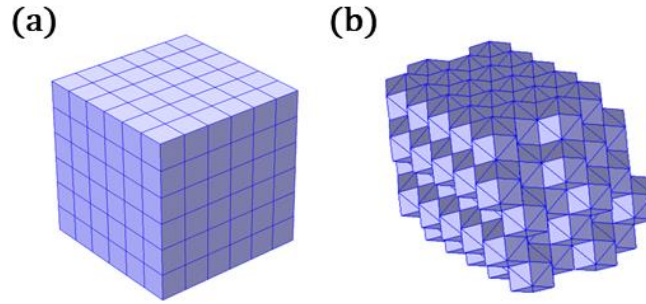
Figure 6. 2 Two object geometries that have been built for simulations in this work. (a) A cubic block with 6×6×6 primary cubes. (b) A layered bulk made up of 5 layers of primary rhombic dodecahedrons.

6.2.2 Defining materials properties

After the geometries were built in COMSOL, materials properties were then defined. The choice of relevant materials properties is determined by the specific problems and the relevant physics involved. Because BTO is both a ferroelectric and a piezoelectric material, both the mechanical and electrostatic properties need to be considered. The properties of BTO vary a lot depending on differences in preparation methods, which leads to different sample grain sizes and crystalline structures [73, 221-225]. There is also a big difference between crystals that are poled or unpoled, in "ceramic" form or single crystal form. The effect of BTO nanocrystal size on their properties was a hot topic dating back to the 1980s, with one popular example being the dramatic dielectric constant enhancement with sample sizes in the 100 nm to 1 μm range [226]. In this work, the "polycrystalline" BTO parameters are used in the COMSOL simulations, which appear to be close to the known properties of the commercial 200 nm BTO nanocrystals under investigation. These are shown in Table 6.1. Other parameters were also tried during the simulation, with some additional results listed in the Appendix.

Table 6. 1 BTO polycrystalline ceramics and single crystals properties that used in simulation [221].

Properties	Values
Density (ρ)	$5700 \ kg \cdot m^3$

172

Compliance matrix (C)	$\begin{bmatrix} 9.1 & -2.7 & -2.9 & 0 & 0 & 0 \\ -2.7 & 9.1 & -2.9 & 0 & 0 & 0 \\ -2.9 & -2.9 & 9.5 & 0 & 0 & 0 \\ 0 & 0 & 0 & 22.8 & 0 & 0 \\ 0 & 0 & 0 & 0 & 22.8 & 0 \\ 0 & 0 & 0 & 0 & 0 & 23.6 \end{bmatrix} \times 10^{-12}[Pa^{-1}]$	
Stiffness matrix (S)	$\begin{bmatrix} 15.04 & 6.56 & 6.59 & 0 & 0 & 0 \\ 6.56 & 15.04 & 6.59 & 0 & 0 & 0 \\ 6.59 & 6.59 & 14.55 & 0 & 0 & 0 \\ 0 & 0 & 0 & 4.39 & 0 & 0 \\ 0 & 0 & 0 & 0 & 4.39 & 0 \\ 0 & 0 & 0 & 0 & 0 & 4.24 \end{bmatrix} \times 10^{10}[Pa]$	
Free relative permittivity (ε_r^T)	$\begin{bmatrix} 1436 & 0 & 0 \\ 0 & 1436 & 0 \\ 0 & 0 & 1680 \end{bmatrix}$	
Clamped relative permittivity (ε_r^S)	$\begin{bmatrix} 1123 & 0 & 0 \\ 0 & 1123 & 0 \\ 0 & 0 & 1256 \end{bmatrix}$	
Piezoelectric charge coefficient (P_{001})	$\begin{bmatrix} 0 & 0 & 0 & 0 & 27 & 0 \\ 0 & 0 & 0 & 27 & 0 & 0 \\ -7.9 & -7.9 & 19.1 & 0 & 0 & 0 \end{bmatrix} \times 10^{-11}[C \cdot N^{-1}]$	
Piezoelectric voltage coefficient ($P_{s_{001}}$)	$\begin{bmatrix} 0 & 0 & 0 & 0 & 11.4 & 0 \\ 0 & 0 & 0 & 11.4 & 0 & 0 \\ -4.3 & -4.3 & 17.4 & 0 & 0 & 0 \end{bmatrix} [C \cdot m^{-2}]$	

Each primary block in Figure 6.2 was considered as a separate domain. Inside the domain, all the unit cells are assumed to hold the same piezoelectric coefficients. Different domains are assumed to hold the same mechanical and electrical properties but allowed to differ in piezoelectric coefficients. In this way, the domains with different piezoelectric coefficients would generate different charges when experiencing the same strain. Equivalently, the blocks would generate different strain when facing the same surface charge.

The piezoelectric coefficients of BTO polycrystalline ceramics in Table 6.1 would generate a net charge in the Z direction when experiencing strain from any directions. These piezoelectric coefficients could be rotated 90° along X and Y axis to acquire the coefficients that generate net charge on the X and Y directions, as shown in (6.11) and (6.12).

P_{100}

$$= \begin{pmatrix} -7.90 \times 10^{-11} & -7.90 \times 10^{-11} & 1.91 \times 10^{-10} & 0 & 0 & 0 \\ 0 & 0 & 0 & 2.70 \times 10^{-10} & 0 & 0 \\ 0 & 0 & 0 & 0 & -2.70 \times 10^{-10} & 0 \end{pmatrix} \quad (6.11)$$

P_{010}

$$= \begin{pmatrix} 0 & 0 & 0 & 0 & 2.70 \times 10^{-10} & 0 \\ -7.90 \times 10^{-11} & -7.90 \times 10^{-11} & 1.91 \times 10^{-10} & 0 & 0 & 0 \\ 0 & 0 & 0 & -2.70 \times 10^{-10} & 0 & 0 \end{pmatrix} \quad (6.12)$$

The orientations of piezoelectric coefficients P_{100} and P_{010} are different, meaning that electric charge at different directions will be generated when experiencing same forces. The values are the same, meaning that the magnitudes of electric charges generated by the same forces are also the same. The definitions of piezoelectric coefficients are listed in equation 2.17.

For example, in equation 6.11, $d_{31} = 1.91 \times 10^{-10} \, C \cdot N^{-1}$, meaning that the crystal will generate 1.91 C charge at X direction when experience a force from Z direction. While in equation 6.12, $d_{32} = 1.91 \times 10^{-10} \, C \cdot N^{-1}$. When experiencing the same force from Z direction, it generates the 1.91 C in Y direction rather than X direction.

Similarly, the {111} piezoelectric coefficients could also be derived by the rotation of P_{001}. The transformed polarization matrices are shown in (6.13) to (6.20):

P_{111}

$$= \begin{pmatrix} -4.56 \times 10^{-11} & -4.56 \times 10^{-11} & 1.10 \times 10^{-10} & -5.71 \times 10^{-11} & 2.13 \times 10^{-10} & 0 \\ -4.56 \times 10^{-11} & -4.56 \times 10^{-11} & 1.10 \times 10^{-10} & 2.13 \times 10^{-10} & -5.71 \times 10^{-11} & 0 \\ -4.56 \times 10^{-11} & -4.56 \times 10^{-11} & 1.10 \times 10^{-10} & -1.56 \times 10^{-10} & -1.56 \times 10^{-10} & 0 \end{pmatrix} \quad (6.13)$$

P_{-111}

$$= \begin{pmatrix} 4.56 \times 10^{-11} & 4.56 \times 10^{-11} & -1.10 \times 10^{-10} & 5.71 \times 10^{-11} & 2.13 \times 10^{-10} & 0 \\ -4.56 \times 10^{-11} & -4.56 \times 10^{-11} & 1.10 \times 10^{-10} & 2.13 \times 10^{-10} & 5.71 \times 10^{-11} & 0 \\ -4.56 \times 10^{-11} & -4.56 \times 10^{-11} & 1.10 \times 10^{-10} & -1.56 \times 10^{-10} & 1.56 \times 10^{-10} & 0 \end{pmatrix} \quad (6.14)$$

P_{1-11}

$$= \begin{pmatrix} -4.56 \times 10^{-11} & -4.56 \times 10^{-11} & 1.10 \times 10^{-10} & 5.71 \times 10^{-11} & 2.13 \times 10^{-10} & 0 \\ 4.56 \times 10^{-11} & 4.56 \times 10^{-11} & -1.10 \times 10^{-10} & 2.13 \times 10^{-10} & 5.71 \times 10^{-11} & 0 \\ -4.56 \times 10^{-11} & -4.56 \times 10^{-11} & 1.10 \times 10^{-10} & 1.56 \times 10^{-10} & -1.56 \times 10^{-10} & 0 \end{pmatrix} \quad (6.15)$$

P_{-1-11}

$$= \begin{pmatrix} 4.56 \times 10^{-11} & 4.56 \times 10^{-11} & -1.10 \times 10^{-10} & -5.71 \times 10^{-11} & 2.13 \times 10^{-10} & 0 \\ 4.56 \times 10^{-11} & 4.56 \times 10^{-11} & -1.10 \times 10^{-10} & 2.13 \times 10^{-10} & -5.71 \times 10^{-11} & 0 \\ -4.56 \times 10^{-11} & -4.56 \times 10^{-11} & 1.10 \times 10^{-10} & 1.56 \times 10^{-10} & 1.56 \times 10^{-10} & 0 \end{pmatrix} \text{(6.16)}$$

P_{11-1}

$$= \begin{pmatrix} -4.56 \times 10^{-11} & -4.56 \times 10^{-11} & 1.10 \times 10^{-10} & -2.13 \times 10^{-10} & 5.71 \times 10^{-11} & 0 \\ -4.56 \times 10^{-11} & -4.56 \times 10^{-11} & 1.10 \times 10^{-10} & 5.71 \times 10^{-11} & -2.13 \times 10^{-10} & 0 \\ 4.56 \times 10^{-11} & 4.56 \times 10^{-11} & -1.10 \times 10^{-10} & -1.56 \times 10^{-10} & -1.56 \times 10^{-10} & 0 \end{pmatrix} \text{(6.17)}$$

P_{-11-1}

$$= \begin{pmatrix} 4.56 \times 10^{-11} & 4.56 \times 10^{-11} & -1.10 \times 10^{-10} & 2.13 \times 10^{-10} & 5.71 \times 10^{-11} & 0 \\ -4.56 \times 10^{-11} & -4.56 \times 10^{-11} & 1.10 \times 10^{-10} & 5.71 \times 10^{-11} & 2.13 \times 10^{-10} & 0 \\ 4.56 \times 10^{-11} & 4.56 \times 10^{-11} & -1.10 \times 10^{-10} & -1.56 \times 10^{-10} & 1.56 \times 10^{-10} & 0 \end{pmatrix} \text{(6.18)}$$

P_{1-1-1}

$$= \begin{pmatrix} -4.56 \times 10^{-11} & -4.56 \times 10^{-11} & 1.10 \times 10^{-10} & 2.13 \times 10^{-10} & 5.71 \times 10^{-11} & 0 \\ 4.56 \times 10^{-11} & 4.56 \times 10^{-11} & -1.10 \times 10^{-10} & 5.71 \times 10^{-11} & 2.13 \times 10^{-10} & 0 \\ 4.56 \times 10^{-11} & 4.56 \times 10^{-11} & -1.10 \times 10^{-10} & 1.56 \times 10^{-10} & -1.56 \times 10^{-10} & 0 \end{pmatrix} \text{(6.19)}$$

P_{-1-1-1}

$$= \begin{pmatrix} 4.56 \times 10^{-11} & 4.56 \times 10^{-11} & -1.10 \times 10^{-10} & -2.13 \times 10^{-10} & 5.71 \times 10^{-11} & 0 \\ 4.56 \times 10^{-11} & 4.56 \times 10^{-11} & -1.10 \times 10^{-10} & 5.71 \times 10^{-11} & -2.13 \times 10^{-10} & 0 \\ 4.56 \times 10^{-11} & 4.56 \times 10^{-11} & -1.10 \times 10^{-10} & 1.56 \times 10^{-10} & 1.56 \times 10^{-10} & 0 \end{pmatrix} \text{(6.20)}$$

6.2.3 Defining domains packing orders

For the cubic cell model, both {111} and {001} cubes are utilized to construct different domain packing orders as shown in Figure 6.3. To simplify the packing order determinations and simulations, different packing orders were constructed in a 2×2×2 block, which were then periodically expanded in three directions to form the 6×6×6 bulk.

Four rhombohedral packing orders, which only uses {111} polarized blocks, are listed in Figure 6.3(b) to 6.3(e). The packing order in Figure 6.3(b) would have a global polarization along (001) direction. This is to simulate the local structure model revealed by PDF, in which the BTO crystals have a local rhombohedral structure but a global tetragonal lattice at room temperature [172, 173, 205]. The packing order in Figure 6.3(c) and (d) would have zero net polarization. This is to simulate a local rhombohedral structure that combine to a cubic lattice at elevated temperature. Figure 6.3(e) shows an example in which the {111} polarizations are forming a closed loop, which resemble the vortices seen in

PTO/STO thin film [139, 140]. Figure 6.3(f) and 6.3(g) shows the packing order of 180° and 90° domains, respectively. They only involved {001} polarized blocks.
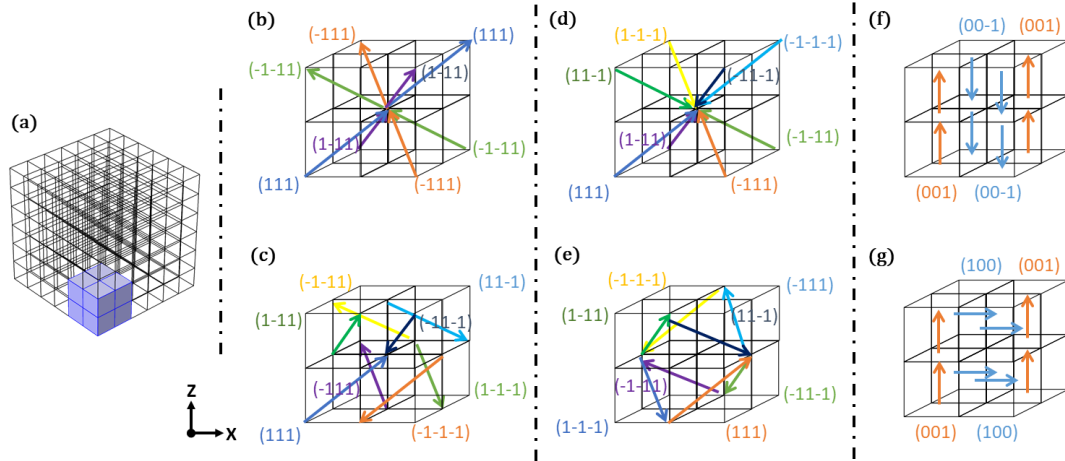
Figure 6. 3 (a) To simplify the simulation, a 2×2×2 block of cubes was chosen from the 6×6×6 bulk to perform as a packing base. (b)-(e) Different combinations of {111} polarized cubes. (f)-(g) Two combinations using {001} polarized cubes.
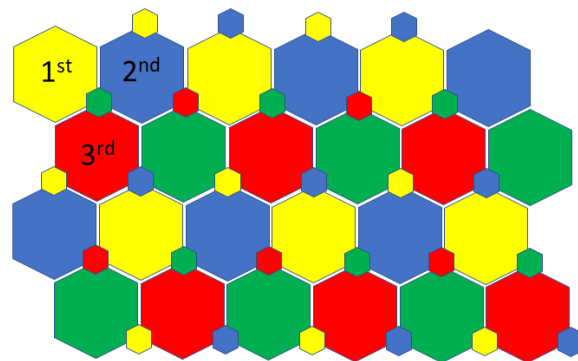
Figure 6. 4 One example that shows the packing of rhombic dodecahedrons. Different colours represent different properties, so that the blocks with the same colour have the same properties. The two adjacent blocks are restricted to have different properties. Once the 1st, 2nd and 3rd blocks are determined, the allocation of the properties (colours) of other blocks in the model are determined.

Each rhombic dodecahedron has 12 facets. Four of the eight {111} oriented piezoelectric coefficients, which have positive polarization along {001} direction, are defined to a closed-packed rhombic dodecahedron model. To satisfy the condition that each pair of adjacent dodecahedrons have different piezoelectric coefficients, the packing freedom is restricted to the first 3 dodecahedrons

packing order. As shown in Figure 6.4, once the 1st-3rd dodecahedrons are determined, the packing of the whole model is determined by translation and extrapolation.

6.2.4 Meshing the grid and solving the equations

The correct meshing of geometries should reduce the memory consumption and increase the accuracy and speed of the calculation. COMSOL has options for a "physics-controlled" mesh and a user-defined mesh available. For the physics-controlled mesh, tetrahedral elements are used to mesh the geometry, with more elements at the most important regions such as the boundary or the vortex of the structure. Through user-defined mesh, more freedoms are unlocked. There are four types of elements available in the user-defined mesh: tetrahedral, hexahedral, triangular prims and pyramids. Also, the choice of which domain to mesh finer and which to do a coarser mesh is also available.

In this work, the default physics-controlled mesh was used with "Finer" precision to ensure reasonable resolution and limited calculations. The mesh has been built for the two geometries shown schematically in Figure 6.5. The stationary solver was invoked to deal with static problems with a relative tolerance threshold of 0.001.
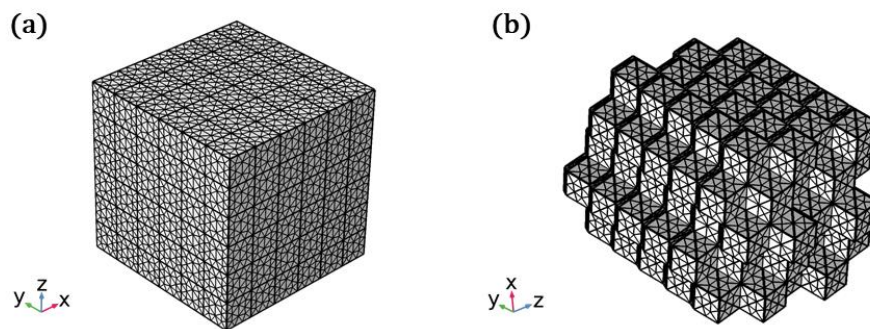
Figure 6. 5 Grid mesh of the geometries used in this work.

To test if the mesh grid is sufficient, the convergence study is performed. Figure 6.6 shows the simulation using different mesh precision. The simulated strains in XZ slices are shown for comparison. It could be seen that the strain distribution varies a bit from 'Extremely coarse' to 'Coarse'. The strain patterns from 'Coarse' to 'Extra fine' looks the same, which indicates the solution is converged when the

gird is smaller than the size in 'Coarse'. Therefore, the 'Finer' precision is sufficient enough for this study.
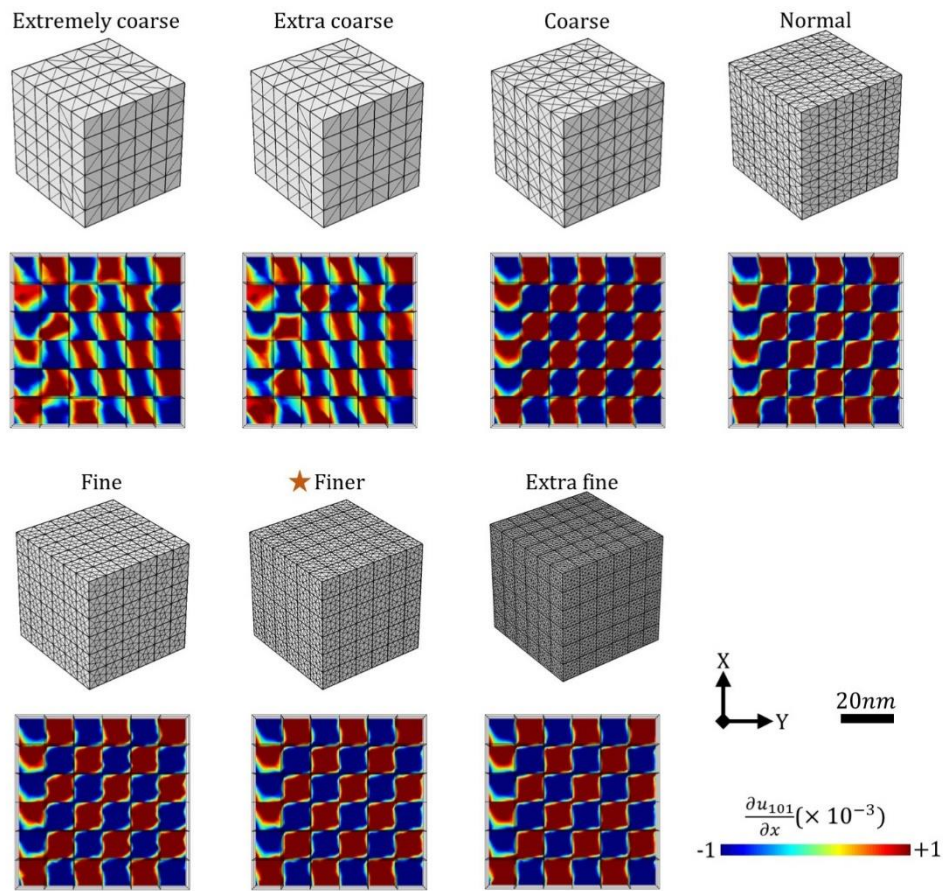
Figure 6. 6 The simulated strain patterns from different precision of meshing grid.

Of all the models that have been simulated during this work, several models gave results that partially match the experimental data. These are illustrated in the next part.

6.3 Simulated results

The main interest of the simulation study is to see how the cubes or dodecahedrons are interacting or fitting with each other, so as to give a strain pattern in space. The focus of the study is the strain pattern phenomenon, rather than testing the theory behind it. Therefore, the boundary conditions are linearly adjusted to better show the strain pattern.

6.3.1 180° domain packing

180° domains are widely found in tetragonal BTO crystals. The only structure difference between the two adjacent domains is that the Ti⁴⁺ displacement directions are opposite, so are the polarizations. The domain definitions are shown in Figure 6.7(a) and (b), while the boundary condition is listed in Figure 6.7(c). The simulations were then performed, and the simulated displacements were calculated. Figure 6.7 (d) to (f) shows three orthogonal displacement field in one XY slice. The displacement field in u_{100} is accumulated along vertical direction at an order of 10^{-12} m, which are not seen in other two displacement fields.
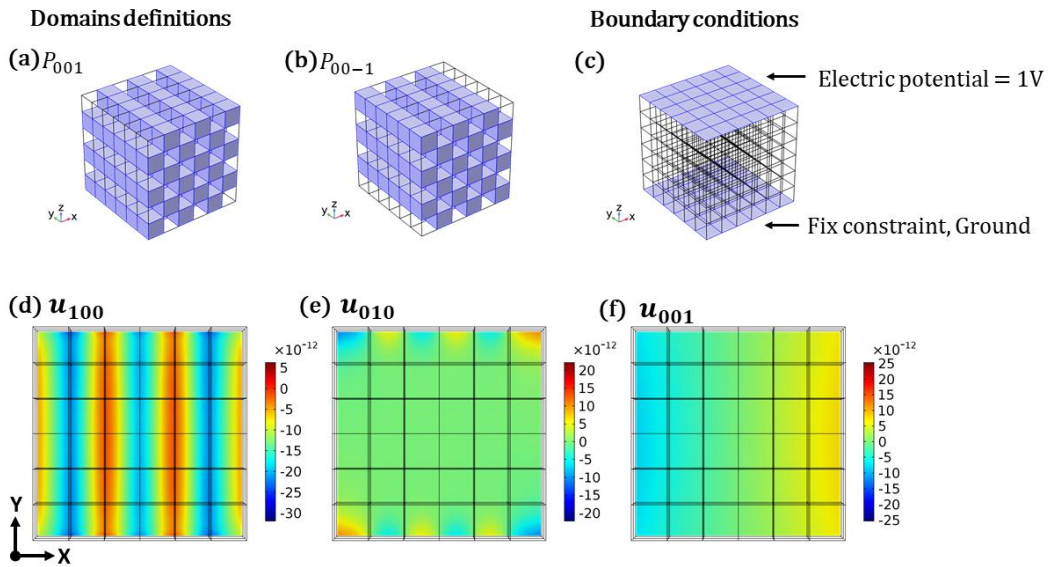
Figure 6. 7 (a)&(b) The domain definitions. (c) The boundary conditions. (d) to (f) The simulated displacement field.

The strain fields were calculated next from the displacement field. Figure 6.8 presents the six strain components in one XY slice. Vertical distributed strain field could be seen in $\partial u_{100}/x$ and $\partial u_{001}/z$, both of which are direct strain component.
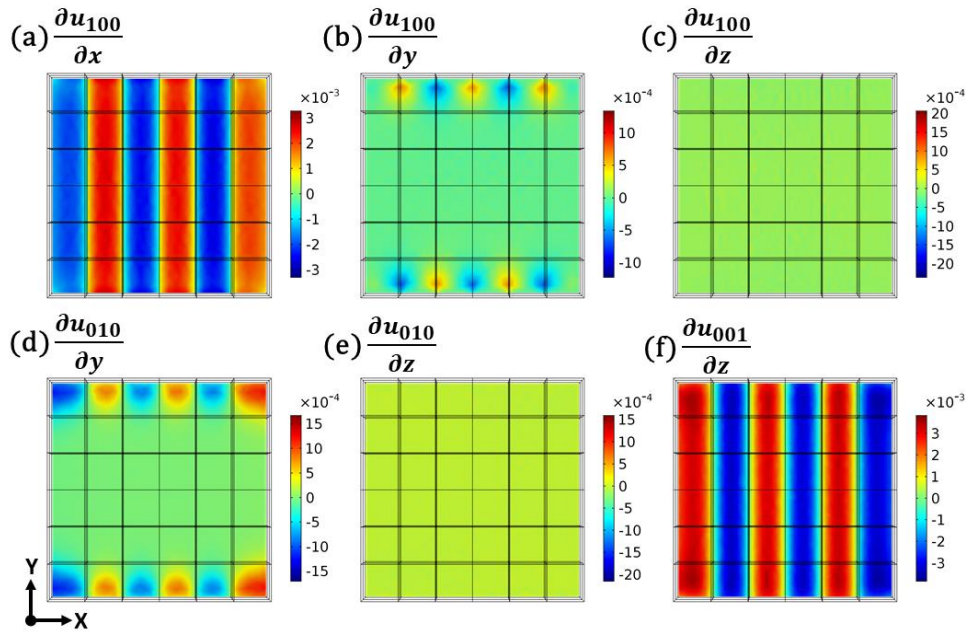
Figure 6. 8 The simulated strain tensors in one XY slice are shown.

After getting the typical strain tensors, the combination of the certain strain components was added up together to simulate the strain field seen in BCDI experiments. The equations are listed in Eq. (4.4) to Eq. (4.6) in Chapter 4. Figure 6.9 shows the simulated strain fields. Of all the nine views to show the strain distributions, two views show vertical strain stripes, and another two views show horizontal strain stripes. There are another two views show strain stripes along the diagonal, which is 45° inclined to the X and Z direction. The remaining three views have weak strain distributions.
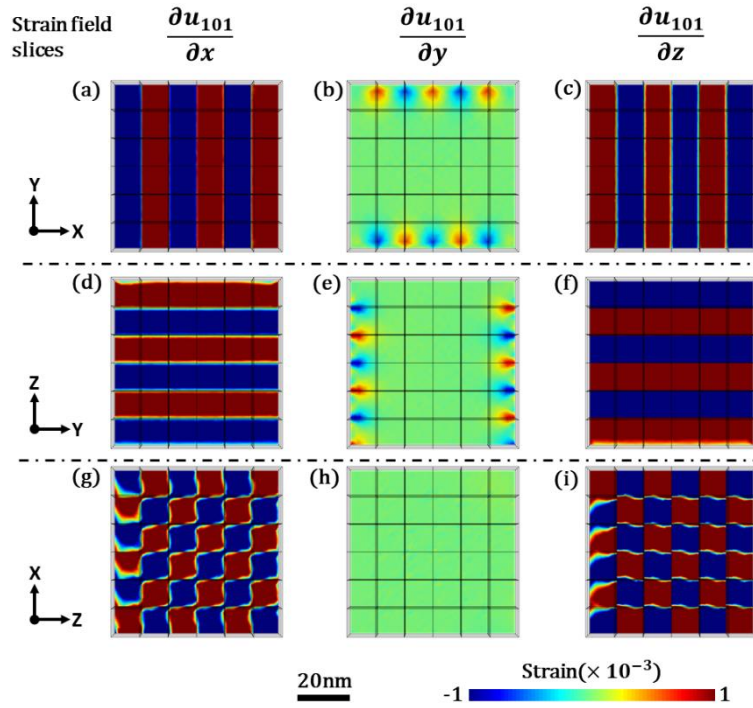
Figure 6. 9 The simulated strain field are presented.

Except the boundary conditions seen in Figure 6.7(c) where the electric potential is applied onto different facets than the piezoelectric blocks array direction, other boundary conditions were also tried. Figure 6.10 shows some boundary conditions and one slice on simulated strain pattern. Because the system involves both mechanical and electrical fields, and the place where the conditions are applied would make a difference. This is same in the real case, where the crystal is surrounded by masses of other crystals. Therefore, we tested different boundary conditions and only selected the best one that fit to our experimental data.
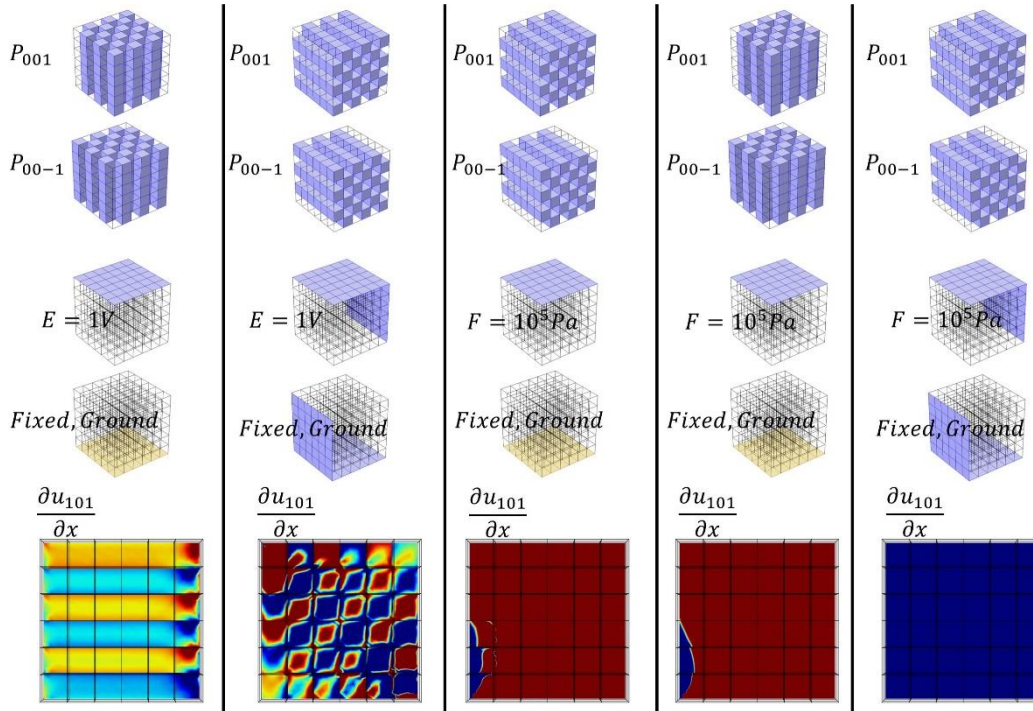
Figure 6. 10 The simulated strain patterns from different boundary conditions and 180° domains arrangement.

6.3.2 90° domain packing

The 90° domains are also commonly found in tetragonal BTO crystals. The packing orders and boundary conditions are shown in Figures 6.11(a) to (c). Figures 6.11(d) to (l) present the simulated results. All the three views showing strain gradient along the X direction have only positive strain distributions. One view in the strain gradient along Y direction shows strain accumulation on the vertices inside the model. This gives a strain distribution close to the diagonal direction. The three views of strain gradient along the Z direction show diagonal, vertical and horizontal stripes accordingly.
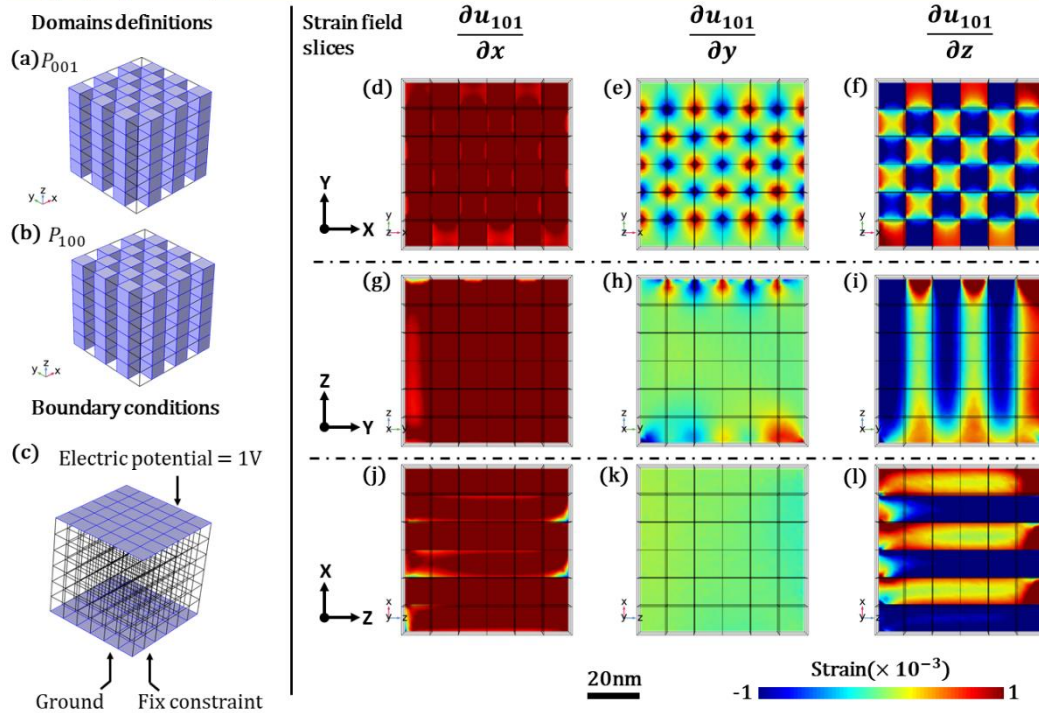
Figure 6. 11 The domain definition, boundary condition and simulated results for a 90° domains packing.

6.3.3 Rhombohedral domain packing

The rhombohedral domains packing order in Figure6.4 is extended into the whole model and shown in Figure 6.12(a) to (d). The simulation results are shown in Figure 6.12(g) to (o). There are two views showing vertical strain stripes and two others showing horizontal stripes. There are another two views showing strain accumulated on the boundaries of inner blocks, which resemble a strain distribution along the diagonal. The three views of strain gradient along the Z direction show only the compressive strain.
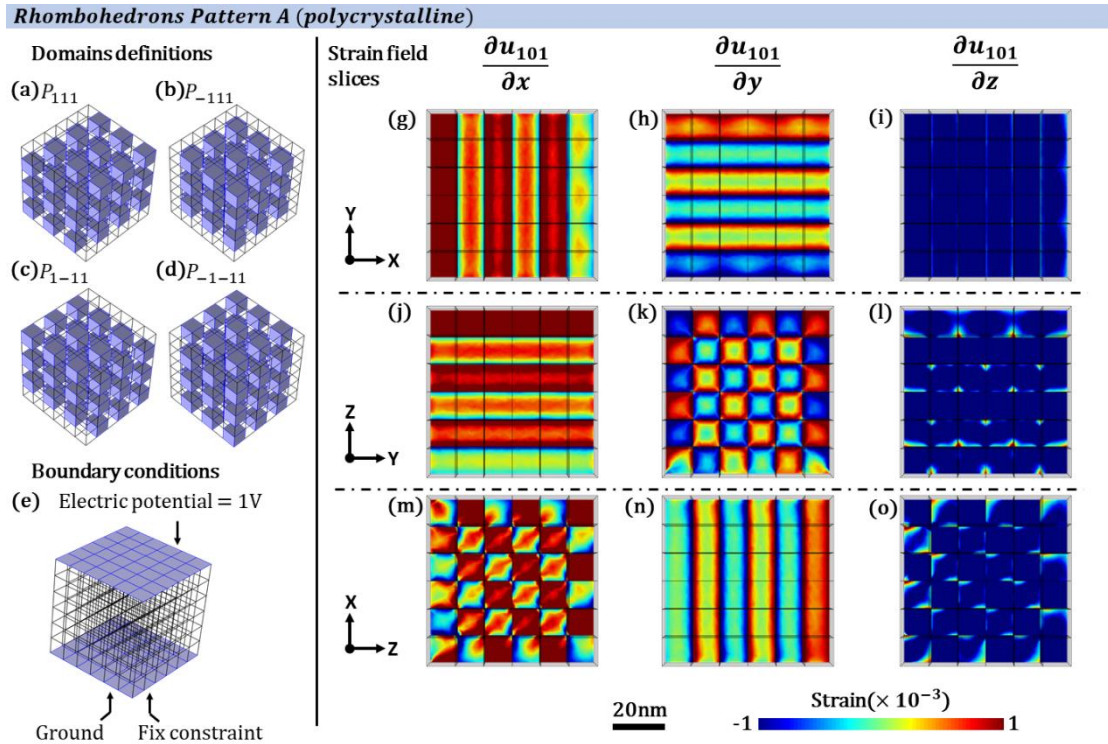
Figure 6. 12 The domain definition, boundary condition and simulated results for the rhombohedral domains defined in Figure 6.3(b).

The extension of packing order in Figure 6.3(c) are shown in Figure 6.13(a) to (h). The simulated results are showing in Figure 6.13(g) to (o). There are two views which have horizontal strain stripes but only one view showing horizontal strain stripes. The diagonal distributed strain stripes exist in two of the views. All the views of strain gradient along Z direction have complicated strain distributions.

184
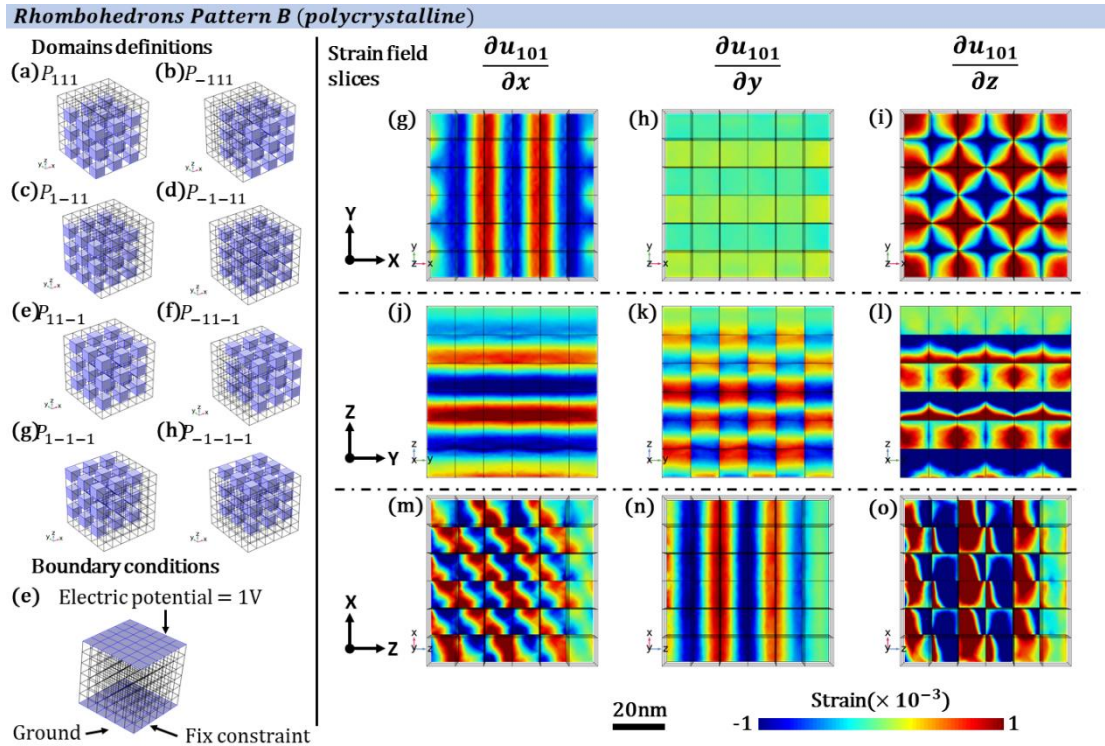
Figure 6. 13 The domain definition, boundary condition and simulated results for the rhombohedral domains defined in Figure 6.3(c).

Figure 6.14 and 6.15 shows the simulation results from domain packing in Figure 6.3(d) and 6.3(e). The strain distributions are rather complicated. In both cases, the XY views show diffuse strain distribution, while YZ views and XZ views show small strain stripes horizontal and vertically. The sizes of the strain stripes are smaller than the block size, typically around 3nm.
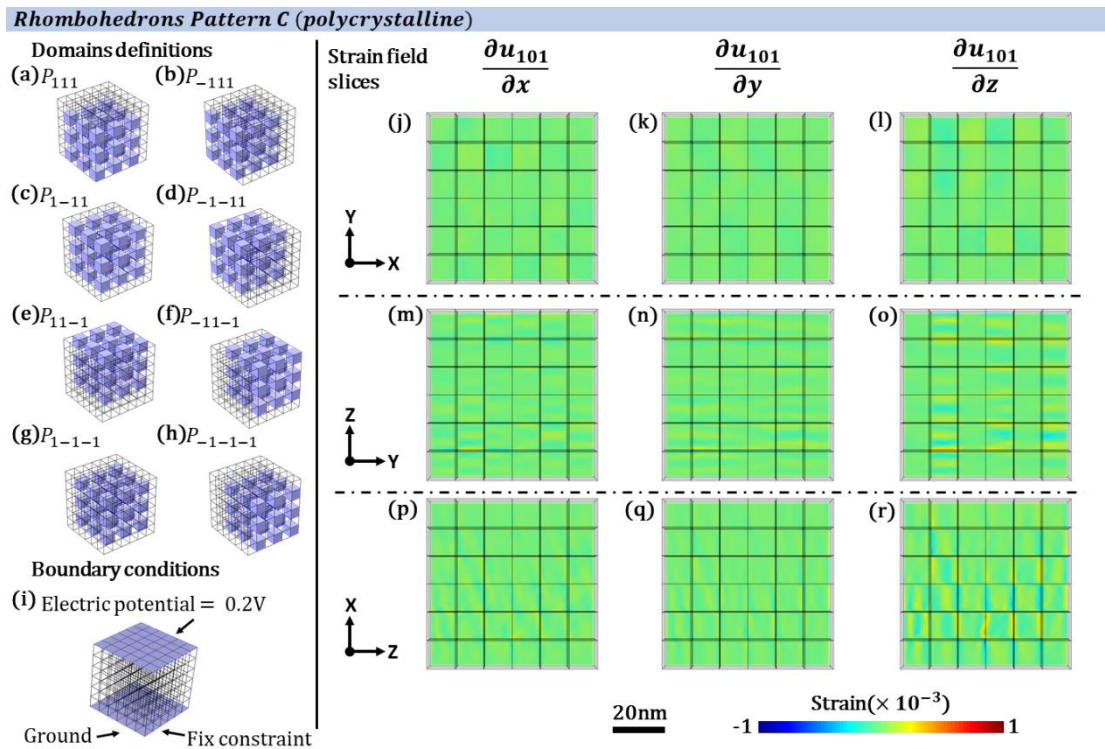
Figure 6. 14 The domain definition, boundary condition and simulated results for the rhombohedral domains defined in Figure 6.3(d).
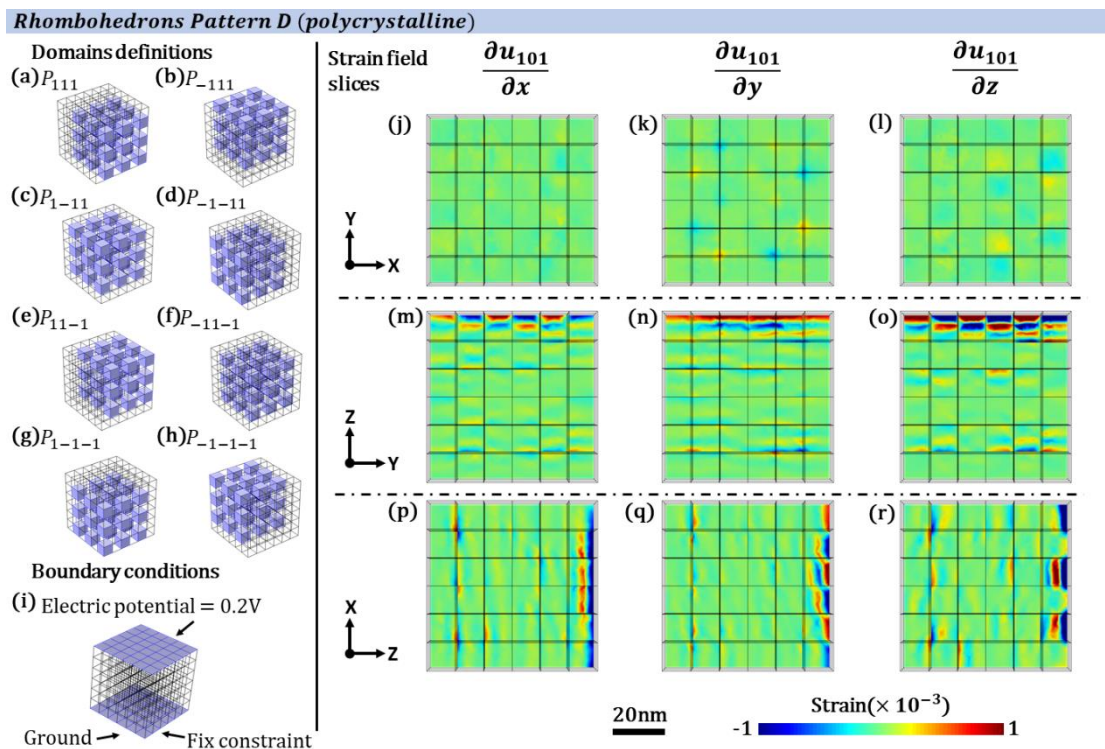
Figure 6. 15 The domain definition, boundary condition and simulated results for the rhombohedral domains defined in Figure 6.3(e).

186
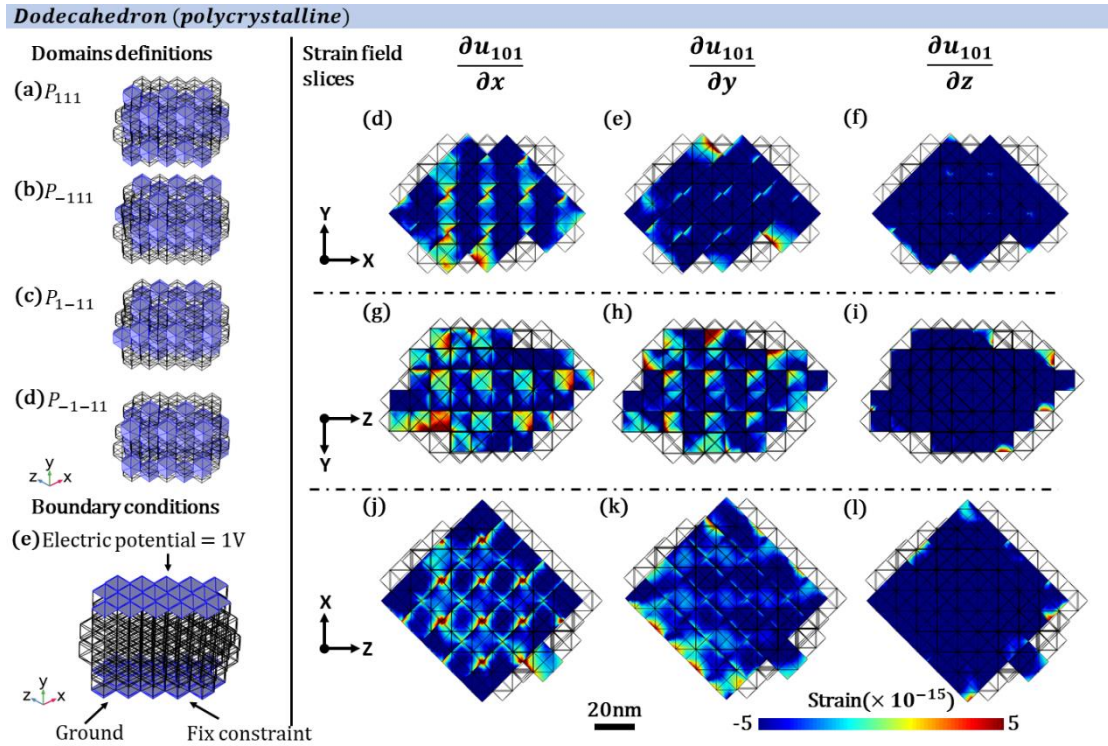
Figure 6. 16 The domain definition, boundary condition and simulated results for the rhombohedral domains in rhombic dodecahedron model.
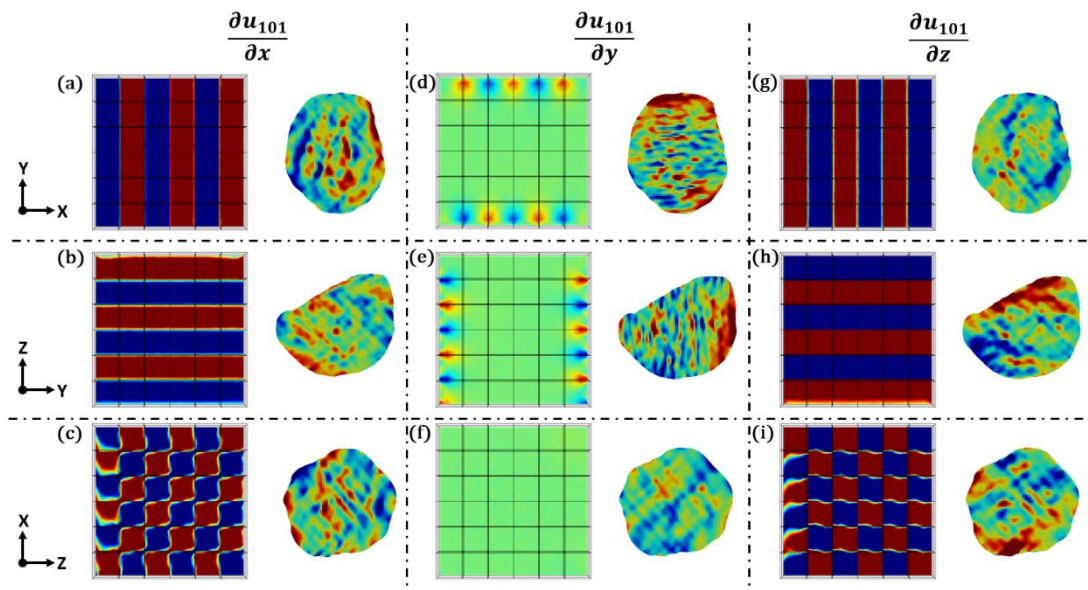
Figure 6. 17 The side-by-side view for comparison. The simulated results are from the simulation of 180 domain packing. The experimental results are from crystal BTO-32 presented in Chapter 4.

Figure 6.16 presents the simulated results using the rhombic dodecahedron model. Four {111} polarizations are defined on the blocks as shown in Figure

6.16 (a) to (d). All the nine views show a dominant distribution of compressive strain.

In summary, different models have been simulated and tested in this Chapter. The model that best fits the results in Chapter 4 is the one containing 180° domain walls. For this 180° domains wall model, there are horizontal, vertical and diagonal strain stripes distributions, which are all seen in the strain images of the crystal studied in Chapter 4. It should be noted that even the best fitting model only partially matches the experimental results. Figure 6.17 shows a side-by-side view of the simulated results and experimental data. Some views have their strain stripe direction matched, but others are not. But the features are clear: there are horizontal, vertical and diagonal strain stripes all over the crystal.

Chapter 7. Unusual breathing behavior of optically excited Barium Titanate nanocrystals

Jiecheng Diao[1], Mathew Cherukara[3], Ross Harder[3], Xiaojing Huang[2], Fucai Zhang[1,4], Bo Chen[1,5], Andrew Ulvestad[3], Sanghoon Song[6], Diling Zhu[6], David Keen[7] and Ian Robinson[1,2,*]

[1] University College, London, WC1E 6BT, UK; i.robinson@ucl.ac.uk (I.R.); jiecheng.diao.18@ucl.ac.uk (J.D.)

[2] Brookhaven National Laboratory, Upton NY 11973, USA; xjhuang@bnl.gov (X.H.);

[3] Argonne National Laboratory, Argonne IL 60439, USA; mcherukara@anl.gov (M.C.); rharder@anl.gov (R.H.); aulvestad@anl.gov (A.U.)

[4] Southern University of Science and Technology, Shenzhen 518055, China; zhangfc@sustech.edu.cn (F.Z.)

[5] School of Materials Science and Engineering, Tongji University, Shanghai 201804, China; bo.chen@tongji.edu.cn (B.C.)

[6] SLAC National Accelerator Laboratory, Menlo Park, CA 94025, USA; sanghoon@slac.stanford.edu (S.S.); dlzhu@slac.stanford.edu (D.Z.)

[7] Rutherford Appleton Laboratory, Harwell Oxford, Didcot OX11 0QX, UK; david.keen@physics.ox.ac.uk (D.K.)

*Correspondence: i.robinson@ucl.ac.uk

Abstract: Coherent X-ray Diffraction patterns were recorded using an X-ray Free-electron Laser illuminating Barium Titanate nanocrystals as a function of time delay after laser excitation. Rather than seeing any significant thermal expansion effects, the diffraction peaks were found to move perpendicular to the momentum transfer direction. This suggests a laser driven rotation of the crystal lattice, which is delayed by the aggregated state of the crystals. Internal deformations associated with crystal contacts were also observed.

Keywords: X-ray pump-probe; coherent imaging; ferroelectric oxide

7.1 Introduction

Barium Titanate, $BaTiO_3$ (BTO), is an important ferroelectric material, which was first used to explain the coupling of lattice distortions with phonon mode softening, leading to its ferroelectric structure [246]. It has the classical phase diagram for a perovskite oxide material, with a cubic structure at high temperature, becoming tetragonal below $T_C = 393$ K and then orthorhombic

below $T_2 = 273$ K [47]. The room temperature tetragonal phase is ferroelectric with an electric polarization along its c-axis attributed to displacement of the perovskite B-site Ti^{4+} ion with respect to the A-site Ba^{2+}, locally displaced towards the unit cell corners.

Nanosized BTO is an important industrial material for making supercapacitors. BTO's dielectric constant peaks as a function of size with a maximum around 140 nm with a factor of three enhancement of dielectric constant resulting in a big improvement in capacitor performance [93]. A major industry is currently building up for energy storage, which is of significant interest in Energy Sciences. Although BTO has clear structural phase transitions, there are studies showing local rhombohedral distortion even in the cubic phase [56,59]. A powder diffraction study proposed a core-shell structure for the nanoparticles, in which the core is tetragonal, and the shell is cubic [147]. The dynamical aspects of this model could in principle explain the enhancement of dielectric constant.

Previous experiments on pump-probe diffraction from BTO thin films at the Linac Coherent Light Source (LCLS) showed a small lattice expansion, but no direct piezoelectric response [234]. A fast sub-10 ps transient increase of the 003 peak intensity was detected, followed by a shift of the rocking curve to lower angles on an acoustic response time of 15 ps. The response indicates a lattice expansion of 0.04% and 0.11% in two different experiments using THz illumination. The expansion was reported to be linear in fluence and attributed to enhanced vibrations of the Ti^{4+} ion, analogous to transient heating, subsequently relaxing on a time scale of 10 ns.

Bragg Coherent Diffraction Imaging (BCDI) is a powerful X-ray technique for investigating the structures of nanocrystals in three dimensions on the 30nm resolution scale [192]. By using an area detector far enough from the sample, the fringes surrounding a Bragg diffraction peak, due to the external shape of the crystals, can be oversampled with respect to their spatial Shannon-Nyquist frequency. Such data can be inverted to images using iterative algorithms, namely the Error Reduction and Hybrid Input-Output methods [19]. These methods depend on a well-defined spatial support function, used as the real-space constraint, which can be provided by a "shrink-wrap" approach [24]. The

advantage of BCDI, which is important here, is its high sensitivity to the distribution of nano-scale strains inside the nanocrystal under investigation [235]. BCDI is a 3D imaging method that is particularly valuable for probing the responses of individual nano-sized crystal grains embedded in an in-situ environment, such as a polycrystalline material, a battery electrode or a working catalyst particle. More details about Bragg coherent diffraction imaging can be found in other specialized reviews [11,13,17,236-240]. In this work, BCDI is combined with laser excitation of the samples in a pump-probe approach to obtain ultrafast time-resolved images of internal strain fields [221].

7.2 Materials and Methods

Barium Titanate (BTO) nanocrystals were obtained commercially from Sigma-Aldrich and were assumed to have been fabricated by hydrothermal synthesis. The crystals were found by Scanning Electron Microscopy (SEM) to have roughly spherical shapes and a size distribution cantered at 200 nm. Crystals were drop-cast from ethanol suspension onto a Si3N4 (SiN) window array provided by Silson. The crystals were bonded to the substrate using 1% Tetraethyl Orthosilicate (TEOS) as an adhesive and calcined in air at 723 K [192]. No particular care was taken to ensure that the crystals were separated from each other on the substrate. They were found to be clustered together in aggregates, which was found to have consequences for the laser excitation described below.

The transmission geometry was used to measure Coherent X-ray Diffraction patterns of the samples. We had previously found [241] this led to slightly higher damage thresholds for the samples to become detached from the substrate by radiation pressure, at least with respect to the commonly used grazing incidence geometry [242]. The samples were mounted on the Huber diffractometer of the X-ray Pump-Probe (XPP) station of the LCLS, an X-ray Free Electron Laser (XFEL) at Stanford.   The 9 keV X-ray beam was focused with in-line X-ray Compound Refractive Lenses (CRLs) and 10-15% attenuators were used to stay below the X-ray damage threshold, as detected by sudden loss of diffraction peaks. 120 Hz repetition rate was used.   2D and 3D Bragg Coherent Diffraction Imaging (BCDI) data at a range of delay times were collected on the CS-Pad detector (pixel size 110 μm) placed 1.575 m downstream of the sample

at 27° Bragg angle in the vertical scattering-plane geometry. After mapping the general behaviour, discussed below, we selected about six nanocrystals for detailed BCDI measurement over 36 hours of "standard configuration" operations at LCLS.

The XPP Ti-sapphire laser was synchronized with the X-ray beam via a motorized delay line, allowing pump-probe delays up to several nanoseconds. The beam came down through the hutch roof and was directed onto the sample by the final focusing mirror on a collinear geometry with about 2° inclination. Temporal overlap was calibrated with a Bi standard. Spatial overlap was set with phosphor screens and checked using diffraction effects seen from the actual samples, as well as with some Au standard crystals [242]. The laser was used on the third harmonic, with wavelength 266 nm, to excite the sample above its band gap of 5 eV. Manual adjustments were made initially of the time delay and the beam position on the sample to explore the response to the laser with a real-time display. Then time-delay scans were made on aligned samples to extract quantitative values for the Bragg peak position on the detector to learn about the laser induced changes of the crystal structure.

7.3 Results

Previous experiments on metal nanocrystals have measured radial oscillatory Bragg peak movements on the detector. These are identified as breathing modes of crystal vibration in which the crystal expands and contracts with a period given by the ratio of the speed of sound to the crystal size [23]. These vibrations represent the impulse response of the crystal to a short thermal pulse applied homogeneously throughout the crystal. The Two Temperature Model (2TM) [243] is invoked to explain how the optical excitation reaches the entire nanocrystal faster than the sound velocity: the optical absorption is relayed by hot electrons which travel rapidly through the crystal before equilibrating their temperature with the lattice. Both the electron transport and electron-phonon coupling take place on a time scale of around 1ps, significantly faster than the acoustic response of the crystal, for which the vibration period is consistent with the speed of sound in the material.

In this study, BTO nanocrystals have tetragonal structure at room temperature with lattice constants close to a=3.99 Å and c=4.01 Å. The split of (110) and (001) Bragg peak is 0.107° at 9 KeV, which is covered by the angle range of detector. We observed two clear Debye-Scherrer (DS) powder rings of spots corresponding to the tetragonally distorted (110) and (101) diffraction peaks. At different positions on the sample, peaks were found to lie along two powder rings separated by 0.107°, as expected. From any single shot of any area on the sample, we saw at least 3-4 diffraction peaks, always located on one or the other powder ring. The spots from individual nanocrystals were well-separated and the number of peaks on the outer (110) ring was roughly half the number on the inner (101) ring, consistent with the multiplicity. Unexpectedly, during real-time monitoring of the diffraction pattern during laser excitation, we found that some of the diffraction spots moved around the DS ring, transverse to the scattering vector direction. This motion reversed when the laser was turned off. Some other spots showed a blinking behaviour, becoming less or more intense upon excitation. Both the pattern movement around the DS ring and blinking are further explored in the time delay scanning study described in the next section. There were also many diffraction spots which did not respond at all to the laser, a behaviour we attribute to blocking of the laser by other nanocrystals within the clusters of crystals seen in the SEM. No significant radial spot motion was detected in this real-time preliminary investigation.

We attribute both responses to crystal rotations, as shown in Figure 7.1. We used a vertical scattering-plane geometry, in which the powder rings lie horizontally on the detector. Any vertical movement of the diffraction peaks involves changing of the Bragg angle. Due to the high coherence of X-ray source and small beam size, each crystal grain generates a separate diffraction pattern along the powder ring without the interference from others, so that the geometry and temporal changes of each individual crystal can directly attributed to its diffraction pattern. The transverse motion on the detector corresponds to a component of rotation around the forward direction, denoted as the "X-axis" in the figure, while the blinking corresponds to transverse rotations on or off the Bragg condition, denoted as the "Z-axis". Rotations of crystals about their third

axis, denoted the "Y-axis", the scattering vector direction, would not have been detected.
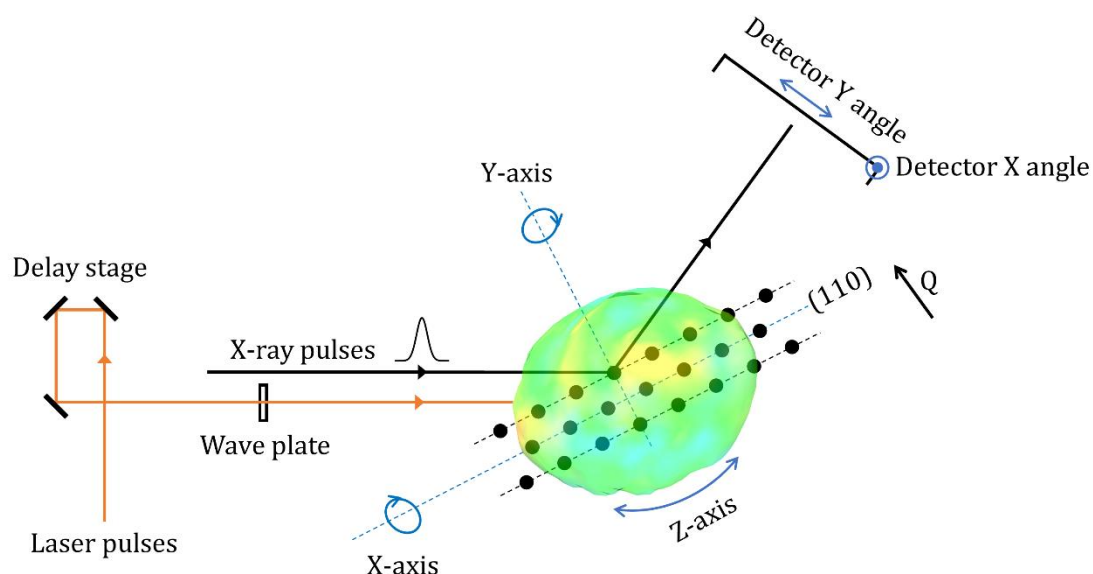
Figure 7. 1 Illustration of the set-up for the X-ray pump-probe experiment performed at LCLS. A 0.5m delay stage is used for making laser pulse time delays up to 3000ps. The wave plate is used to control the fluence of the laser pulses. The X, Y and Z axes of the crystal under Bragg condition are shown and the (110)/(101) Bragg planes are indicated schematically. Rotation of crystal around the X-axis causes the diffraction pattern to move in the X direction on detector, which is around the (110)/(101) powder ring. Rotation around the Z-axis results in a scanning of crystal through its Bragg condition and leads to an intensity difference. This is the "blinking" phenomenon seen in the experiment. Any rotation around the Y-axis is not detected. Movements in the Y direction on the detector would indicate lattice expansions or contractions.

Crystals were then selected for further investigation using two approaches. Time delay scans were performed after centering a selected nanocrystal in the X-ray beam and on the maximum of its rocking curve; these allowed detailed measurement of the Bragg peak position on the detector with sub-pixel accuracy as a function of time delay. The Centre of Mass (COM) of the diffraction pattern was viewed as the pattern centre and was tracked over different time delay scans. Figure 7.2a shows the rotation angle variation of diffraction pattern centre from the position at the start of measurement, along the X and Y directions of the detector. Zone 1 and Zone 2 were acquired from different scans and combined together. Waterfall plots of these position changes can be seen in Figure 7.2c to 7.2f. Figure 7.2b shows the intensity plot over different delay times. There is a

clear difference between Zone 1 and Zone 2. In Zone 1, the intensity is higher and the period of oscillation is shorter, around 100 ps. While in Zone 2, there is a 450 ps periodic oscillation when time delay is over 1500 ps.
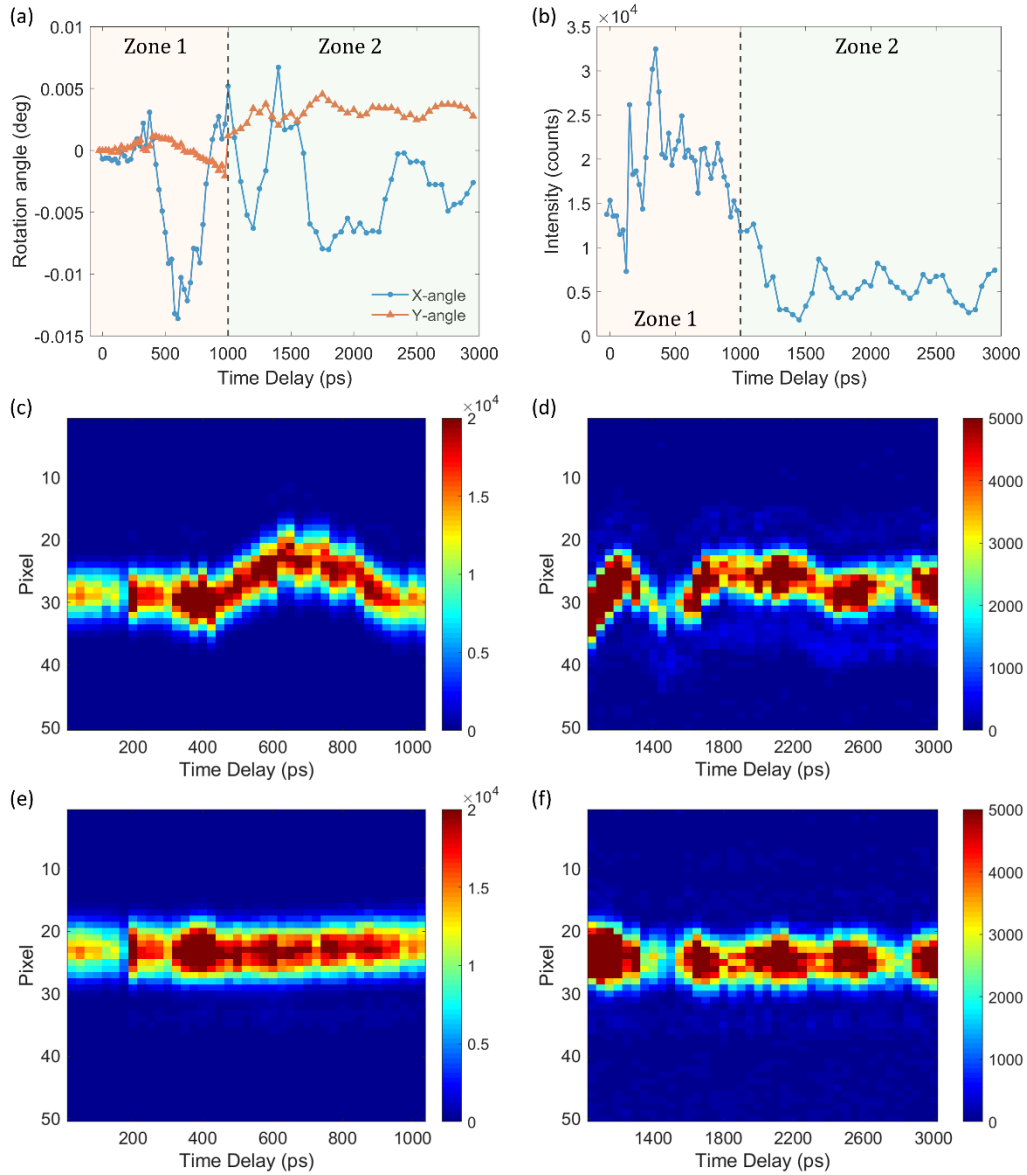
Figure 7. 2 (a) The rotation of a (110) BTO diffraction pattern along the X and Y directions of the detector as a function of laser pump-probe delay. (b) Intensity plot of diffraction pattern for different laser-pulse delays. Zone 1 and Zone 2 were recorded before and after a BCDI measurement. (c)-(f) Waterfall plots of transverse (X) and radial (Y) slices through the diffraction pattern for different time delays. The first (c, d) and second (e, f) rows display positions in the X and Y directions, respectively.

The time scale for both X-axis and Z-axis rotations was the same, so we conclude it was just due to its chance orientation of the crystal around the (110) Q-vector

of the measurement. There is an interesting delayed onset of the motion in Figure 7.2a, around 250 ps, seen on this crystal and several others. This can be understood as the laser and X-ray beam are not hitting the same crystal in the BTO nanocrystal aggregates and acoustic coupling between them. The randomly oriented individual crystals are assumed to be bonded together into aggregates as shown in Figure 7.3. This sketch shows how there can be a delay between the X-ray diffraction signal and the laser heating. The X-ray penetration depth of 15 μm can reach many 200 nm-sized crystals within the aggregate, while the laser is absorbed only by the surface layer. One crystal inside (coloured blue) is illuminated by the X-ray and gives rise to the diffraction and BCDI images, while the laser is directly heating other crystals on the front of the sample. It takes time for the mechanical response to the laser heating to transfer from the front side to the inside, which explains the time delay before the onset of the motion observed. To the extent that BTO is a piezoelectric material, where the laser excitation could lead to a piezoelectric deformation, we cannot identify whether the observed delay of the X-ray diffraction signal is purely thermally driven or whether the piezoelectric response also makes contributions.
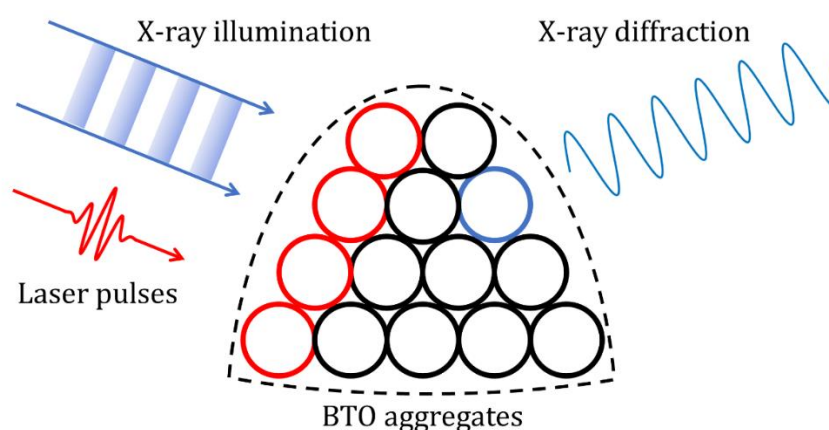
Figure 7. 3 Illustration of the time delay between laser heating and x-ray diffraction response. All the crystals (circles) are illuminated by the X-ray beam, while only the crystal colored blue is at the correct Bragg angle to give the X-ray diffraction signal. The laser is absorbed by the front row of crystals, colored red.

At strategic points on these time delay scans, BCDI experiments were performed to map out the single crystal shape and displacement field in 3 dimensions. The (110) diffraction pattern from the selected crystal was first centered to

maximum intensity position by adjusting the sample stage. Then a series of 2D diffraction pattern data were taken by collecting rocking curve scans across the Bragg condition, with angular steps fine enough to oversample the coherent diffraction patterns. These 2D datasets were stacked into 3D and then inverted to real-space images using iterative algorithms, alternating cycles of error reduction and hybrid input-output [19], using a "shrink-wrap" support [24] and combining with partial coherence correction [244]. The data inversion was carried out in the detector-pixel-angle coordinate system and then transformed to the laboratory coordinates in the standard way [235]. The first column of Figure 7.4 shows the central slice of the 3D diffraction patterns at different time delays, while the second and third columns shows their corresponding reconstructed Bragg density slice and displacement slice, respectively. The displacement shown at each point in the crystal is derived from the phase of the complex image and given as the projection of the 3D displacement u along the Q-vector, using the relation $\Phi = Q \cdot u$ [239]. For a perfect single crystal, the Bragg density map would have only one centre in the middle and monotonically decrease towards the surface. In this case, however, there are several high-density regions distributed inside the single crystal indicating a complex nature, as shown in second column of Figure 7.4. The displacement map is also seen to be changing with time delay. The crystal has a positive displaced region seen before the laser pump at -50 ps. After +50 ps of pump-probe delay, the positive displaced region diminishes, while there are negative displaced regions appearing at the surface, which could arise from contacts with surrounding crystals showing a compressive strain. When the laser pump delay reaches +500 ps to +700 ps, a positive displaced region is showing up on the surface. Upon +900 ps laser delay, the positive region inside the crystal comes back.
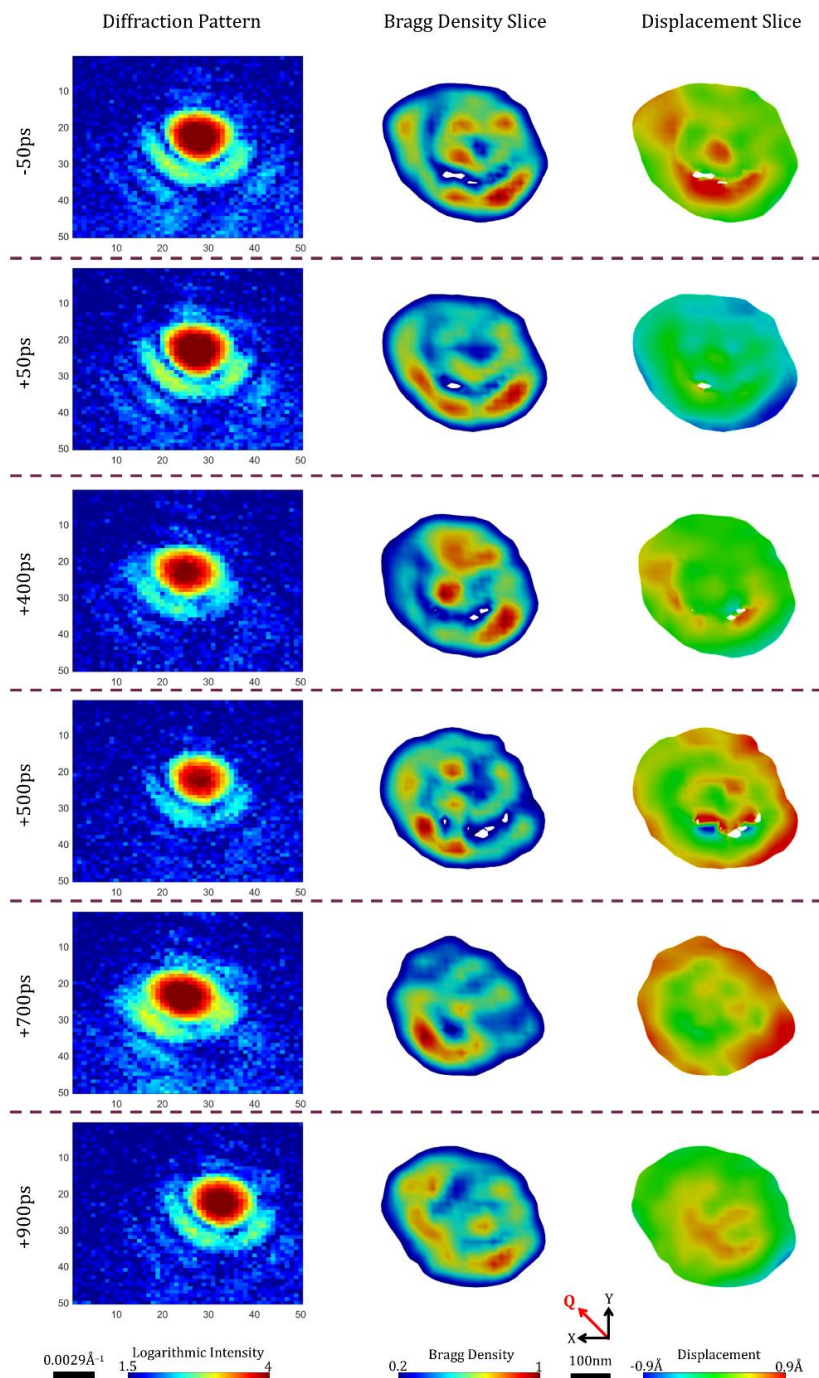
Figure 7. 4 (110) diffraction patterns and their reconstructed images of the same BTO crystal shown in Figure 7.2 after different pump-probe delays. The first column shows the central slices of 3D diffraction patterns of a single crystal after different laser delays. The powder ring direction is horizontal as shown in the figure. These 3D diffraction patterns were inverted into 3D real-space images. The second column are slices of reconstructed Bragg density (image amplitude), which gives the shape and crystal ordering information. The third column are slices of retrieved displacement field projected along the Q-vector (shown inset in red). The positive and negative value represent tensile and compressive displacement, respectively.

BCDI cannot directly see the small crystal rotation as indicated in Figure 7.2 but is sensitive to any inhomogeneous shearing of the crystal lattice which also contributes to the peak motions. By directly viewing the crystal in 3D, however, we find both the Bragg density slices and displacement slices are complex and continuously changing inside a single crystal grain following laser excitation. The surface displacement fields are different from the centre indicating the presence of lattice shearing. We think these sharp dynamic changes are plausible given that the crystal is in close contact with other crystal grains.

7.4 Discussion

Our XFEL experiment clearly shows that rotations of the BTO nanocrystals are induced by laser excitation on a 100 ps time scale, appropriate for an acoustic response of the material. An observed response time delay around 200 ps could be attributed to generation of acoustic waves at some distance from the part of the sample probed with the X-ray diffraction. The longitudinal and transverse speeds of sound of BTO (in sintered ceramics) are 4800 m/s and 2400 m/s [26,], so the 250 ps time delay corresponds to a distance between the excitation and its observation of 1.2 μm or 0.6 μm. The apparent vibration period of 450 ps would correspond to the breathing of a slab of nanocrystals 1.1 μm or 0.55 μm thick. Both these lengths are greater than the 200 nm size of the particles being measured with the X-rays, so we consider this represents a collective response of several nanocrystals bonded together into aggregates.

Conflicts of Interest: The authors declare no financial conflict of interest.

Chapter 8. Conclusion

The domain structures in barium titanate (BTO) nanocrystals have been the focus of this thesis. Bragg coherent X-ray diffraction imaging (BCDI) was used to probe the displacement and strain distribution inside BTO crystals. Finite element analysis (FEA) has been used to simulate the strain patterns from different domain configurations.

Large 90° domains with size of 100 nm were located in one BTO nanocrystal and studied in Chapter 3. This sample was selected because it had a characteristic diffraction pattern with intensity distributed on both (110) and (101) powder rings with strong interferences in between. The reconstruction of the diffraction patterns with more than one centre usually failed, as shown both experimentally and by simulation. The trick that was found to be useful was to cut and split apart the two diffraction patterns on the detector images, and then reconstruct the two parts separately before combining the real space images together. The crystal was then heated up and cooled down across its tetragonal-cubic phase transition temperature of 393 K. The large 90° domains were found to come back at the same place after returning to the tetragonal phase from the cubic phase.

The local structure of BTO crystals has long been discussed, as X-ray and neutron scattering studies have shown that the local structure could be in a low-symmetry state like orthorhombic or rhombohedral, while the global phase remains still tetragonal or cubic [172, 173, 205]. To understand whether this ambiguity applied to our BTO commercial nanocrystals, we performed X-ray total scattering measurements and found that the nanocrystals were mostly tetragonal in both global and local structure at room temperature, presented in Section 4.3. The temperature dependent X-ray total scattering also shows an elevated phase transition temperature, compared with the values in bulk BTO. This is easy to rationalize as the strain in nanocrystals can be higher than bulk material, which leads to higher transition temperature [50].

During the BCDI experiments, repeated several times at the 34-ID-C beamline of APS, some well-faceted crystals were observed by their strongly modulated diffraction fringes. This allowed the crystallographic orientations to be

determined, fully in some cases, to establish a coordinate system to interpret the strains. When their strain components were calculated, some unexpected strain stripes were found, as presented in Section 4.2. The directions of the strain stripes are mostly along {100} or {110}. The two-dimensional Autocorrelation function (2D ACF) was calculated on the selected regions to quantitatively measure the stripe periods, which were distributed from 30nm to 50nm.

To further understand the behaviour of these strain stripes, we tracked two faceted crystals crossing their phase transition in detail by heating and cooling. This experiment was at ID-01 of ESRF and described in Section 5.1. The diffraction of crystal A was found to locate at the tetragonal (101) powder ring, with some intensity distributed on to the (110) powder ring as well. The crystal was then heated up to the cubic phase and cooled down to the tetragonal phase again. During the process, the diffraction pattern was found to move from (101) powder ring to (110) powder ring. This indicates a reorientation of c-axis after crossing the phase transition. The BCDI reconstructions were performed for each temperature with a 5 K step. The slice view shows that the strain stripes inside the crystal also change their direction through the heating and cooling. This match of c-axis reorientation and strain stripe direction switching indicates that the strain stripes could come from the ferroelectric domain walls. However, there was some residue of the stripe pattern with a different spacing and orientation, in the cubic phase as well; this same behaviour was recently reported [227].

The two classical ferroelectric domain-wall configurations are 90° and 180° walls, both of which could give a stripe-like polarization pattern as shown in Figure 8.1. Figure 8.1(a) shows a 180° domain-wall pattern with the c-axis pointing vertically. If the c-axis is switched to horizontal direction, the polarization pattern would also switch direction, as shown in Figure 8.1(b). 180° domain walls are always parallel to the c-axis, namely the crystallographic (001) direction. Figure 8.1(c) shows an example of 90° domain walls. The c-axis for the blue stripes is pointing horizontal, while for the orange stripes it is pointing vertical. If both blue and orange stripes change polarization direction, then the stripes direction could keep as the same, or it could form another domain

mapping as shown in Figure 8.1(d). From Figure 8.1 we can see that both 90° and 180° domain walls can have their polarization stripes rotating 90° if the c-axis is switched to another a-axis direction. So, both of these ferroelectric domain pictures match the stripe switching seen in Crystal A in Chapter 5.

The Crystal B is an example where the Bragg peak didn't move across powder rings but coming back to the original powder ring. This is explained as the crystal didn't change its c-axis direction after going to cubic and coming back to tetragonal structure.
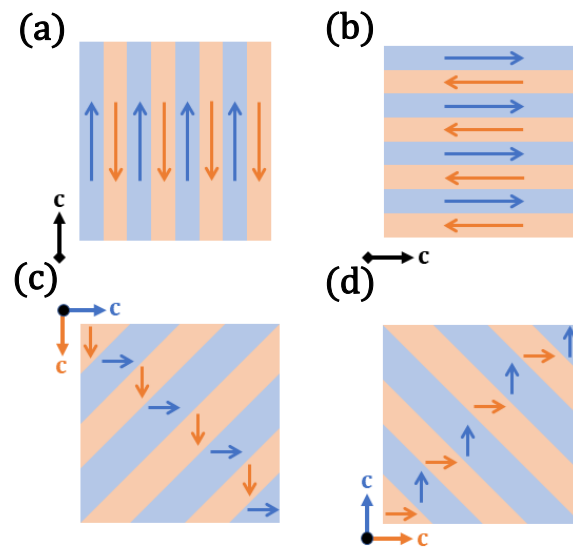
Figure 8. 1 Polarization patterns from 90° and 180° domain walls before and after switching c-axis.

To understand the ferroelectric strain stripes observed in Crystal A, different models have been built in Chapter 6 to simulate them. While both 90° and 180° domains configuration give stripes like strain, the 180° domains model seems to work better. It has 6 views out of 9 views showing {001} or {110} directional stripes.

However, the poor mismatch in side-by-side view also triggers the question whether the strain stripes are physically real or there are other mechanisms behind it. We are worrying about the Fourier termination ripples and the resulting two effects. The first one is the cropping of dataset, which gives the stripes parallel to the facets. As we tested this effect by playing with the cropping, there seem to be no change in the stripe distribution. We are still

looking for ways to thoroughly understand this point. The second one being the aliasing of the fast Fourier transform by not having enough zero padding. This will lead to the fringes being parallel to the detector edges. We noted that there are some simulation works describing these effects in BCDI and we also want to dig into this question more in the future work [248].

Despite the works done by us and described in this thesis, and others, there are still many uncertainties and mysteries about ferroelectric nanoparticles worth exploring in the future.

Firstly, it would be interesting to see how the domains in nanocrystals behave when they react to different stimuli. We have tried temperature in this work, but other conditions could also be interesting. Our group is currently studying the domains response in BTO nanocrystals under DC electric fields (and possibly current) at APS 34-ID-C. In that work, the BTO nanocrystals were dropped onto a grid of Au electrodes with gaps. The crystals that filled the gap and connected the two electrodes are the ones of interest. To get more control of which crystal to look at, metallic coating (Pt) could be used to weld the interested crystal with the electrode using Focused Ion Beam (FIB).

It could also be interesting to do it at X-ray free electron laser facility to explore the relation between ultra-fast laser pump and the piezoelectric response or the changes of strain stripes in BTO nanocrystal. In principle, a laser couples exclusively with the electrons of the sample, which then couple to the ions, creating local charges and a response which can be seen as strain in BCDI. In Chapter 7, we have done such an experiment at X-ray Pump Probe (XPP) beamline at the Linac Coherent Light Source (LCLS) to study the phenomenon of optical laser excitation of the same commercial BTO nanocrystals. Rather than seeing any directly interpretable piezoelectric response or strain evolution, the crystals were mostly found to rotate driven by the laser and the response was significantly delayed up to 500 ps. This was attributed to the aggregated state of the BTO particles which tend to clump together on the supporting substrate [228]. Figure 7.3 shows the model that used to depict the observed phenomenon. For a future study, it would be interesting to locate a crystal with strain stripes inside and study how these evolve under ultra-fast laser pulse. Since the

classical domain wall structure can migrate without any involvement of major defects (vacancies or dislocations), it could be that the strain response to the laser-induced electrons is extremely fast.

Secondly, the electrical, mechanical properties and domain configurations in BTO vary a lot with sample preparation. Therefore, it's interesting to study BTO crystals with different preparation route and properties. One direction would be to study the strain distribution in polycrystalline and epitaxial BTO thin film. We have performed growth studies to optimize the growth-parameter window of BTO strained films in the UCL laboratory of Prof. Pavlo Zubko. This has been listed in the appendix.

For future BCDI experiments, our plan is to use reactive ion etching (RIE) to cut out BTO blocks with variable sizes. Assuming the strain from lattice mismatch is preserved after etching, it would be interesting to explore if there is any stripe like feature inside and how they distribute under different strain state. It would also be interesting to examine the misfit dislocations associated with the growth on the different substrates. The reciprocal space maps shown in Fig I.3 indicate a small amount of relaxation of the in-plane lattice constant due to the misfit. This is expected to appear as an array of misfit dislocations and associated local strains, which can be imaged with BCDI. This has not been achieved before as far as we know.

A further plan is to look at the films with Bragg ptychography, where the RIE step is not required. For this, 2D scans of a coherent beam across the sample are made with overlapping probe positions. Because the diffraction of a thin film is elongated in the Q-direction perpendicular to the film, the Ewald sphere cuts through the diffraction measure the full 2D speckle pattern due to the in-plane structure [229]. In ptychography, the redundancy of data in the overlap allows a solution of the phase problem to yield wide-field images [230]. This should allow access to the structure of the misfit dislocations and associated domains of the BTO thin films which have been prepared on different substrates. The domains are expected to appear phase shifted with respect to each other and the domain wall strain will be seen in the phase structure at the boundaries.

Reference

[1] J. Als-Nielsen and D. McMorrow, Elements of modern X-ray physics, Wiley, New York, (2011). http://dx.doi.org/10.1002/9781119998365

[2] P. Willmott, Wiley, An introduction to synchrotron radiation: techniques and applications, New York, (2011). http://dx.doi.org/10.1002/9781119970958

[3] G. Materlik, T. Rayment, D. I. Stuart, Diamond light source: status and perspective, Phil. Trans. R. Soc. A, **373**, 20130161 (2015). http://dx.doi.org/10.1098/rsta.2013.0161

[4] X. Huang, M. Wojcik, N. Burdet, I. Peterson, G. R. Morrison, D. J. Vine, D. Legnini, R. Harder, Y. S. Chu and I. K. Robinson, Quantitative X-ray wavefront measurements of Fresnel zone plate and K-B mirrors using phase retrieval, Optics Express, **21**, 24038 (2012). https://doi.org/10.1364/oe.20.024038

[5] L. Li, Y. Xie, E. Maxey and R. Harder, Methods for operando coherent X-ray diffraction of battery materials at the Advanced Photon Source, Journal of Synchrotron Radiation, **26**, 220 (2019). https://doi.org/10.1107/S1600577518016697

[6] M. Ross, K-B Mirrors Harness X-rays for Science, SLAC News (2011). https://www6.slac.stanford.edu/news/2011-10-11-kb-mirrors-harness-xrays-for-science.aspx

[7] Q. Zhang, M. Polikarpov, N. Klimova, H. B. Larsen, R. Mathiesen, H. Emerich, G. Thorkildsen, I. Snigireva and A. Snigiev, Investigation of 'glitches' in the energy spectrum induced by single-crystal diamond compound X-ray refractive lenses, Journal of Synchrotron Radiation, **26**, 109 (2019). https://doi.org/10.1107/S1600577518014856

[8] D. J. Batey, S, Cipiccia, F. Van Assche, S. Vanheule, J. Vanmechelen, M. N. Boone, and C. Rau, Spectroscopic imaging with single acquisition ptychography and a hyperspectral detector, Scientific Reports, **9**, 12278 (2019). https://doi.org/10.1038/s41598-019-48642-y

[9] D. Sayre, Some implications of a theorem due to Shannon, Acta Cryst., **5**, 843 (1952). https://doi.org/10.1107/S0365110X52002276

[10] I. K. Robinson, I. A. Vartanyants, G. J. Williams, M. A. Pfeizer, J. A. Pitney, Reconstruction of the Shapes of Gold Nanocrystals Using Coherent X-Ray Diffraction, Phys. Rev. Lett., **87**, 195505 (2001). https://doi.org/10.1103/PhysRevLett.87.195505

[11] I. Robinson and R. Harder, Coherent X-ray diffraction imaging of strain at the nanoscale, Coherent X-ray diffraction imaging of strain at the nanoscale, Nat. Mater., **8**, 291 (2009). https://doi.org/10.1038/nmat2400

[12] F. Hofmann, E. Tarleton, R. J. Harder, N. W. Phillips, P. W. Ma, J. N. Clark, I. K. Robinson, B. Abbey, W. Liu & C. E. Beck, 3D lattice distortions and defect

structures in ion-implanted nano-crystals. Scientific Reports, **7**, 1–10 (2017). https://doi.org/10.1038/srep45993

[13] G. Xiong, O. Moutanabir, M. Reiche, R. Harder and I. Robinson, Coherent X-Ray Diffraction Imaging and Characterization of Strain in Silicon-on-Insulator Nanostructures, Adv. Mater., **26**, 7747 (2014). https://doi.org/10.1002/adma.201304511

[14] J. N. Clark, J. Ihli, A. S. Shpyrko, Y. -Y. Kim, A. N. Kulak, J. M. Campbell, G. Nisbet, F. C. Meldrum and I. Robinson, Three-dimensional imaging of dislocation propagation during crystal growth and dissolution, Nat. Mater., **14**, 780 (2015). https://doi.org/10.1038/nmat4320

[15] A. Ulvestad, A. Singer, J. N. Clark, H. M. Cho, J. W. Kim, R. Harder, J. Maser, Y. S. Meng and O. G. Shpyrko, Topological defect dynamics in operando battery nanoparticles, Science, **348**, 1344 (2015). https://10.1126/science.aaa1313

[16] A. R. Sandy, L. B. Lurio, S. G. J. Mochrie, A. Malik, G. B. Stephenson, J. F. Pelletier, & M. Sutton, (1999). Design and characterization of an undulator beamline optimized for small-angle coherent X-ray scattering at the advanced photon source. Journal of Synchrotron Radiation, **6**, 1174 (1999). https://doi.org/10.1107/S0909049599009590

[17] J. Miao, T. Ishikawa, I. Robinson and M. Murnane, Beyond crystallography: Diffractive imaging using coherent x-ray light sources, Science, **348**, 530 (2015) https://doi.org/10.1126/science.aaa1394

[18] L. Wu, P. Juhas, S. Yoo and I. Robinson, Complex imaging of phase domains by deep neural networks, IUCrJ, **8**, 12 (2021). https://doi.org/10.1107/S2052252520013780

[19] J. R. Fienup, Phase retrieval algorithms: A comparison. Appl. Opt. **21**, 2758 (1982). https://doi.org/10.1364/AO.21.002758

[20] J. P. Abrahams, & A. G. W. Leslie, Methods used in the structure determination of bovine mitochondrial F1 ATPase. Acta Crystallographica Section D: Biological Crystallography, **52**, 30 (1996). https://doi.org/10.1107/S0907444995008754

[21] D. R. Luke, Relaxed averaged alternating reflections for diffraction imaging, Inverse Problems, **21**, 37 (2005). https://doi.org/10.1088/0266-5611/21/1/004

[22] H. H. Bauschke, P. L. Combettes, & D. R. Luke, Phase retrieval, error reduction algorithm, and Fienup variants: a view from convex optimization. Journal of the Optical Society of America A, **19**, 1334 (2002). https://doi.org/10.1364/josaa.19.001334

[23] H. H. Bauschke, P. L. Combettes, & D. R. Luke, Hybrid projection-reflection method for Phase Retrieval. Journal of the Optical Society of America A, **20**, 1025 (2003). https://doi.org/10.1364/JOSAA.20.001025

[24] S. Marchesini. A unified evaluation of iterative projection algorithms for phase retrieval. Rev. Sci. Instrum. **78**, 011301 (2007). https://doi.org/10.1063/1.2403783

[25] C. C. Chen, J. W. Miao, C. W. Wang, and T. K. Lee, Application of optimization technique to noncrystalline x-ray diffraction microscopy: Guided hybrid input-output method, Phys. Rev. B, **76**, 064113 (2007). https://doi.org/10.1103/PhysRevB.76.064113

[26] T. Egami & S.J.L. Billinge, Underneath the Bragg peaks: Structural analysis of complex materials. Kidlington, Oxford (2012).

[27] M. E. Lines and A. M. Glass, Principles and Applications of Ferroelectrics and Related Materials, Oxford University Press (2001). https://doi.org/10.1093/acprof:oso/9780198507789.001.0001

[28] E. R. Caley, J. F. C. Richards, Theophrastus On Stones, The Ohio State University, Columbus (1956). http://hdl.handle.net/1811/32541

[29] S. B. Lang, Pyroelectricity: From ancient curiosity to modern imaging tool. Physics Today, **58**, 31 (2005). https://doi.org/10.1063/1.2062916

[30] J. Curie & P. Curie, Contractions and expansions produced by voltages in hemihedral crystals with inclined faces, Comptes Rendus, **93**, 1137 (1881).

[31] J. Valasek, Piezo-electric and allied phenomena in Rochelle salt. Physical Review, **17**, 475 (1921). https://doi.org/10.1103/PhysRev.17.475

[32] G. Busch & P. Scherrer, A new seignette-electric substance, Ferroelectric, **23**, 737 (1935). https://doi.org/10.1080/00150198708224825

[33] W. Cai & A. Katrusiak, Structure of the high-pressure phase IV of KH_2PO_4 (KDP). Dalton Transactions, **42**, 863 (2013). https://doi.org/10.1039/c2dt32131a

[34] S. Horiuchi, Y. Tokunaga, G. Giovannetti, S. Picozzi, H. Itoh, R. Shimano, R. Kumai, & Y. Tokura, Above-room-temperature ferroelectricity in a single-component molecular crystal. Nature, **463**, 789 (2010). https://doi.org/10.1038/nature08731

[35] A. Katrusiak, & M. Szafranski, Ferroelectricity in NH$\cdots$N hydrogen bonded crystals. Physical Review Letters, **82**, 576 (1999). https://doi.org/10.1103/PhysRevLett.82.576

[36] M. Szafrański, A. Katrusiak, & G. J. McIntyre, Proton disorder in NH$\cdots$N bonded [dabcoH]$^+$I$^-$ relaxor: New insights into H-disordering in a one-dimensional H_2O ice analogue. Crystal Growth and Design, **10**, 4334 (2010). https://doi.org/10.1021/cg100247g

[37] A. von Hippel, R. G. Breckenridge, F. G. Chesley & L. Tisza, High dielectric constant ceramics. Industrial & Engineering Chemistry, **38**, 1097 (1946). https://doi.org/10.1021/ie50443a009

[38] S. Roberts, Dielectric Properties of Lead Zirconate and Barium-Lead Zirconate. Journal of the American Ceramic Society, **33**, 63 (1950). https://doi.org/10.1111/j.1151-2916.1950.tb14168.x

[39] G. Shirane, & K. Suzuki, Crystal structure of $Pb(Zr-Ti)O_3$, J. Phys. Soc. Jpn., **7**, 333 (1952). https://doi.org/10.1143/JPSJ.7.333

[40] V. Garcia, S. Fusil, K. Bouzehouane, S. Enouz-Vedrenne, N. D. Mathur, A. Barthélémy & M. Bibes, Giant tunnel electroresistance for non-destructive readout of ferroelectric states. Nature, **460**, 81 (2009). https://doi.org/10.1038/nature08128

[41] K. H. Noh, B. Yang, S. W. Lee, S. S. Lee, H. B. Kang, & Y. J. Park, Issues and reliability of high-density FeRAMs. Japanese Journal of Applied Physics, **42**, 2096 (2003). https://doi.org/10.1143/jjap.42.2096

[42] M. Nespolo, Lattice versus structure, dimensionality versus periodicity: a crystallographic Babel, J. Appl. Crystallogr. **52**, 451 (2019). https://doi.org/10.1107/S1600576719000463

[43] M. Nespolo, The lattice sickness pandemic, IUCr Newsletter **27**, 2 (2019) https://www.iucr.org/news/newsletter/volume-27/number-2/the-lattice-sickness-pandemic

[44] IUCr Online Dictionary of Crystallography. https://dictionary.iucr.org/Lattice_system

https://dictionary.iucr.org/Crystal_system

https://dictionary.iucr.org/Crystal_family

[45] IUCr Online Dictionary of Crystallography.

https://dictionary.iucr.org/Goldschmidt_tolerance_factor

[46] F. S. Galasso, Structure, properties, and preparation of perovskite-type compounds, London, Pergamon Press; 1969. https://doi.org/10.1016/c2013-0-02117-2

[47] A. von Hippel, Ferroelectricity, Domain Structure, and Phase Transitions of Barium Titanate, Rev. Mod. Phys. **22**, 221 (1950). https://doi.org/10.1103/RevModPhys.22.221

[48] F. Jona & G. Shirane, Ferroelectric crystals, London, Pergamon Press; 1962. https://doi.org/10.1002/zamm.19630431016

[49] T. Ishidate, S. Abe, H. Takahashi & N. Mori, Phase Diagram of $BaTiO_3$, **78**, 2397 (1997). https://doi.org/10.1103/PhysRevLett.78.2397

[50] K. J. Choi, M. Biegalski, Y. L. Li, A. Sharan, J. Schubert, R. Uecker, P. Reiche, Y. B. Chen, X. Q. Pan, V. Gopalan, L. -Q. Chen, D. G. Schlom & C. B. Eom, Enhancement of ferroelectricity in strained $BaTiO_3$ thin films. Science, **306**, 1005 (2004). https://doi.org/10.1126/science.1103218

[51] J. C. Slater, The lorentz correction in barium titanate. Physical Review, **78**, 748 (1950). https://doi.org/10.1103/PhysRev.78.748

[52] W. Cochran, Crystal stability and the theory of ferroelectricity. Advances in Physics, **9**, 387 (1960). https://doi.org/10.1080/00018736000101229

[53] C. H. Ahn, K. M. Rabe, & J. Triscone, Ferroelectricity at the Nanoscale: Local Polarization in Oxide Thin Films and Heterostructures, Science, **303**, 488 (2004). http://doi.org/10.1126/science.1092508

[54] R. Comes, M. Lambert, & A. Guinier, The chain structure of $BaTiO_3$ and $KNbO_3$, Solid State Communications, **6**, 715 (1968). https://doi.org/10.1016/0038-1098(68)90571-1

[55] A. S. Chaves, F. C. S. Barreto, & R. A. Noqueira, Thermodynamics of an eight-site order-disorder model for ferroelectrics, Physical Review B, **13**, 207 (1976). https://doi.org/10.1103/PhysRevB.13.207

[56] J. Hlinka, T. Ostapchuk, D. Nuzhnyy, J. Petzelt, P. Kuzel, C. Kadlec, P. Vanek, I. Ponomareva, & L. Bellaiche, Coexistence of the phonon and relaxation soft modes in the terahertz dielectric response of tetragonal $BaTiO_3$. Physical Review Letters, **101**, 167402 (2008). https://doi.org/10.1103/PhysRevLett.101.167402

[57] W. X. Zhou & A. Ariando, Review on ferroelectric/polar metal. JJAP, **59**, SI0802 (2020). https://doi.org/10.35848/1347-4065/ab8bbf

[58] R. Z. Tai, K. Namikawa, A. Sawada, M. Kishimoto, M. Tanaka, P. Lu, K. Nagashima, H. Maruyama, M. Ando, Picosecond view of microscopic-scale polarization clusters in paraelectric $BaTiO_3$. Physical Review Letters, **93**, 087601 (2004). https://doi.org/10.1103/PhysRevLett.93.087601

[59] E. A. Stern, Character of order-disorder and displacive components in barium titanate, Physical Review Letters, **93**, 037601 (2004). https://doi.org/10.1103/PhysRevLett.93.037601

[60] Y. Isohama, N. Nakajima, H. Maruyama, Y. Tezuka, & T. Iwazumi, Tetragonal-cubic phase transition in $BaTiO_3$ probed by resonant X-ray emission spectroscopy. Journal of Electron Spectroscopy and Related Phenomena, **184**, 207 (2011). https://doi.org/10.1016/j.elspec.2010.12.023

[61] L. Landau, On the theory of phase transitions, translated and reprinted from Landau L.D. "Collected Papers", **1**, 234 (1969) Originally published in Zh. Eksp. Teor. Fiz. https://pdfs.semanticscholar.org/60d6/3a992ed0944d72a0b54c8eb182cbed14d1fa.pdf

[62] W. Cao, Constructing Landau-Ginzburg-Devonshire type models for ferroelectric systems based on symmetry. Ferroelectrics, **375**, 28 (2008). https://doi.org/10.1080/00150190802437845

[63] A. Devonshire, Theory of barium titanate. Philosophical Magazine, **40**, 1040 (1949). https://doi.org/10.1080/14786444908561372

[64] M. D. Glinchuk, B. Y. Zaulychny, & V. A. Stephanovich, Depolarization field in thin ferroelectric films with account of semiconductor electrodes. Ferroelectrics, **316**, 1(2005). https://doi.org/10.1080/00150190590963057

[65] A. P. Levanyuk, B. A. Strukov, & A. Cano, Background dielectric permittivity: Material constant or fitting parameter, Ferroelectrics, **503**, 94(2016). https://doi.org/10.1080/00150193.2016.1218245

[66] M. D. Glinchuk, E. A. Eliseev, & A. N. Morozovska, Influence of built-in internal electric field on ferroelectric film properties and phase diagram. Ferroelectrics, **354**, 86 (2007). https://doi.org/10.1080/00150190701454628

[67] I. H. Kim, I. H. Kim, K. O. Jang, K. R. Sin & C. J. Kim, A new higher-order Landau–Ginzburg–Devonshire theory for $KNbO_3$ crystal. Phase Transitions, **91**, 1189 (2018). https://doi.org/10.1080/01411594.2018.1536269

[68] T. Yamamoto, Crystallographic, Dielectric and Piezoelectric Properties of $PbZrO_3$-$PbTiO_3$ System by Phenomenological Thermodynamics. Jpn. J. Appl. Phys., **37**, 6041 (1998). https://iopscience.iop.org/article/10.1143/JJAP.37.6041/meta

[69] A. S. Chaves, & S. P. S. Porto, Generalized Lyddane-Sachs-Teller relation. Solid State Communications, **13**, 865 (1973). https://doi.org/10.1016/0038-1098(73)90386-4

[70] M. M. Vijatović, J. D. Bobić, & B. D. Stojanović, History and challenges of barium titanate: Part II, Science of Sintering, 40, 235 (2008). https://doi.org/10.2298/SOS0803235V

[71] B. D. Stojanovic, C. Jovalekic, V. Vukotic, A. Z. Simoes, & J. A. Varela, Ferroelectric properties of mechanically synthesized nanosized barium titanate. Ferroelectrics, **319**, 65 (2005). https://doi.org/10.1080/00150190590965424

[72] W. David Kingery, H. K. Bowen, Donald R. Uhlmann Introduction to Ceramics, John Wiley & Sons, Inc (1976). https://doi.org/10.1149/1.2133296

[73] J. Gao, D. Xue, W. Liu, C. Zhou, & X. Ren, Recent progress on $BaTiO_3$-based piezoelectric ceramics for actuator applications. Actuators, **6**, 24 (2017). https://doi.org/10.3390/act6030024

[74] G. H. Haertling, Ferroelectric Ceramics: History and Technology. Ferroelectricity: The Fundamentals Collection, **818**, 157 (2007). https://doi.org/10.1002/9783527618002.ch6

[75] S. E. Park, & T. R. Shrout, Ultrahigh strain and piezoelectric behaviour in relaxor based ferroelectric single crystals. Journal of Applied Physics, **82**, 1804 (1997). https://doi.org/10.1063/1.365983

[76] Q. M. Zhang, & J. Zhao, Electromechanical properties of lead zirconate titanate piezoceramics under the influence of mechanical stresses. IEEE Transactions on Ultrasonics, Ferroelectrics, and Frequency Control, **46**, 1518 (1999). https://doi.org/10.1109/58.808876

[77] Y. M. You, W. Q. Liao, D. Zhao, H. Y. Ye, Y. Zhang, Q. Zhou, X. Niu, J. Wang, P. Li, D. Fu, Z. Wang, S. Gao, K. Yang, J. Liu, J. Li, Y. Yan, & R. G. Xiong, An organic-inorganic perovskite ferroelectric with large piezoelectric response. Science, **357**, 306 (2017). https://doi.org/10.1126/science.aai8535

[78] S. Wada, H. Kakemoto & T. Tsurumi, Enhanced Piezoelectric Properties of Piezoelectric Single Crystals by Domain Engineering. Materials Transactions, **45**, 178 (2004). https://doi.org/10.2320/matertrans.45.178

[79] A. J. Bell, Phenomenologically derived electric field-temperature phase diagrams and piezoelectric coefficients for single crystal barium titanate under fields along different axes. Journal of Applied Physics, **89**, 3907 (2001). https://doi.org/10.1063/1.1352682

[80] S. Wada, K. Yako, H. Kakemoto, T. Tsurumi & T. Kiguchi, Enhanced piezoelectric properties of barium titanate single crystals with different engineered-domain sizes. Journal of Applied Physics, **98**, 014109 (2005). https://doi.org/10.1063/1.1957130

[81] S. Wada, K. Takeda, T. Muraishi, H. Kakemoto, T. Tsurumi, & T. Kimura, Preparation of [110] grain oriented barium titanate ceramics by templated grain growth method and their piezoelectric properties. Japanese Journal of Applied Physics, **46**, 7039 (2007). https://doi.org/10.1143/JJAP.46.7039

[82] N. Ma, B. P. Zhang, W. G. Yang, & D. Guo, Phase structure and nano-domain in high performance of $BaTiO_3$ piezoelectric ceramics. Journal of the European Ceramic Society, **32**, 1059 (2012). https://doi.org/10.1016/j.jeurceramsoc.2011.11.014

[83] S. Shao, J. Zhang, Z. Zhang, P. Zheng, M. Zhao, J. Li, & C. Wang, Erratum: High piezoelectric properties and domain configuration in $BaTiO_3$ ceramics obtained through solid-state reaction route. Journal of Physics D: Applied Physics, **42**, 189801 (2009). https://doi.org/10.1088/0022-3727/42/18/189801

[84] T. Karaki, K. Yan, & M. Adachi, Subgrain microstructure in high-performance $BaTiO_3$ piezoelectric ceramics. Applied Physics Express, **1**, 111402 (2008). https://doi.org/10.1143/APEX.1.111402

[85] Y. Huan, X. Wang, J. Fang & L. Li, Grain size effect on piezoelectric and ferroelectric properties of $BaTiO_3$ ceramics. Journal of the European Ceramic Society, **34**, 1445(2014). https://doi.org/10.1016/j.jeurceramsoc.2013.11.030

[86] P. Zheng, J. L. Zhang, Y. Q. Tan, & C. L. Wang, Grain-size effects on dielectric and piezoelectric properties of poled $BaTiO_3$ ceramics. Acta Materialia, **60**, 5022 (2012). https://doi.org/10.1016/j.actamat.2012.06.015

[87] R. E. Newnham, Properties of materials. Oxford University Press Inc. (2005).

[88] H. Kniepkamp and W. Heywang, Depolarization effects in polycrystalline barium titanate, Z. Angew. Phys., **6**, 385 (1954).

[89] K. Uchino, E. Sadanaga & T. Hirose, Dependence of the crystal structure on particle size in barium titanate. Journal of the American Ceramic Society, **72**, 1555(1989). https://doi.org/10.1111/j.1151-2916.1989.tb07706.x

[90] T. Hoshina, H. Kakemoto, T. Tsurumi, S. Wada, & M. Yashima, Size and temperature induced phase transition behaviors of barium titanate nanoparticles. Journal of Applied Physics, **99**, 1 (2006). https://doi.org/10.1063/1.2179971

[91] W. Y. Shih, W. H. Shih, & I. A. Aksay, Size dependence of the ferroelectric transition of small BaTiO3 particles: Effect of depolarization. Physical Review B, **50**, 15575 (1994). https://doi.org/10.1103/PhysRevB.50.15575

[92] W. R. Buessem, L. E. Cross & A. K. Goswami, Effect of two-dimensional pressure on the permittivity of fine- and coarse-grained barium titanate. Journal of the American Ceramic Society, **49**, 36 (1966). https://doi.org/10.1111/j.1151-2916.1966.tb13145.x

[93] G. Arlt, D. Hennings, & G. De With, Dielectric properties of fine-grained barium titanate ceramics. Journal of Applied Physics, 58, 1619 (1985). https://doi.org/10.1063/1.336051

[94] Z. Zhao, V. Buscaglia, M. Viviani, M. T. Buscaglia, L. Mitoseriu, A. Testino, M. Nygren, M. Johnsson, P. Nanni, Grain-size effects on the ferroelectric behaviour of dense nanocrystalline BaTiO$_3$ ceramics. Physical Review B, **70**, 024107 (2004). https://doi.org/10.1103/PhysRevB.70.024107

[95] M. Frey, & D. Payne, Grain-size effect on structure and phase transformations for barium titanate. Physical Review B, **54**, 3158 (1996). https://doi.org/10.1103/PhysRevB.54.3158

[96] G. Arlt, The influence of microstructure on the properties of ferroelectric ceramics. Ferroelectrics **104**, 217 (1990). https://doi.org/10.1080/00150199008223825

[97] M. Reis, Landau Theory. Fundamentals of Magnetism, **52**, 177 (2013). https://doi.org/10.1016/b978-0-12-405545-2.00011-4

[98] J. Junquera & P. Ghosez, Critical thickness for ferroelectricity in perovskite ultrathin films. Nature, **422**, 506 (2003). https://doi.org/10.1038/nature01501

[99] Y. S. Kim, D. H. Kim, J. D. Kim, Y. J. Chang & T. W. Noh, Critical thickness of ultrathin ferroelectric BaTiO$_3$ thin film. Applied Physics Letter, **86**, 102907 (2005) https://doi.org/10.1038/nature01501

[100] I. P. Batra, P. Wurfel, & B. D. Silverman, New type of first-order phase transition in ferroelectric thin films. Physical Review Letters, **30**, 384 (1973). https://doi.org/10.1103/PhysRevLett.30.384

[101] I. P. Batra, P. Wurfel & B. D. Silverman, Phase transition, stability, and depolarization field in ferroelectric thin films. Physical Review B, **8**, 3257 (1973). https://doi.org/10.1103/PhysRevB.8.3257

[102] R. Waser, Solubility of Hydrogen Defects in Doped and Undoped $BaTiO_3$. Journal of the American Ceramic Society, **71**, 58 (1988). https://doi.org/10.1111/j.1151-2916.1988.tb05760.x

[103] Y. M. Baikov & E. K. Shalkova, Hydrogen in perovskites. Journal of Solid State Chemistry, **97**, 224 (1992). https://doi.org/10.1016/0022-4596(92)90027-S

[104] S. Kapphan and G. Weber, IR-absorption study of H and D-impurities in $BaTiO_3$ crystals. Ferroelectrics, **37**, 673 (1981). https://doi.org/10.1080/00150198108223518

[105] A. Jovanović, M. Wöhlecke, S. Kapphan, A. Maillard, & G. Godefroy, Infrared spectroscopy of hydrogen centers in undoped and iron-doped $BaTiO_3$ crystals. Journal of Physics and Chemistry of Solids, **50**, 623 (1989). https://doi.org/10.1016/0022-3697(89)90457-5

[106] S. J. Pennycook, & D. E. Jesson, High-resolution incoherent imaging of crystals. Physical Review Letters, **64**, 938 (1990). https://doi.org/10.1103/PhysRevLett.64.938

[107] D. Lee, H. Lu, Y. Gu, S. Y. Choi, S. D. Li, S. Ryu, T. R. Paudel, K. Song, E. Mikheev, S. Lee, S. Stemmer, D. A. Tenne, S. H. Oh, E. Y. Tsymbal, X. Wu, L. Q. Chen, A. Gruverman & C. B. Eom, Emergence of room-temperature ferroelectricity at reduced dimensions. Science, **349**, 1314 (2015). https://doi.org/10.1126/science.aaa6442

[108] S. D. Kim, G. T. Hwang, K. Song, C. K. Jeong, K. I. Park, J. Jang, K. -H. Kim, J. Ryu & S. Y. Choi, Inverse size-dependence of piezoelectricity in single $BaTiO_3$ nanoparticles. Nano Energy, **58**, 78 (2018). https://doi.org/10.1016/j.nanoen.2018.12.096

[109] Y. L. Tang, Y. L. Zhu, X. L. Ma, A. Y. Borisevich, A. N. Morozovska, E. A. Eliseev, Y. J. Wang, Y. B. Xu, Z. D. Zhang, & S. J. Pennycook, Observation of a periodic array of flux-closure quadrants in strained ferroelectric $PbTiO_3$ films. Science, **348**, 547 (2015). https://doi.org/10.1126/science.1259869

[110] I. Grinberg, V. R. Cooper & A. M. Rappe, Relationship between local structure and phase transitions of a disordered solid solution. Nature, **419**, 909 (2002). https://doi.org/10.1038/nature01115

[111] C. L. Johnson, M. J. Hytch & P. R. Buseck, Nanoscale waviness of low-angle grain boundaries. Proceedings National Academy of Sciences, **101**, 17936 (2004). https://doi.org/10.1073/pnas.0408348102

[112] M. J. Hytch, J. L. Putaux & , J. M. Pénisson, Measurement of the displacement field of dislocations to 0.03Å by electron microscopy. Nature, **423**, 270 (2003). https://doi.org/10.1038/nature01638

[113] M. J. Hytch, E. Snoeck & R. Kilaas, Quantitative measurement of displacement and strain fields from HREM micrographs. Ultramicroscopy, **74**, 131 (1998). https://doi.org/10.1016/S0304-3991(98)00035-7

[114] A. Gruverman & S. V. Kalinin, Piezoresponse force microscopy and recent advances in nanoscale studies of ferroelectrics. Journal of Materials Science, **41**, 107 (2006). https://doi.org/10.1007/s10853-005-5946-0

[115] S. V. Kalinin, A. Rar & S. Jesse, A decade of piezoresponse force microscopy: Progress, challenges, and opportunities. IEEE Transactions on Ultrasonics, Ferroelectrics, and Frequency Control, **53**, 2226 (2006). https://doi.org/10.1109/TUFFC.2006.169

[116] A. Gruverman, O. Auciello, J. Hatano & S. V. Kalinin, Scanning force microscopy as a tool for nanoscale study of ferroelectric domains. Ferroelectrics, **184**, 11 (1996). https://doi.org/10.1080/00150199608230240

[117] E. Soergel, Piezoresponse force microscopy (PFM). Journal of Physics D: Applied Physics, **44**, 464003 (2011). https://doi.org/10.1088/0022-3727/44/46/464003

[118] S. Somnath, A. Belianinov, S. V. Kalinin, & S. Jesse, Full information acquisition in piezoresponse force microscopy. Applied Physics Letters, **107**, 263102 (2015). https://doi.org/10.1063/1.4938482

[119] B. J. Rodriguez, C. Callahan, S. V. Kalinin, & R. Proksch, Dual-frequency resonance-tracking atomic force microscopy. Nanotechnology, **18**, 475504 (2007). https://doi.org/10.1088/0957-4484/18/47/475504

[120] G. Catalan, J. Seidel, R. Ramesh, & J. F. Scott, Domain wall nanoelectronics. Reviews of Modern Physics, **84**, 119 (2012). https://doi.org/10.1103/RevModPhys.84.119

[121] C. Kittel, Theory of the structure of ferromagnetic domains in films and small particles. Physical Review, **70**, 965 (1946). https://doi.org/10.1103/PhysRev.70.965

[122] C. Kittel, Physical Theory of Ferromagnetic Domains. Reviews of Modern Physics, **21**, 541 (1949). https://doi.org/10.1103/RevModPhys.21.541

[123] T. Mitsui & J. Furuichi, Domain structure of rochelle salt and KH_2PO_4. Physical Review, **90**, 193 (1953). https://doi.org/10.1103/PhysRev.90.193

[124] A. Schilling, T. B. Adams, R. M. Bowman, J. M. Gregg, G. Catalan, & J. F. Scott, Scaling of domain periodicity with thickness measured in BaTiO$_3$ single crystal lamellae and comparison with other ferroics. Physical Review B, **74**, 024115 (2006). https://doi.org/10.1103/PhysRevB.74.024115

[125] C. A. Randall, N. Kim, J.-P. Kucera, W. Cao, & T. R. Shrout, Intrinsic and Extrinsic Size Effects in Fine-Grained Morphotropic-Phase-Boundary Lead Zirconate Titanate Ceramics. Journal of the American Ceramic Society, **81**, 677 (2005). https://doi.org/10.1111/j.1151-2916.1998.tb02389.x

[126] A. Schilling, R. M. Bowman, J. M. Gregg, G. Catalan & Scott, J. F., Ferroelectric domain periodicities in nanocolumns of single crystal barium titanate. Applied Physics Letters, 89, 212902 (2006). https://doi.org/10.1063/1.2393145

[127] G. Catalan, A. Lubk, A. H. G. Vlooswijk, E. Snoeck, C. Magen, A. Janssens, G. Rispens, G. Rijnders, D. H. A. Blank & B. Noheda, Flexoelectric rotation of polarization in ferroelectric thin films. Nature Materials, **10**, 963 (2011). https://doi.org/10.1038/nmat3141

[128] P. Zubko, S. Gariglio, M. Gabay, P. Ghosez & J. M. Triscone, Interface physics in complex oxide heterostructures. Annual Review of Condensed Matter Physics, **2**, 141 (2011). https://doi.org/10.1146/annurev-conmatphys-062910-140445

[129] H. Y. Hwang, Y. Iwasa, M. Kawasaki, B. Keimer, N. Nagaosa, & Y. Tokura, Emergent phenomena at oxide interfaces. Nature Materials, **11**, 103 (2012). https://doi.org/10.1038/nmat3223

[130] I. Kornev, H. Fu & L. Bellaiche, Ultrathin Films of Ferroelectric Solid Solutions under a Residual Depolarizing Field, Physical Review Letter, **93**, 196104 (2004). https://doi.org/10.1103/PhysRevLett.93.196104

[131] I. Ponomareva, I. I. Naumov, I. Kornev, H. Fu, & L. Bellaiche, Atomistic treatment of depolarizing energy and field in ferroelectric nanostructures. Physical Review B, **72**, 140102 (2005). https://doi.org/10.1103/PhysRevB.72.140102

[132] I. I. Naumov, L. Bellaiche, & H. Fu, Unusual phase transitions in ferroelectric nanodisks and nanorods, Nature, **432**, 737 (2004). https://doi.org/10.1038/nature03107

[133] A. Schilling, D. Byrne, G. Catalan, K. G. Webber, Y. A. Genenko, G. S. Wu, J. F. Scott & J. M. Gregg, Domains in Ferroelectric Nanodots, Nano Lett., **9**, 3359 (2009). https://doi.org/10.1021/nl901661a

[134] B. J. Rodriguez, X. S. Gao, L. F. Liu, W. Lee, I. I. Naumov, A. M. Bratkovsky, D. Hesse & M. Alexe, Vortex Polarization States in Nanoscale Ferroelectric Arrays, Nano Lett., **9**, 1127 (2009). https://doi.org/10.1021/nl8036646

[135] L. J. Mcgilly, A. Schilling & J. M. Gregg, Domain bundle boundaries in single crystal BaTiO$_3$ lamellae: searching for naturally forming dipole flux-

closure/quadrupole chains, Nano Lett., **10**, 4200 (2010). https://doi.org/10.1021/nl102566y

[136] R. G. P. Mcquaid, L. J. Mcgilly, P. Sharma, A. Gruverman & J. M. Gregg, Mesoscale flux-closure domain formation in single-crystal BaTiO$_3$. Nature Communications, **2**, 404 (2011). https://doi.org/10.1038/ncomms1413

[137] C. T. Nelson, B. Winchester, Y. Zhang, S. Kim, A. Melville, C. Adamo, C. M. Folkman, S. H. Baek, C. B. Eom, D. G. Schlom, L. Q. Chen, X. Pan, Spontaneous Vortex Nanodomain Arrays at Ferroelectric, Nano Lett., **11**, 828 (2011). https://doi.org/10.1021/nl1041808

[138] C. Jia, K. W. Urban, M. Alexe, D. Hesse & I. Vrejoiu, Direct Observation of Continuous Electric Dipole Rotation in Flux-Closure Domains in Ferroelectric Pb(Zr,Ti)O$_3$, Science, **311**, 1420 (2011). http://doi.org/10.1126/science.1200605

[139] Y. L. Tang, Y. L. Zhu, X. L. Ma, A. Y. Borisevich, A. N. Morozovska, E. A. Eliseev, W. Y. Wang, Y. B. Xu, Z. D. Zhang & S. J. Pennycook, Observation of a periodic array of flux-closure quadrants in strained ferroelectric PbTiO$_3$ films. Science, **348**, 547 (2015). https://doi.org/10.1126/science.1259869

[140] A. K. Yadav, C. T. Nelson, S. L. Hsu, Z. Hong, J. D. Clarkson, C. M. Schleputz, A. R. Damodaran, P. Shafer, E. Arenholz, L. R. Dedon, D. Chen, A. Vishwanath, A. M. Minor, L. Q. Chen, J. F. Scott, L. W. Martin & R. Ramesh, Observation of polar vortices in oxide superlattices, Nature, **530**, 198 (2016). https://doi.org/10.1038/nature16463

[141] S. Das, Y. L. Tang, Z. Hong, M. A. P. Gonçalves, M. R. McCarter, C. Klewe, K. X. Nguyen, F. Gomez-Ortiz, P. Shafer, E. Arenholz, V. A. Stoica, S. -L. Hsu, B. Wang, C. Ophus, J. F. Liu, C. T. Nelson, S. Saremi, B. Prasad, A. B. Mei, D. G. Schlom, J. Iniguez, P. Garcia-Fernandez, D. A. Muller, L. Q. Chen, , J. Junquera, L. W. Martin, & R. Ramesh, Observation of room-temperature polar skyrmions. Nature, **568**, 368 (2019). https://doi.org/10.1038/s41586-019-1092-8

[142] S. Seki, X. Z. Yu, S. Ishiwata & Y. Tokura, Observation of skyrmions in a multiferroic material. Science, **336**, 198 (2012). https://doi.org/10.1126/science.1214143

[143] Y. J. Wang, Y. P. Feng, Y. L. Zhu, Y. L. Tang, L. X. Yang, M. J. Zou, W. R. Geng, M. J. Han, X. W. Guo, B. Wu & X. L. Ma, Polar meron lattice in strained oxide ferroelectrics. Nature Materials, **19**, 881 (2020). https://doi.org/10.1038/s41563-020-0694-8

[144] H. Kishi, Y. Okino, M. Honda, Y. Iguchi, M. Imaeda, Y. Takahashi, H. Ohsato, & T. Okuda, The effect of MgO and rare-earth oxide on formation behavior of core-shell structure in BaTiO$_3$. Japanese Journal of Applied Physics, **36**, 5954 (1997). https://doi.org/10.1143/jjap.36.5954

[145] K. Bi, M. Bi, Y. Hao, W. Luo, Z. Cai, X. Wang & Y. Huang, Ultrafine core-shell $BaTiO_3$@SiO_2 structures for nanocomposite capacitors with high energy density. Nano Energy, **51**, 513 (2018). https://doi.org/10.1016/j.nanoen.2018.07.006

[146] S. Wada, H. Yasuno, T. Hoshina, S. M. Nam, H. Kakemoto & T. Tsurumi, Preparation of nm-sized barium titanate fine particles and their powder dielectric properties. Japanese Journal of Applied Physics, **42**, 6188 (2003). https://doi.org/10.1143/jjap.42.6188

[147] T. Hoshina, S. Wada, Y. Kuroiwa & T. Tsurumi, Composite structure and size effect of barium titanate nanoparticles. Applied Physics Letters, **93**, 2006 (2008). https://doi.org/10.1063/1.3027067

[148] T. Hoshina, Size effect of barium titanate: Fine particles and ceramics. Journal of the Ceramic Society of Japan, **121**, 156 (2013). https://doi.org/10.2109/jcersj2.121.156

[149] F. Li, S. Zhang, D. Damjanovic, L. Q. Chen, & T. R. Shrout, Local Structural Heterogeneity and Electromechanical Responses of Ferroelectrics: Learning from Relaxor Ferroelectrics. Advanced Functional Materials, **28**, 1801504 (2018). https://doi.org/10.1002/adfm.201801504

[150] K. Hirota, S. Wakimoto & D. E. Cox, Neutron and X-ray scattering studies of relaxors. Journal of the Physical Society of Japan, **75**, 111006 (2006). https://doi.org/10.1143/JPSJ.75.111006

[151] H. Takenaka, I. Grinberg & A. M. Rappe, Anisotropic local correlations and dynamics in a relaxor ferroelectric. Physical Review Letters, **110**, 147602 (2013). https://doi.org/10.1103/PhysRevLett.110.147602

[152] I. K. Jeong, T. W. Darling, J. K. Lee, T. Proffen, R. H. Heffner, J. S. Park, K. S. Hong, W. Dmowski & T. Egami, Direct observation of the formation of polar nanoregions in $Pb(Mg_{1/3}Nb_{2/3})O_3$ using neutron pair distribution function analysis. Physical Review Letters, **94**, 147602 (2005). https://doi.org/10.1103/PhysRevLett.94.147602

[153] M. Tyunina & J. Levoska, Coexistence of ferroelectric and relaxor properties in epitaxial films of $Ba_{1-x}Sr_xTiO_3$. Physical Review B, **70**, 132105 (2004). https://doi.org/10.1103/PhysRevB.70.132105

[154] G. H. Haertling, Ferroelectric Ceramics: History and Technology. Ferroelectricity: The Fundamentals Collection, **818**, 157 (2007). https://doi.org/10.1002/9783527618002.ch6

[155] I. Levin, D. S. Keeble, G. Cibin, H. Y. Playford, M. Eremenko, V. Krayzman, W. J. Laws & I. M. Reaney, Nanoscale Polar Heterogeneities and Branching Bi-Displacement Directions in $K_{0.5}Bi_{0.5}TiO_3$. Chemistry of Materials, **31**, 2450 (2019). https://doi.org/10.1021/acs.chemmater.8b05187

[156] M. Eremenko, V. Krayzman, A. Bosak, H. Y. Playford, K. W. Chapman, J. C. Woicik, B. Ravel & I. Levin, Local atomic order and hierarchical polar

nanoregions in a classical relaxor ferroelectric. Nature Communications, **10**, 2728 (2019). https://doi.org/10.1038/s41467-019-10665-4

[157] G. Burns & F. H. Dacol, Crystalline ferroelectrics with glassy polarization behavior. Physical Review B, **28**, 2527 (1983). https://doi.org/10.1103/PhysRevB.28.2527

[158] B. Mihailova, U. Bismayer, B. Güttler, M. Gospodinov, A. Boris, C. Berndhard, & M. Aroyo, Nanoscale phase transformations in relaxor-ferroelectric lead scandium tantalate and lead scandium niobate. Zeitschrift Fur Kristallographie, **220**, 740 (2005). https://doi.org/10.1524/zkri.220.8.740.67075

[159] O. Noblanc, P. Gaucher & G. Calvarin, Structural and dielectric studies of $Pb(Mg_{1/3}Nb_{2/3})O_3$-$PbTiO_3$ ferroelectric solid solutions around the morphotropic boundary. Journal of Applied Physics, **79**, 4291(1996). https://doi.org/10.1063/1.361865

[160] G. Xu, Competing orders in PZN-xPT and PMN-xPT relaxor ferroelectrics. Journal of the Physical Society of Japan, **79**, 33 (2010). https://doi.org/10.1143/JPSJ.79.011011

[161] G. Xu, Z. Zhong, Y. Bing, Z. G. Ye & G. Shirane, Electric-field-induced redistribution of polar nano-regions in a relaxor ferroelectric. Nature Materials, **5**, 134 (2006). https://doi.org/10.1038/nmat1560

[162] D. La-Orauttapong, J. Toulouse, J. L. Robertson & Z. G. Ye, Diffuse neutron scattering study of a disordered complex perovskite crystal. Physical Review B, **64**, 212101 (2001). https://doi.org/10.1103/PhysRevB.64.212101

[163] G. Xu, G. Shirane, J. R. D. Copley & P. M. Gehring, Neutron elastic diffuse scattering study of $Pb(Mg_{1/3}Nb_{2/3})O_3$. Physical Review B, **69**, 064112 (2004). https://doi.org/10.1103/PhysRevB.69.064112

[164] E. Dul'kin, M. Roth, P. E. Janolin, & B. Dkhil, Acoustic emission study of phase transitions and polar nanoregions in relaxor-based systems: Application to the $Pb(Zn_{1/3}Nb_{2/3})O_3$ family of single crystals. Physical Review B, **73**, 012102 (2006). https://doi.org/10.1103/PhysRevB.73.012102

[165] C. Laulhé, F. Hippert, J. Kreisel, M. Maglione, A. Simon, J. L. Hazemann, & V. Nassif, EXAFS study of lead-free relaxor ferroelectric $Ba(Ti_{1-x}Zr_x)O_3$ at the Zr K edge. Physical Review B, **74**, 014106 (2006). https://doi.org/10.1103/PhysRevB.74.014106

[166] D. Fu, H. Taniguchi, M. Itoh, S. Koshihara, N. Yamamoto & S. Mori, Relaxor $Pb(Mg_{1/3}Nb_{2/3})O_3$: A Ferroelectric with Multiple Inhomogeneities, Physical Review Letter, **103**, 207601 (2009). https://doi.org/10.1103/PhysRevLett.103.207601

[167] S. Miao, J. Zhu, X. Zhang, & Z. Y. Cheng, Electron diffraction and HREM study of a short-range ordered structure in the relaxor ferroelectric. Physical Review B, **65**, 052101 (2002). https://doi.org/10.1103/PhysRevB.65.052101

[168] V. V. Shvartsman, B. Dkhil & A. L. Kholkin, Mesoscale domains and nature of the relaxor state by piezoresponse force microscopy. Annual Review of Materials Research, **43**, 423 (2013). https://doi.org/10.1146/annurev-matsci-071312-121632

[169] V. V. Shvartsman & A. L. Kholkin, Evolution of nanodomains in $0.9Pb(Mg_{1/3}Nb_{2/3})O_3$-$0.1PbTiO_3$ single crystals. Journal of Applied Physics, 101, 064108 (2007). https://doi.org/10.1063/1.2713084

[170] V. V. Shvartsman & A. L. Kholkin, Polar structure of $Pb(Mg_{1/3}Nb_{2/3})O_3$-$PbTiO_3$ relaxors: piezoresponse force microscopy approach. Journal of Advanced Dielectrics, **2**, 1241003 (2012). https://doi.org/10.1142/s2010135x12410032

[171] G. H. Kwei, S. J. L. Bilinge, S. -W. Cheong & J. G. Saxton, Pair-distribution functions of ferroelectric perovskites: Direct observation of structural ground states. Ferroelectrics, **164**, 57 (1995). https://doi.org/10.1080/00150199508221830

[172] M. S. Senn, D. A. Keen, T. C. A. Lucas, J. A. Hriljac & A. L. Goodwin, Emergence of Long-Range Order in $BaTiO_3$ from Local Symmetry-Breaking Distortions. Physical Review Letters, **116**, 207602 (2016). https://doi.org/10.1103/PhysRevLett.116.207602

[173] J. R. Neilson & T. M. McQueen, Representational analysis of extended disorder in atomistic ensembles derived from total scattering data. Journal of Applied Crystallography, **48**, 1560 (2015). https://doi.org/10.1107/S1600576715016404

[174] B. Ravel, E. A. Stern, R. I. Vedrinskii & V. Kraizman, Local structure and the phase transitions of $BaTiO_3$. Ferroelectrics, **206**, 407 (1998). https://doi.org/10.1080/00150199808009173

[175] R. E. Cohen, Origin of ferroelectricity in perovskite oxides. Nature, **358**, 136 (1992). https://doi.org/10.1038/358136a0

[176] D. G. Schlom, L. Q. Chen, C. B. Eom, K. M. Rabe, S. K. Streiffer, and J. -M. Triscone, Annu. Strain tuning of ferroelectric thin films, Rev. Mater. Res. **37**, 589 (2007). https://doi.org/10.1146/annurev.matsci.37.061206.113016

[177] A. R. Damodaran, J. C. Agar, S. Pandya, Z. Chen, L. Dedon, R. Xu, B. Apgar, S. Saremi, and L. W. Martin, New modalities of strain-control of ferroelectric thin films, J. Condens. Matter Phys. **28**, 263001 (2016). https://doi.org/10.1088/0953-8984/28/26/263001

[178] P. Keller, H. Ferkel, K. Zweiacker, J. Naser, J. -U. Meyer, and W. Riehemann, The application of nanocrystalline $BaTiO_3$-composite films as CO_2-sensing layers, Sensors and Actuators B **57**, 39 (1999). https://doi.org/10.1016/S0925-4005(99)00151-3

[179] J. E. Spanier, A. M. Kolpak, J. J. Urban, I. Grinberg, L. Ouyang, W. S. Yun, A. M. Rappe, and H. Park, Ferroelectric phase transition in individual single-crystalline

BaTiO$_3$ nanowires, Nano. Lett. **6**, 735 (2006).
https://doi.org/10.1021/nl052538e

[180] M. B. Smith, K. Page, T. Siegrist, P. L. Redmond, E. C. Walter, R. Seshadri, L. E. Brus, and M. L. Steigerwald, Crystal structure and the paraelectric-to-ferroelectric phase transition of nanoscale BaTiO$_3$, J. Am. Chem. Soc. **130**, 6955 (2008). https://doi.org/10.1021/ja0758436

[181] M. Taherinejad, and D. Vanderbilt, Bloch-type domain walls in rhombohedral BaTiO$_3$, Phys. Rev. Lett. **86**, 155138 (2012). https://doi.org/10.1103/PhysRevB.86.155138

[182] A. S. Everhardt, S. Matzen, N. Domingo, G. Catalan, and B. Noheda, Ferroelectric domain structures in low-strain BaTiO$_3$, Adv. Electron. Mater. **2**, 1500214 (2016). https://doi.org/10.1002/aelm.201500214

[183] G. Catalan, Physics of ferroic and multiferroic domain walls, Springer series in materials science, vol 198. Springer, Berlin, Heidelberg (2014). https://doi.org/10.1007/978-3-642-55375-2_9

[184] G. Xiong, O. Moutanabbir, M. Reiche, R. Harder, and I. Robinson, Coherent X-Ray diffraction imaging and characterization of strain in silicon-on-insulator nanostructures, Advanced Materials **26**, 7747 (2014). https://doi.org/10.1002/adma.201304511

[185] T. A. Assefa, Y. Cao, J. Diao, R. J. Harder, W. Cha, K. Kisslinger, G. D. Gu, J. M. Tranquada, M. P. M. Dean, and I. K. Robinson, Scaling behavior of low-temperature orthorhombic domains in the prototypical high-temperature superconductor La$_{1.875}$Ba$_{0.125}$CuO$_4$, Phys. Rev. B **101**, 054104 (2020). https://doi.org/10.1103/PhysRevB.101.054104

[186] S. Labat, M. I. Richard, M. Dupraz, M. Gailhanou, G. Beutier, M. Verdier, F. Mastropietro, T. W. Cornelius, T. U. Schulli, J. Eymery, and O. Thomas, Inversion domain boundaries in GaN wires revealed by coherent Bragg imaging, ACS Nano **9**, 9210 (2015). https://doi.org/10.1021/acsnano.5b03857

[187] X. Huang, W. Yang, R. Harder, Y. Sun, M. Lu, Y. S. Chu, I. Robinson, and H. K. Mao, Deformation twinning of a silver nanocrystal under high pressure, Nano Letters **15**, 7644 (2015). https://doi.org/10.1021/acs.nanolett.5b03568

[188] M. Hytch, F. Houdellier, F. Hue, E. Snoeck, Measurement of the displacement field of dislocations to 0.03 Å by electron microscopy, Nature **453**, 1086 (2008) https://doi.org/10.1038/nature01638

[189] D. Karpov, Z. Liu, T. dos Santos Rolo, R. Harder, P. V. Balachandran, D. Xue, T. Lookman, and E. Fohtung, Three-dimensional imaging of vortex structure in a ferroelectric nanoparticle driven by an electric field, Nat. Commun. **8**, 280 (2017). https://doi.org/10.1038/s41467-017-00318-9

[190] K. Ohwada, K. Sugawara, T. Abe, T. Ueno, A. Machida, T. Watanuki, S. Ueno, I. Fujii, S. Wada, and Y. Kuroiwa, Development of an apparatus for Bragg coherent

X-ray diffraction imaging, and its application to the three-dimensional imaging of BaTiO$_3$ nano-crystals, Jpn. J. Appl. Phys. **58**, SLLA05 (2019). https://doi.org/10.7567/1347-4065/ab38dd

[191] R. Harder, and I. Robinson, Coherent X-Ray Diffraction Imaging of Morphology and Strain in Nanomaterials, JOM. **65**, 1202 (2013). https://doi.org/10.1007/s11837-013-0682-4

[192] M. Monteforte, A. K. Estandarte, B. Chen, R. Harder, M. H. Huang, and I. Robinson, Novel silica stabilization method for the analysis of fine nanocrystals using coherent X-ray diffraction imaging, J. Synchrotron Rad. **23**, 953 (2016). https://doi.org/10.1107/S1600577516006408

[193] J. Ahrens, B. Geveci and C. Law, ParaView: an end-user tool for large data visualization. Elsevier, Visualization Handbook (2005) https://doi.org/10.1016/B978-012387582-2/50038-1

[194] Z. Wang, O. Gorobtsov, A. Singer, An algorithm for Bragg coherent x-ray diffractive imaging of highly strained nanocrystals, New J. Phys. **22**, 013021 (2020). https://doi.org/10.1088/1367-2630/ab61db

[195] B. K. P. Horn, Closed-form solution of absolute orientation using unit quaternions. Journal of the Optical Society of America A, **4**, 629 (1987). https://doi.org/10.1364/josaa.4.000629

[196] B. K. P. Horn, H. M. Hilden & S. Negahdaripour, Closed-form solution of absolute orientation using orthonormal matrices. Journal of the Optical Society of America A, **5**, 1127 (1988). https://doi.org/10.1364/josaa.5.001127

[197] J. D. Hamilton, Time series analysis. Princeton University Press, (1994).

[198] G. E. P. Box, G. N. Jenkins, G. C. Reinsel & G. M. Ljung Time series analysis: forecasting and control. Wiley, (2016).

[199] F. Li, S. Zhang, T. Yang, Z. Xu, N. Zhang, G. Liu, J. Wang, J. Wang, Z. Cheng, Z. Ye, J. Luo, T. R. Shrout & L. Q. Chen, The origin of ultrahigh piezoelectricity in relaxor-ferroelectric solid solution crystals. Nature Communications, **7**, 13807 (2016). https://doi.org/10.1038/ncomms13807

[200] D. Vanderbilt & R. D. King-Smith, Electric polarization as a bulk quantity and its relation to surface charge. Physical Review B, **48**, 4442 (1993). https://doi.org/10.1103/PhysRevB.48.4442

[201] X. Zhu, J. Wang, Z. Zhang, J. Zhu, S. Zhou, Z. Liu & N. Ming, Atomic-scale characterization of barium titanate powders formed by the hydrothermal process. Journal of the American Ceramic Society, **91**, 1002 (2008). https://doi.org/10.1111/j.1551-2916.2007.02227.x

[202] D. R. Chen & X. L. Jiao, Solvothermal synthesis and characterization of barium titanate powders. J. Am. Ceram. Soc., **83**, 2037 (2000). https://doi.org/10.1111/j.1151-2916.2000.tb01606.x

[203] L. R. Prado, N. S. de Resende, R. S. Silva, S. M. S. Egues & G. R. Salazar-Banda, Influence of the synthesis method on the preparation of barium titanate nanoparticles. Chemical Engineering and Processing: Process Intensification, **103**, 12 (2016). https://doi.org/10.1016/j.cep.2015.09.011

[204] M. Boulos, S. Guillemet-Fritsch, F. Mathieu, B. Durand, T. Lebey & V. Bley, Hydrothermal synthesis of nanosized $BaTiO_3$ powders and dielectric properties of corresponding ceramics. Solid State Ionics, **176**, 1301 (2005). https://doi.org/10.1016/j.ssi.2005.02.024

[205] D. A. Keen & A. L. Goodwin, The crystallography of correlated disorder. Nature, **521**, 303 (2015). https://doi.org/10.1038/nature14453

[206] A. F. Suzana, S. Liu, J. Diao, L. Wu, T. A. Assefa, M. Abeykoon, R. Harder, W. Cha, E. S. Bozin and I. K. Robinson. Structural explanation of the dielectric enhancement of barium titanate nanoparticles grown under hydrothermal conditions, submitted to Advanced Functional Materials.

[207] M. Monteforte, A. K. Estandarte, B. Chen, R. Harder, M. H. Huang & I. K. Robinson, Novel silica stabilization method for the analysis of fine nanocrystals using coherent X-ray diffraction imaging. Journal of Synchrotron Radiation, **23**, 953 (2016). https://doi.org/10.1107/S1600577516006408

[208] X. Moya, E. Stern-Taulats, S. Crossley, D. González-Alonso, S. Kar-Narayan, A. Planes, L. Manosa & N. D. Mathur, Giant electrocaloric strength in single-crystal $BaTiO_3$. Advanced Materials, **25**, 1360 (2013). https://doi.org/10.1002/adma.201203823

[209] J. J. Wang, B. Wang & L. Q. Chen, Understanding, Predicting, and Designing Ferroelectric Domain Structures and Switching Guided by the Phase-Field Method. Annual Review of Materials Research, **49**, 127 (2019). https://doi.org/10.1146/annurev-matsci-070218-121843

[210] J. Wang, M. Kamlah & T. Y. Zhang, Phase field simulations of low-dimensional ferroelectrics. Acta Mechanica, **214**, 49 (2010). https://doi.org/10.1007/s00707-010-0322-9

[211] Q. Li, V. A. Stoica, M. Paściak, Y. Zhu, Y. Yuan, T. Yang, M. R. McCarter, S. Das, A. K. Yadav, S. Park, C. Dai, H. J. Lee, Y. Ahn, S. D. Marks, S. Yu, C. Kadlec, T. Sato, M. C. Hoffmann, M. Chollet, M. E. Kozina, S. Nelson, D. Zhu, D. A. Walko, A. M. Lindenberg, P. G. Evans, L. Q. Chen, R. Ramesh, L. W. Martin, V. Gopalan, J. W. Freeland, J. Hlinka & H. Wen, Subterahertz collective dynamics of polar vortices. Nature, **592**, 376 (2021). https://doi.org/10.1038/s41586-021-03342-4

[212] P. Fedeli, M. Kamlah & A. Frangi, Phase-field modelling of domain evolution in ferroelectric materials in the presence of defects. Smart Materials and Structures, **28**, 035021 (2019). https://doi.org/10.1088/1361-665X/aafff8

[213] L. Q. Chen, Phase-field method of phase transitions/domain structures in ferroelectric thin films: A review. Journal of the American Ceramic Society, **91**, 1835 (2008). https://doi.org/10.1111/j.1551-2916.2008.02413.x

[214] Y. L. Li, S. Y. Hu, S. Choudhury, M. I. Baskes, A. Saxena, T. Lookman, Q. X. Jia, D. G. Schlom & L. Q. Chen, Influence of interfacial dislocations on hysteresis loops of ferroelectric films. Journal of Applied Physics, **104**, 104110 (2008). https://doi.org/10.1063/1.3021354

[215] A. K. Tagantsev, Landau expansion for ferroelectrics: Which variable to use, Ferroelectrics, **375**, 19 (2008). https://doi.org/10.1080/00150190802437746

[216] J. Wang & T. Y. Zhang, Size effects in epitaxial ferroelectric islands and thin films. Physical Review B, **73**, 144107 (2006). https://doi.org/10.1103/PhysRevB.73.144107

[217] P. Wu & Y. Liang, Lattice phase field model for nanomaterials. Materials, **14**, 7317 (2021). https://doi.org/10.3390/ma14237317

[218] L. Q. Chen, Phase-field models for microstructure evolution. Annual Review of Materials Science, **32**, 113 (2002). https://doi.org/10.1146/annurev.matsci.32.112001.132041

[219] A. J. Ardell, Gradient energy, interfacial energy and interface width. Scripta Materialia, **66**, 423 (2012). https://doi.org/10.1016/j.scriptamat.2011.11.043

[220] W. G. Cady, Piezoelectricity: an introduction to the theory and applications of electromechanical phenomena in crystals. New York (2018).

[221] D. Berlincourt & H. Jaffe, Elastic and piezoelectric coefficients of single-crystal barium titanate. Physical Review, **111**, 143 (1958). https://doi.org/10.1103/PhysRev.111.143

[222] A. C. Dent, C. R. Bowen, R. Stevens, M. G. Cain & M. Stewart, Effective elastic properties for unpoled barium titanate. Journal of the European Ceramic Society, **27**, 3739 (2007). https://doi.org/10.1016/j.jeurceramsoc.2007.02.031

[223] J. J. Wang, F. Y. Meng, X. Q. Ma, M. X. Xu & L. Q. Chen, Lattice, elastic, polarization, and electrostrictive properties of $BaTiO_3$ from first-principles. Journal of Applied Physics, **108**, 034107 (2010). https://doi.org/10.1063/1.3462441

[224] M. de Jong, W. Chen, H. Geerlings, M. Asta & K. A. Persson, A database to enable discovery and design of piezoelectric materials. Scientific Data, **2**, 150053 (2015). https://doi.org/10.1038/sdata.2015.53

[225] M. de Jong, W. Chen, T. Angsten, A. Jain, R. Notestine, A. Gamst, M. Sluiter, C. K. Ande, S. van der Zwaag, J. J. Plata, C. Toher, S. Curtarolo, G. Ceder, K. A. Persson & M. Asta, Charting the complete elastic properties of inorganic crystalline compounds. Scientific Data, **2**, 150009 (2015). https://doi.org/10.1038/sdata.2015.9

[226] T. Hoshina, Y. Kigoshi, S. Hatta, H. Takeda & T. Tsurumi, Domain contribution to dielectric properties of fine-grained $BaTiO_3$ ceramics. Japanese Journal of Applied Physics, **48**, 09KC01 (2009). https://doi.org/10.1143/JJAP.48.09KC01

[227] N. Oshime, K. Ohwada, A. Machida, N. Fukushima, S. Ueno, I. Fujii, S. Wada, K. Sugawara, A. Shimada, T. Ueno, T. Watanuki, K. Ishii, H. Toyokawa, K. Momma, S. Kim, S. Tsukada, Y. Kuroiwa, The ferroelectric phase transition in a 500 nm sized single particle of $BaTiO_3$ tracked by coherent X-ray diffraction. Japanese Journal of Applied Physics, **61**, SN1008 (2022) https://doi.org/10.35848/1347-4065/ac7d94

[228] J. Diao, M. Cherukara, R. Harder, X. Huang, F. Zhang, B. Chen, A. Ulvestad, S. Song, D. Zhu, D. Keen and Ian Robinson, Unusual breathing behavior of optically excited barium titanate nanocrystals. Crystals, **10**, 365 (2020). https://doi.org/10.3390/cryst10050365

[229] L. Wu, Y. Shen, A. M. Barbour, W. Wang, D. Prabhakaran, A. T. Boothroyd, C. Mazzoli, J. M. Tranquada, M. P. M. Dean & I. K. Robinson, Real Space imaging of Spin Stripe Domain Fluctuations in a Complex Oxide, Physical Review Letters **127**, 275301 (2021). https://doi.org/10.1103/PhysRevLett.127.275301

[230] M. Dierolf, A. Menzel, P. Thibault, P. Schneider, C. M. Kewish, R. Wepf, O. Bunk, Pfeiffer, F. Ptychographic X-ray computed tomography at the nanoscale. Nature, **467**, 436 (2010). https://doi.org/10.1038/nature09419

[231] G. Xiong, J. N. Clark, C. Nicklin, J. Rawle & I. K. Robinson, Atomic diffusion within individual gold nanocrystal, Scientific Report, **4**, 6765 (2014) https://doi.org/10.1038/srep06765

[232] F. Hoffman, E. Tarleton, R. J. Harder, N. W. Philips, P. Ma, J. N. Clark, I. K. Robinson, B. Abbey, W. Liu & C. E. Beck, 3D lattice distortion and defects structures in ion-implanted nanocrystals, Scientific Report, **7**, 45993 (2017). https://doi.org/10.1038/srep45993

[233] F. Hoffman, B. Abbey, W. Liu, R. Xu, B. F. Usher, E. Balaur & Y. Liu, X-ray micro-beam characterization of lattice rotations and distortions due to an individual dislocation, Nature Communication, **4**, 2774 (2013). https://doi.org/10.1038/ncomms3774.

[234] F. Chen, Y. Zhu, S. Liu, Y. Qi, H. Y. Hwang, N. C. Brandt, J. Lu, F. Quirin, H. Enquist, P. Zalden, T. Hu, J. Goodfellow, M. -J. Sher, M. C. Hoffmann, D. Zhu, H. Lemke, J. Glownia, M. Chollet, A. R. Damodaran, J. Park, Z. Cai, I. W. Jung, M. J. Highland, D. A. Walko, J. W. Freeland, P. G. Evans, A. Vailionis, J. Larsson, K. A. Nelson, A. M. Rappe, K. Sokolowski-Tinten, L. W. Martin, H. Wen, A. M. Lindenberg, Ultrafast terahertz-field-driven ionic response in ferroelectric $BaTiO_3$, Phys. Rev. B, **94**, 180104 (2016). https://doi.org/10.1103/PhysRevB.94.180104

[235] M. A. Pfeifer, G. J. Williams, I. A. Vartanyants, R. Harder, I.K. Robinson, Three-dimensional mapping of a deformation field inside a nanocrystal. Nature **442**, 63 (2006). https://doi.org/10.1038/nature04867

[236] I. Robinson, T. Assefa, Y. Cao, G. Gu, R. Harder, E. Maxey, M. Dean, Domain texture of the orthorhombic phase of $La_{2-x}Ba_xCuO_4$. J. Supercond. Nov. Magn., **33**, 99 (2020). https://doi.org/10.1007/s10948-019-05252-z

[237] A.K. Estandarte, C.M. Lynch, M. Monteforte, J. Rawle, C. Nicklin & I. Robinson, Bragg coherent diffraction imaging of iron diffusion into gold nanocrystals, New J. Phys., **20**, 113026 (2018) https://doi.org/10.1088/1367-2630/aaebc1

[238] J. Diao, B. Chen, W. Lin, Q. Luo, X. Liu, J. Shen & I. Robinson, Nucleation of fractal nanocrystallites upon annealing of Fe-based metallic glass. J. Mater. Res., **32**, 1880 (2017). https://doi.org/10.1557/jmr.2017.79

[239] B. Chen, J. Diao, Q. Luo, J. Rawle, X. Liu, C. Nicklin, J. Shen & I. Robinson, In-situ investigation of crystallization and structural evolution of a metallic glass in three dimensions at nano-scale. Mater. Des., **190**, 108551 (2020). https://doi.org/10.1016/j.matdes.2020.108551

[240] J. Ihli, J.N. Clark, A.S. Cote, Y.-Y. Kim, A.S. Schenk, A.S. Kulak, T.P. Comyn, O. Chammas, R.J. Harder, D.M. Duffy, I.K. Robinson, F.C. Meldrum, Strain-relief by single dislocation loops in calcite crystals grown on self-assembled monolayers. Nat. Commun., **7**, 11878 (2016). https://doi.org/10.1038/ncomms11878

[241] D. Berlincourt & H. Jaffe, Elastic and Piezoelectric Coefficients of Single-Crystal Barium Titanate, Phys. Rev. **111**, 143 (1958). https://doi.org/10.1103/PhysRev.111.143

[242] J.N. Clark, L. Beitra, G. Xiong, A. Higginbotham, D.M. Fritz, H.T. Lemke, D. Zhu, M. Chollet, G.J. Williams, M. Messerschmidt, B. Abbey, R.J. Harder, A.M. Korsunsky, J.S. Wark, D.A. Reis, I.K. Robinson, Imaging transient melting of a nanocrystal using an X-ray laser, PNAS, **112**, 7444 (2015). https://doi.org/10.1073/pnas.1417678112

[243] J.N. Clark, L. Beitra, G. Xiong, A. Higginbotham, D.M. Fritz, H.T. Lemke, D. Zhu, M. Chollet, G.J. Williams, M. Messerschmidt, B. Abbey, R.J. Harder, A.M. Korsunsky, J.S. Wark, I.K. Robinson, Ultrafast Three-Dimensional Imaging of Lattice Dynamics in Individual Gold Nanocrystals. Science **341**, 56 (2013). https://doi.org/10.1126/science.1236034

[244] P.B. Allen, Theory of Thermal Relaxation of Electrons in Metals. Phys. Rev. Lett., **59**, 1460 (1987). https://doi.org/10.1103/PhysRevLett.59.1460

[245] J.N. Clark, X. Huang, R. Harder & I.K. Robinson High-resolution three-dimensional partially coherent diffraction imaging. Nat. Commun. **3**, 993 (2012). https://doi.org/10.1038/ncomms1994

[246] S. Kashida, I. Hatta, A. Ikushima, Y. Yamada, Ultrasonic velocities in $BaTiO_3$, J. Phys. Soc. Jpn, **34**, 997 (1973). https://doi.org/10.1143/JPSJ.34.997

[247] T. Ogawa, T. Ikegaya, Elastic constants measured from acoustic wave velocities in barium titanate piezoelectric ceramics, Jpn J. Appl. Phys. **54**, 011501 (2015). http://dx.doi.org/10.7567/JJAP.54.011501

[248] Y. Gao, X. Huang, H. Yan & G. J. Williams, Bragg coherent diffraction imaging by simultaneous reconstruction of multiple diffraction peaks, Physical Review B, **103**, 014102 (2021). http://dx.doi.org/10.1103/PhysRevB.103.014102

Appendices

A. One set of procedures for alignment and measurement using Rigaku diffractometer

1. Alignment:

a. Control→Manual; Attenuator→Auto; All slits→0.03 mm
b. Determining Z-axis
   Moving θ/2θ, X, Y to 0
   Scanninging Z with range: ±1mm; Steps: 0.002mm; Normal Value: -1.78mm
c. Determining ω-angle
   *Setting θ/2θ to 0.5°
   *Doing ω [-1°,1°] scan
   *Setting 2θ/ω to 0°
d. Determining Z-axis again (Range: ±0.1mm; Steps: 0.002mm – half place)
e. Determining Y-axis (Range: ±3mm; Steps: 0.01mm)
f. Determining X-axis
   * Setting receiving slit to 0.3mm; Setting incidence slit to 0.5mm
   * Going to substrate Bragg angle
   (46.06° for DSO 110, 46.52° for STO, 45.52° for KTO, 45.22° for NSO)
   * Doing ω scan to adjust
   * Doing X scan with relative ±3mm
g. Aligning Phi
   101 peak for 110 DSO [a'=3.94 Å]: Chi=44.985°, 2th=32.069°;
   101 peak for 001 STO [a=3.905 Å]: Chi=45°, 2th=32.397°;
   101 peak for 110 NSO [a'=4.010 Å]: Chi=44.885°, 2th=31.565°;
   101 peak for 001 KTO [a=3.988 Å]: Chi=45°, 2th=31.726°;

2. 2θ-ω scan

Goal: Calculating average c lattice params and total thickness of thin film
Way: Doing 2θ-ω scan with speed: 0.5°/min, range: absolute 15°-60°.

3. Rocking curve scan

Goal: Assess the crystallinity of the sample (FWHM of a rocking curve peak)
Way: Measuring intensity as a function of w (2θ fixed)
2θ-ω goes to (001)/(002) interested film peak; ω scan in range of [-3°,3°] with speed: 0.5°/min, step:0.001°.

4. X-ray reflectivity

Goal: Calculating thickness of thin film
Way: Intensity oscillations have spacings related to the film thickness
a. Setting θ/2θ to 0.5°

b. Doing ω [-1°,1°] scan with speed 1°/min
c. Doing 2θ-ω Absolute 0.1°-10°

5. Reciprocal space map

Goal: Determine periodic domain structure, relaxation effect
Way: In tetragonal, Qx(h=k) value of substrate and grown sample is same
means coherent (no relaxation)
STO (103) reflection origin: 2th=77.278°, w=57.074°;
NSO (103) reflection origin: 2th=73.6°, w=55.6°;

B. One set of procedures for doing BCDI at APS 34-ID-C
1. Optics alignment and preparation

The alignments of optics are usually done by the beamline staff prior to the user operation. Taking APS 34-ID-C as an example, the optics and equipment inside the experiment hutch are: Filter box → Fast shutter → JJ slit → KB mirror → Sample Stage → Vacuum X-ray Flight Path → Detector. In alignments, standard samples like Au are used. The slits and KB mirrors alignments can be down by scanning labx and check the intensity shape.

For making the BCDI measurement easier, the centre of rotation is also found in X and Y direction and marked in confocal microscope. This can be simply found by rotation the sample stage (theta). If there is no confocal microscope available and centre of rotation is not determined before the experiment, one can also find it using crystal diffraction by the following steps:

Changing theta angle a bit, then move LabX positive and negative to see the intensity change. If the intensity drops in both directions, then it's in the centre. If it drops one side and rise the other side, then it's misaligned and need to change LabY correspondingly:

Y (X-ray beam)

Theta

X
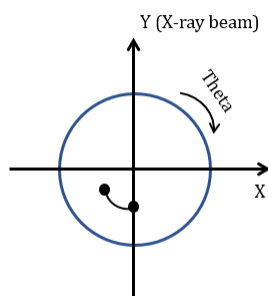
2. Sample mounting and set up experimental condition
Some general condition for an in-situ BCDI experiment includes temperature, voltage, pressure. We have tried heating, cooling and charging/discharging before at both APS 34-ID-C and I-13.

3. Sample flattening by using camera (X-ray eye) downstream

Aligning sample surface to be parallel to the X-ray beam. Generally, there are two ways to align.

Method 1:

(a) Set Phi=0°; Chi=90°; Theta=0°.

(b) Move SamZ to the position that just cutting the direct beam spot.

(c) Adjust Phi and tuning SamZ to make reflective spot and direct beam spot to coincide.

(d) Move Theta to 90°.

(e) Do (b) & (c) again, but this time adjust Chi instead of Phi.

Method 2:

(a) Set Phi=0°; Chi=90°; Theta=0°.

(b) Move SamZ to the position that just cutting the direct beam spot.

(c) Rotate Phi to completely cut direct beam spot at two side, phi1 and phi2, then change phi=phi1/phi2.

(d) Move Theta to 90°.

(e) Do (b) & (c) again, but this time adjust Chi instead of Phi

4. Adjusting centre of rotation

Moving the region of interest into the centre of rotation in confocal microscope in X and Y direction. The sample height, which is Z direction, is also adjusted in confocal microscope.

5. Setting up UB matrix (optional)

For going to multiple diffraction peaks of a single crystal, it's useful to set up the UB matrix before the measurement. This includes:

(a) Setting incident angle by "freeze" (may need "sigtau" to free the fixed flat angle).

(b) Setting up lattice constant and wavelength.

(c) Setting up or0 and or1.

6. Moving to designed Bragg angle and hunting for peaks.
7. Picking up Bragg peaks and doing rocking curve scan measurement.

C. Identification of dislocation in Figure 3.6

BCDI has the ability to locate the dislocation line inside a nanoparticle and identify the type of dislocation line by its characteristic strain field. The characteristic feature of any dislocation is a low-density core in the Bragg

density map and a phase/displacement field around this core. A screw dislocation has a linear relation of displacement as a function of orientation angle given by [11]:

$$u_{screw} = \frac{b}{2\pi} * \theta$$

[u_{screw}: displacement field around screw dislocation; b: Burgers vector; θ: spiral angle around screw dislocation]

An edge dislocation has linear relation plus 2 modulations given by the extra atomic planes [13]:

$$u_{edge} = \frac{b}{2\pi} * (\theta + \frac{\sin(2\theta) - \cos(2\theta)}{4 - 4\nu} + \frac{(4\nu - 2) * log^r}{4 - 4\nu})$$

[u_{edge}: displacement field around the edge dislocation; b: Burgers vector; θ: spiral angle around the edge dislocation; r: radius of the circle around the edge dislocation; ν: Poisson's ratio of the material.]

In this case, the simulated edge dislocation displacement field is plotted in figure 3.7(c). The radial distance r is 30nm and Poisson's ration is 0.23. The value of the Burgers vector is 2.83Å, which is the d-spacing of the corresponding lattice plane.

D. Robustness of fringe cropping and its influence on final reconstruction

We studied the influence of fringes between twin peaks (e.g. Figure 3.1b) on the quality of the final reconstruction.
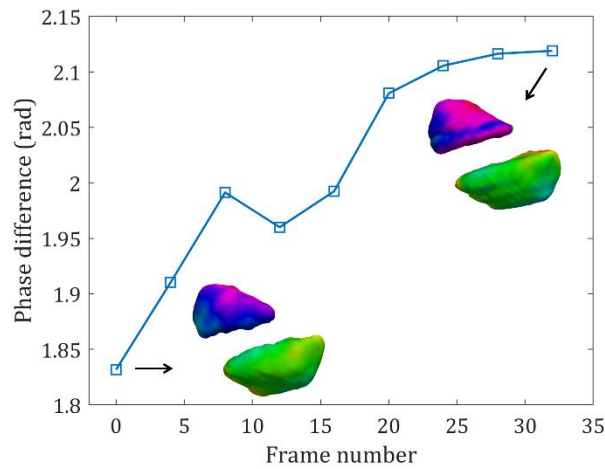
In this case, by adding more of the intermediary fringe frames into the reconstruction, the shape of the crystal, which is defined by Bragg density, remains largely unchanged. However, the relative displacement between the two domains was found to increases gradually and approaches a maximum of 0.2873 rad difference when adding all the fringes. The resolution is expected to improve slightly with more fringes. In this case, however, the resolution was found to remain around 8.4nm.

A redrawing of Figure 3.1, after taking all the fringes into the reconstruction, is shown in Figure D2.
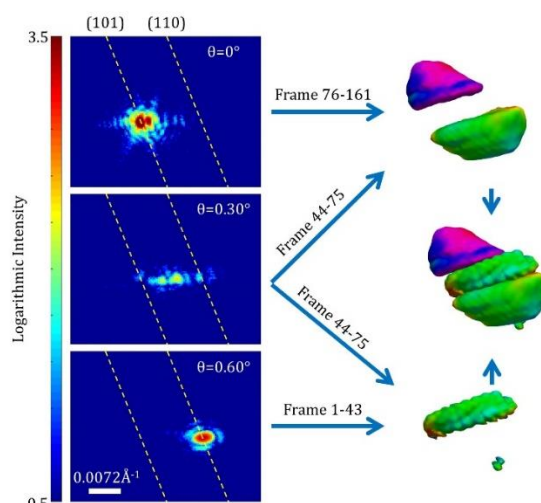
Figure D2. Reconstruction of the separated Bragg peaks with all the intermediary fringes added to both peaks.

E. Combine reconstruction of crystal in Figure 3.1

The diffraction patterns in Figure 1 were reconstructed by separating the two Bragg peaks and manually merging the resulting images. If instead, the reconstructions were carried out on the full data without cropping or separating the peaks, the results are shown in Figure E3.
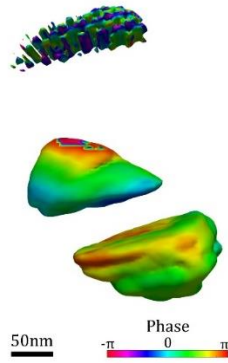
Figure E1. Full-data reconstructed images of the nanoparticles shown in Figure 3.1.

F. Displacement field difference of the nanoparticle in Figure 3.3

To calculate the average displacement field of each grain, the nanoparticle is split at its twin domain boundary, as shown in Figure F1. Because of the discontinuity near the twin boundary, so the volume within 30nm of the boundary is not counted. The average displacement of each region and the displacement difference is listed in Table F1 along with its standard error.
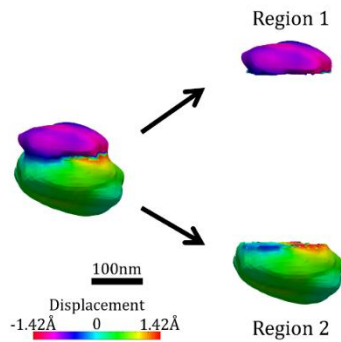
Figure F1. Splitting the nanoparticle into two regions at its twin boundary. The region near the twin boundary is omitted when calculating the average displacement of that region.

Table F1. Measured average displacement of the grains and their difference of the crystal in Figure 3.3.

	Temperature (K)	Average displacement of region 2 (Å)	Average displacement of region 1 (Å)	Displacement difference (Å)
Heating up	387.2	0.381±0.001	-0.764±0.003	1.145±0.003
	389.9	0.085±0.002	-0.612±0.003	0.697±0.003
	392.6	0.105±0.002	-0.072±0.005	0.177±0.005
Cooling down	390.2	0.113±0.002	-0.055±0.008	0.167±0.008
	387.6	0.137±0.003	-0.163±0.005	0.300±0.005
	384.9	0.075±0.003	-0.347±0.003	0.423±0.003
	379.7	0.240±0.002	-0.435±0.003	0.675±0.003
	371.7	0.316±0.002	-0.726±0.002	1.042±0.002
	366.9	0.201±0.003	-0.881±0.002	1.082±0.002

For the heating period, there is a linear relationship with slope k=-0.48±0.26 and coefficient of determination R^2=0.9982.

For the cooling period, the linear fitting gives k=-0.21±0.10 with R^2=0.9427.

G. Slices showing displacement fields in Crystal A and B

$T = 100°C$

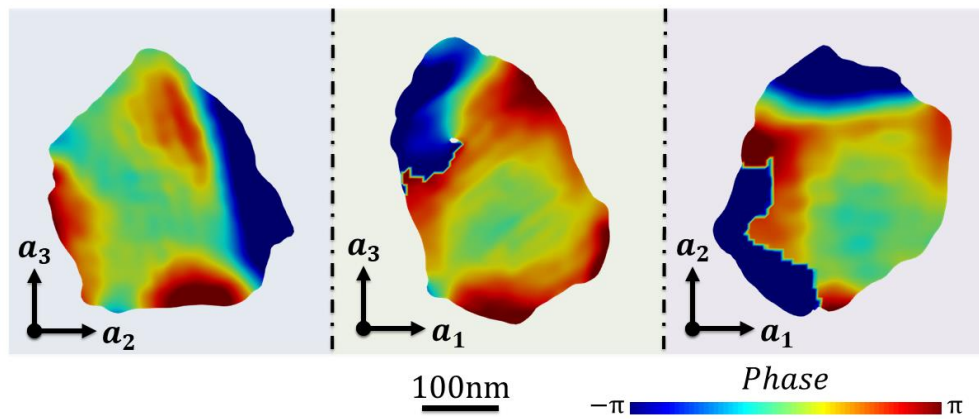Figure G.1 The central slices of Crystal A are presented with phase.
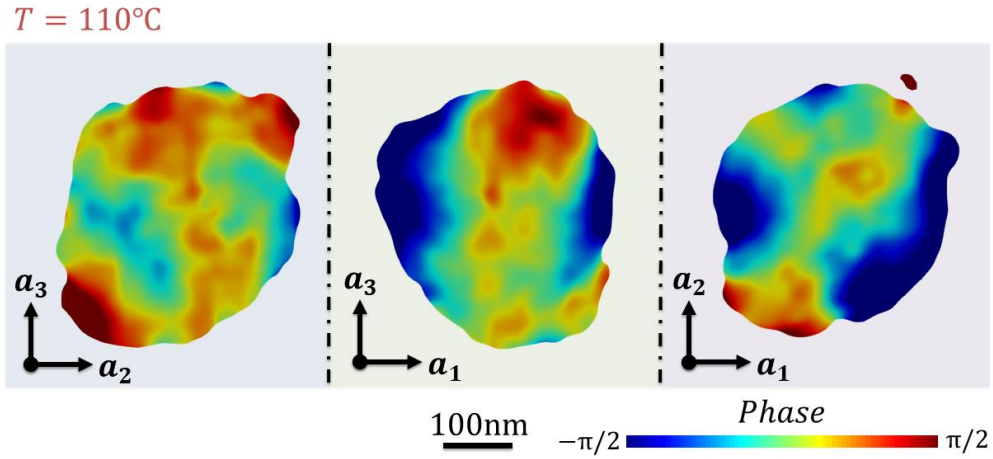
$T = 110°C$

100nm

Phase

$-\pi/2$ ▬▬ $\pi/2$

Figure G.2 The central slices of Crystal B are presented with phase.

H. Simulations using other parameters

We noticed the mechanical and electrical parameters of BTO particles vary a lot from different preparation methods. Here we listed some simulated results from different BTO particles parameters.

2nd set parameters: BTO single crystals	
Properties	Values
Density (ρ)	$6020\ kg \cdot m^3$
Compliance matrix (C)	$\begin{bmatrix} 8.05 & -2.35 & -5.24 & 0 & 0 & 0 \\ -2.35 & 8.05 & -5.24 & 0 & 0 & 0 \\ -5.24 & -5.24 & 15.7 & 0 & 0 & 0 \\ 0 & 0 & 0 & 18.4 & 0 & 0 \\ 0 & 0 & 0 & 0 & 18.4 & 0 \\ 0 & 0 & 0 & 0 & 0 & 8.8 \end{bmatrix} \times 10^{-12}[Pa^{-1}]$
Stiffness matrix (S)	$\begin{bmatrix} 27.51 & 17.90 & 15.16 & 0 & 0 & 0 \\ 17.90 & 27.51 & 15.16 & 0 & 0 & 0 \\ 15.16 & 15.16 & 16.49 & 0 & 0 & 0 \\ 0 & 0 & 0 & 5.43 & 0 & 0 \\ 0 & 0 & 0 & 0 & 5.43 & 0 \\ 0 & 0 & 0 & 0 & 0 & 11.31 \end{bmatrix} \times 10^{10}[Pa]$
Free relative permittivity (ε_r^T)	$\begin{bmatrix} 2920 & 0 & 0 \\ 0 & 2920 & 0 \\ 0 & 0 & 168 \end{bmatrix}$
Clamped relative permittivity (ε_r^S)	$\begin{bmatrix} 1970 & 0 & 0 \\ 0 & 1970 & 0 \\ 0 & 0 & 111 \end{bmatrix}$

236

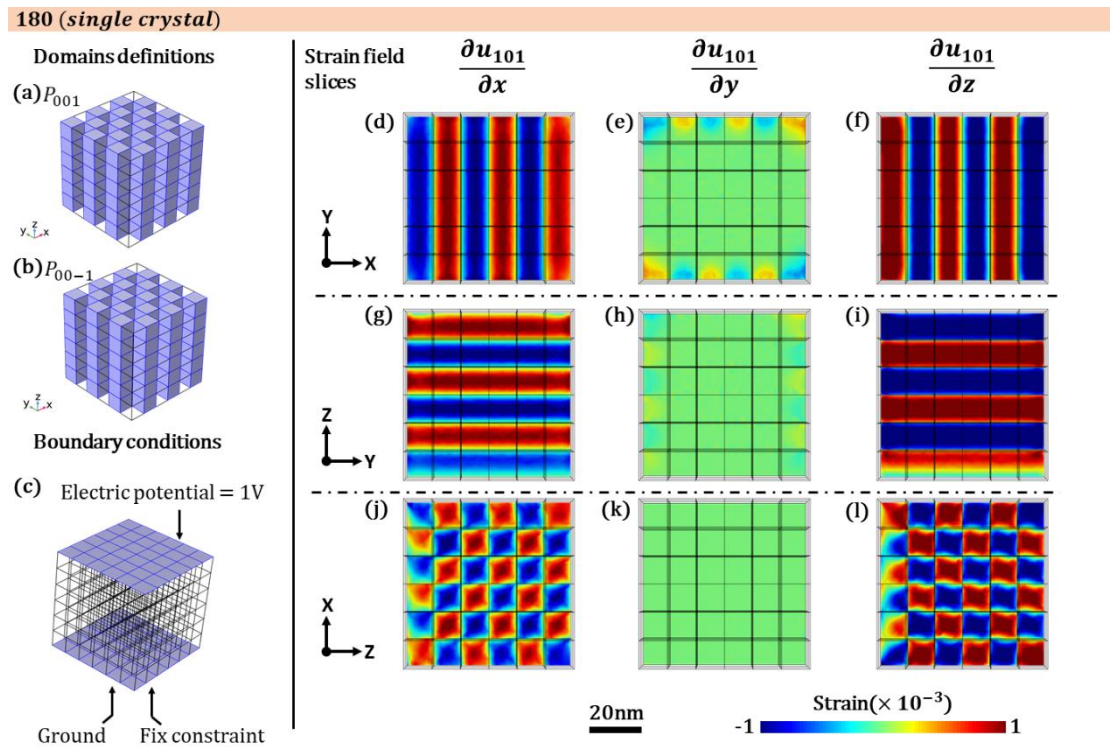| Piezoelectric charge coefficient (P_{001})	$\begin{bmatrix} 0 & 0 & 0 & 0 & 39.2 & 0 \\ 0 & 0 & 0 & 39.2 & 0 & 0 \\ -3.45 & -3.45 & 8.56 & 0 & 0 & 0 \end{bmatrix} \times 10^{-11} [C \cdot N^{-1}]$
Piezoelectric voltage coefficient ($P_{s_{001}}$)	$\begin{bmatrix} 0 & 0 & 0 & 0 & 21.30 & 0 \\ 0 & 0 & 0 & 21.30 & 0 & 0 \\ -2.69 & -2.69 & 3.65 & 0 & 0 & 0 \end{bmatrix} [C \cdot m^{-2}]$

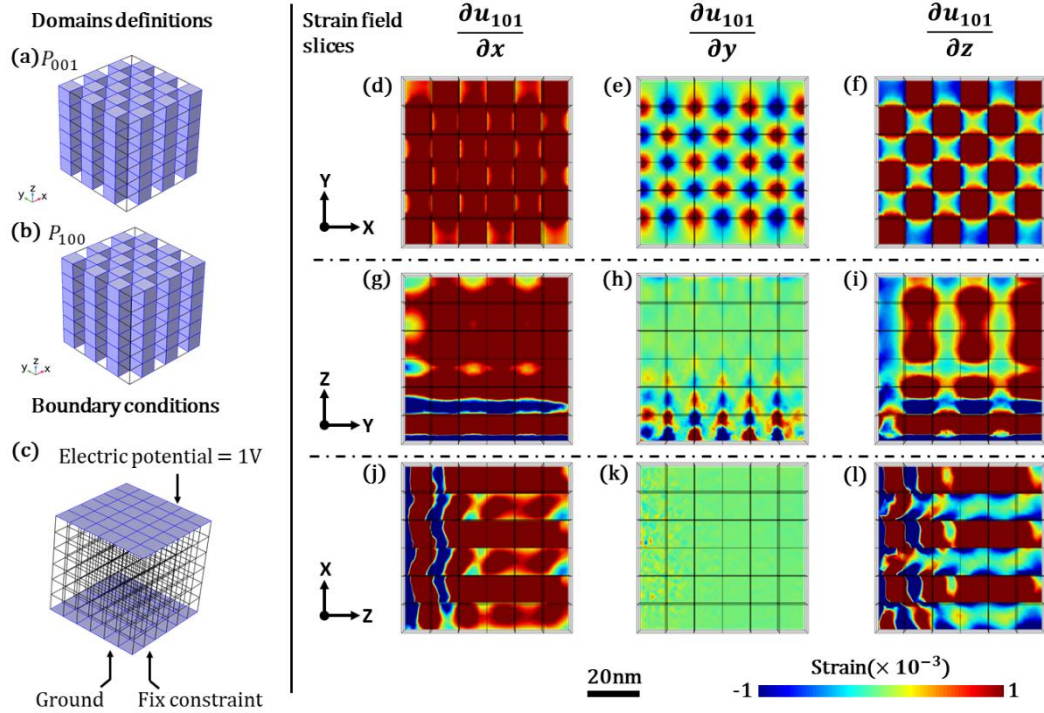Figure H.1 The domain definition, boundary condition and simulated results for a 180° domains packing using single crystal parameters.

Figure H.2 The domain definition, boundary condition and simulated results for a 90° domains packing using single crystal parameters.

Figure H.3 The domain definition, boundary condition and simulated results for the rhombohedral domains defined in Figure 6.3(b). Single crystal parameters are used.

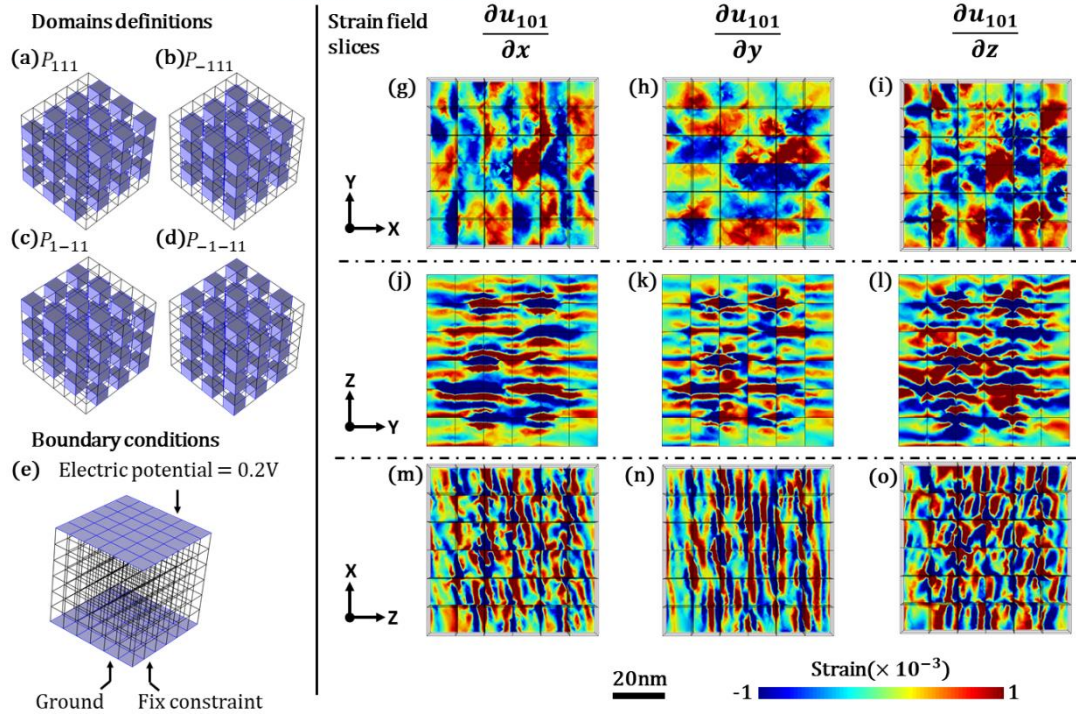**238**

Figure H.4 The domain definition, boundary condition and simulated results for the rhombohedral domains defined in Figure 6.3(c). Single crystal parameters are used.

Figure H.5 The domain definition, boundary condition and simulated results for the rhombohedral domains defined in Figure 6.3(d). Single crystal parameters are used.

Figure H.6 The domain definition, boundary condition and simulated results for the rhombohedral domains defined in Figure 6.3(e). Single crystal parameters are used.
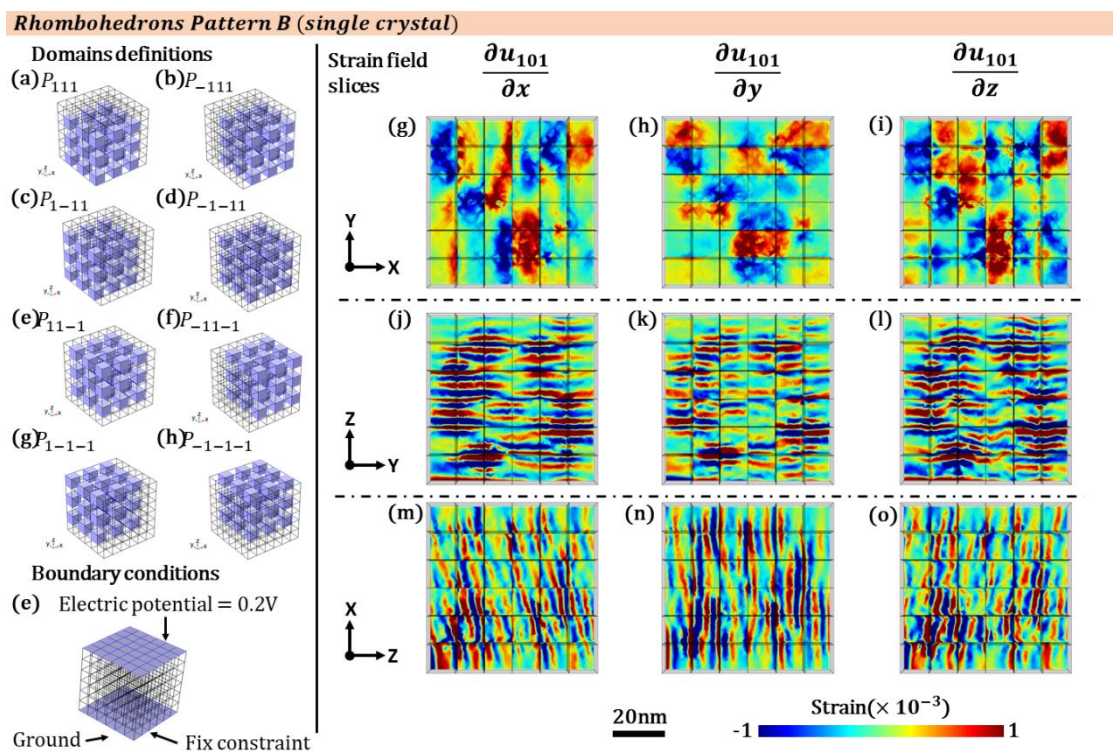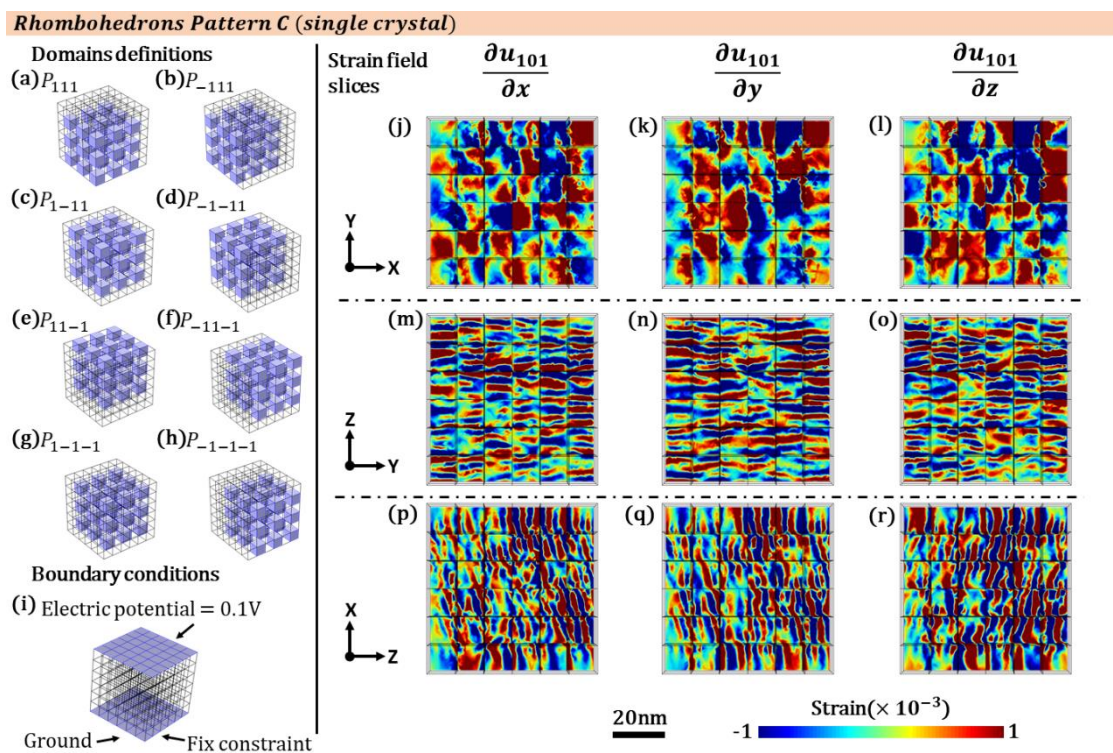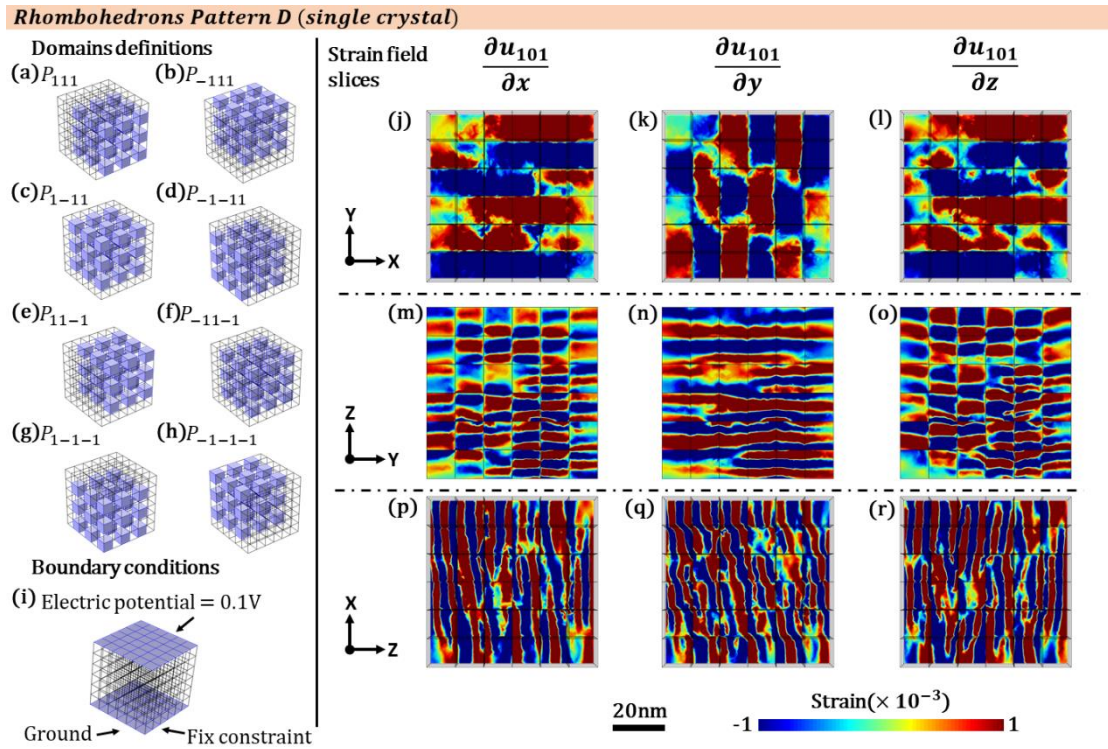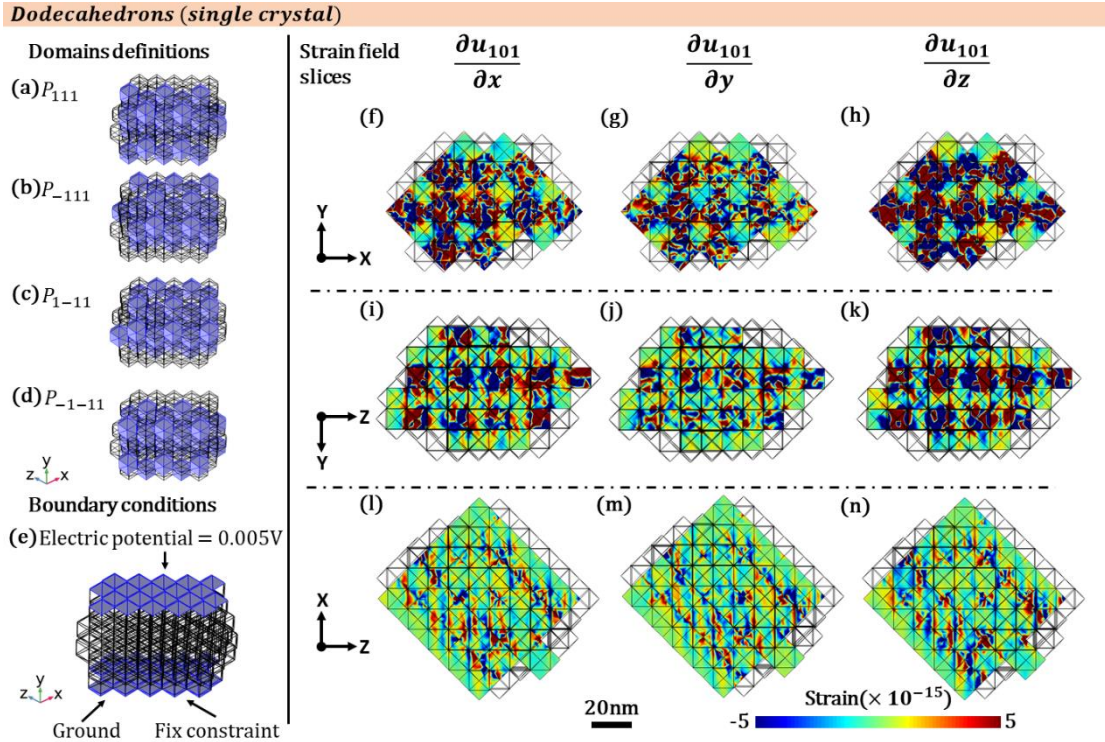
Figure H.7 The domain definition, boundary condition and simulated results for the rhombohedral domains in rhombic dodecahedron model using single crystal parameters.

Here are the simulated results from a self-defined parameters.

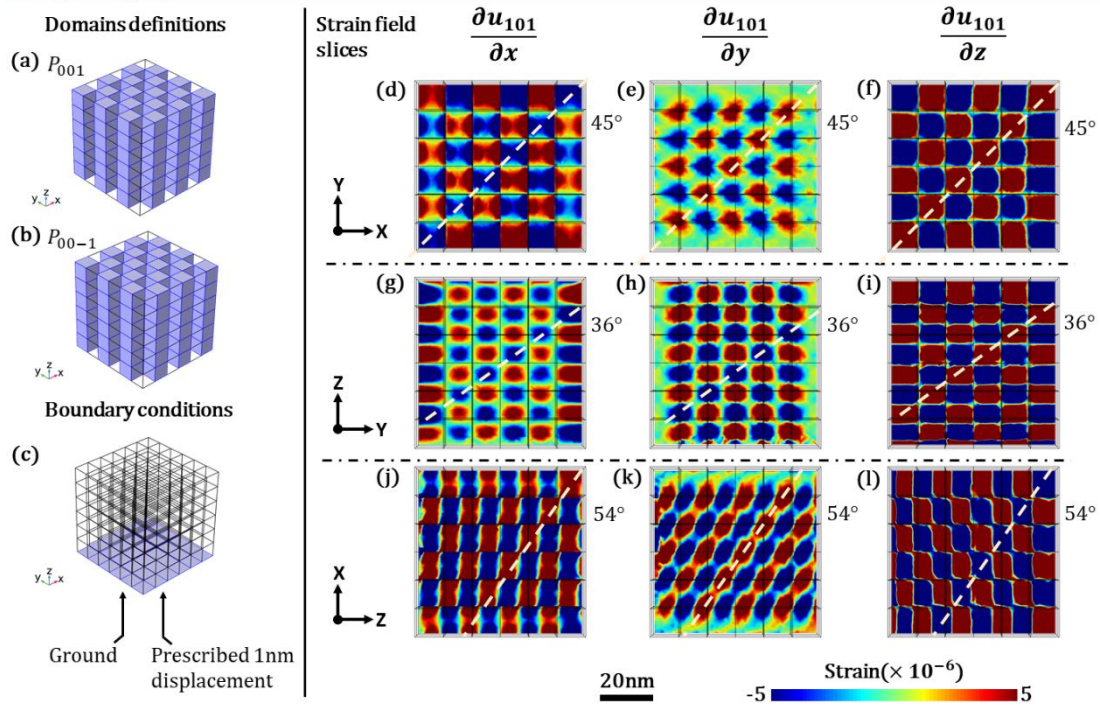| BTO Isotropic Mixed	
Properties	Values
Density (ρ)	$5890 \ kg \cdot m^3$
Compliance matrix (C)	$\begin{bmatrix} 15.7 & -3.68 & -3.68 & 0 & 0 & 0 \\ -3.68 & 15.7 & -3.68 & 0 & 0 & 0 \\ -3.68 & -3.68 & 15.7 & 0 & 0 & 0 \\ 0 & 0 & 0 & 8.84 & 0 & 0 \\ 0 & 0 & 0 & 0 & 8.84 & 0 \\ 0 & 0 & 0 & 0 & 0 & 8.84 \end{bmatrix}$ $\times 10^{-12}[Pa^{-1}]$
Free relative permittivity (ε_r^T)	$\begin{bmatrix} 2920 & 0 & 0 \\ 0 & 2920 & 0 \\ 0 & 0 & 168 \end{bmatrix}$
Piezoelectric charge coefficient (P_{001})	$\begin{bmatrix} 0 & 0 & 0 & 0 & 27 & 0 \\ 0 & 0 & 0 & 27 & 0 & 0 \\ -7.9 & -7.9 & 19.1 & 0 & 0 & 0 \end{bmatrix} \times 10^{-11}[C \cdot N^{-1}]$

Figure H.8 The domain definition, boundary condition and simulated results for a 180° domains packing using mixed parameters.

The self-defined simulated results in Figure H.8 look interesting, but we think the parameters are not realistic. The simulated results from single crystal BTO parameters are listed from Figure H.1 to H.7. The 180 domain wall results in Figure H.1 seems to be similar to Figure 6.6, but with weaker strain field. Others do not fit the experimental figure.

I. Progress on barium titanate thin film growth

Some general methods to make thin film are listed in Table I.1. Among these methods, molecular beam epitaxial (MBE), pulse laser decomposition (PLD) and sputtering are known to grow good quality films.

Table I.1 Different physical and chemical deposition method to prepare thin films.

Physical deposition	Chemical deposition
Vacuum thermal evaporation	Sol-gel technique
Electron beam evaporation	Chemical bath deposition

Pulse laser decomposition	Spray pyrolysis technique
Arc evaporation	Electroplating technique
Molecular beam epitaxy	Electroless deposition
Ion plating evaporation	Low pressure chemical vapor deposition (CVD)
Direct current sputtering	Plasma enhanced CVD
Radio frequency sputtering	Atomic layer deposition

I.1 Off-axis radiofrequency magnetron sputtering

Sputtering is a type of physical vapor decomposition. Generally, it involves energetic particles hitting and ejecting the target materials, which then deposit onto the substrate. In this work, off-axis radiofrequency (RF) magnetron sputtering has been used to prepare epitaxial $BaTiO_3$ thin film. The setup is developed and patented by C. B. EOM [1], while the chamber actually in use is in UCL and designed by Pavlo and Marios.

Figure I.1 shows the EOS chamber that are used to deposit $PbTiO_3$ sample in Pavlo's group. It shares similarity of regular sputtering. Upon sputtering, the gas valve would be open and let the Ar and O_2 gas flow coming into the chamber. The Ar^+ plasma would be attracted by the cathode and bombard the target materials, which then eject the materials into the chamber. These ejected atoms then flow to the heated substrate and deposit onto it layer by layer.
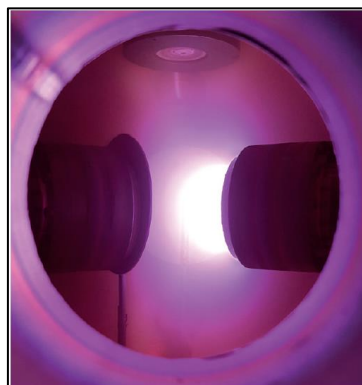
Figure I.1 A photo of the EOS chamber.

There are several optimizations for the system in use to deposit oxide thin film.

1) Off-axis geometry

The off-axis geometry means the target materials and substrate heater stage are not collinear. This is to prevent the re-sputtering process caused by O^{2-} ions. If the substrate is in line with the target, the O^{2-} ions that are released from the target could be driven towards the substrate directly and causing defects. In practice, the heater is place vertically downward, which is 90° to the target.

2) Oscillating RF field

The electric field is set up between target and heater stage to attract the Ar^+ ion to hit the target materials, so as to increase the sputtering speed. An oscillating RF field is used instead of a direct current, which is normally used to sputter metals. This is because many perovskite oxide materials are insulators. An oscillating field can neutralize the charge built on surface due to Ar^+ ion accumulation. Therefore, during the sputtering process, the Ar^+ ions in chamber are attracted to the target in half of the time, and the Ar^+ ions on surface are being repelled from the target surface in the other half.

3) Magnetrons

Magnetrons are put behind the target, with N side magnetrons being put at the centre and S side magnetrons being put at the edge. In such way, the Ar^+ ions being repelled from the target surface would be kept around the target, so as to increase the sputtering rate.

4) Pre-sputtering

Because different element in oxide materials would have different sputtering yield, a pre-sputtering process is carried out before the real sputtering of making thin films. After pre-sputtering for a certain time, the sputtering yield of different element would reach an equilibrium, so as to keep the stoichiometry of the sputtered thin film.

I.2 Materials

The target bulk materials BTO has an in-plane lattice constant a=4.006Å. A series of substrate materials have been used in this study to provide different amount of strain that applied to the sample.

$SrTiO_3$(STO) has cubic structure with a lattice constant of 3.905Å at room temperature and above. It goes through an antiferrodistortive phase transition at 110K, in which the oxygen octahedral is rotated around the tetragonal c axis [2]. STO is a quantum paraelectrics. It has a hypothetical ferroelectricity under Curie-Weiss temperature of 35K, but such ferroelectric order is prevented by quantum fluctuation and the soft-mode frequency never become unstable [3-4].

$DyScO_3$ (DSO) and $NdScO_3$ (NSO) are two types of scandates with large rare-earth element ions, both of which have orthorhombic structure at room temperature. DSO has a lattice of a=5.440Å, b=5.717Å and c=7.903Å. It can be described as a pseudocubic lattice with a_1=3.946Å and a_2=3.952Å. While NSO has a lattice of a=5.575Å, b=5.776Å and c=8.003Å, which can be viewed as a pseudocubic structure with a_1=4.002Å and a_2=4.014Å. These two rare-earth scandates oxide can be grown into large single crystal and ideal for epitaxial thin film growth.

$KTaO_3$(KTO) is also a quantum paraelectric materials as STO and has a hypothetical ferroelectricity transition below 0K. It maintains cubic symmetry with a lattice constant of 3.989Å at room temperature.

Table I.2 The lattice constant of the substrate materials in use and their misfit strain comparing with BTO.

Substrate Materials	Lattice constant at room temperature	Misfit strain to BTO
001 STO	$a_1=a_2$=3.905Å	-2.5%
110 DSO	a=3.946Å; a_2=3.952Å	-1.5%; -1.3%
001 KTO	$a_1=a_2$=3.989Å	-0.4%
110 NSO	a_1=4.002Å; a_2=4.014Å	-0.1%; +0.2%.

I.3 Parameters optimization

In a real sputtering process, many factors are coming into effect. But there are only a few parameters in use to tweak the sputtering condition.

1) RF power

An increase in RF power would increase the sputtering rate.

2) Ar and O_2 gas flow

O_2 gas flow are important to keep the stoichiometry of sputtered thin film.

3) Pressure

A higher pressure would increase the sputtering rate.

4) Substrate temperature

A higher substrate temperature would increase the diffusion speed and help the sputtered film to reach a thermal dynamically stable crystal structure. If the temperature is too high, the as-sputtered species would vapor again. Tweaking the substrate temperature is used the most in this work to find a good sputtering condition, because it doesn't involve pre-sputtering process.

In the past a year and a half, a number of sputtering parameters have been used to optimize the sputtered thin film. We have made some good quality films, but the condition seems not stable.

Figure I.2 shows the measured and simulated θ-2θ scan of 001 peak and 002 peak. From 001 peak, the simulation shows the lattice constant c to be 4.082Å, thickness to be 58 unit cells (u.c.) and RMS to be 0.007796. Similarly, the lattice constant is 4.092Å, thickness is 58 u.c. and RMS is 0.016867 from simulating 002 peak. Both two reflections have well-defined sample fringes.
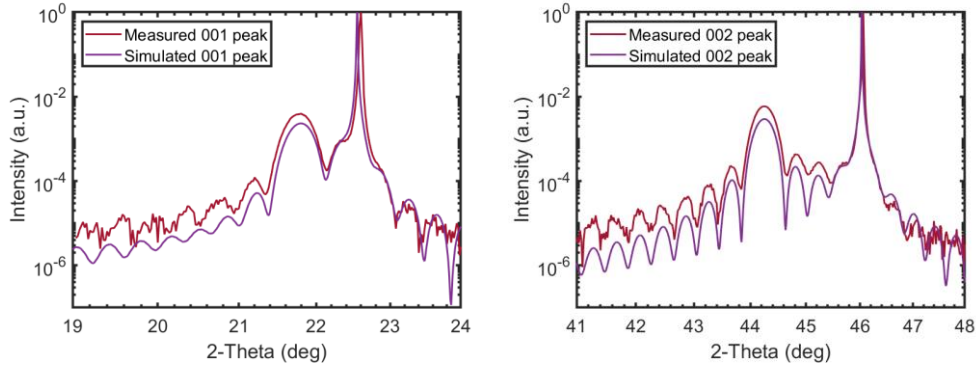
Figure I.2 Measured and simulated θ-2θ scan of one BTO//DSO film at 001 and 002 reflections.
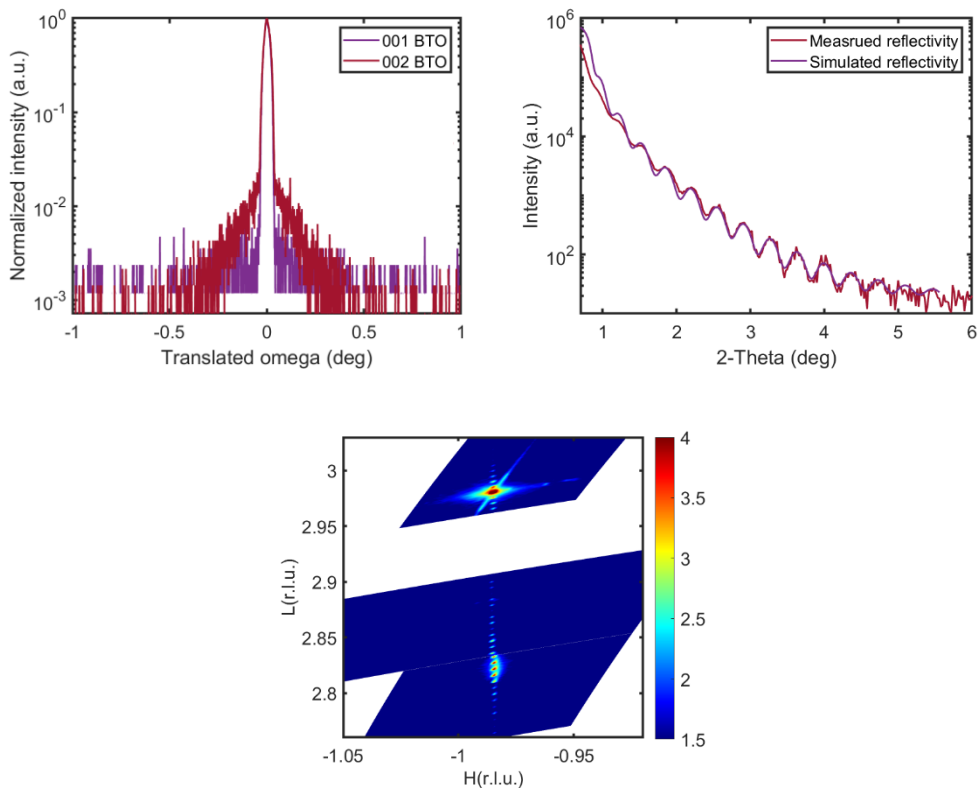

Figure I.3 (a) Measured rocking curve scan on 001 and 002 reflection of the BTO//DSO thin film. (b) Measured and simulated reflectivity curves. (c) Measured 103 reciprocal space map.

Figure I.3a shows the measured rocking curve scan at 001 and 002 peak. The intensity has been normalized and omega value been centred. The narrow distribution of the rocking curve scan indicates the sample film has a narrow distribution of out-of-plane lattice constant, which is a sign of high quality. Figure I.3b presents the measured and simulated reflectivity. The simulated curve gives

a thickness of 236.9Å. In comparison, the thicknesses from simulating 001 and 002 θ-2θ scan are 236.7Å and 237.3Å, which show good consistency. Figure I.3c shows the RSM of the off-specular 103 peaks from substrate DSO and sample BTO. Both substrate and sample peak share the same in-plane reciprocal space index, indicating a coherent in-plane structure with same lattice constant. The sample peak has a small distribution along H direction, revealing a narrow distribution in in-plane direction.

Similar to BTO//DSO thin film, we have made the strained BTO//STO and BTO//KTO. Figure I.4 shows the theta-2theta scan and the reciprocal space map of the best films grown so far.

The strained BTO//STO film has a lattice constant of 4.175Å and a thickness of 87 u.c. with RMS of 0.0015394. The RSM shows sample peak is largely strained, but a little diffusion is still visible, which is a sign of imperfection in lattice constant distribution. Given that the BTO sample and STO substrate has a huge 2.5% compressive strain, and the sample layer has a thickness of 363Å, it might be approaching the critical thickness. Future works will be carried out to optimize the parameters and finding the critical thickness.

The strained BTO//KTO film has a lattice constant of 4.041Å and a thickness of 59 u.c.. The RMS is 0.005338. The RSM presents a purely strained sample peak.
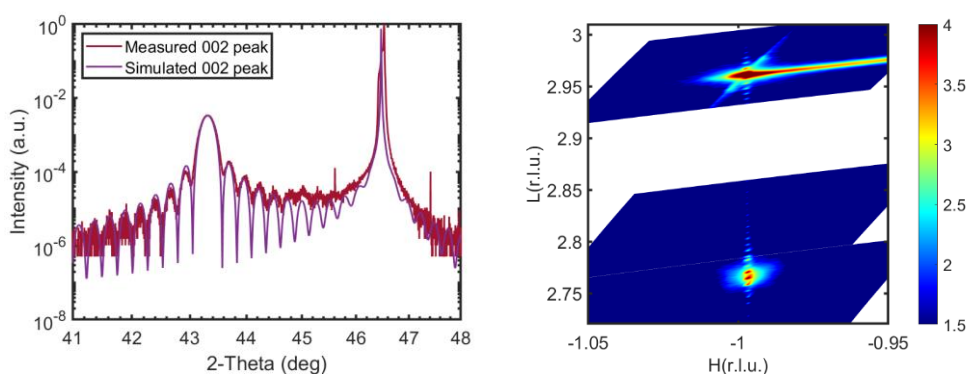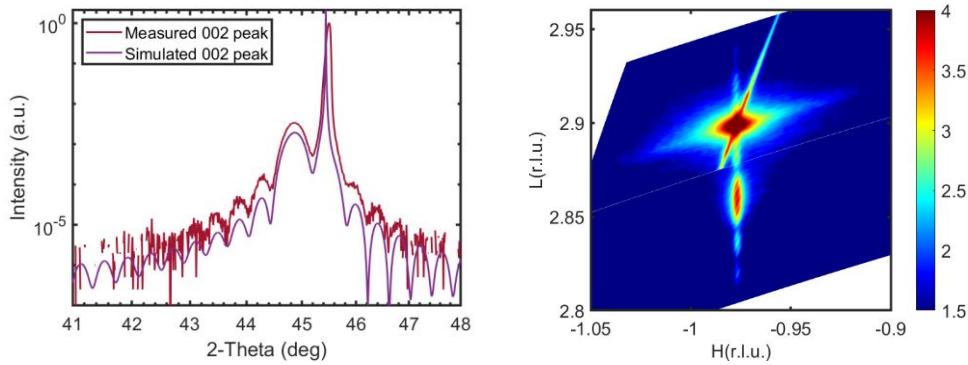
Figure I.4 Left column shows the measured the simulated θ-2θ scan of BTO//STO, BTO//KTO, respectively. The right column presents the corresponding RSM.

I.4 Problems

There are still problems with the current BTO thin film growth. The two main problems are the bad reproducibility and rough sample surface.

Of the films growing so far, the film has weak tendency when tweaking the parameters. In some cases, even with the same parameters, it produces films of different qualities. Figure I.5 shows the θ-2θ scan of two films grown with exactly the same parameters. The second film has visible sample fringes which are not seen in the first film. In addition, the out-of-plane lattice constants are also different.
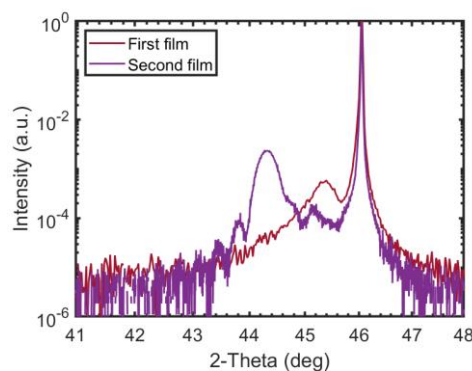
Figure I.5 Measured θ-2θ scan of two BTO//DSO films grown with the same parameters.

We have been testing several assumptions, but still on our way to tackle the issue. The first thing coming in mind is the substrate cleaning issue. Some extra

cleaning steps have been taken, and we plan to use microscope on every substrate before growth to make sure the substrates have good surface. The second thing we are concerned are the temperature drifting of the sample chamber. We have been tweaking the temperature a lot and grow one film at a time instead of two. The third thing we think is there could be contamination on the target materials due to other sputtering process.

Reference

[1] C. -B. Eom, US Patent App. 20130327634. https://patents.justia.com/patent/20130327634

[2] F. Lan, H. Chen, H. Lin, Y. Bai, Y. Yu, T. Miao, Y. Zhu, T. Z. Ward, Z. Gai, W. Wang, L. Yin, E. W. Plummer, J. Shen, PNAS, 116, 4141 (2019). https://doi.org/10.1073/pnas.1819641116

[3] E. K. H. Salje, O. Aktas, M. A. Carpenter, V. V. Laguta and J. F. Scott, PRL 111, 247603 (2013). https://doi.org/10.1103/PhysRevLett.111.247603

[4] J. H. Haeni, P. Irvin, W. Chang, R. Uecker, P. Reiche, Y. L. Li, S. Choudhury, W. Tian, M. E. Hawley, B. Craigo, A. K. Tagantsev, X. Q. Pan, S. K. Streiffer, L. Q. Chen, S. W. Kirchoefer, J. Levy and D. G. Schlom, Nature 430 758 (2004). https://doi.org/10.1038/nature02773